Behavior of CLT-concrete composite floor with dovetail notched connectors

Vanthet Ouch

COLLEGE DOCTORAL BRETAGNE SCIENCES POUR L'INGENIEUR

INSA INSTITUT NATIONAL DES SCIENCES APPLIQUÉES RENNES

THESE DE DOCTORAT DE

L'INSTITUT NATIONAL DES SCIENCES APPLIQUEES DE RENNES

ECOLE DOCTORALE N° 647
Sciences pour l'Ingénieur
Spécialité : *Génie civil*

Par

Vanthet OUCH

Behavior of CLT-concrete composite floor with dovetail notched connectors

Thèse présentée et soutenue à **l'INSA Rennes, le 15/Novembre/2023**
Unité de recherche : EA 3913 Le laboratoire de Génie Civil et Génie Mécanique (LGCGM)
Thèse N° : 23ISAR 32 / D23 - 32

Rapporteurs avant soutenance :

Jose GOUVEIA HENRIQUES	Assistant Professor, Université Hasselt
Emmanuel FERRIER	Professeur, Université Claude Bernard Lyon 1
Sovann Sathya RATH	Enseignant-Chercheur, Institut de technologie du Cambodge

Composition du Jury :

Président :	AbdelHamid BOUCHAIR	Professeur, Université Clermont Auvergne
Examinateurs :	Jose GOUVEIA HENRIQUES	Assistant Professor, Université Hasselt
	Emmanuel FERRIER	Professeur, Université Claude Bernard Lyon 1
	Sovann Sathya RATH	Enseignant-Chercheur, Institut de technologie du Cambodge
	Pierre LATTEUR	Professeur, Université Catholique de Louvain
	AbdelHamid BOUCHAIR	Professeur, Université Clermont Auvergne
Dir. de thèse :	Hugues SOMJA	Professeur, INSA Rennes
Co-Dir. de thèse :	Sovanvichet LIM	Enseignant-Chercheur, Institut de technologie du Cambodge
Co-enc. de thèse :	Piseth HENG	Chercheur, INSA Rennes

COLLEGE DOCTORAL BRETAGNE SCIENCES POUR L'INGENIEUR

INSA INSTITUT NATIONAL DES SCIENCES APPLIQUÉES RENNES

Behavior of CLT-concrete composite floor with dovetail notched connectors

Vanthet OUCH

Doctoral thesis

Rennes, France 2023

Résumé en français

1. Introduction

1.1 Contexte

À la recherche de solutions durables pour les bâtiments, les planchers composites bois-béton (TCC) ont été étudiés pour équilibrer les impacts environnementaux avec les performances structurelles et économiques au lieu des structures en béton traditionnelles qui produisent de fortes émissions de carbone [1][2]. Un plancher TCC est formé en posant un panneau de béton sur un panneau de bois et en les reliant ensemble à l'aide de systèmes de connexion par cisaillement. L'avantage de la combinaison du béton dans la partie compression et du bois dans la partie traction a été décrit en détail par de nombreuses recherches [3]-[11].

Pour le matériau bois dans les structures TCC, afin de répondre au diamètre limité et à la stabilité dimensionnelle des rondins de bois dans les systèmes de plancher, des produits en bois d'ingénierie avec des propriétés physiques et mécaniques améliorées ont été développés [12]. Parmi les produits en bois d'ingénierie disponibles, il est observé que le bois lamellé-croisé (CLT) suscite un intérêt croissant en raison de son agencement transversal des planches de bois dans le panneau CLT, ce qui minimise la disparité directionnelle, fournissant une haute résistance et rigidité dans les deux directions (plancher porteur dans les deux sens) [13].

Concernant le système de connexion béton-bois, différents types de connecteurs de cisaillement dans les structures composites bois-béton ont été étudiés dans le passé, allant des plus flexibles (simples clous ou vis) aux plus rigides (encoches ou connecteurs continus avec de la colle) [4] [14] [15]. Le connecteur à encoche est souvent mis en avant comme le type le plus performant en termes de rigidité et de résistance au cisaillement, tout en maintenant la simplicité de l'application sur site et le contrôle de la qualité. Cependant, le connecteur à encoche présente un comportement très fragile en cas de rupture si aucun raidisseur métallique n'est utilisé [14]. Pour améliorer la ductilité après le pic de performance, des attaches supplémentaires encastrées dans les encoches (pénétrant dans le bois) ont été ajoutées et étudiées par de nombreux chercheurs [4],[16]-[20]. Il convient de noter que l'installation de ces éléments en acier nécessite des outils et des compétences et ralentit le processus de construction.

Dans ce contexte, un nouveau système de connexion à encoche en forme de queue d'aronde pour les planchers composites CLT-béton est proposé et conceptualisé (voir Figure 1a) par Thierry Soquet, architecte de l'agence Architecture Plurielle et concepteur du bâtiment Horizons Bois à Rennes, France, en collaboration avec l'INSA Rennes [21]. La forme particulière de l'encoche en queue d'aronde est capable de limiter la séparation (soulèvement) entre les panneaux de béton et de CLT, tandis que la cage d'armature en forme de V à l'intérieur de l'encoche améliore la résistance au soulèvement et fournit une action de goujon supplémentaire à l'encoche en béton.

1.2 Objectifs du travail et méthodologies

Cette recherche vise à caractériser le comportement local du connecteur à encoche en queue d'aronde proposé et à évaluer la performance globale du plancher composite CLT-béton avec des connecteurs à encoche en queue d'aronde comme système de connexion (voir Figure 1b,c). Cette encoche est proposée en raison de l'assemblage simple et rapide du plancher composite. Tout d'abord, les performances mécaniques

du connecteur à encoche en queue d'aronde telles que la résistance, la rigidité et la ductilité sont caractérisées en effectuant une série de tests de pushout. Ensuite, les résultats des tests sont utilisés comme base pour développer un modèle par éléments finis (EF) afin d'évaluer davantage le mécanisme de transfert de charge du membre composite. De plus, une étude paramétrique utilisant un modèle EF validé est réalisée pour définir la configuration optimisée des connecteurs à encoche en termes de résistance, rigidité, ductilité et modes de rupture. Parallèlement aux tests expérimentaux et à l'étude numérique, une approche analytique alternative utilisant un modèle de bielles et tirants et des équations simplifiées est formulée pour estimer la résistance du connecteur à encoche en fonction des résultats dérivés de l'étude paramétrique.

Suite au comportement local des connecteurs à encoche, le comportement global des planchers composites avec connecteurs à encoche est étudié à travers une série de tests de flexion afin de définir la rigidité en flexion, la résistance et le mode de rupture des planchers composites étudiés. La méthode analytique gamma est ensuite adoptée pour confirmer les résultats des tests obtenus. Enfin, un modèle de plaque orthotrope utilisant un logiciel d'ingénierie est également développé pour une utilisation pratique, permettant aux ingénieurs d'estimer la réponse structurelle de ce type de plancher composite.

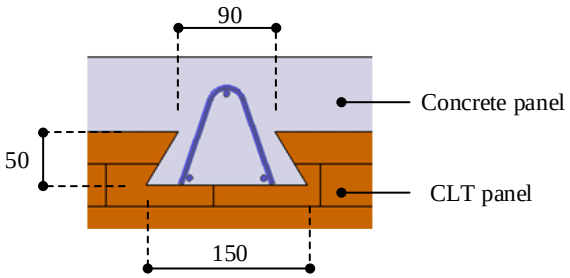

i. Configuration des encoches (unité en mm)

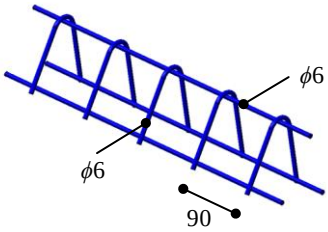

ii. Cage d'armature en forme de V (unité en mm)

a. Système de connexion à encoche en queue d'aronde

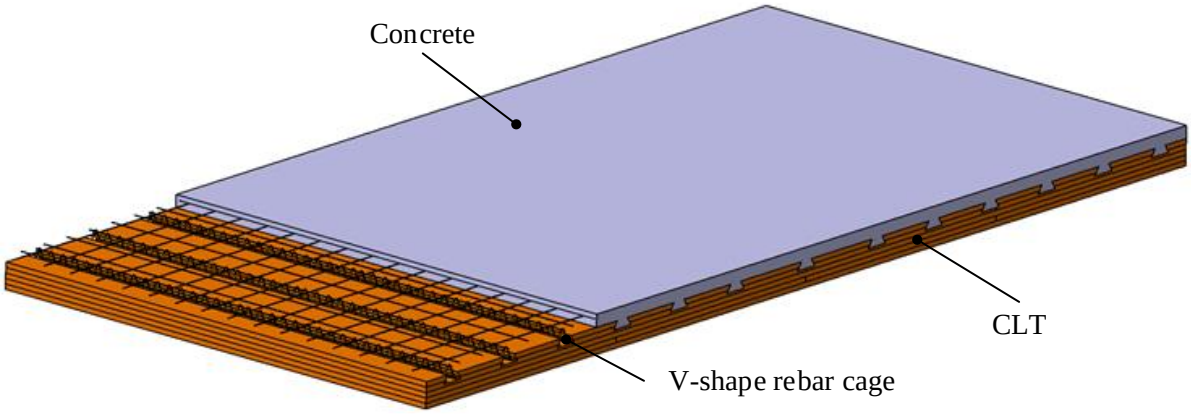

b. Plancher composite CLT-béton, nommé système HOBOA

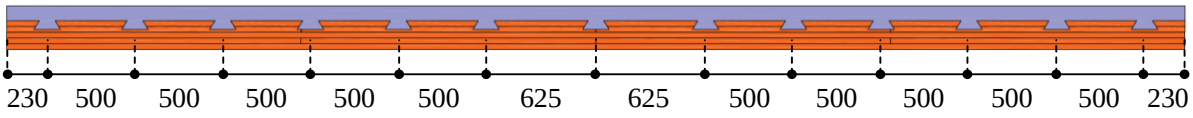

c. Espacement des connecteurs

Figure 1: Plancher composite CLT-béton, nommé système HOBOA avec connexion par encoches.

2. Le comportement local du système de connexion à encoches

Dans cette section, le comportement des connecteurs à encoches est d'abord étudié en réalisant un programme expérimental de trois tests de pushout symétriques. Les résultats de ces tests permettent de déterminer la résistance au cisaillement, la rigidité, la capacité de déformation et le mode de rupture des connecteurs à encoches. Ensuite, le développement d'un modèle tridimensionnel par éléments finis (EF) des tests de pushout est présenté et validé par comparaison avec les résultats expérimentaux. Le modèle EF validé est en outre utilisé pour mieux comprendre les mécanismes de transfert de charge au niveau du système de connexion et pour réaliser une étude paramétrique afin d'examiner l'influence des paramètres importants liés aux propriétés des matériaux et aux géométries du test de pushout sur le comportement du système de connexion. Ensuite, un modèle de bielles et tirants est développé à partir des résultats du modèle EF afin d'estimer la résistance du système de connexion actuel si le mode de rupture est régi par la rupture par cisaillement du béton.

2.1 Test expérimental de pushout

2.2.1 Éprouvette de test

Trois éprouvettes (nommées 1B-1, 1B-2 et 1B-3) ont été fabriquées. Chaque éprouvette était constituée de deux panneaux CLT collés l'un à l'autre et placés entre deux panneaux en béton armé. Chaque panneau en béton armé était relié au panneau CLT par deux connecteurs à encoches. Les dimensions des trois éprouvettes, illustrées à la Figure 2, étaient identiques à l'exception de la largeur *b*. La largeur de l'éprouvette 1B-1 était de 500 mm tandis que celle des éprouvettes 1B-2 et 1B-3 a été ajustée de 500 mm à 400 mm.

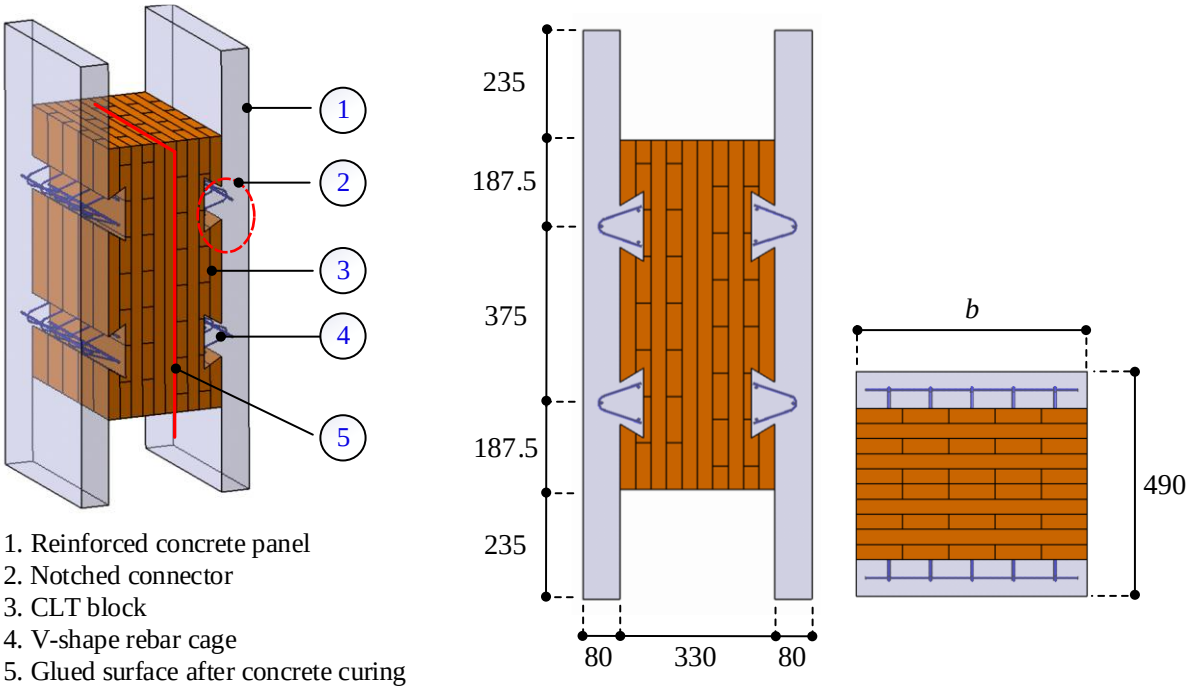

1. Reinforced concrete panel
2. Notched connector
3. CLT block
4. V-shape rebar cage
5. Glued surface after concrete curing

a. Description des spécimens b. Dimensions des spécimens (unité en mm)

Figure 2: Description et dimensions des spécimens de pushout.

Dans cette recherche, un béton de classe de résistance C35/45 a été utilisé et formulé selon la norme EN 206-1 [22], avec la classe d'environnement XF1. En utilisant des essais de compression standard pour la résistance à la compression et des essais brésiliens pour la résistance à la traction, la valeur moyenne de la résistance à la compression et de la résistance à la traction du panneau en béton de tous les tests de pushout est de 34,38 kN et 3,04 kN, respectivement. Le panneau CLT était composé de planches de bois massif d'une classe minimale de C24 et d'une densité moyenne de 420 kg/m^3, spécifiée dans le document technique du produit TOT'm X [23]. En revanche, les barres d'acier pour le panneau en béton et le connecteur à encoche ont une limite d'élasticité nominale de 500 MPa.

2.2.2 Configuration des tests, procédure de chargement et instrumentation

La configuration des tests et la procédure de chargement ont été réalisées conformément à l'Annexe B de l'Eurocode 4 [24], avec des ajustements pour s'adapter à la configuration du plancher composite CLT-béton. Comme illustré à la Figure 3, la configuration des tests comprenait un vérin de force d'une capacité de 1500 kN, une pièce en acier HEB-300 pour le chargement, une éprouvette et une table d'acier de support. Sur la surface supérieure du bloc CLT de l'éprouvette, le vérin de force appliquait une charge verticale uniforme via le profil HEB-300, tandis que la table d'acier de support fournissait une réaction aux panneaux en béton armé.

La force générée par le vérin hydraulique était mesurée à l'aide d'un capteur de force. Les déplacements relatifs entre les panneaux CLT et béton (glissements et soulèvements) pendant le test étaient mesurés à l'aide de la méthode de corrélation d'images numériques (DIC). La précision déterminée pour ce test est actuellement de ± 0,1 mm.

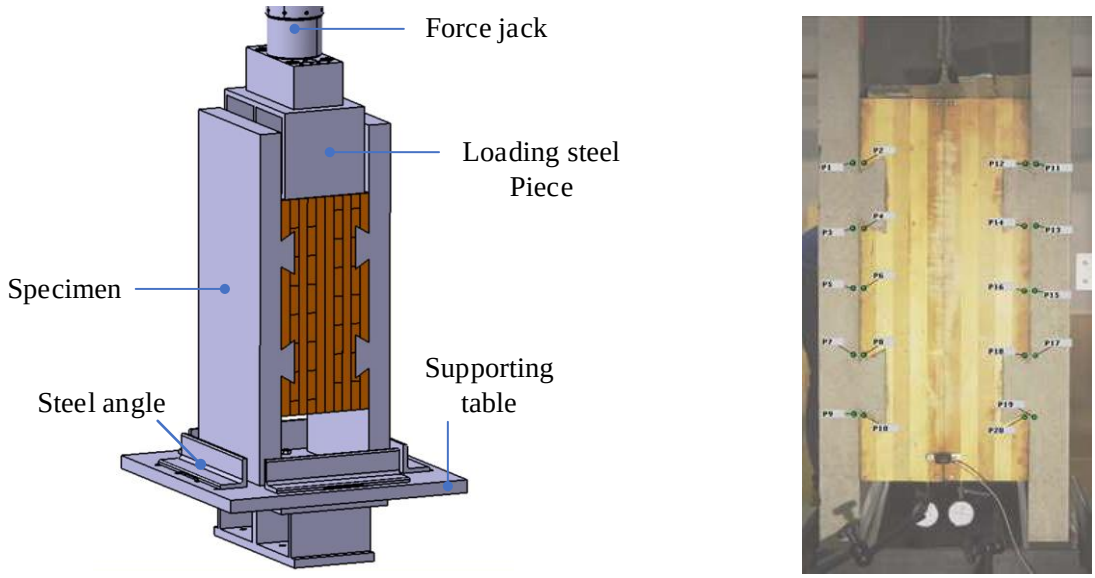

a. Configuration du test de pushout

b. Mesure DIC (corrélation d'images numériques)

Figure 3: Configuration du test de pushout et zones de mesure par corrélation d'images numériques des tests de pushout.

2.2.3 Résultats des tests

2.2.3.1 Observations et mode de rupture

Les forces équivalentes par connecteur par mètre de largeur linéaire étaient de 420 kN/m, 428 kN/m et 464 kN/m pour les tests 1B-1, 1B-2 et 1B-3, respectivement (voir Figure 4a). Globalement, les courbes ont présenté un comportement linéaire jusqu'à ce que la rupture. Dans les trois tests, le mode de rupture était dominé par une rupture fragile par cisaillement de l'une des couches transversales extérieures du panneau CLT (voir Figure 4b).

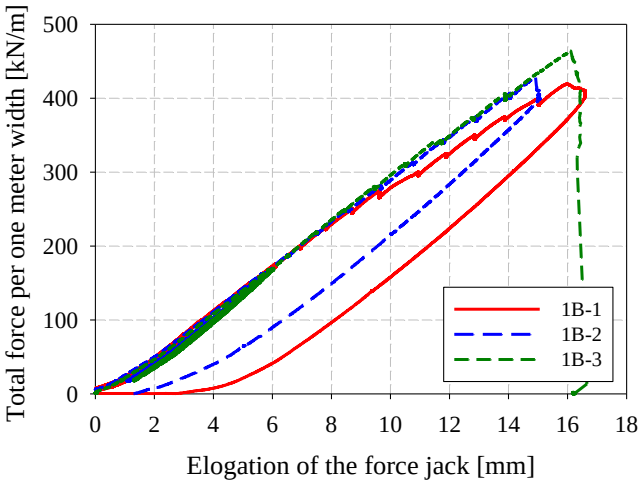

a. Courbes force-allongement

b. Mode de rupture des spécimens

Figure 4: Courbes force-allongement du vérin et mode de rupture des spécimens dans les tests de pushout.

2.2.3.2 Interprétation des tests expérimentaux

La Figure 5 illustre l'évolution des glissements moyens et des soulèvements moyens en fonction de la force par connecteur par mètre de largeur dérivée de la méthode de corrélation d'images numériques (DIC). Les plateaux horizontaux peuvent être liés aux pauses effectuées pendant le chargement afin d'observer l'évolution des dommages dans les spécimens. La valeur maximale ainsi que les glissements moyens et les soulèvements correspondants sont répertoriés dans le Tableau 1. La force maximale moyenne est de 437 kN/m avec un coefficient de variation de 5 %, ce qui indique une faible dispersion expérimentale de la résistance de connexion des trois tests. En raison de la variation significative de la résistance du bois due aux caractéristiques naturelles ou aux défauts, il est surprenant qu'une si faible dispersion des forces ait été observée, étant donné que la rupture était gouvernée par la rupture par cisaillement de la couche transversale du panneau CLT dans les trois tests de pushout.

Le Tableau 1 fournit également les valeurs du module de glissement pour un connecteur à encoche par mètre de largeur à l'état limite de service (K_s) et à l'état limite ultime (K_u), qui peuvent être définies en utilisant l'approche proposée par Ceccotti [14]. Les rigidités présentent une grande déviation par rapport à la déviation des forces maximales appliquées (5 %). Cette grande déviation de la rigidité pourrait provenir en partie de la précision de la mesure des glissements par la méthode DIC pour de faibles valeurs. Il convient

de rappeler que la précision de cette technique dans ces tests était de ±0,1 mm, ce qui correspond à environ 10 % des glissements maximaux.

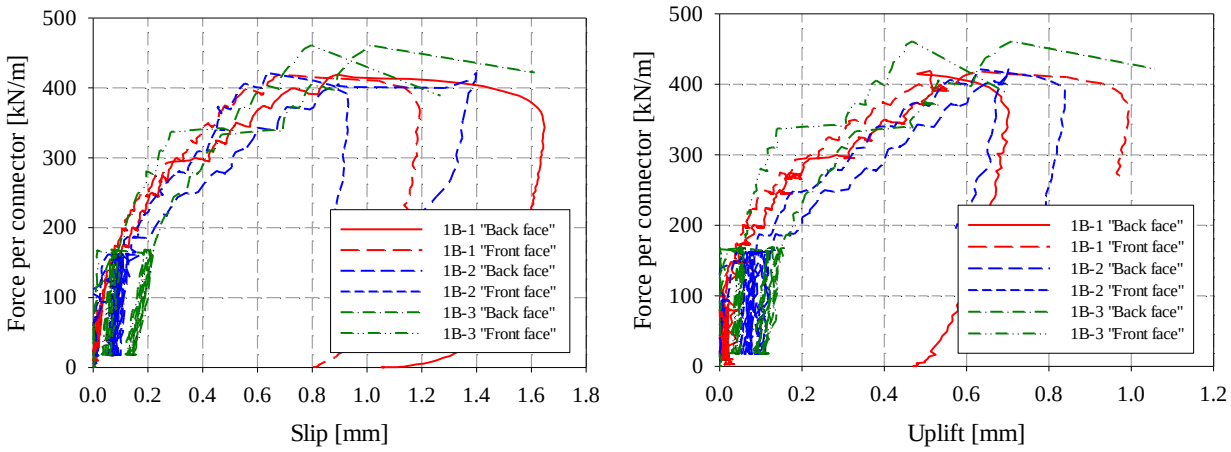

a. Force par connecteur versus glissements b. Force par connecteur versus soulèvements

Figure 5: Courbes de glissement et de soulèvement des trois tests de pushout.

Tableau 1: Valeurs de la force maximale et des modules de glissement pour un connecteur par un mètre de la largeur.

Test	F_{max} [kN/m]	$\delta_{F_{max}}$ [mm]	$g_{F_{max}}$ [mm]	K_s [N/mm/m]	K_u [N/mm/m]
1B-1	420	0.79	0.57	1.81×10^6	1.14×10^6
1B-2	428	1.02	0.67	1.38×10^6	0.85×10^6
1B-3	464	0.9	0.59	1.29×10^6	1.10×10^6
Avg. (CoV)	437 (5%)	-	-	1.49×10^6 (19%)	1.03×10^6 (25%)

2.2 Étude numérique

2.2.1 Établissement du modèle

Afin de développer un modèle EF 3D complet représentant les tests de pushout réels, le programme ABAQUS [25] a été utilisé. Tous les composants de l'éprouvette ainsi que le bloc de chargement en acier ont été modélisés (voir Figure 6a). Pour réduire le coût computationnel et le temps de simulation, seule un quart de la configuration du test a été pris en compte en tirant parti de la disposition symétrique et des conditions aux limites. Des conditions aux limites symétriques ont été appliquées sur les surfaces en rouge et en bleu (voir Figure 6b), restreignant les déplacements dans la direction X et dans la direction Z, respectivement. Le support a été modélisé en appliquant une contrainte rigide à la surface inférieure du panneau en béton qui suit rigidement le mouvement d'un point de référence (voir Figure 6c). Tous les degrés de liberté de ce point de référence ont été fixés. Le chargement a été simulé en appliquant un déplacement imposé à un autre point de référence qui gouverne un déplacement rigide de la bride supérieure du bloc de chargement HEA-300 (voir Figure 6d).

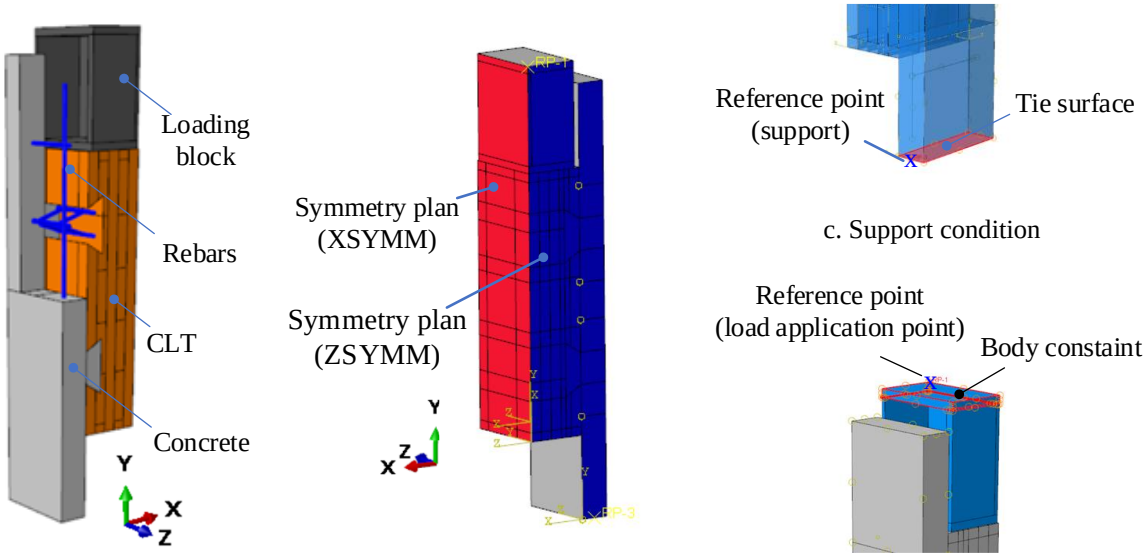

a. Géométrie b. Condition de symétrie d. Condition de chargement

Figure 6: Géométrie et conditions aux limites du modèle EF.

En termes de modélisation des matériaux, le béton a été considéré comme un matériau isotrope non linéaire [26]. Le modèle de plasticité endommageable du béton (CDP) disponible dans Abaqus/Explicit a été adopté [27] pour reproduire correctement les deux principaux comportements du béton (écrasement en compression et fissuration en traction). Les paramètres pour définir le potentiel de flux et la surface de rendement, incluant l'angle de dilatation Ψ, l'excentricité ε, le rapport de résistance à la compression biaxiale sur la résistance à la compression uniaxiale f_{b0}/f_{c0}, le facteur de forme pour la surface de rendement K_c, et le paramètre de viscosité υ, ont été définis comme indiqué dans le Tableau 2. En revanche, le bois a été considéré comme un matériau orthotrope en supposant que la rigidité et la résistance dans les directions radiale et tangentielle étaient identiques. Les rigidités mécaniques ont été déduites des spécifications techniques [28], comme indiqué dans le Tableau 3. La plasticité du bois a été définie en utilisant le critère de limite orthotrope proposé par Hill [29], qui est une extension du critère de Von-Mises. Enfin, les barres d'acier ont été considérées comme un matériau isotrope et ont montré un comportement élasto-plastique bilinéaire dans le modèle EF. Les propriétés, basées sur des tests expérimentaux de la littérature [30], sont résumées dans le Tableau 4.

Tableau 2: Paramètres du modèle de plasticité endommageable du béton.

Ψ [^{0}]	ϵ	f_{b0}/f_{c0}	K_c	υ
40	0.1	1.16	0.67	0

Tableau 3: Propriétés élastiques du matériau bois utilisées dans le modèle EF.

E_1 (MPa)	E_2=E_3 (MPa)	G_{12}=G_{13} (MPa)	G_{23} (MPa)	v_{12}=v_{13}=v_{23}
11000	370	690	127	0

Note: Les abonnements 1, 2, 3 se réfèrent aux directions longitudinale, transversale et radiale, respectivement.

Tableau 4: Propriétés de traction des armatures en acier [30].

f_y (MPa)	f_u (MPa)	E (GPa)	ε_y [-]	ε_u [-]	v
500	635	200	0.00317	0.14559	0.3

Le panneau en béton, le panneau CLT et le bloc de chargement HEA-300 ont été maillés à l'aide d'éléments hexaédriques avec intégration réduite et contrôle du flambage (C3D8R), tandis que les barres d'acier ont été modélisées à l'aide d'éléments de poutre à deux nœuds (B31). Un maillage plus fin (5 mm) a été généré dans la région voisine du système de connexion (voir Figure 7a). Le reste avait une taille de 10 mm.

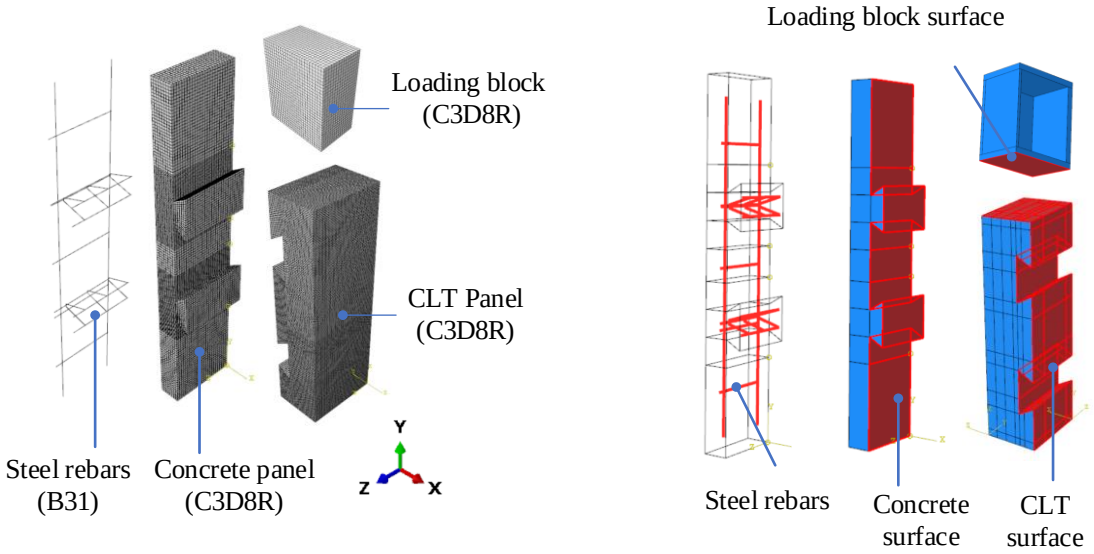

a. Le maillage des composants b. Surface de contact de chaque composant

Figure 7: La sélection du maillage et des surfaces de contact dans le modèle EF.

La contact surface à surface entre le panneau en béton et le panneau CLT ainsi qu'entre le bloc de chargement (HEA 300) et le panneau CLT (voir Figure 7b) a dû être prise en compte. Les propriétés de contact ont été définies par des formulations de contact dur et de pénalisation de frottement pour les comportements normal et tangentiel, respectivement. Dans cette étude, le coefficient de frottement pour les contacts entre le béton et le bois, et entre l'acier et le bois, étaient respectivement de 0,62 [31] et 0,50 [32]. En outre, une contrainte intégrée a été adoptée pour l'interaction entre l'armature en acier et le panneau en béton.

2.2.2 Validation du modèle

Le mode de défaillance simulé était gouverné par la rupture par cisaillement roulant du panneau CLT, reproduisant le même mode de défaillance que dans les tests expérimentaux. Les Figure 8a,b illustrent la forme déformée et la contrainte de cisaillement roulant à une charge maximale obtenue dans le modèle EF. En raison de la configuration du bloc de chargement qui couvre toute la surface supérieure du panneau CLT, une partie de la charge a été transférée directement à l'encoche en béton sous forme de force compressive dans la couche longitudinale et le reste a été transmis par action de cisaillement roulant des couches

transversales (voir Figure 8c). Par conséquent, la véritable résistance au cisaillement roulant devrait être inférieure à la force maximale obtenue lors de l'essai.

La Figure 9a présente la comparaison des courbes force-glissement obtenues à partir du modèle EF et des tests expérimentaux. On peut voir que le modèle EF a estimé une charge maximale d'environ 431 kN, ce qui est en bon accord avec la valeur expérimentale, avec une différence d'environ 2 pour cent. Cependant, le comportement du connecteur à encoche dans le modèle EF est plus rigide, car un glissement plus petit a été obtenu à la charge maximale par rapport aux résultats expérimentaux. En fait, lors des tests expérimentaux, plusieurs chargements cycliques ont été appliqués, et des pauses fréquentes ont été prises pour observer les fissures dans le béton. Cela a généré des glissements supplémentaires en raison des déformations de fluage supplémentaires. Afin de pouvoir comparer les résultats avec ceux du modèle EF, les glissements causés par les chargements cycliques et les pauses ont été retirés des résultats. La Figure 9b présente les nouvelles courbes charge-glissement. Un meilleur accord des courbes a été obtenu. La comparaison entre les résultats obtenus à partir du modèle EF et ceux des tests expérimentaux est résumée dans le Tableau 5. Les différences de force maximale F_{max} et de glissement correspondant $\delta_{F_{max}}$ étaient respectivement de 2 pour cent et 3 pour cent, tandis que des écarts plus élevés de module de glissement ont été observés avec 22 pour cent et 8 pour cent pour les valeurs à l'ELS et à l'ELS, respectivement. La précision de la technique de corrélation d'images numériques adoptée dans les tests de poussée était de 0,1 mm. Par conséquent, il est difficile d'obtenir des valeurs expérimentales précises du module de glissement, car la connexion est très rigide.

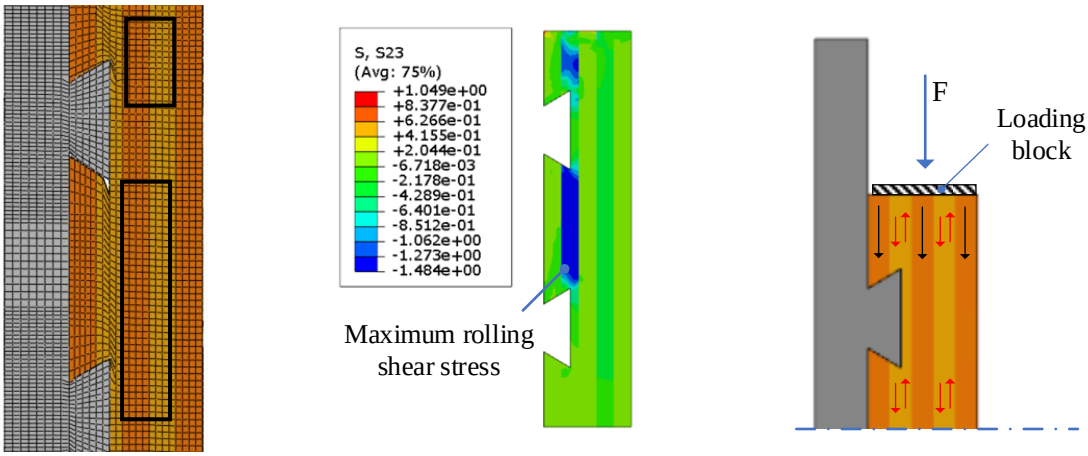

a. Forme déformée b. Contrainte de cisaillement roulant c. Mécanisme de transfert de charge

Figure 8: Forme déformée de la couche transversale, contrainte de cisaillement roulant et mécanisme de transfert de charge du bloc de chargement dans le modèle EF.

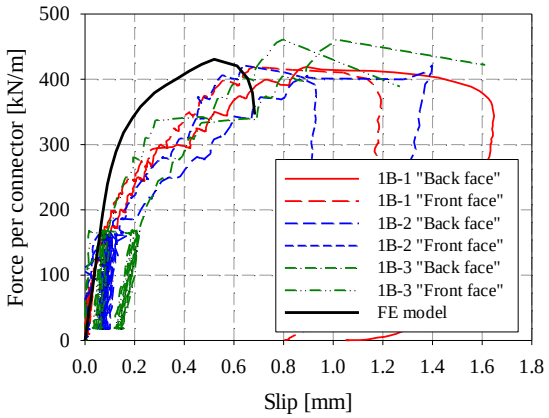

a. Courbes charge-glissement expérimentales originales

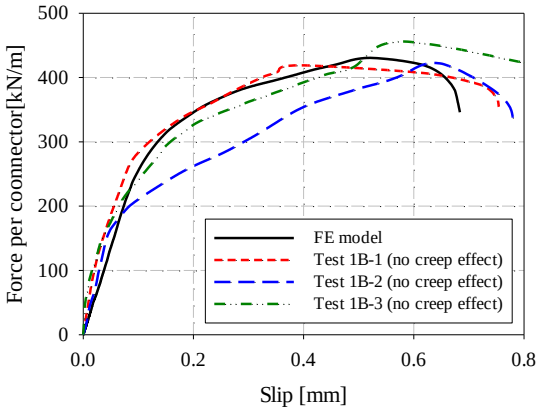

b. Courbes charge-glissement modifiées

Figure 9 : Comparaison des courbes charge-glissement.

Tableau 5: Résultats du modèle EF et des tests expérimentaux.

Test	F_{max} [kN/m]	$\delta_{F_{max}}$ [mm]	K_s [N/mm/m]	K_u [N/mm/m]
Avg.	437	0.54	3.48×10^6	2.24×10^6
FEM	431	0.52	2.73×10^6	2.43×10^6
Diff.	2%	3%	22%	8%

Note: Diff.=(Avg.-FEM)/FEM

2.3 Étude paramétrique

Pour obtenir une compréhension approfondie du comportement mécanique et pour prédire les mécanismes possibles du système de connexion à encoche, une étude paramétrique a été réalisée à l'aide du modèle EF validé. Dans cette étude paramétrique, six paramètres différents ont été considérés, comprenant la résistance du béton f_c, l'épaisseur du panneau en béton h_c, la longueur du talon du panneau CLT l_t, la longueur de l'encoche l_n, la profondeur de l'encoche d_n, et la section transversale des barres d'armature en forme de V à l'intérieur du système de connexion à encoche A_s (voir Figure 10). Les propriétés des matériaux et les géométries du panneau CLT (propriétés mécaniques et épaisseur) n'ont pas été modifiées, car elles étaient fixées dans le processus industriel. De plus, l'angle encoché de $59{,}04^0$ a été maintenu inchangé pour conserver la forme encochée, tandis que les barres d'armature en forme de V ont été ajustées pour s'adapter à l'intérieur du connecteur encoché. Il convient de noter que le cas "C-Ref" a été utilisé comme cas de référence pour cette étude. Les valeurs des paramètres sont détaillées dans le Tableau 6.

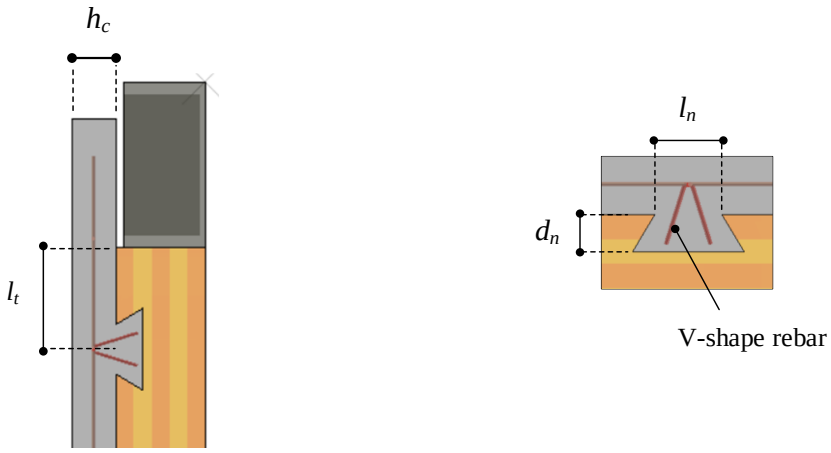

Figure 10 : Paramètres étudiés dans le modèle EF de l'éprouvette de poussée.

Tableau 6 : Résumé des paramètres étudiés.

Étude paramétrique		f_c [MPa]	h_c [mm]	l_t [mm]	l_n [mm]	d_n [mm]	A_s [mm^2]
Case							
Reference	C-Ref	35	80	187.5	90	50	141.37
C1	C1-1	25	80	187.5	90	50	141.37
	C1-2	45					
C2	C2-1	35	50				
	C2-2		100				
C3	C3-1		80	375			
C4	C4-1			187.5	40		
	C4-2				140		
C5	C5-1				90	25	
C6	C6-1					50	0
	C6-2						56.55

Les résistances mécaniques, les raideurs et les mécanismes de rupture des cas étudiés dans l'étude paramétrique sont résumés dans le Tableau 7. La valeur entre parenthèses fait référence au ratio entre les résultats de chaque cas et ceux du cas de référence C-Ref. Les principaux résultats suivants peuvent être mis en évidence:

- La résistance du béton n'a eu aucun impact sur la capacité portante de l'éprouvette. Cependant, en utilisant un béton de moindre résistance, on a observé des dommages plus importants dans les encoches en béton, entraînant un glissement plus important au niveau de la charge maximale. Ainsi, une raideur plus faible a été obtenue dans ce cas. Aucune ductilité n'a été observée après la charge maximale car la rupture était gouvernée par la résistance au cisaillement roulant de la couche transversale du panneau CLT.

- L'épaisseur du panneau en béton a eu une influence légère sur la résistance de l'éprouvette, car la rupture était gouvernée par la rupture au cisaillement roulant dans la couche transversale du panneau CLT. Une variation des modules de glissement a été constatée dans une gamme de 20 % par rapport au cas de référence (C-Ref). Des dommages plus importants en traction des encoches en béton ont été observés en adoptant une épaisseur moindre du panneau en béton.

- L'augmentation de la longueur du talon du panneau CLT de 187,5 mm à 375 mm a suffi pour obtenir la rupture du côté béton de la connexion à encoche avec une augmentation de la force maximale d'environ 22 % par rapport au cas de référence (C-Ref). Une petite amélioration du comportement post-maximum a été obtenue. En termes de modules de glissement, une diminution d'environ 20 % a été observée en comparaison avec le cas C-Ref.

- La variation de la longueur de l'encoche a entraîné une modification de la capacité portante de l'éprouvette. Lorsque la longueur de l'encoche a diminué de 90 mm à 40 mm, la rupture a été obtenue par cisaillement du béton de l'encoche. Les modules de glissement ont diminué presque de moitié par rapport à ceux du cas C-Ref, en raison des dommages précoces de l'encoche en béton. Une légère ductilité a également été obtenue après la charge maximale. En revanche, lorsque la longueur de l'encoche a augmenté, la rupture de l'éprouvette était gouvernée par la rupture au cisaillement roulant du panneau CLT. Dans ce cas, des modules de glissement plus élevés ont été observés, avec une différence d'environ 15 % par rapport au cas C-Ref.

- Une réduction de la profondeur de l'encoche à une valeur inférieure à l'épaisseur de la première couche longitudinale du panneau CLT a entraîné une augmentation de la zone de la couche transversale du panneau CLT. En conséquence, une résistance et une raideur plus élevées d'environ 20 % ont été obtenues par rapport au cas C-Ref. Bien que la rupture au cisaillement du système de connexion se soit produite du côté béton, aucune amélioration de la ductilité n'a été remarquée, ce qui était probablement dû à la longueur d'ancrage insuffisante des barres d'armature en forme de V.

- Une plus grande quantité de barres d'armature en forme de V a augmenté la résistance de la connexion à encoche. Lorsqu'aucune armature de cisaillement n'était utilisée, l'éprouvette était gouvernée par la rupture au cisaillement de l'encoche en béton. Aucune ductilité n'a été remarquée après la charge maximale.

Tableau 7: Résumé des résultats obtenus de l'étude paramétrique.

Étude paramétrique	F_{max} [kN]	K_s [N/mm/m]	K_u [N/mm/m]	Mode de rupture
C-Ref	431	2.73×10^6	2.43×10^6	RS
C1-1	429 (1.00)	2.58×10^6 (0.95)	2.03×10^6 (0.84)	RS
C1-2	430 (1.00)	2.73×10^6 (1.00)	2.63×10^6 (1.08)	RS
C2-1	419 (0.97)	2.17×10^6 (0.79)	1.96×10^6 (0.81)	RS
C2-2	435 (1.01)	2.87×10^6 (1.05)	2.62×10^6 (1.08)	RS
C3-1	526 (1.22)	2.51×10^6 (0.92)	1.95×10^6 (0.80)	CS
C4-1	425 (0.99)	1.51×10^6 (0.55)	1.11×10^6 (0.45)	CS
C4-2	370 (0.86)	2.88×10^6 (1.05)	2.80×10^6 (1.15)	RS
C5-1	515 (1.20)	2.78×10^6 (1.04)	2.54×10^6 (1.14)	CS
C6-1	364 (0.84)	2.63×10^6 (0.97)	2.60×10^6 (1.07)	CS
C6-2	427 (0.99)	2.68×10^6 (0.87)	2.36×10^6 (0.97)	RS+CS

En conclusion, suite aux résultats des simulations numériques de l'étude paramétrique, des résistances élevées et des modules de glissement élevés du système de connexion ont été obtenus sous l'influence des paramètres étudiés. Ainsi, il est possible d'améliorer la ductilité de la connexion à entaille en priorisant la rupture par cisaillement du béton de l'entaille, à condition qu'un nombre suffisant de barres d'armature en forme de V soient placées à l'intérieur de l'entaille. Cette priorisation peut être obtenue en augmentant l'espacement entre les connecteurs, afin d'augmenter la résistance au cisaillement transversal du panneau CLT. La rupture du béton devrait se produire pour une charge supérieure de 22 % à la résistance expérimentale obtenue par les tests de poussée. Cependant, ces conclusions doivent être confirmées par des investigations expérimentales supplémentaires.

2.4 Évaluation analytique de la résistance de la connexion à encoches

Dans cette section, l'évaluation de différentes approches analytiques pour estimer les capacités portantes du système de connexion à encoches est examinée. Suite aux deux modes de défaillance avec leurs résistances correspondantes obtenues expérimentalement et numériquement, des méthodes analytiques sont adoptées pour estimer la résistance au cisaillement de l'encoche en béton et la résistance au cisaillement de roulement du panneau CLT. De plus, les formules pour définir les modes de défaillance restants, y compris les résistances à la compression du béton et du bois, sont également fournies.

2.4.1 Résistance au cisaillement de l'encoche en béton

Pour définir la résistance au cisaillement de l'encoche en béton, un modèle bielle-tirant a été développé. Le modèle bielle-tirant du panneau en béton a été élaboré sur la base des forces de contact et de la carte des contraintes principales obtenues à partir du modèle EF de l'essai expérimental (cas C-Ref). Cependant, certains paramètres ont été modifiés, notamment le nombre de barres en forme de V et le coefficient de frottement afin d'obtenir une défaillance par cisaillement dans le béton. Le coefficient de frottement de 0,4 entre le panneau en béton et le panneau CLT a été adopté conformément à la valeur recommandée par l'Eurocode 5 [35], tandis que le nombre de barres en forme de V a été réduit de cinq barres (141,37 mm²) à trois barres (56,55 mm²).

Le modèle bielle-tirant a été développé à partir des résultats de la simulation numérique où les barres en forme de V dans les deux connecteurs à encoches subissaient une contrainte de limite élastique (voir Figure 11). À un niveau de charge de 0,92F_{max} correspondant à un glissement de 1,6 mm, toutes les barres en forme de V dans les encoches du modèle EF ont subi une contrainte de limite élastique d'environ 500 MPa (voir Figure 11c).

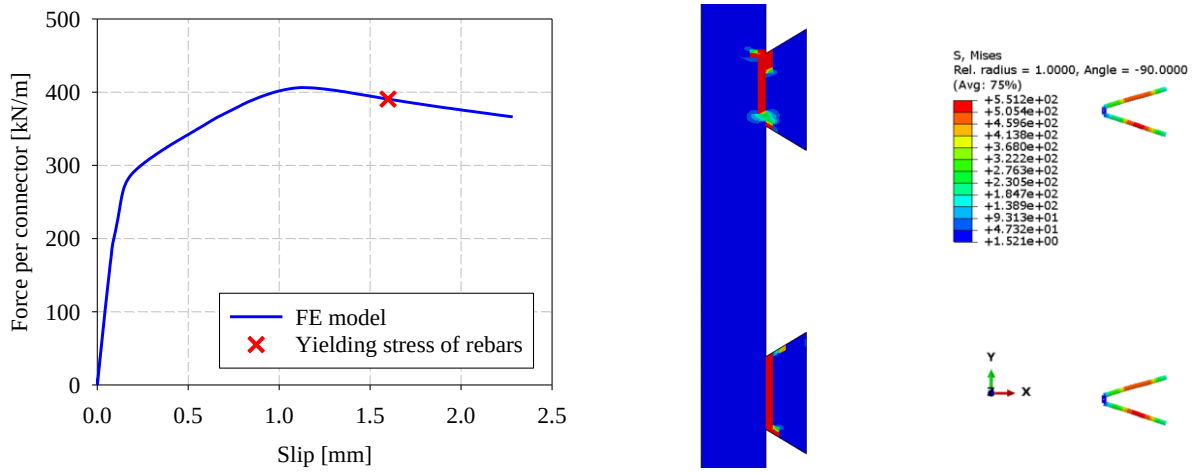

a. Courbe force-glissement du modèle EF b. Endommagement en traction c. Contrainte des barres en forme de V

Figure 11: Courbe force-glissement, endommagement en traction du panneau en béton, et contrainte des barres en forme de V à l'étape de chargement post-pic du modèle EF.

Pour le développement du modèle bielle-tirant sur l'ensemble du panneau en béton de l'éprouvette de poussée, les forces de contact appliquées au panneau en béton ainsi que les forces de réaction sur le panneau en béton étaient nécessaires. Ces détails pouvaient être obtenus à partir du modèle EF en extrayant les forces résultantes des forces normales de contact et des forces de friction de contact à la surface de contact entre les panneaux en béton et en CLT. La Figure 12a montre les zones soumises aux forces de contact (couleurs noir et rouge) et les diagrammes de force dans le modèle EF. Le Figure 12b,c montrent la numérotation des forces résultantes sur les connecteurs d'encoche supérieur et inférieur, respectivement. Les valeurs des forces de contact ainsi que l'angle des orientations des forces par rapport à l'axe vertical sont rapportées dans le Tableau 8. Il a été constaté que les forces de contact étaient concentrées dans la région voisine des deux connecteurs à encoches.

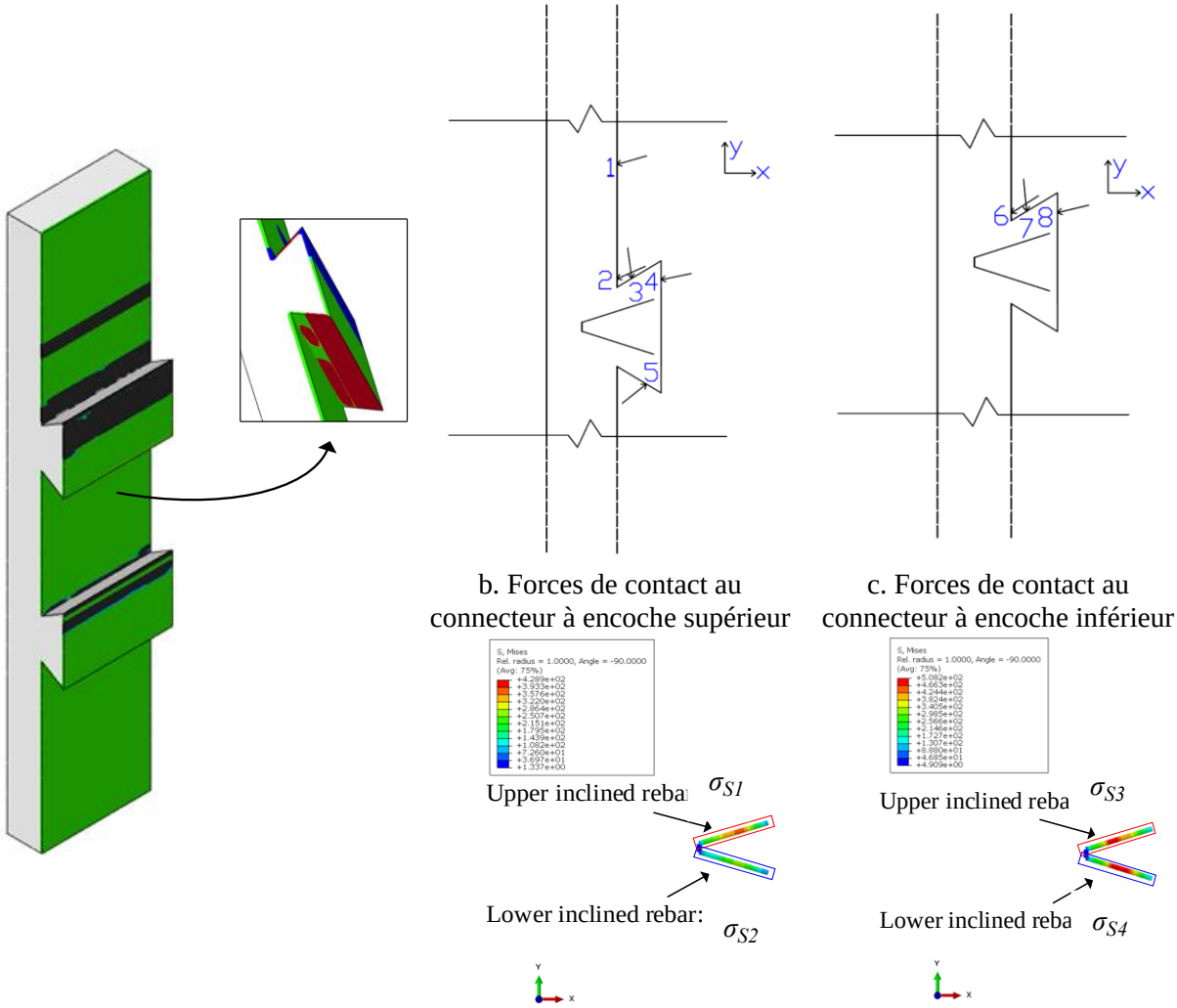

a. Zones soumises aux forces de contact

b. Forces de contact au connecteur à encoche supérieur

c. Forces de contact au connecteur à encoche inférieur

d. Contraintes des barres en forme de V au connecteur à encoche supérieur

e. Contraintes des barres en forme de V au connecteur à encoche inférieur

Figure 12: Forces de contact et contraintes en traction des barres en forme de V obtenues à partir du modèle EF au niveau de charge maximal.

Tableau 8: Forces de contact et leur orientation à chaque emplacement le long de la couche d'interface du panneau en béton au niveau de charge maximal.

Position	1	2	3	4	5	6	7	8
F_x [kN/m]	-2.30	-42.05	49.37	-68.46	27.80	-21.11	44.82	-88.09
F_y [kN/m]	-0.79	-18.52	-370.88	-9.82	59.52	-11.28	-376.39	-11.98
θ [^{0}]	71.08	66.23	7.58	81.84	25.03	61.88	6.79	82.26

Tableau 9: Force de réaction du panneau en béton et contrainte des barres en forme de V obtenues au point de limite élastique des barres en forme de V.

RF_x [kN/m]	RF_y [kN/m]	Mz [kNm/m]	σ_{S1} [MPa]	σ_{S2} [MPa]	σ_{S3} [MPa]	σ_{S4} [MPa]
102	743	24	505	539	511	551

Tableau 9 résume les forces de réaction dans les directions horizontale et verticale, le moment de réaction, ainsi que la contrainte en traction des barres en forme de V. σ_{S1} et σ_{S2} désignent la contrainte dans la barre inclinée supérieure et inférieure du connecteur à encoche supérieur, respectivement, tandis que σ_{S3} et σ_{S4} représentent la contrainte dans la barre inclinée supérieure et inférieure du connecteur à encoche inférieur, respectivement (Figure 12d,e).

Le modèle bielle-tirant a été dessiné comme illustré dans la Figure 13a, suivant la carte des contraintes principales et les forces de contact du panneau en béton, lorsque les barres en forme de V dans les deux connecteurs à encoches ont subi une contrainte de limite élastique. Certains nœuds, notamment les nœuds 1, 3, 5, 6, 13 et 15, ont été positionnés en fonction de l'orientation des forces de contact, tandis que les tirants $T_{4\rightarrow5}$, $T_{4\rightarrow6}$, $T_{14\rightarrow15}$ et $T_{14\rightarrow16}$ représentaient les barres en forme de V. La disposition des nœuds de modèle bielle-tirant et l'orientation des forces de contact dans les connecteurs à encoches supérieur et inférieur à l'étape de chargement post-pic sont détaillées dans la Figure 13b.

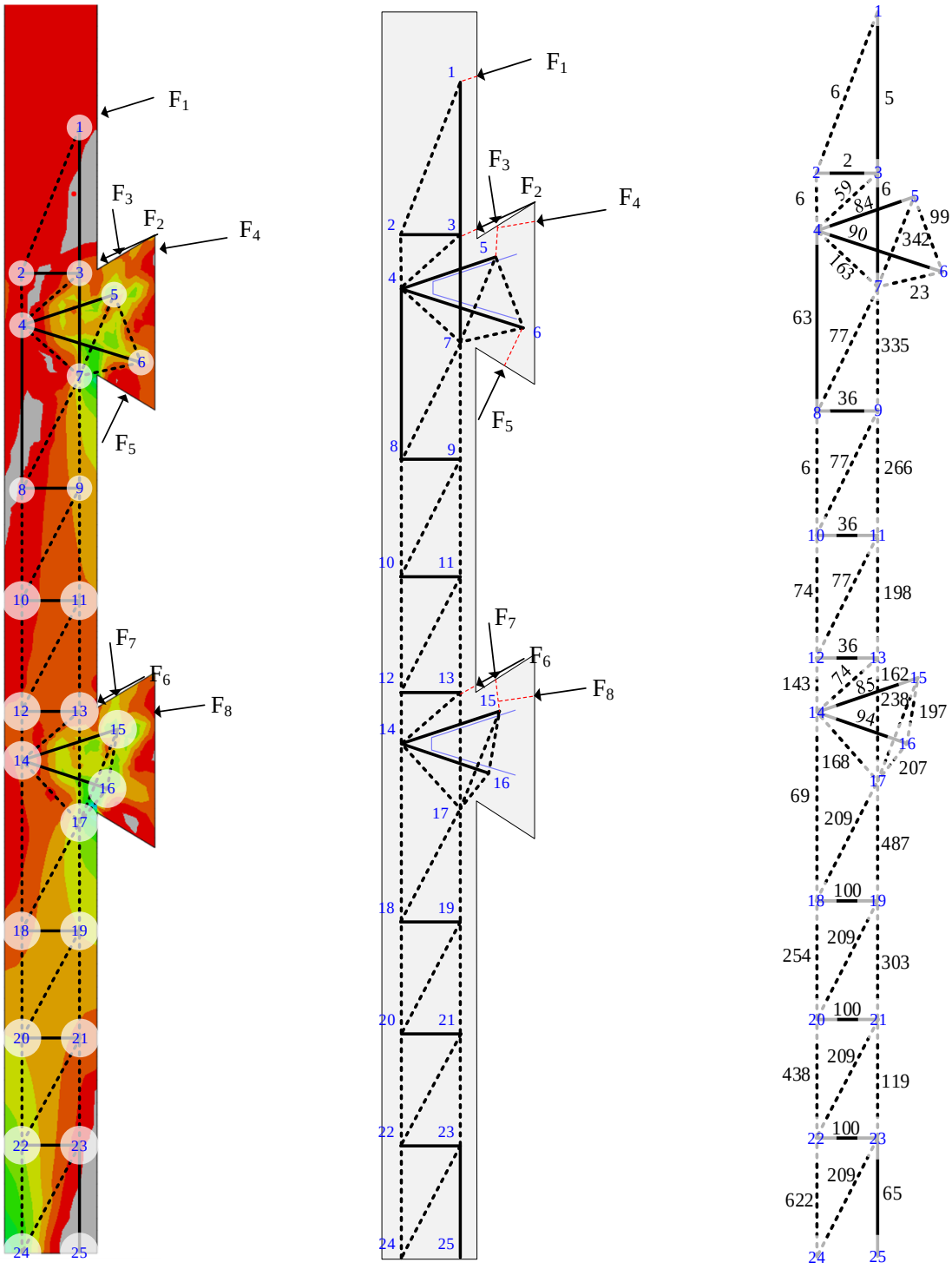

a. Carte des contraintes et force externe appliquée

b. Modèle bielle-tirant

c. Force interne du modèle bielle-tirant

Figure 13: Modèle bielle-tirant déduit de la carte des contraintes principales du modèle EF et des forces internes obtenues du modèle modèle bielle-tirant à la contrainte de limite élastique des barres en forme de V.

En résolvant les équations d'équilibre, les résultats des forces internes de chaque bielle compressive et tirant de traction ont été obtenus et sont décrits dans la Figure 13c. Pour vérifier le modèle bielle-tirant proposé, les comparaisons entre les résultats obtenus à partir du modèle bielle-tirant et ceux du modèle EF sont résumées dans le Tableau 10. Globalement, il a été observé qu'un meilleur accord entre les modèles bielle-tirant et EF a été établi lorsque les barres en forme de V ont subi des contraintes de limite élastique dans les deux connecteurs à encoches à l'étape de chargement post-pic. À l'exception du moment de flexion au support, la plus grande différence n'était que de deux pour cent pour les forces de réaction et les contraintes de traction des barres en forme de V. Pour le moment de flexion, le modèle EF a montré une différence de 8 pour cent plus élevée que le modèle bielle-tirant, ce qui pourrait être dû à la position inexacte des forces de contact obtenues.

Tableau 10: Comparaison des résultats entre le modèle bielle-tirant et le modèle EF.

Test	RF_x [kN/m]	RF_y [kN/m]	M_z [kN.m/m]	$T_{4\rightarrow5}$ [kN/m]	$T_{4\rightarrow6}$ [kN/m]	$T_{14\rightarrow15}$ [kN/m]	$T_{14\rightarrow16}$ [kN/m]
Modèle EF	102	743	24	86	91	87	94
Modèle bielle-tirant	100	740	22	84	90	85	94
Diff.	0.98	1.00	0.92	0.98	0.98	0.98	1.00

2.4.2 Résistance au cisaillement de roulement du panneau CLT et résistance à la compression du béton et du bois dans la connexion à encoches

Le comportement de cisaillement de roulement de la couche transversale du panneau CLT a été identifié comme la principale cause de défaillance de l'éprouvette de poussée. Pour évaluer la résistance au cisaillement de roulement de la couche transversale du panneau CLT, une formule analytique simple est adoptée comme indiqué dans l'équation (1).

$$F_r = f_r b l_{eff} \quad (1)$$

où f_r représente la résistance caractéristique au cisaillement de roulement; b est la largeur de l'éprouvette; l_{eff} est la longueur effective de la couche transversale soumise à la charge de cisaillement. La longueur effective de la couche transversale, comme indiquée dans l'équation (1), a été calculée en mesurant la longueur du bois soumis à une contrainte de cisaillement de roulement élevée dans le modèle EF au niveau de charge maximal.

La résistance à la compression de l'encoche en béton $F_{c,con.}$ peut être évaluée à l'aide de l'équation (2) [33]:

$$F_{c,con.} = f_c b d_n \quad (2)$$

où f_c est la résistance à la compression du béton, b est la largeur de l'éprouvette, et d_n est la profondeur de l'encoche

Pour l'écrasement du bois dans la connexion à encoches, seule la couche longitudinale du CLT est supposée transférer la charge. Par conséquent, la résistance à la compression $F_{c,tim.}$ peut être déterminée par l'expression suivante [33]:

$$F_{c,tim.}=f_{c,0}bh_{l,CLT} \quad (3)$$

où $f_{c,0}$ est la résistance à la compression du bois parallèle au fil du bois, tandis que $h_{l,CLT}$ est l'épaisseur de la couche longitudinale du panneau CLT.

3. Comportement global du plancher composite CLT-béton

Dans cette section, le comportement global des planchers composites CLT-béton (système HOBOA) avec le système de connexion étudié est évalué. Tout d'abord, une série de deux tests de flexion à grande échelle est réalisée avec différentes hypothèses de condition de support. Ensuite, une application numérique de la méthode gamma est présentée pour le plancher composite CLT-béton étudié et la comparaison entre les résultats obtenus des essais expérimentaux et ceux de la méthode gamma est effectuée. Pour évaluer le comportement du plancher composite CLT-béton, modèle d'ingénierie simple (modèle de plaque orthotrope dans le programme d'ingénierie [34]) sont utilisés. De plus, une discussion sur le comportement bidimensionnel à l'aide du modèle de plaque orthotrope est également menée pour optimiser et fournir un modèle précis pour représenter le plancher bidirectionnel réel (effet bidimensionnel) sous hypothèses de système de support, de configuration de charge et de propriétés mécaniques de la section transversale du plancher composite dans la direction transversale.

3.1 Tests de flexion expérimentaux

3.1.1 Éprouvettes et configuration des essais

Des tests de flexion expérimentaux ont été réalisés pour évaluer les performances mécaniques globales des planchers composites CLT-béton avec le système de connexion à encoches à queue d'aronde. Deux grandes éprouvettes composites (HBF1 et HBF2) ont été soumises à des tests de flexion à quatre points afin de valider l'efficacité des nouveaux connecteurs. Pour les configurations des tests de flexion, un système de support linéaire et un système de support ponctuel ont été considérés et mis en œuvre pour représenter le comportement réel du système de plancher. La Figure 1 présente la configuration de l'éprouvette dans les tests de flexion. Pour les deux tests, du béton de classe de résistance C35/45 a été utilisé, tandis que le panneau CLT TOT'm X [23] de classe de résistance C24 a été utilisé pour la partie bois de l'éprouvette.

La configuration des essais comprenait une éprouvette de dalle, deux supports, un vérin de force d'une capacité de 1500 kN, et un système de chargement pour appliquer une charge à quatre points sur l'éprouvette (voir Figure 14). Deux types de supports ont été adoptés, notamment le support 1 (deux supports ponctuels aux coins) et le support 2 (support linéaire). Dans cette configuration d'essai, la charge était appliquée verticalement depuis le vérin de force sur l'éprouvette à travers le système de chargement.

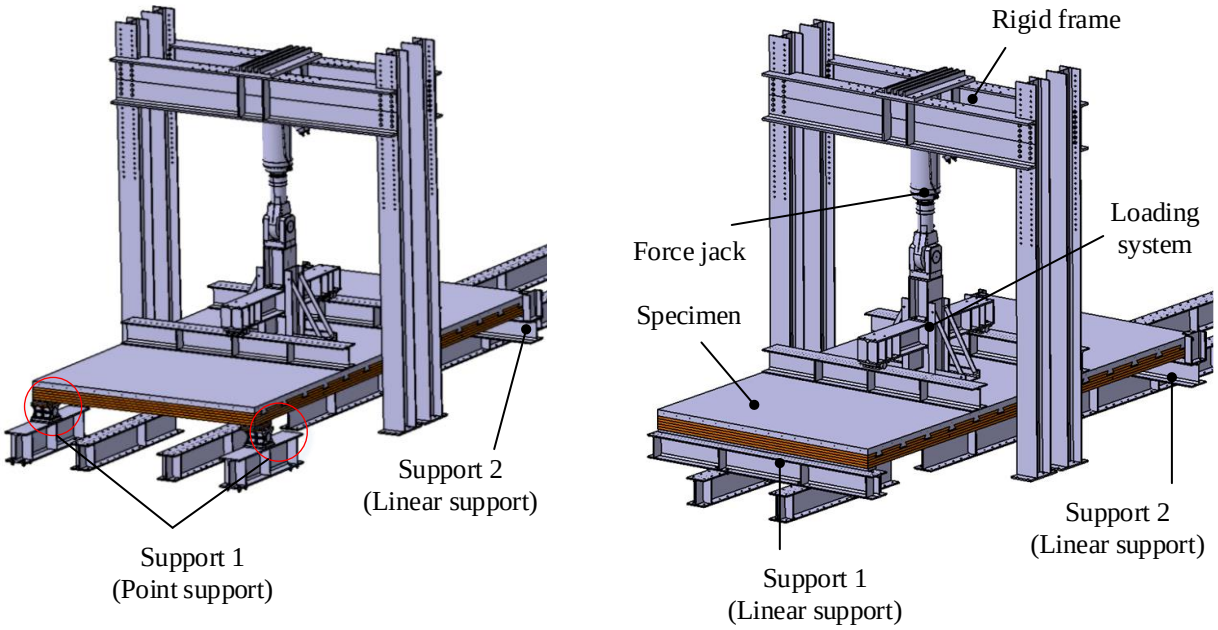

a. Configuration d'essai HBF1 b. Configuration d'essai HBF2

Figure 14: Configurations des essais de flexion.

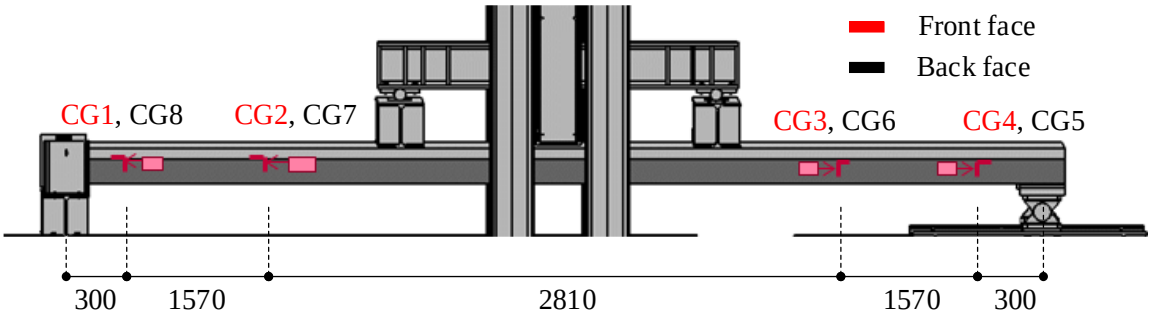

a. Positions des capteurs LVDT (unité en mm)

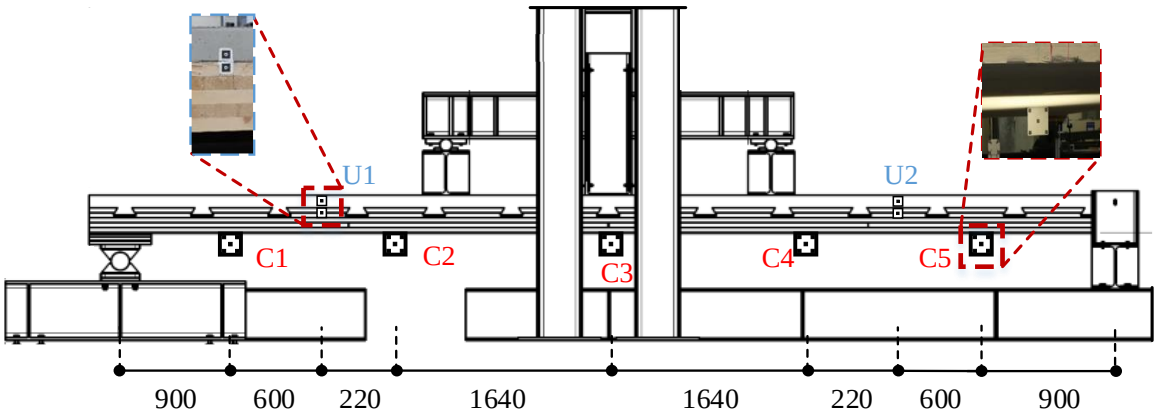

b. Mesures par corrélation d'images numériques (DIC) (unité en mm)

Figure 15: Positions des capteurs LVDT et mesures par la méthode DIC lors des tests de flexion.

3.1.2 Instrumentation et procédure de chargement

La force générée par le vérin hydraulique a été mesurée par des capteurs de force intégrés doubles (± 500 kN et ± 1500 kN). Les glissements entre les panneaux CLT et béton dans la direction horizontale ont été déterminés à l'aide de 8 capteurs LVDT (4 sur chaque face le long de l'éprouvette) notés CG1 à CG8 avec une capacité de ± 2,5 mm (voir Figure 15a). De plus, le tassement des supports dans la direction verticale a été mesuré à l'aide de 4 capteurs LVDT (un à chaque coin de l'éprouvette) notés CD1 à CD4 avec une capacité de ± 25 mm. En plus des capteurs analogiques, trois caméras photo à haute résolution ont également été installées sur la face avant de l'éprouvette pour une mesure alternative à l'aide de la technologie de corrélation d'images numériques (DIC) (voir Figure 15b).

Les procédures de chargement ont été menées conformément à l'Eurocode 4 [24]. La charge de défaillance a été estimée à 403 kN. Un cycle supplémentaire à un niveau de charge correspondant à l'état limite ultime estimé a ensuite été effectué avant que la charge ne soit augmentée de manière monotone jusqu'à la défaillance, avec une vitesse de chargement de 1 mm/min.

3.1.3 Résultats expérimentaux et discussion

3.1.3.1 Observations et mode de défaillance

La Figure 16a illustre les courbes enveloppes du flèche au milieu de portée mesurées par le point C3 à l'aide de la méthode de mesure DIC en fonction de la force. La réponse globale des éprouvettes était presque linéaire jusqu'à la défaillance des éprouvettes aux niveaux de charge de 590 kN et 725 kN pour les tests HBF1 et HBF2, respectivement (le poids propre de l'éprouvette et du système de chargement n'étant pas inclus). Il est clairement visible à partir des résultats des essais de flexion (Figure 16b) que la conception de la dalle composite CLT-béton n'est pas limitée par la résistance, car une valeur très élevée de la force a été obtenue par rapport au niveau de conception des combinaisons de charges.

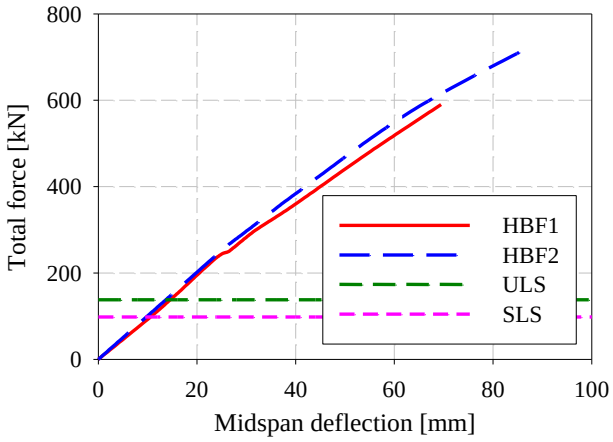

a. Courbes enveloppes de la flèche au milieu de portée en fonction de la force

i. Test HBF1

ii. Test HBF2

b. Mode de défaillance des essais de flexion

Figure 16: Évolution de la force et de la flèche au milieu de portée obtenues par la méthode DIC.

Pour le test HBF1, au niveau de charge de 290 kN, des fissures sont apparues et se sont propagées dans le béton au niveau du connecteur à encoches près des supports ponctuels sur les deux faces de l'éprouvette. Ces fissures ont conduit à une rupture par cisaillement locale du panneau en béton et du panneau CLT au niveau de charge de 590 kN. Pour le test HBF2, des fissures ont été observées dans les connecteurs à encoches lors du premier cycle à un niveau de charge de 158 kN. À un niveau de charge de 725 kN, de nombreuses planches de bois ont été rompues et des bruits forts de rupture du bois ont été entendus. Il a été décidé d'arrêter le chargement afin d'éviter un effondrement fragile du système, car la défaillance semblait être gouvernée par la rupture des couches de CLT en tension (voir Figure 16c).

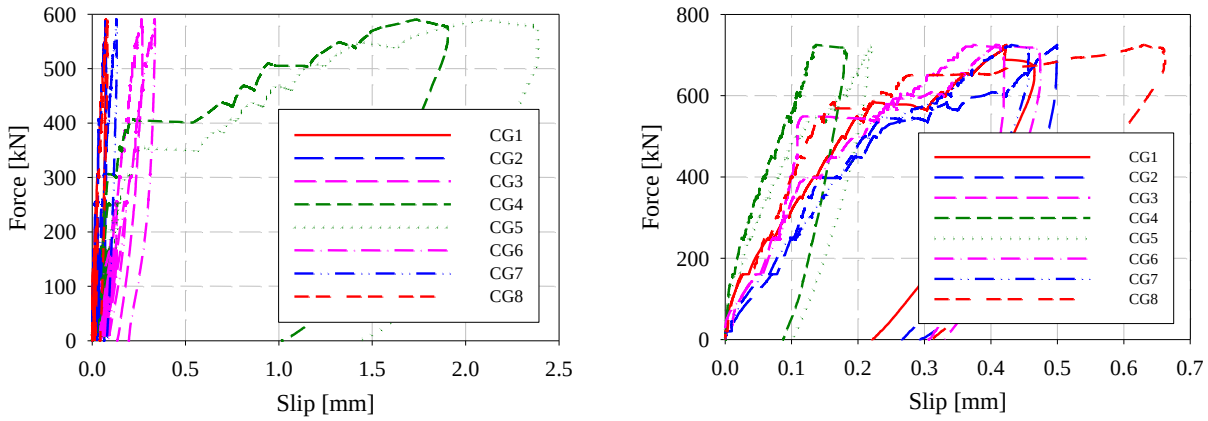

i. Test HBF1 ii. Test HBF2

a. Évolution des glissements

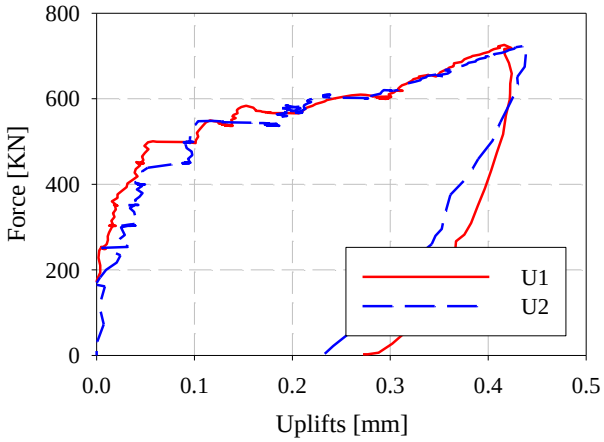

b. Évolution des soulèvements

Figure 17 : Évolution des glissements et des soulèvements en fonction de la force lors des essais de flexion.

3.1.3.2 Interprétation des tests expérimentaux

La Figure 17a présente l'évolution des glissements en fonction de la force pour les deux tests HBF1 et HBF2. Pour le test HBF1, les grandes valeurs de glissements mesurées par les capteurs CG4 et CG5 étaient des déplacements relatifs causés par des fissures de cisaillement près des supports ponctuels. Avec les deux supports linéaires dans le test HBF2, la distribution des glissements est devenue régulière. De plus, l'évolution des soulèvements aux points U1 et U2 pour le test HBF2 est décrite dans la Figure 17b.

Tableau 11 présente les résultats des planchers TCC testés considérés sur un mètre. La rigidité à la flexion du plancher composite CLT-béton, EI, est obtenue à l'aide des équations de la théorie des poutres en mécanique des structures, particulièrement à partir de la théorie des poutres d'Euler-Bernoulli. À partir de la comparaison dans le Tableau 11, il apparaît que le plancher TCC supporté par le système de supports ponctuels (HBF1) offre logiquement une performance structurale inférieure par rapport au plancher supporté par le système de support linéaire (HBF2). En effet, ayant des supports ponctuels à une extrémité, la déflexion entre les supports ponctuels (déflexion transversale) de l'éprouvette HBF1 impacte la déflexion longitudinale, rendant ainsi l'éprouvette HBF1 moins rigide que l'éprouvette HBF2.

Tableau 11: Résultats des planchers TCC obtenus à partir des tests de flexion considérés par mètre.

Test	F_{max} [kN/m]	$\delta_{F_{max}}$ [mm]	EI [Nmm^2/m]	M_{exp} [kNm/m]
HBF1	184	69	1.40×1013	200
HBF2	227	88	1.52×1013	251
Ratio (HBF1/HBF2)	0.81	0.78	0.92	0.80

3.2 Analytical method for CLT-concrete floor in uniaxial bending

Cette section présente l'estimation des performances structurales des spécimens testés à l'aide d'une méthode de calcul simplifiée, communément appelée "méthode gamma", décrite à l'Annexe C de l'Eurocode 5 [35], souvent utilisée pour la conception des planchers composites bois-béton. Jiang et al. [36] ont proposé une modification de la méthode gamma spécifiquement pour les planchers composites CLT-béton avec des panneaux CLT à 5 couches. Dans leur approche, la rigidité à la flexion effective est la somme de deux parties (voir Figure 18). La première partie comprend le panneau en béton avec les couches longitudinales centrale et inférieure du panneau CLT, tandis que la deuxième partie ne concerne que la couche longitudinale supérieure du panneau CLT. Les formules détaillées pour définir la rigidité à la flexion effective peuvent être trouvées dans [36].

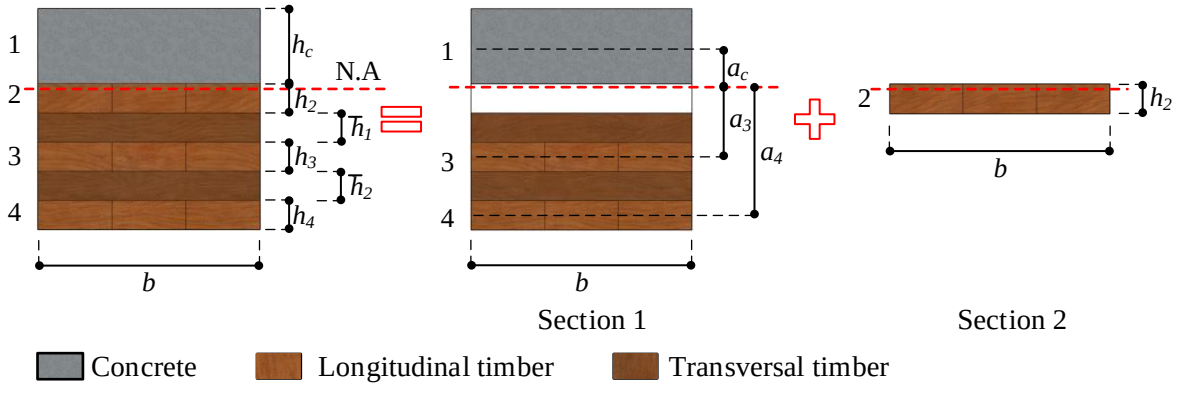

Figure 18: Calcul des dalles composites CLT-béton à 5 couches [36].

Les paramètres pour l'application numérique de la méthode gamma à la configuration des tests HBF1 et HBF2 sont donnés dans le Tableau 12 et le Tableau 13. Le Tableau 12 présente la configuration géométrique et le module de glissement pour le calcul de la méthode gamma. Le Tableau 13 rapporte les propriétés mécaniques du béton et du bois pour l'application de la méthode gamma.

Les résultats de la résistance F_{max}, de la rigidité à la flexion effective $(EI)_{eff}$, et des facteurs γ des spécimens dans les tests HBF1 et HBF2 sont donnés dans le Tableau 14. La résistance du plancher composite est limitée par le panneau CLT sous flexion combinée et tension axiale dans les deux tests, avec une valeur comprise entre 195 kN et 200 kN par mètre de largeur. Il y a une différence minimale dans la force maximale, que l'on utilise K_s ou K_u.

Tableau 12: Paramètres pour la méthode gamma des tests HBF1 et HBF2.

Test	K_s [N/mm/m]	K_u [N/mm/m]	h_c [mm]	h_2,h_3,h_4 [mm]	$\bar{h}_1$,$\bar{h}_2$ [mm]	L [mm]
HBF1	1.49×10^6	1.03×10^6	85	33	33	6440
HBF2						6540

Tableau 13: Propriétés mécaniques du béton et du bois pour l'application de la méthode gamma.

Paramètres	E_c [MPa]	E_2,E_3,E_4 [MPa]	G_R [MPa]	f_{cm} [MPa]	$f_{t,0}$ [MPa]	f_m [MPa]	f_v [MPa]	f_r [MPa]	F_N [kN]
Value	36689	11500	60	55	23	38	5.56	1.49	437

Tableau 14: La rigidité à la flexion effective et la charge de rupture obtenues à partir de la méthode gamma, exprimées dans l'Eurocode 5 [35], ensuite modifiées par Jiang et al [36].

Tests		$(K/s)_c$ [N/mm^2/m]	γ_c	γ_4	F_{max} [kN/m]	$(EI)_{eff}$ [N.mm^2/m]
HBF1	K_s	1.10×10^6	0.60	0.95	200	1.59×10^{13}
	K_u	0.94×10^6	0.56	0.95	196	1.56×10^{13}
HBF2	K_s	1.10×10^6	0.61	0.95	196	1.59×10^{13}
	K_u	0.94×10^6	0.57	0.95	195	1.57×10^{13}

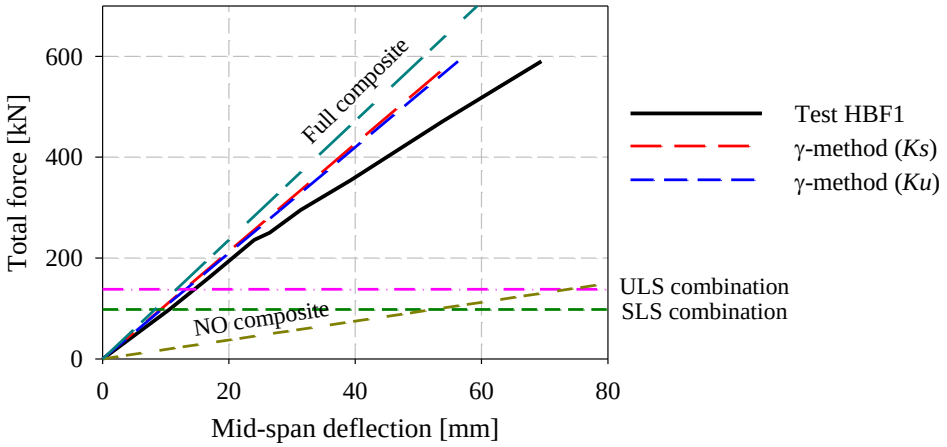

a. Test HBF1

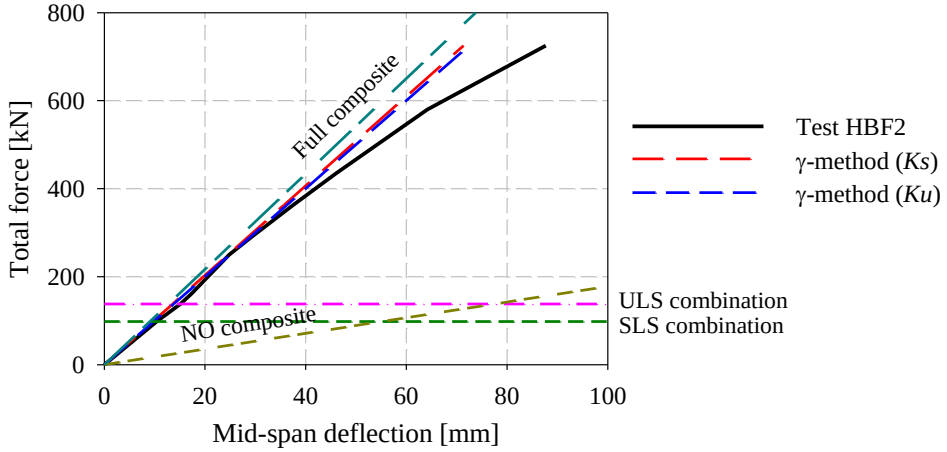

b. Test HBF2

Figure 19: Courbes force-déformation des méthodes gamma et des tests de flexion.

De plus, les déformations au milieu de portée et les résistances du plancher composite obtenues à partir du calcul à l'aide de la méthode gamma sont comparées aux résultats déduits des tests expérimentaux. Le calcul analytique est effectué en utilisant soit K_s soit K_u comme rigidité du connecteur. La Figure 19 illustre la comparaison des courbes force-déformation obtenues à partir des tests HBF1 et HBF2 et des calculs utilisant la méthode gamma avec le module de glissement du système de connexion K_s ou K_u. De cette figure, on peut observer que la méthode gamma fournit une bonne estimation des déformations pour des valeurs de charge faibles à modérées, mais n'est logiquement pas capable de capturer le comportement non linéaire près de l'effondrement. Il a été montré que la méthode gamma présente une meilleure corrélation dans le test HBF2, car des supports linéaires ont été utilisés pour les deux supports, correspondant au comportement unidimensionnel. Le test HBF1 génère une déformation plus élevée, contribuée par une déformation supplémentaire entre les supports ponctuels dans la direction transversale. De plus, l'effet de l'efficacité de la connexion, calculée par la méthode gamma avec γ_c=0 (absence totale de plancher composite) et γ_c=1 (plancher composite complet), est également présenté sur la figure. Ce résultat montre que le système de connexion tend à atteindre presque un degré de connexion complet.

3.3 Effets bidimensionnels sur le plancher composite CLT-béton

Dans cette section, le plancher composite CLT-béton est étudié sous l'effet de flexion bidimensionnelle. Un modèle de plaque orthotrope est développé à l'aide d'un logiciel d'ingénierie simple pour étudier l'effet de flexion bidimensionnelle du système HOBOA avec des supports ponctuels à une extrémité et un support linéaire à l'autre extrémité de l'échantillon. Pour obtenir des résultats satisfaisants, il convient de prêter attention aux détails du modèle autour des supports ponctuels.

3.3.1 Modèles de plancher composite en flexion bidimensionnelle

Pour le modèle de plaque orthotrope, les propriétés de la section transversale sont définies par la matrice de rigidité C, comme suit :

$$C = \begin{bmatrix} D_{11} & D_{12} & 0 & 0 & 0 & 0 & 0 & 0 \\ D_{21} & D_{22} & 0 & 0 & 0 & 0 & 0 & 0 \\ 0 & 0 & D_{33} & 0 & 0 & 0 & 0 & 0 \\ 0 & 0 & 0 & D_{44} & 0 & 0 & 0 & 0 \\ 0 & 0 & 0 & 0 & D_{55} & 0 & 0 & 0 \\ 0 & 0 & 0 & 0 & 0 & D_{66} & D_{67} & 0 \\ 0 & 0 & 0 & 0 & 0 & D_{76} & D_{77} & 0 \\ 0 & 0 & 0 & 0 & 0 & 0 & 0 & D_{88} \end{bmatrix} \quad (4)$$

où

$[D_{11} - D_{33}]$ décrit la matrice de rigidité à la flexion;

$[D_{44} - D_{55}]$ décrit la matrice de rigidité au cisaillement;

$[D_{66} - D_{88}]$ décrit la matrice de rigidité de membrane.

Dans cette section, l'effet de flexion bidimensionnelle du plancher composite CLT-béton est étudié. Un modèle de plaque orthotrope est développé à l'aide d'un logiciel d'ingénierie simple [34] pour étudier l'effet de flexion bidimensionnelle du système HOBOA avec des supports ponctuels à une extrémité et un support linéaire à l'autre extrémité de l'échantillon. Pour obtenir des résultats satisfaisants, il convient de prêter attention aux détails du modèle autour des supports ponctuels. Dans la matrice de rigidité C, les termes D_{11} et D_{22} sont désignés comme la rigidité à la flexion du plancher composite dans les directions longitudinale $(EI)_{eff}$ et transversale $(EI)_{eff,T}$, respectivement. La méthode de calcul pour la rigidité à la flexion du plancher composite dans la direction longitudinale $(EI)_{eff}$ est décrite dans la section 3.2. Pour la rigidité à la flexion du plancher composite dans la direction transversale $(EI)_{eff,T}$, la méthode gamma décrite à l'Annexe B de l'Eurocode 5 [35] est adoptée en considérant trois couches effectives de la section transversale du plancher composite, comprenant la couche supérieure en béton et deux couches longitudinales en bois du panneau CLT. On suppose qu'aucune action composite n'est considérée au niveau de la couche d'interface du plancher composite dans la direction transversale. De plus, la section transversale en béton du plancher

composite dans la direction transversale doit inclure la présence de la section en entaille, en condition fissurée (voir Figure 20).

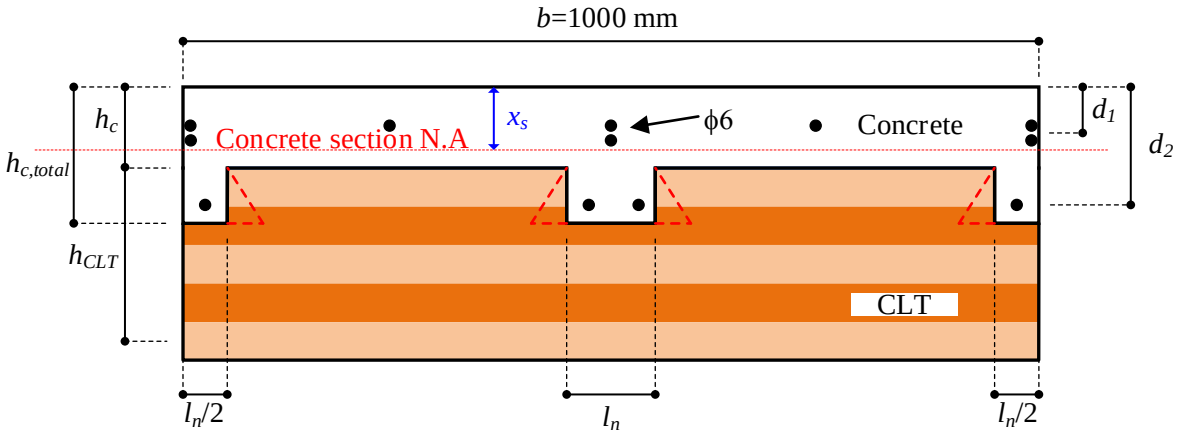

Figure 20: Section transversale du plancher composite par un mètre de largeur.

Concernant le terme D_{33} dans la matrice de rigidité à la flexion, il est désigné comme la rigidité en torsion du plancher composite GI, qui est inclus dans le modèle de plaque par l'addition de la rigidité en torsion du panneau en béton GI_{con} et du panneau CLT GI_{CLT}, dont le calcul est décrit dans [37]. Quant aux termes extradiagonaux D_{12} et D_{21}, ils sont négligés dans la matrice de rigidité [38]. Le Tableau 15 rapporte les paramètres à utiliser dans la matrice de rigidité C des modèles de plaque.

Tableau 15: Paramètres pour la matrice de rigidité dans les modèles de plaque orthotrope des tests HBF1 et HBF2.

Test	Condition de support	$(EI)_{eff}$ [kN.m^2/m]	$(EI)_{eff,T}$ [kN.m^2/m]	GI [kN.m^2/m]
HBF1	2 supports linéaires	15900	1887	958
HBF2	1 support linéaire et 2 supports ponctuels	15900	1887	958

Deux types de configuration de support sont adoptés pour le plancher composite CLT-béton : le support linéaire, qui est conceptualisé pour représenter le mur de support, et le support ponctuel, qui est conceptualisé pour représenter la colonne de support. Pour modéliser le système de support ponctuel (support de plaque), les dimensions réelles et les rigidités du support doivent être prises en compte afin de ne pas surestimer les déformations transversales (voir Figure 21a). Pour le système de support linéaire, des supports articulés sont appliqués le long d'une ligne dans la direction transversale du modèle de plancher (voir Figure 21b). De plus, pour la configuration de chargement, la charge répartie est appliquée. Ce type de chargement est couramment pris en compte dans la pratique pour la conception (voir Figure 22).

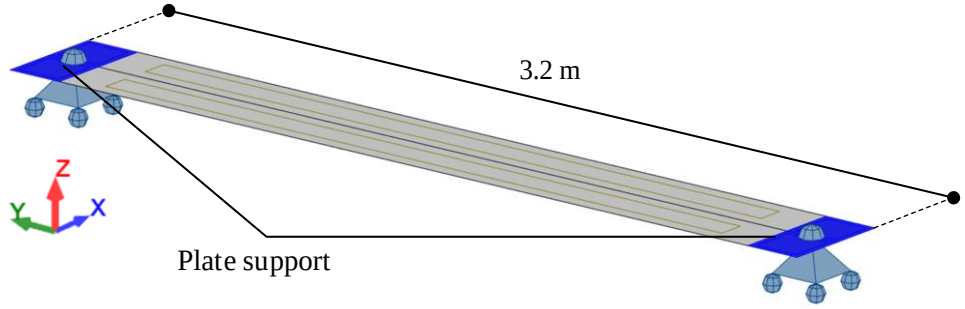

a. Support de plaque

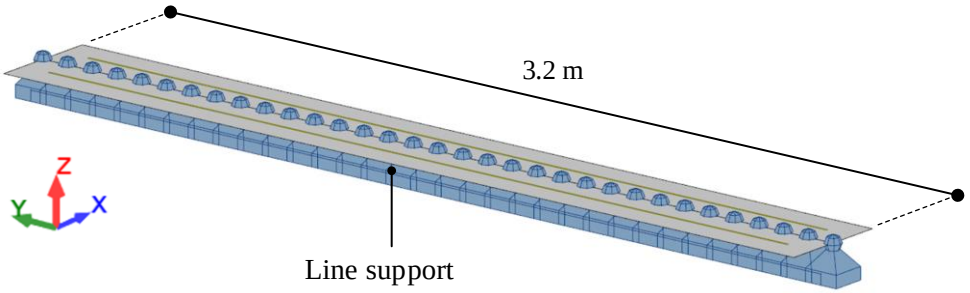

b. Support linéaire

Figure 21: Conditions de support dans le modèle de plancher composite.

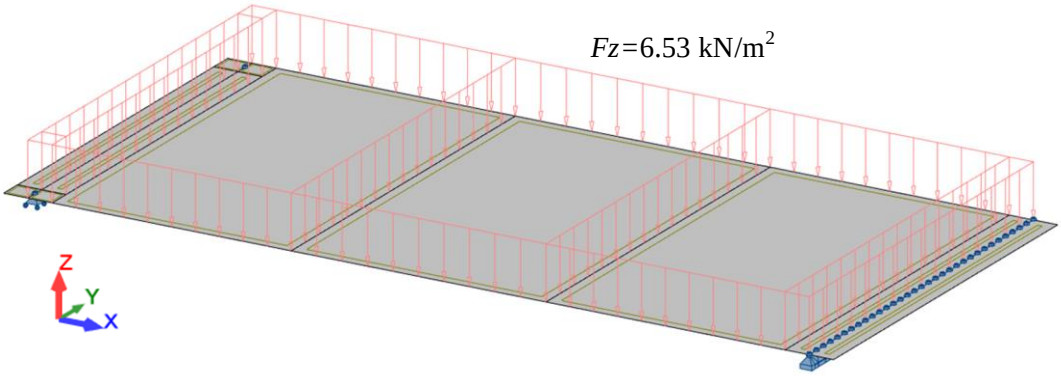

Figure 22: Configurations de chargement appliquées sur le modèle de plaque.

Tableau 16 résume la comparaison de la flèche maximale au milieu de portée dans les directions longitudinale ($w_{max,L}$) et transversale ($w_{max,T}$), obtenue à partir des tests expérimentaux et des modèles de plaque orthotrope au niveau de charge SLS. Les valeurs entre parenthèses représentent le ratio des résultats obtenus à partir des modèles de plaque orthotrope par rapport aux tests de flexion. Il convient de noter que la flèche maximale expérimentale entre les supports ponctuels dans la direction transversale pour le test HBF1 n'était pas disponible.

Tableau 16: Les déformations en milieu de portée [mm] déduites des tests expérimentaux et du modèle de plaque orthotrope au niveau de charge SLS.

Test	Tests de flexion		Modèle de plaque orthotrope		
	$w_{max,L}$ [mm]	$w_{max,T}$ [mm]	$w_{max,L}$ [mm]	$w_{max,T}$ [mm]	$\frac{w_{max,T}}{w_{max,L}}$
HBF1	10.57	--	11.46 (1.08)	6.25	0.55
HBF2	10.42	0	9.70 (0.93)	0	

Pour le modèle de plancher composite soumis à un effet de flexion bi-dimensionnelle (test HBF1), le modèle de plaque fournit des résultats satisfaisants. Par conséquent, le modèle de plaque orthotrope peut être préféré car il offre une représentation affinée du comportement transversal. Cependant, le manque de mesures expérimentales locales ne permet pas de valider pleinement sa précision. D'après le Tableau 16, comparé au plancher soumis à un effet de flexion unidimensionnelle, le plancher soumis à un effet de flexion bi-dimensionnelle a montré une augmentation de la déflexion en milieu de portée de 25 % et a obtenu un ratio w_T/w_L de 55 %. Cette déflexion significative en milieu de portée entre les supports ponctuels devrait être prise en compte dans la conception pour la fixation des façades et pour la vérification des fissures transversales au-dessus des supports.

4. Conclusions et recherches futures

Cette thèse a étudié un nouveau système de plancher composite en CLT-béton, appelé HOBOA. La connexion entre les matériaux est réalisée par des encoches. Elles ne nécessitent aucun composant métallique supplémentaire pour relier le bois et le béton afin d'empêcher la séparation par soulèvement des matériaux, grâce à leur forme spécifique et à la présence d'armatures à l'intérieur de l'encoche en béton. La recherche comprenait des tests expérimentaux, des simulations numériques et des développements analytiques afin de comprendre d'une part le comportement local de la connexion encochée, et d'autre part le comportement global du plancher composite.

Ainsi, le comportement du connecteur encoché proposé a d'abord été étudié pour déterminer la résistance, la rigidité et les performances post-pic. Les conclusions suivantes tirées des études expérimentales, numériques et analytiques du connecteur encoché peuvent être énoncées :

- La série de trois tests de poussée symétriques a montré une haute résistance au cisaillement et une rigidité élevée des connecteurs, mais avec une faible ductilité, car le mode de défaillance de tous les spécimens était gouverné par la résistance au cisaillement de laminage de la couche croisée du panneau CLT.
- Le modèle numérique des tests de poussée a été réalisé en tenant compte de la géométrie réelle, des interactions interfaciales, des propriétés des matériaux et des conditions aux limites. Il a été capable de reproduire le même mode de défaillance et de donner une bonne concordance de la courbe force-déplacement par rapport aux tests de poussée, validant ainsi le modèle.

- Le modèle expérimental validé des tests de poussée (cas C-Ref) a ensuite été utilisé pour mener une étude paramétrique en variant les géométries et les propriétés des matériaux. Les résultats ont montré que le système de connexion maintenait une résistance élevée et une rigidité élevée pour toutes les valeurs des paramètres étudiés. De plus, il a été démontré qu'il serait possible d'améliorer la ductilité de la connexion encochée en priorisant la défaillance du béton en cisaillement au niveau du plan de cisaillement de l'encoche en béton, si un nombre suffisant d'armatures en forme de V était placé à l'intérieur de l'encoche. Cette priorisation peut être obtenue en augmentant l'espacement entre les connecteurs encochés. La défaillance par cisaillement du béton devrait se produire pour une charge de 22 % supérieure à la résistance expérimentale obtenue à partir des tests de poussée. Ces résultats numériques appellent à une validation expérimentale.
- En considérant quatre mécanismes de défaillance possibles du système de connexion, des méthodes analytiques dérivées des codes de conception ont été testées pour évaluer la capacité de charge de l'éprouvette de poussée par comparaison avec les résultats expérimentaux et numériques. Pour la résistance au cisaillement du béton au niveau du plan de cisaillement de l'encoche en béton, un modèle bielle-tirant a été développé, en tenant compte de la carte des contraintes principales et des forces de contact du panneau en béton obtenues à partir du modèle de test de poussée. Pour la résistance au cisaillement de laminage du panneau CLT, une équation analytique simple a été trouvée applicable pour déterminer la résistance au cisaillement de laminage de la couche croisée du panneau CLT. Les deux autres mécanismes de défaillance possibles dans la connexion encochée, y compris la défaillance en compression du béton et la défaillance en compression du bois à la surface portante de l'encoche en béton, devaient être estimés par l'expression proposée dans la spécification technique CEN/TS 19103 [33].

À la suite de la caractérisation approfondie des connecteurs à encoches en queue d'aronde, des planchers composites béton-CLT à grande échelle utilisant ces encoches comme système de connexion ont été étudiés. Le comportement du plancher composite a été caractérisé par la réalisation de deux essais de flexion positive à grande échelle. Les résultats expérimentaux ont ensuite été comparés à ceux estimés par la méthode gamma et à un modèle numérique simple. L'étude des planchers composites et ses résultats sont présentés comme suit :

- Une série de deux essais de flexion à quatre points à grande échelle a été réalisée sur des planchers composites béton-CLT, avec une portée d'environ 6,5 m et une largeur de 3,2 m. Le premier spécimen, HBF1, était soutenu par un support linéaire à une extrémité et par deux supports ponctuels à l'autre extrémité ; le second spécimen, HBF2, reposait sur deux supports linéaires. Les deux spécimens ont démontré de fortes résistances à la flexion. En raison de la condition de support, l'essai HBF1 a été soumis à un effet de flexion bidimensionnel, tandis que l'essai HBF2 a été soumis à un effet de flexion unidimensionnel.
- La méthode gamma telle qu'exprimée dans l'Eurocode 5 [35], modifiée ultérieurement par Jiang et al. [36], a été adoptée pour déterminer la rigidité à la flexion efficace, la flèche en milieu de portée et la capacité de charge du plancher composite. Les estimations obtenues par la méthode

gamma ont montré une bonne concordance avec les résultats des tests. Cependant, la méthode gamma a fourni une meilleure estimation pour l'essai en effet de flexion unidimensionnel (HBF2).

- Un modèle de plaque orthotrope a été développé comme outil simplifié pour estimer le comportement du plancher composite en effet de flexion bidimensionnel. Les résultats ont montré que le modèle de plaque orthotrope doit tenir compte de la rigidité torsionnelle et considérer la section béton avec présence de l'encoche, en condition fissurée, pour calculer la rigidité à la flexion du plancher composite dans la direction transversale. Pour la condition de support ponctuel, les dimensions réelles et la rigidité du support doivent être modélisées.

5. Références

[1] Schreyer, F., Luderer, G., Rodrigues, R., Pietzcker, R. C., Baumstark, L., Sugiyama, M., ... & Ueckerdt, F. (2020). Common but differentiated leadership: strategies and challenges for carbon neutrality by 2050 across industrialized economies. Environmental Research Letters, 15(11), 114016.

[2] Cabeza, L. F., Q. Bai, P. Bertoldi, J.M. Kihila, A.F.P. Lucena, É. Mata, S. Mirasgedis, A. Novikova, Y. Saheb, 2022: Buildings. In IPCC, 2022: Climate Change 2022: Mitigation of Climate Change. Contribution of Working Group III to the Sixth Assessment Report of the Intergovernmental Panel on Climate Change [P.R. Shukla, J. Skea, R. Slade, A. Al Khourdajie, R. van Diemen, D. McCollum, M. Pathak, S. Some, P. Vyas, R. Fradera, M. Belkacemi, A. Hasija, G. Lisboa, S. Luz, J. Malley, (eds.)]. Cambridge University Press, Cambridge, UK and New York, NY, USA. doi: 10.1017/9781009157926.011.

[3] Dias, A. (2018). Design of timber-concrete composite structures: A state-of-the-art report by COST Action FP1402/WG 4. Shaker Verlag.

[4] Yeoh, D., Fragiacomo, M., De Franceschi, M., & Heng Boon, K. (2011). State of the art on timber-concrete composite structures: Literature review. Journal of structural engineering, 137(10), 1085-1095.

[5] Boccadoro, L., Zweidler, S., Steiger, R., & Frangi, A. (2017). Bending tests on timber-concrete composite members made of beech laminated veneer lumber with notched connection. Engineering Structures, 132, 14-28.

[6] Dias, A. M. P. G., Skinner, J., Crews, K., & Tannert, T. (2016). Timber-concrete-composites increasing the use of timber in construction. European Journal of Wood and Wood Products, 74, 443-451.

[7] Boccadoro, L., & Frangi, A. (2014). Experimental analysis of the structural behavior of timber-concrete composite slabs made of beech-laminated veneer lumber. Journal of performance of constructed facilities, 28(6), A4014006.

[8] Jelusic, P., & Kravanja, S. (2017). Optimal design of timber-concrete composite floors based on the multi-parametric MINLP optimization. Composite structures, 179, 285-293.

[9] Müller, K. (2020). Timber-concrete composite slabs with micro-notches (Doctoral dissertation, ETH Zurich).

[10] Liang, S., Gu, H., Bergman, R., Kelley, S. 2020. Comparative life-cycle assessment of a mass timber building and concrete alternative. Wood and Fiber Science 52(2): 217-229.

[11] Yeoh, D. E. C. (2010). Behavior and design of timber-concrete composite floor system. (Doctoral dissertation, University of Canterbury).

[12] Gong, M. 2019. Lumber-Based Mass Timber Products in Construction. Timber Buildings and Sustainability. IntechOpen.

[13] Crespell, P. and Gaston, C. 2011. The Value Proposition for Cross-Laminated Timber. FPInnovations, Pointe-Claire, Quebec City, Canada.

[14] Ceccotti, A. (2002). Composite concrete-timber structures. Progress in structural engineering and materials, 4(3), 264-275.

[15] Dias, A. M. P. G. (2005). Mechanical behavior of timber–concrete joints. Doc-toral Thesis. Civil Engineering, University of Coimbra, Portugal.

[16] Boccadoro, L. (2016). Timber-concrete composite slabs made of beech laminated veneer lumber with notched connection. IBK Bericht, 371.

[17] Van der Linden, M. (1999). Timber concrete composite floors. PhD. Delft University of Technology, The Netherlands.

[18] Gutkowski, R. M., Brown, K., Shigidi, A., & Natterer, J. (2004). Investigation of notched composite wood–concrete connections. Journal of Structural Engineering, 130(10), 1553-1561.

[19] Deam, B. L., Fragiacomo, M., & Buchanan, A. H. (2008). Connections for composite concrete slab and LVL flooring systems. Materials and Structures, 41, 495-507.

[20] Boccadoro, L., Zweidler, S., Steiger, R., & Frangi, A. (2017). Bending tests on timber-concrete composite members made of beech laminated veneer lumber with notched connection. Engineering Structures, 132, 14-28.

[21] Ouch, V., Heng, P., Nguyen, Q. H., Somja, H., & Soquet, T. (2021, June). A notched connection for CLT-concrete composite slabs resisting to uplift without metallic connectors: experimental investigation. In Fib Symposium 2021: Concrete Structures: New Trends for Eco-Efficiency and Performance.

[22] EN 206, B. S. (2013). Concrete-Specification, performance, production and conformity. British Standards Institution, Her Majesty Stationery Office, London, United Kingdom.

[23] Avis-Technique. 3.3/17-925 v1, Panneaux bois `a usages structurel – mur et plancher, Wood structural panels, 2017.

[24] European standard EN 1994-1-1, Eurocode 4: Design of composite steel and concrete structures - Part 1-1: General rules and rules for buildings, CEN, Brussels (2004).

[25] Dassault Systems Simulia Corporation, ABAQUS Analysis User's Manual 6.10-EF, Dassault Systems Simulia Corporation, Providence, RI, USA, 2010.

[26] Cedolin, L., Dei Poli, S., & Crutzen, Y. R. (1977). Triaxial stress-strain relationship for concrete. Journal of the Engineering Mechanics Division, 103(3), 423-439.

[27] Alfarah, B., López-Almansa, F., & Oller, S. (2017). New methodology for calculating damage variables evolution in Plastic Damage Model for RC structures. Engineering structures, 132, 70-86.

[28] European standard EN 338, Structural Timber—Strength Classes, CEN, Brussels (2003).

[29] Hill, R. (1998). The mathematical theory of plasticity (Vol. 11). Oxford university press.

[30] T. Kartheek, T. V. Das, 3D modelling and analysis of encased steel-concrete composite columnusing ABAQUS. Materials Today: Proceedings, 27, 1545-1554. using ABAQUS. Materials Today: Proceedings, 27 (2020), 1545-1554.

[31] Aira, J. R., Arriaga, F., Íñiguez-González, G., & Crespo, J. (2014). Static and kinetic friction coefficients of Scots pine (Pinus sylvestris L.), parallel and perpendicular to grain direction. Materiales de Construcción, 64(315), e030-e030.

[32] Van de Kuilen, J. W. G. (2004). 3D-numerical modelling of DVW-reinforced timber joints. In 8th World Conference on Timber Engineering (pp. 137-142). WCTE 2004 Secretariat.

[33] CEN/TS 19103 :2021. Eurocode 5 : Design of Timber Structures - Structural design of timber-concrete composite structures – Common rules and rules for buildings. European Committee for Standardization (CEN): Brussels, Belgium, 2021.

[34] Autodesk, I. (2017). Robot Structural Analysis Professional.

[35] European standard EN 1995-1-1, Eurocode 5: Design of timber structures- Part 1-1: General — Common rules and rules for buildings, CEN, Brussels (2004).

[36] Jiang, Y., & Crocetti, R. (2019). CLT-concrete composite floors with notched shear connectors. Construction and Building Materials, 195, 127-139.

[37] Gustafsson, A. (2019). The CLT Handbook: CLT structures-facts and planning. Swedish Wood.

[38] Akter, S. T., Bader, T. K., & Serrano, E. Stiffness of cross-laminated timber (CLT) wall-to-floor-to-wall connections in platform-type structures. In World Conference on Timber Engineering, 2021.

This page is intentionally left blank.

Abstract

This doctoral thesis presents a study on the behavior of composite floors with novel dovetail notched connectors. This composite floor consists of topping concrete and bottom timber panel linking with an interlocking system of the dovetail notched connector at the interface layer. For the timber panel, cross-laminated timber (CLT) is adopted in this study due to benefits from two-way load bearing performance and its high mechanical properties. The structural efficiency of the TCC floor mainly depends on the governing behavior of the connection system to transfer shear load between concrete and timber, and to limit relative slips and uplifts. However, design codes of notched connection for TCC floors are not yet available for practical applications. It is, therefore, necessary to verify whether the existing standard codes are applicable, or if a new design approach needs to be developed for the new configuration of the dovetail notched connectors which are adopted in CLT-concrete composite floors.

In the first step, the behavior of the dovetail notched connector is characterized. A series of pushout tests are performed to determine the strength, stiffness, and ductility of the notched connector. The obtained test results are used as a basis for developing finite element (FE) model in order to further assess the load transfer mechanism and behavior of each element of the composite member. Furthermore, the parametric study using validated FE model are conducted to define the optimized configuration for structural performance of notched connectors in terms of strength, stiffness, ductility, and failure modes. In parallel to experimental tests and numerical study, an alternative analytical approach using strut-and-tie model and simplified equations are formulated to estimate the resistance of the notched connector based on the results derived from the parametric study.

Following the local behavior of notched connectors, the global behavior of CLT-concrete composite floors with notched connectors is studied. A series of full-scale four-point bending tests are conducted to characterize the mechanical properties of the composite floors. The analytical gamma method is then adopted to confirm the obtained test results. Additionally, beam grid model and orthotropic plate model using engineering software are also developed for practical use which allows engineers to estimate the structural response of such composite floor.

In conclusion, this research project, after all, aims to provide the development of a practical design approach and recommendations for the design of the TCC floor with the new configuration of the shear connector based on the validation of experimental test, numerical study, and analytical approach.

Keywords: Shear notched connectors, CLT-concrete composite floors, pushout tests, flexural tests, gamma method, beam grid model, orthotropic plate model, strut-and-tie model

This page intentionally left blank.

Résumé

This doctoral thesis presents a study on the behavior of composite floors with novel dovetail notched connectors. This composite floor consists of topping concrete and bottom timber panel linking with an interlocking system of the dovetail notched connector at the interface layer. For the timber panel, cross-laminated timber (CLT) is adopted in this study due to benefits from two-way load bearing performance and its high mechanical properties. The structural efficiency of the TCC floor mainly depends on the governing behavior of the connection system to transfer shear load between concrete and timber, and to limit relative slips and uplifts. However, design codes of notched connection for TCC floors are not yet available for practical applications. It is, therefore, necessary to verify whether the existing standard codes are applicable, or if a new design approach needs to be developed for the new configuration of the dovetail notched connectors which are adopted in CLT-concrete composite floors.

In the first step, the behavior of the dovetail notched connector is characterized. A series of pushout tests are performed to determine the strength, stiffness, and ductility of the notched connector. The obtained test results are used as a basis for developing finite element (FE) model in order to further assess the load transfer mechanism and behavior of each element of the composite member. Furthermore, the parametric study using validated FE model are conducted to define the optimized configuration for structural performance of notched connectors in terms of strength, stiffness, ductility, and failure modes. In parallel to experimental tests and numerical study, an alternative analytical approach using strut-and-tie model and simplified equations are formulated to estimate the resistance of the notched connector based on the results derived from the parametric study.

Following the local behavior of notched connectors, the global behavior of CLT-concrete composite floors with notched connectors is studied. A series of full-scale four-point bending tests are conducted to characterize the mechanical properties of the composite floors. The analytical gamma method is then adopted to confirm the obtained test results. Additionally, beam grid model and orthotropic plate model using engineering software are also developed for practical use which allows engineers to estimate the structural response of such composite floor.

In conclusion, this research project, after all, aims to provide the development of a practical design approach and recommendations for the design of the TCC floor with the new configuration of the shear connector based on the validation of experimental test, numerical study, and analytical approach.

Keywords: Shear notched connectors, CLT-concrete composite floors, pushout tests, flexural tests, gamma method, beam grid model, orthotropic plate model, strut-and-tie model

This page intentionally left blank.

Acknowledgements

This doctoral thesis is mainly conducted at the department of civil engineering, at INSA de Rennes (France) and the department of civil engineering, at ITC (Cambodia) with the financial support from French government scholarship program (BGF), co-funded by the Ministry of Education, Youth and Sport of Cambodia (MoEYS), along with the partial support from the LGCGM laboratory at INSA de Rennes.

I would like to express my sincere gratitude to my principal supervisor, Professor Hugues SOMJA, at INSA de Rennes, co-supervisors, Dr. Sovanvichet LIM, at ITC and another co-supervisor, Dr. Piseth HENG, at INSA de Rennes, for all their support and guidance in both technical works and administrative procedures during this PhD journey. I am especially indebted to Dr. Piseth HENG, a man of noble character which is hard to find, but one in a milestone, I myself is able to find one as my supervisor.

This voyage through my PhD has introduced me to remarkable individuals, including my beloved best friends, Thaileng OENG and Sela HOEUN, as well as esteemed seniors Davin SANG, Rithy Mardy HORM, Yeakleang MUY, Lynita SAROU, Sokvisal MOM, Sounean HENG, Theany TO, Pisey KEO, and Try MENG. I am also grateful for the camaraderie of my fellow colleagues: Adham RAHIM, Maël Sonna DONKO, Mouad MADHOUNI, Murillo Vinícius Bento SANTANA, Yassir WARDI, and Mohammad ABDALLAH.

Lastly, my boundless gratitude extends to my family for their unwavering love and constant encouragement. Your support has been my rock, and I hold you close to my heart. I love you all infinitely.

Rennes, August 2023

Vanthet OUCH

This page is intentionally left blank.

Contents

CHAPTER 1

Introduction

This page is intentionally left blank.

Contents

This page is intentionally left blank.

1.1 Background

Being responsible for around 39 percent of all carbon emissions around the world, the building and construction sectors are considered as the main contributor to climate change [1]. The devastating consequences of climate change urge the involved organizations to revolutionize building materials and construction methods in order to achieve 100 percent net zero emissions buildings by 2050 [2]. With such an objective, sustainable solutions for buildings have been widely studied. As an alternative to the traditional concrete or timber structures, Timber Concrete Composite (TCC) floors might be an interesting solution that balances environmental impacts with structural and economical performances. A TCC floor is formed by laying a concrete panel on top of a timber panel and connecting them together using shear connection systems. This combination takes advantages of the high performances of concrete in compression and of timber in tension, while the connection system is responsible for the transfer of shear forces between the two materials.

For the timber part of TCC floors, engineered wood products are normally employed as an alternative to classic wooden logs in order to meet the design requirement in terms of higher cross-section size, strength to weight ratio, and dimensional stability. Among available engineered wood products, cross-laminated timber (CLT) is selected for this research. CLT is a lumber-based product made by laminating the timber boards in alternating arrangements at a precise angle, typically at 90 degrees, and gluing them together using hydraulic or vacuum press techniques [3]. The alternation of timber boards in the CLT panel minimizes the directional disparity, providing high strength and stiffness in both directions (two-way load bearing floor). Besides the benefit of mechanical performance, many advantages in manufacturing, installation, environmental impact, and cost competitiveness can be seen as the key aspects for the success of the CLT in building applications [4].

Apart from the mechanical properties of concrete and timber panels, the structural response of such a composite system is heavily dependent on the strength, stiffness, and ductility performances of the used connection system. Different types of shear connection systems have been developed in the past including steel fasteners, notches, and glue in order to enhance the structural performance and cost-efficiency of TCC structures [5]. Among them, the notched connection might be considered as the most effective system due to its high strength and stiffness as well as the convenience in construction. However, for notched connections, steel fasteners are in general inserted in the timber and connected to the concrete to improve the shear strength and ductility of the connection as well as the uplift resistance between the concrete and timber. These steel fasteners are expensive and time-consuming in the construction process.

In this context, a novel notched connection system with a dovetail shape for CLT-concrete composite floors is proposed and conceptualized by Thierry Soquet, an architect of the Architecture Plurielle agency and a designer of the Horizons Bois building in Rennes, France, in collaboration with INSA Rennes [6]. The configuration of the dovetail notched connection in this study is shown in Figure 1a. The particular shape of the notch is able to limit the separation between the concrete and CLT panels. Furthermore, the V-shape rebar cage inside the notch improves the uplift resistance and provides an additional dowel action to the concrete notch. Consequently, this connection system should avoid the use of anchored steel screws or fasteners, thus facilitating onsite erection. Figure 1b presents the configuration of CLT-concrete composite floor, named HOBOA system, with dovetail notches as the connection system.

This new solution of TCC floors can raise growing interests for the quick and easy erection work. However, a practical knowledge of this new structure has to be developed to implement it widely on non-residential or industrial structures. In response, this doctoral research is devoted to characterizing the whole composite HOBOA floor system, including the study of the local behavior of the dovetail notched connection system, and the study of the global behavior of composite floors in one-dimensional and bi-dimensional bending effects.

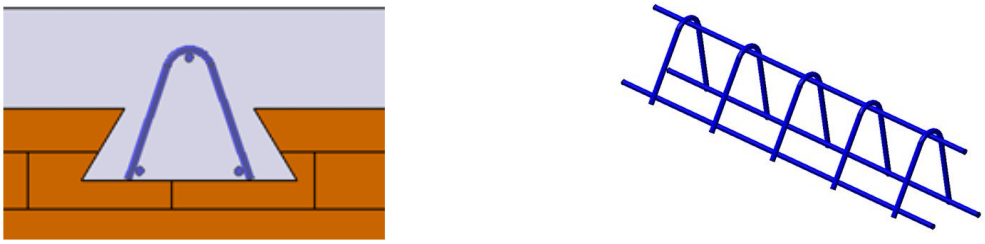

i. Notched configuration ii. V-shape rebar cage

a. Dovetail notched connection system

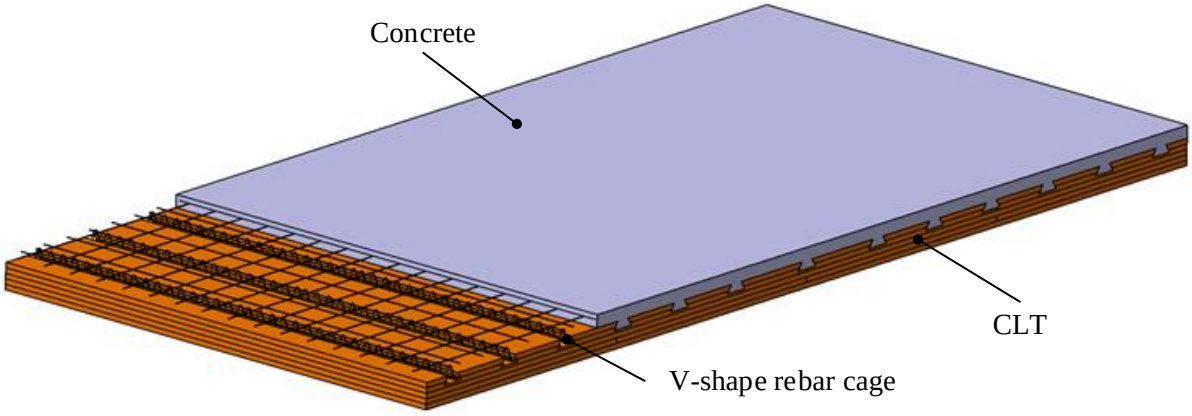

b. CLT-concrete composite floor, named HOBOA system

Figure 1: CLT-concrete composite floor, named HOBOA system with connection made by notches.

1.2 Aims of the work and methodologies

The main objective of this research is to characterize the local behavior of the proposed dovetail notched connector and to assess the global performance of the TCC floor (HOBOA system) with this novel notched connector as the connection system. By using such notched connectors, an efficient construction technique can be obtained due to the simple and fast assembly of the composite floor with high shear capacities of the shear connection. However, it is still needed to verify whether the existing standard codes provisions are applicable, or a new design approach needs to be developed for the new configuration of the TCC floor.

To attain the objectives of this research, the following list of tasks is pursued as follows:

1. Investigation of the local behavior of notched connectors
    - A series of pushout tests of the timber-to-concrete connection is first conducted at LGCGM laboratory of National Institute of Applied Sciences of Rennes (INSA

Rennes), to determine the resistance and stiffness as well as the failure mode of the connection system.

- A full three-dimensional finite element (FE) model of the pushout test is developed and validated based on the experimental results in order to further understand the load transfer mechanism of the connection system.
- To extend the possibility of adopting notched connections, a parametric study using the validated FE model is conducted to investigate the influence of important parameters relating to material properties and geometries on the behavior of the connection system.
- Design formulae from different standards are afterwards tested to estimate the strength of the current notched connection corresponding to different failure modes and verified against the results obtained from the parametric study.
- A strut-and-tie model of the concrete panel in pushout specimen is developed to model the load transfer mechanism from the CLT panel and to estimate the shear resistance of the concrete notch.

2. Study of the global behavior of the TCC floor with notches as the connection system
   - A series of four-point flexural tests is carried out on a full-scale specimen of the TCC floor in order to verify the validity of the new notched connector and to determine the flexural capacities of the TCC system.
   - The estimation of TCC structural performance is then quantified by the uniaxial bending design method, known as the gamma method, and is compared against the test results.
   - To provide a simplified numerical tool for engineer and designer to assess the structural response of TCC floors, an orthotropic plate model using a simple engineering software is developed.
3. Redaction of a proposition for the design guidance for the HOBOA system based on the validation of experimental tests, analytical methods, and numerical simulations.

1.3 Limitations

It is impossible to study every detail of the composite floor since this thesis is a first step to assess the behavior of the TCC floor (HOBOA system) and its dovetail notched connectors, thus the boundary of the study is restricted to basics defined as follows:

- Normal concrete is used for the concrete part, while cross-laminated timber (CLT) with 5-layers is selected for the timber part of the composite floor.
- Long-term behavior of composite floors and notched connectors is not studied in detail. The influence of the variation in time of mechanical properties, including creep, shrinkage, and moisture content of timber and concrete on the structural behavior of composite floors is not discussed quantitatively.
- The vibration performance, fire resistance, and sound insulation properties are not considered.

- This thesis explores the behavior of composite floor in positive bending. The structural behavior of a continuous floor is not addressed.

1.4 Outline of thesis

The general structure of the thesis is visualized in Figure 2. The first step of this research work is a comprehensive review of literature presented in chapter 2. In this chapter, the relevant background on development and structural behaviors of timber-concrete composite floors are summarized including a general description of TCC floors, characteristics of timber and concrete, a review of connection system used in TCC systems, structural analysis and design methods for TCC floors, and numerical study of TCC systems using the FE model.

Chapter 3 describes the local behavior of the notched connector. An experimental program of three symmetrical pushout tests is first conducted to determine the mechanical properties and failure mechanism of the notched connector. A detailed Finite Element model of the pushout test is made and validated based on experimental test results to further understand the load-carrying mechanism of the connection system. Furthermore, a parametric study using the validated FE model is carried out to investigate the influence of material properties and geometries of notched connectors on the connection behavior. Finally, analytical methods, with reference to the results obtained in the parametric study, are developed to estimate the load-carrying resistance of the notched connector.

Chapter 4 addresses the global behavior of TCC floors using the connection system studied in chapter 3. First, a series of two full-scale bending tests (HBF1 and HBF2) is conducted with different assumptions of support condition in the test setup. The composite floor of test HBF1 is subjected to bi-dimensional bending effect (two-way deflection), while the composite floor of test HBF2 is subjected to one-dimensional bending effect (one-way deflection). The experimental results are then compared with the estimations obtained from the gamma method. Furthermore, two simple engineering models: beam grid model and orthotropic plate model are made to assess the structural behavior of the TCC floor. A discussion on the composite floor in bi-dimensional bending effect using the orthotropic plate model is also conducted to optimize and provide an accurate model to represent the actual two-way composite floor behavior.

Chapter 5 proposes design recommendations for the TCC floor with dovetail notched connectors based on the technical specification CEN/TS 19103 [7], enhanced by the findings in chapter 3 and chapter 4.

Finally, chapter 6 concludes over the significance of this research and provides an outlook for future research.

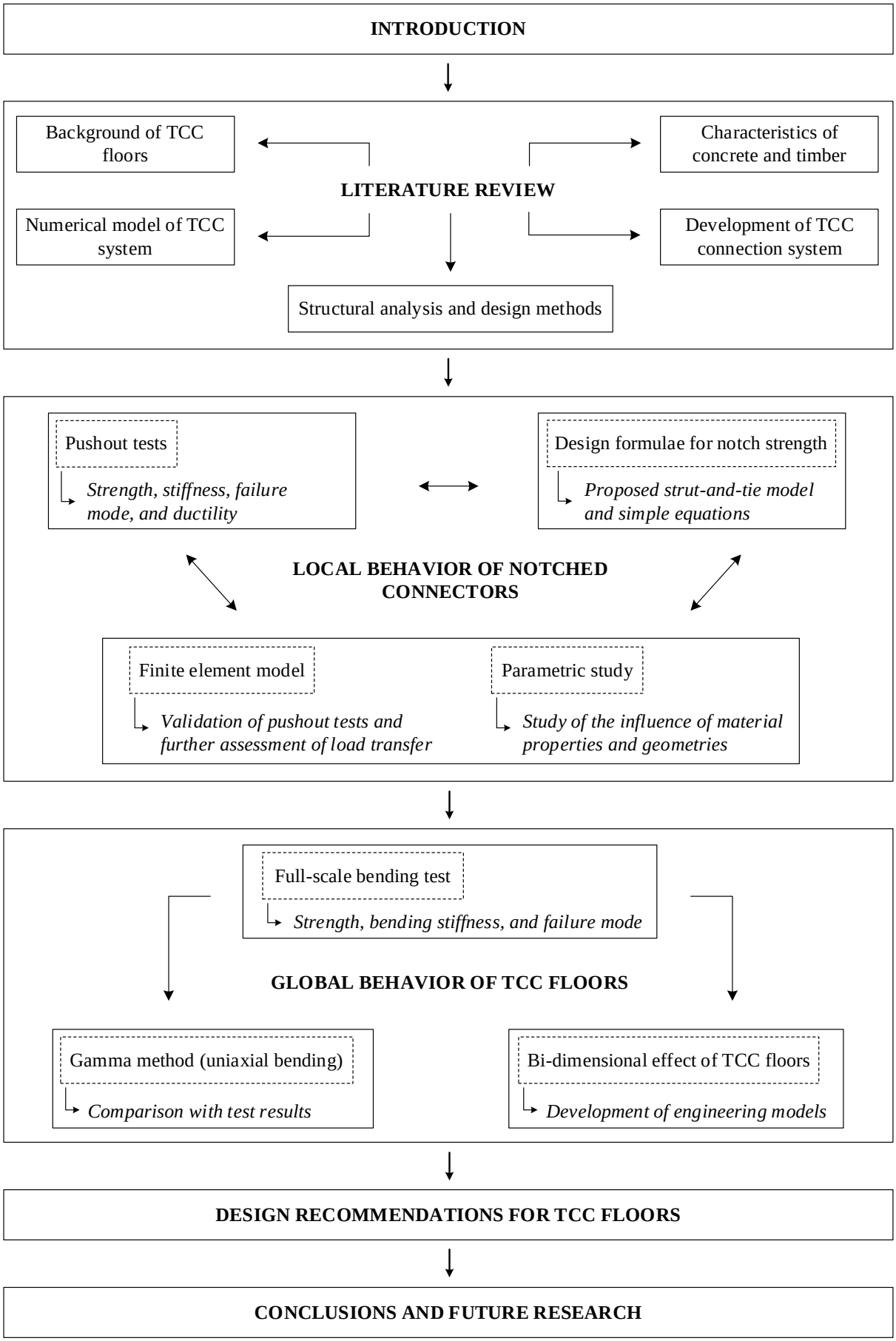

Figure 2: Overview of the thesis.

1.5 References

[1] Schreyer, F., Luderer, G., Rodrigues, R., Pietzcker, R. C., Baumstark, L., Sugiyama, M., ... & Ueckerdt, F. (2020). Common but differentiated leadership: strategies and challenges for carbon neutrality by 2050 across industrialized economies. Environmental Research Letters, 15(11), 114016.

[2] Cabeza, L. F., Q. Bai, P. Bertoldi, J.M. Kihila, A.F.P. Lucena, É. Mata, S. Mirasgedis, A. Novikova, Y. Saheb, 2022: Buildings. In IPCC, 2022: Climate Change 2022: Mitigation of Climate Change. Contribution of Working Group III to the Sixth Assessment Report of the Intergovernmental Panel on Climate Change [P.R. Shukla, J. Skea, R. Slade, A. Al Khourdajie, R. van Diemen, D. McCollum, M. Pathak, S. Some, P. Vyas, R. Fradera, M. Belkacemi, A. Hasija, G. Lisboa, S. Luz, J. Malley, (eds.)]. Cambridge University Press, Cambridge, UK and New York, NY, USA. doi: 10.1017/9781009157926.011

[3] Brandner, Reinhard. (2013). Production and Technology of Cross Laminated Timber (CLT): A state-of-the-art Report. Paper presented at the Focus Solid Timber Solutions - European Conference on Cross Laminated Timber (CLT), Graz.

[4] Crespell, P. and Gaston, C. 2011. The Value Proposition for Cross-Laminated Timber. FPInnovations, Pointe-Claire, Quebec City, Canada.

[5] Ceccotti, A. (1995). Timber-concrete composite structures. Timber engineering, step, 2(1), E13.

[6] Ouch, V., Heng, P., Nguyen, Q. H., Somja, H., & Soquet, T. (2021, June). A notched connection for CLT-concrete composite slabs resisting to uplift without metallic connectors: experimental investigation. In Fib Symposium 2021: Concrete Structures: New Trends for Eco-Efficiency and Performance.

[7] CEN/TS 19103 :2021. Eurocode 5 : Design of Timber Structures - Structural design of timber-concrete composite structures – Common rules and rules for buildings. European Committee for Standardization (CEN): Brussels, Belgium, 2021.

CHAPTER 2

Literature review

This page is intentionally left blank.

Contents

This page is intentionally left blank.

2.1 Introduction

This chapter presents the relevant available background on development and structural behavior of timber-concrete composite floors. Section 2.2 provides history and various advantages of timber-concrete composite structures. Then, characteristics of concrete and timber are detailed in sections 2.3 and 2.4, respectively. A comprehensive review on the development and structural performance of the connection system is described in section 2.5. In section 2.6, structural analysis and design methods are provided to estimate the bending stiffness of composite member cross-section and the ultimate strength of connection system. Lastly, the numerical study of timber-concrete composite structure using finite element model is described in section 2.7.

2.2 Timber-concrete composite floors

2.2.1 Presentation of TCC floors system

The timber-concrete composite (TCC) floor is structured by connecting the concrete panel and the timber panel together using a proper connection system. Concrete with high compressive strength is placed on top of the timber panel with higher resistance in tension and bending. In this arrangement, the best characteristics of each material of the TCC floor are mobilized under the positive bending as concrete is normally placed in compression zone, and timber part is located where tension zone is developed.

In traditional reinforced concrete structures, the ineffective cracked tensile zone, accounting for approximately 2/3 of the cross-section at the lower part, is often disregarded [1], and the tensile force is carried by the steel rebar reinforcement. In TCC structures, the tensile zone of reinforced concrete section and reinforcement bars are substituted by the timber cross-section to resist the tensile force (see Figure 1). The increased area of timber section replaces a small cross-section of rebar reinforcement due to the lower strength and stiffness of timber compared to those of steel reinforcement. Besides the benefit of exploiting the best mechanical characteristic of each material, the TCC floor provides further advantages in comparison to reinforced concrete. The combination of concrete and timber results in a reduction of self-weight, leading to lower seismic force on the structure, lower foundation requirement, and lower soil improvement [2], [3], [4], [5]. The durability of the concrete also improves, as the moisture absorption does not occur in the cracked zone of the concrete when the tensile-exposed concrete section is replaced [6]. Since the volume of concrete is reduced with the application of prefabricated timber elements, the construction process can be achieved faster [1], [2], [7]. In addition, using timber in a structure can limit the carbon footprint since timber is a sustainable material that requires less energy and produces less CO_2 in its manufacture [7], [8], [9]. Another benefit of using timber is the carbon storage (net storage of CO_2) resulting from the combined effect of photosynthesis and respiration in tree leaves needed for tree growth and health [10].

Compared to pure timber floors, TCC floors can better control midspan deflection and therefore enable a larger span due to the higher strength and stiffness provided by the additional concrete section [4], [11]. One study suggested that the load-carrying capacity and flexural stiffness of the TCC floor can increase up to three times and six times, respectively, compared to the timber floor system [12]. Additionally, the topping concrete acts as a barrier to improve sound insulation, to improve fire

resistance, to increase thermal mass for regulating the internal temperature in the building, and to enhance vibration resistance due to the increase of structural mass [13], [14], [15].

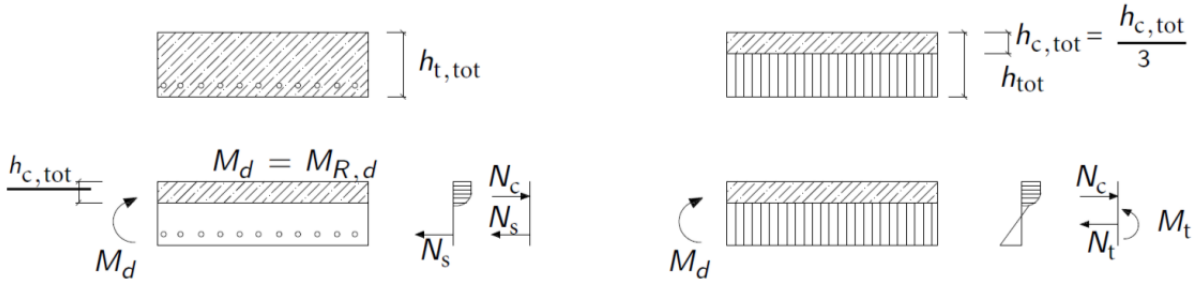

a. Reinforced concrete floor system b. TCC floor system

Figure 1: Load transfer of a reinforced concrete floor and TCC floor [1].

Müller [7] summarizes the advantages of TCC floors compared to pure timber floors and reinforced concrete floors, as listed in Table 1.

Table 1: Advantages of TCC floors compared to pure timber and reinforced concrete floors.

Compared to pure timber floors	**Compared to reinforced concrete floors**
- increase stiffness	- lower self-weight
- increase load-carrying capacity	- accelerate construction process
- improve sound insulation	- lower energy consumption and CO_2 emission
- improve vibration behavior	- allow carbon storage
- improve fire resistance	- achieve higher level of prefabrication

Even if TCC floors are gaining interest and are being implemented on various sites, one of the drawbacks of TCC systems is the preparation and installation of the connection system at the interface layer, which can add to the total cost of the construction [16]. Furthermore, construction methods also raise a question. It should be noted that concrete can be prefabricated or cast onsite. When adopting onsite casting methods, wet concrete is cast and cured on the dry timber which can result in degradation of timber strength and delamination of the timber from the moisture absorption for a long period of time [17]. The moisture transfer from the concrete also leads to a change of curing condition and water content which reduces the concrete quality [18]. To address this concern, a plastic film can be implemented at the interface layer to prevent moisture transfer. However, the unsettled condition of plastic film during the concrete casting results in gaps at location of the connection system, particularly when notch-type connections are adopted, as confirmed by experimental tests [19]. Song et al. [18] proposed the application of epoxy adhesives to the surface of timber panel before the concrete casting in order to prevent the water absorption from wet concrete to timber. In addition, concrete should be low-shrinkage and self-compacting [19] by using additional plasticizer and fine aggregate to limit the gap governed by geometry at corner of the notch connector.

For the TCC floor, concrete can be placed on top of a solid beam or an engineered wood beam to form a ribbed system, referred as T-beam type floor (see Figure 2a). As an alternative, timber panels made of engineered wood products can be connected to a concrete slab to create a flat slab system (see Figure 2b). In high rise buildings, the flab slab TCC floor, which has a larger span-to-depth ratio, is more

practical since it maximizes the clear span in each storey of the building in comparison to a high cross-section of the T-beam type floor. Additionally, the timber panel of the flat slab floor can be treated as a framework in the construction process to cast the top concrete part and can be used as a biophilic ceiling after the construction. Conversely, T-beam type TCC floors are generally used in bridge constructions and industrial buildings since they can offer wider spans by increasing the beam height [7]. In addition, the spaces between TCC beams can be used for pipes and cables service in buildings.

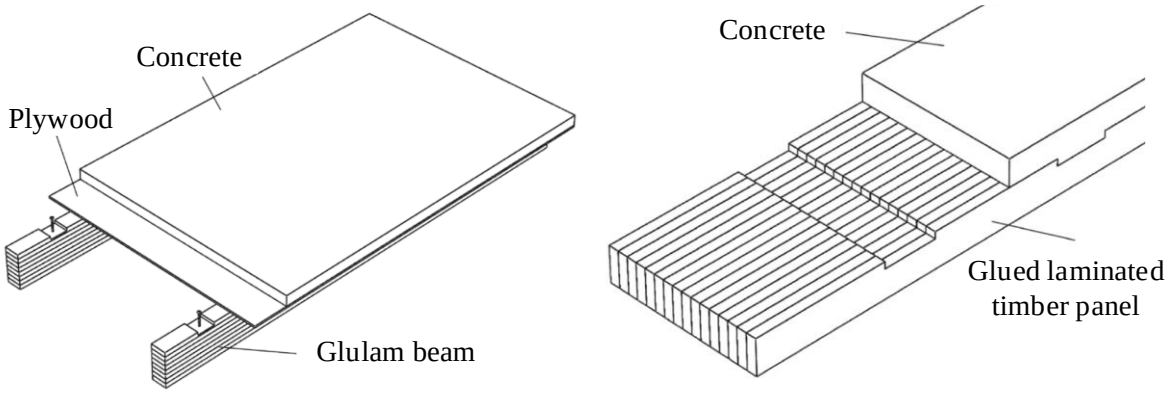

a. T-beam type TCC floor system b. Flat slab TCC floor system

Figure 2: Two types of TCC floor systems [16].

2.2.2 A brief history of TCC floors system

The concept of the TCC floor was emerged in response to the steel shortage that occurred after the World Wars, as steel was commonly used for reinforcement in reinforced concrete components [21]. Many efforts were made to apply TCC technique in new buildings or highways, refurbishment of existing floors, and reinforcement in bridge constructions. The first appearance of the TCC system was a patent granted to Muller in 1922 with the document entitled “Slab made of upright standing wooden planks or boards and concrete top layer” [22]. In his study, nails and steel brace systems were adopted as the connection system between concrete and timber beams. Subsequently, Otto Schaub filed other patents in 1931 [23] for a “Wood reinforced concrete structural member” in the United States, and in 1939 [24] for a “Composite floor made of wooden ribs and concrete slab” in Germany. This system adopted steel Z-profiles and I-profiles as the interlayer connection system in order to enhance the composite action between concrete and timber (see Figure 3). Despite these early developments, few reports on the application of TCC techniques were available until the development of new joint technologies and calculation models in 1970s [1]. In addition, as stated in the literature review of Yeoh [9] on the development of timber-concrete systems, the floor design at the earliest time did not comply with the current regulations in terms of sound insulation and fire resistance.

The timber-concrete composite technique can be adopted to renovate or refurbish the existing buildings. In 1960, a historical building with more than 10000 m^2 in Bratislava, former Czechoslovakia, was renovated as reported by Poštulka [25]. The floor system was strengthened by connecting existing timber panels and beams to new cast concrete panels using a connection system of nails. A similar application on another building with 1000 m^2 of timber floors in Lodz, Poland, was reported by Godycki [26]. In both cases, the strengthening by TCC technique cost less than half in comparison to a new floor construction. Other renovations of historic buildings in Italy by strengthening the existing timber with

additional concrete were described by Turrini et al. [27] and Blasi et al. [28]. In an experimental study, Van der linden et al. [29] also proposed a technique of renovation on old timbers by adding a concrete slab with an L-shaped sheet metal nail plate system embedded in concrete.

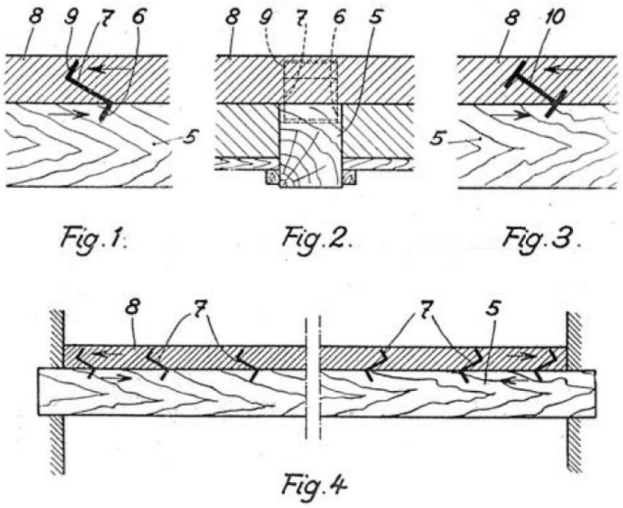

Figure 3: Steel Z-profiles and I-profiles between timber and concrete by Otto Schaub [24].

Besides the renovation and strengthening of existing structures, TCC technique has also been adopted for new building floors. Natterer et al. [30] described a solution of TCC floor in a multi-storey residential building in Switzerland by connecting concrete slab with nail-laminated timber slab using post-stressed dowels. Poutanen [31] described the application of prefabricated members on floor and wall using TCC technique. Nail plates and steel U clamps were adopted as the connection system between concrete and timber members. As mentioned in his publication, until 1990, this solution was applied to more than 400000 m^2 by nine different producers.

The interest in TCC techniques was also found in new bridge constructions. The earliest application of TCC technique on bridge structures could be found in the United States starting from 1930s [32]. In 1943, by aiming to limit the use of steel, a composite bridge was constructed in Florida by linking the concrete panel with the timber beam using triangle steel plates driven into grooves of the timber parts. In California, United States, one of the first composite bridges was built by fastening concrete slab to Douglas fir beam using the spiral dowel after composite design and construction were introduced into the American Association of State Highway Officials Specifications in 1944 [33]. According to The US National Bridge Inventory, more than 180 TCC bridges built during the world wars are still in service today [34].

The use of TCC system spread to Australia and New Zealand after the Second World War and then to many parts of central Europe since 1990s. Balough [35] reported that at least a few hundred of TCC bridges have been known and are still in service until today. In 1957, the first bridge in New Zealand was constructed across Mangaharekeke stream near the northern boundary of Kaingaroa forest using TCC solution with a connection system of groove connectors and triangle steel plates [36]. More TCC bridges were built for heavy traffic in two forms: T-beam and flat slab bridges [37]. Glue combined with mechanical fasteners was adopted as the connection system in T-beam bridges while notches and triangular steel plates were used in flat slab bridges. T-beam bridges included the Poporangi stream bridge with 10.8 m long, which was completed in 1970 and the Tauranga-Taupo River bridge with a

span of 24.5 m, which was completed in 1981. The latter flat slab type system was applied to TCC bridge with a total span of 6 m.

Additionally, a research project named “the Nordic Timber Bridge” was conducted in Helsinki University of Technology [38]. The fatigue tests of four different connection types (Xp, Xe, VN, and XN) were conducted to determine their strength and stiffness which were required for the joints in the longer span of timber-concrete composite bridges. The experimental specimens were composed of two glued laminated beams with dimensions of 240 mm in width and 750 mm in height, connected to a 350 mm thick concrete layer using different types of connection systems such as notches and steel fasteners. The length of experimental specimens in the fatigue tests was 1200 mm. The schematic presentation of the specimens is detailed in Figure 4. Theses studied connection systems were served as a guide for the design of many TCC bridges in Finland and some other countries.

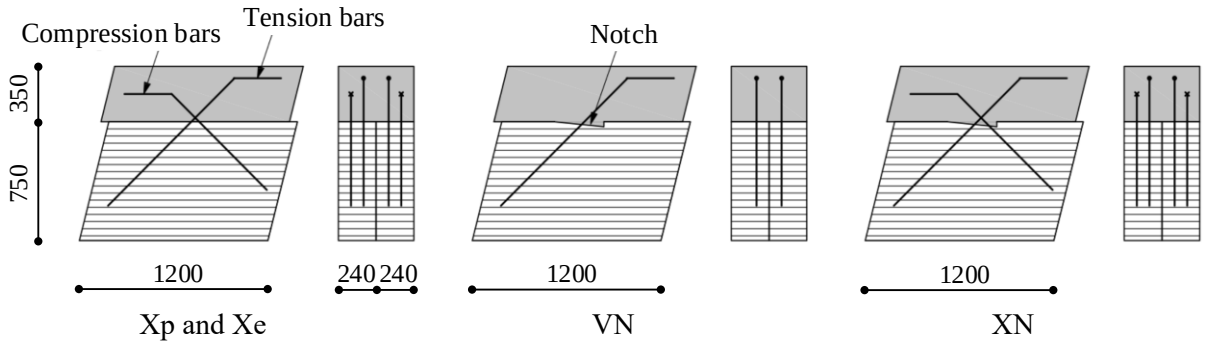

Figure 4: Test specimens of TCC floors in a Nordic Timber Bridge project of Helsinki University of Technology (dimensions in mm) [38].

2.3 Mechanical behavior of concrete

Concrete is an engineering composite material produced by integrating dried components of gravel, sand, and cement with water to create one homogeneous mixture [39]. The proportions of each element result in varying concrete strengths which can range up to 90 MPa [40]. Concrete is commonly regarded as a compressive material owing to its high resistance in compression compared to resistance in tension. Its tensile strength is assumed to be ten times lower than its compression strength [41]. Figure 5 presents the typical stress-strain relation in uniaxial compression and tension behavior [42]. In compression, concrete exhibits nearly linear behavior up to 40 percent of the concrete compressive strength, f_{cm}, followed by gradual increase up to the concrete compressive strength at corresponding compressive strain ε_{c1}. In post-peak behavior, concrete strength descends into a softening region until reaching ultimate strain ε_{cu1}. In tension, the stress-strain curve is approximately linearly elastic up to the maximum tensile strength, f_{ctm}, followed by a gradual decrease to zero.

The mechanical performance of concrete at early ages and beyond can be influenced by the creep and shrinkage effects due to the ambient humidity, the dimensions of the element, and the composition of the concrete [40]. Creep is influenced by the maturity of the concrete when the load is first applied and depends on the duration and magnitude of the loading, while shrinkage is defined as the volume reduction as a consequence of the moisture migration when concrete surface is exposed to a lower relative humidity environment than the initial one in its own pore system. Creep and shrinkage of concrete have been given a great deal of attention during the past century, especially during the 1970s and 1980s, driven by the need to quantify the long-term deformation and behavior [43]. The calculation

of the effect of creep and shrinkage is provided in standards, as for example the Eurocode 2 design code [40]. It should be noted that time effects won't be addressed in this work.

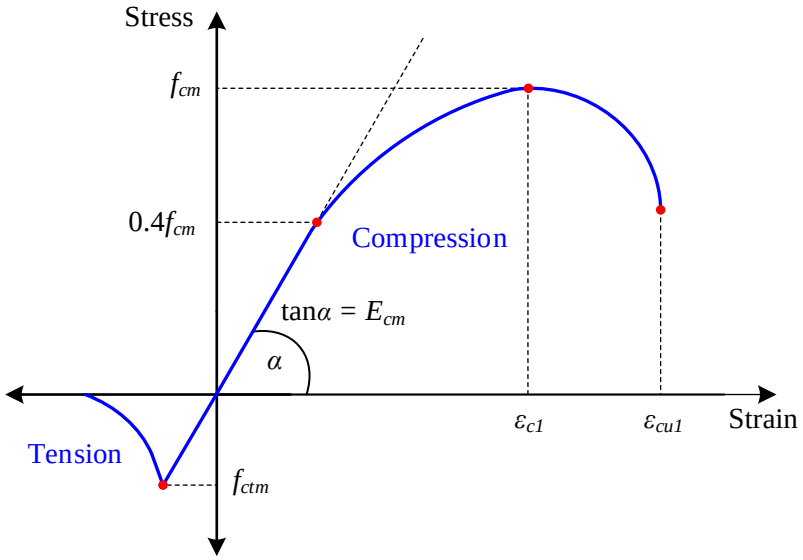

Figure 5: Typical stress-strain relationship of concrete in uniaxial compression and tension [42].

To model the instantaneous nonlinear behavior, concrete can be simulated using concrete damaged plasticity (CDP) models. The failure mode of this kind of models is based on two main failure mechanisms which are cracks in tension and crushing in compression. Lubliner et al. [44] developed a plasticity model assuming of non-associated potential plastic flow in order to characterize the behavior of concrete. The yield condition of the concrete behavior is based on the loading function with modifications suggested by Lee et al. [45] to account for different tension and compression strength evolutions, while the flow potential is defined by using Drucker-Prager hyperbolic function. To determine the flow potential and yield surface of the concrete behavior, the model depends on four constitutive parameters including the shape factor for yield surface k_c, the dilatation angle Ψ, the ratio of biaxial compressive strength to uniaxial compressive strength f_{b0}/f_{c0}, and the eccentricity ε, which are detailed in [45].

The stress-strain relationships and corresponding damage parameters used in this research are based on the primary model proposed by Alfarah et al. [46]. The uniaxial compressive and tensile responses of concrete are described by damaged plasticity as shown in Figure 6. The continuous line curve illustrates the constitutive law of the concrete material while the dash line illustrates the loading/unloading branches. Parameters f_{cm} and f_{ctm} are compressive and tensile strengths, with corresponding strains ε_{cm} and ε_{tm}, respectively. ε_c^{pl} and ε_c^{el} are strains of the plastic and elastic damaged components in compression behavior. ε_t^{pl} and ε_t^{el} are strains of the plastic and elastic damaged components in tension behavior. For the compression curve in Figure 6a, it is divided into three segments. In the first segment, concrete behaves linearly from the initial load (zero stress) up to a stress of $0.4f_{cm}$, which is given in eq. (1):

$$\sigma_{c,1}(\varepsilon_c)=E_0\varepsilon_c \quad (1)$$

In the second segment of the stress-strain relationship, the concrete is characterized by stress hardening in quadratic curve which is in between the stress of $0.4f_{cm}$ and f_{cm}:

$$\sigma_{c,2}(\varepsilon_c)=\frac{E_{ci}\frac{\varepsilon_c}{f_{cm}}-\left(\frac{\varepsilon_c}{\varepsilon_{cm}}\right)^2}{1+\left(E_{ci}\frac{\varepsilon_{cm}}{f_{cm}}-2\right)\frac{\varepsilon_c}{\varepsilon_{cm}}}f_{cm} \tag{2}$$

where the initial tangent modulus of deformation of concrete for zero stress E_{ci} and the undamaged modulus of deformation of concrete E_0 are given by $E_{ci} = 10000(f_{cm})^{1/3}$ and $E_0 = E_{ci}(0.8+0.2f_{cm}/88)$ (in MPa).

The third segment of the stress-strain relationship of concrete in compression can be computed as the following equations:

$$\sigma_{c,3}(\varepsilon_c)=\left(\frac{2+\gamma_c f_{cm}\varepsilon_{cm}}{2f_{cm}}-\gamma_c\varepsilon_c+\frac{\varepsilon_c^2\gamma_c}{2\varepsilon_{cm}}\right)^{-1} \tag{3}$$

with

$$\gamma_c=\frac{\pi^2 f_{cm}\varepsilon_{cm}}{2\left[\frac{G_{ch}}{l_{eq}}-0.5f_{cm}\left(\varepsilon_{cm}(1-b)+b\frac{f_{cm}}{E_0}\right)\right]^2} \tag{4}$$

$$b=\varepsilon_c^{pl}/\varepsilon_c^{ch} \tag{5}$$

$$G_{ch}=(f_{cm}/f_{tm})^2 G_F \tag{6}$$

$$G_F=0.073(f_{cm})^{0.18} \tag{7}$$

where G_{ch} is the crushing energy per unit area, l_{eq} is the characteristic length, and G_F is the fracture energy per unit area. Parameter b is the ratio between strain of plastic damaged component ε_c^{pl} to strain of crushing undamaged component ε_c^{ch}.

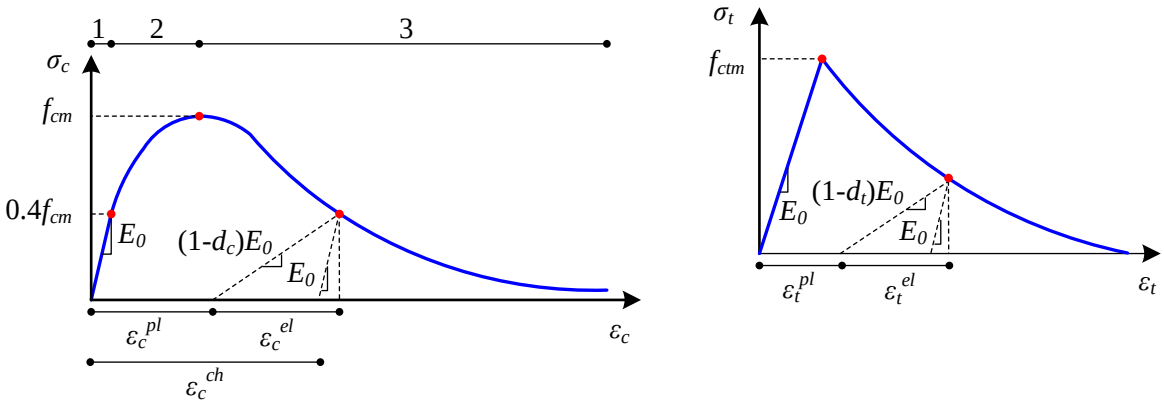

a. Compression b. Tension

Figure 6: Stress-strain curves of concrete under uniaxial loading [46].

In tension, the tensile stress increases linearly up to a maximum stress of f_{ctm}. After the concrete starts cracking at the state of failure stress, the concrete is defined by the softening of the stress-strain response in the manner of exponentially decreasing to zero stress. The relationship between tensile stress $\sigma_t(w)$ (for crack width w) and maximum tensile strength f_{ctm} is given by:

$$\frac{\sigma_t(w)}{f_{ctm}} = \left[1+\left(c_1\frac{w}{w_c}\right)^3\right]e^{-c_2\frac{w}{w_c}} - \frac{w}{w_c}\left(1+c_1^3\right)e^{-c_2} \tag{8}$$

with

$$w_c = 5.14 G_F / f_{ctm} \tag{9}$$

In addition, concrete is accompanied by damage when loading beyond the peak stress in compression f_{cm} and tension f_{ctm}. For the uniaxial loading, the stress-strain relation in the damaged plasticity behavior (see Figure 6) can be characterized by following equations:

$$\sigma_c(\varepsilon_c) = (1-d_c)E_0\left(\varepsilon_c - \varepsilon_c^{pl}\right) \tag{10}$$

$$\sigma_t(\varepsilon_t) = (1-d_t)E_0\left(\varepsilon_t - \varepsilon_t^{pl}\right) \tag{11}$$

where d_c and d_t are the compression and tension damaged parameters ranged from zero for undamaged, to one for fully damaged state. The computation of values d_c and d_t is described in detail in [46].

2.4 Timber

2.4.1 Mechanical properties of timber

Timber has been utilized in construction throughout history and continues to be a relevant building material today. The structural strength of timber relates to the properties of the tree trunk, also known as wood, in the longitudinal direction of the grains of the pipe shaped cellulose [47]. At the microscopic level, timber can be defined as an orthogonally anisotropic material with three axes of symmetry, including the longitudinal axis (L) which is parallel to the longitudinal grain of the timber, the radial axis (R) which is perpendicular to the longitudinal grain of the timber, and tangential axis (T) which is parallel to the annual rings of the timber (see Figure 7).

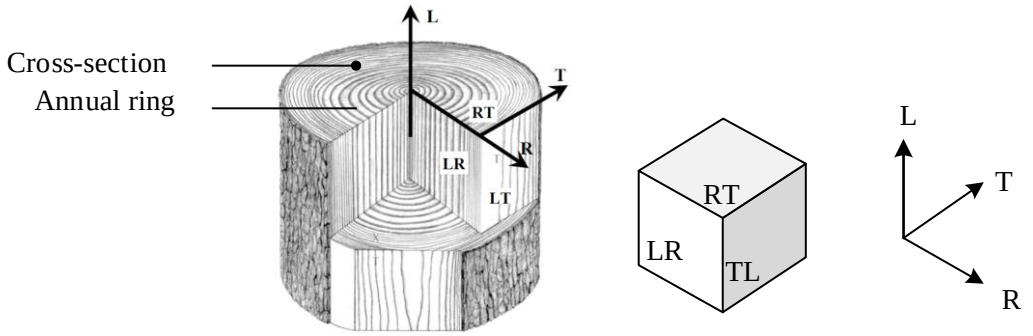

Figure 7: Structural directions of timber in the tangential (T), radial (R), and longitudinal (L) directions [48].

The mechanical properties of timber can be assessed by two methods, which are the visual grading methods (e.g., NF BN 52-001 [49] or EN 14081 [50]), and the machine grading (destructive) methods (e.g., EN 14080 [51] or EN 338 [52]). Figure 8 presents the typical stress-strain curves for timber in various directions [53]. It was found that the timber behaved in a linear elastic way followed by a little plasticity deformation under the axial tension in longitudinal direction. In contrast, when it was loaded in axial compression along the longitudinal direction, high plasticity deformation was noticed. For the compressive behavior in both tangential and radial directions, similar behavior was achieved. For this reason, timber is sometimes considered as an orthotropic material with identical behavior in tangential and radial directions. The stress-strain curves of the timber are usually obtained from small clear specimens free of visual defects such as knots, finger joints, taper, and distortion. At full scale, the behavior of timber is influenced to some degree by the defects mentioned.

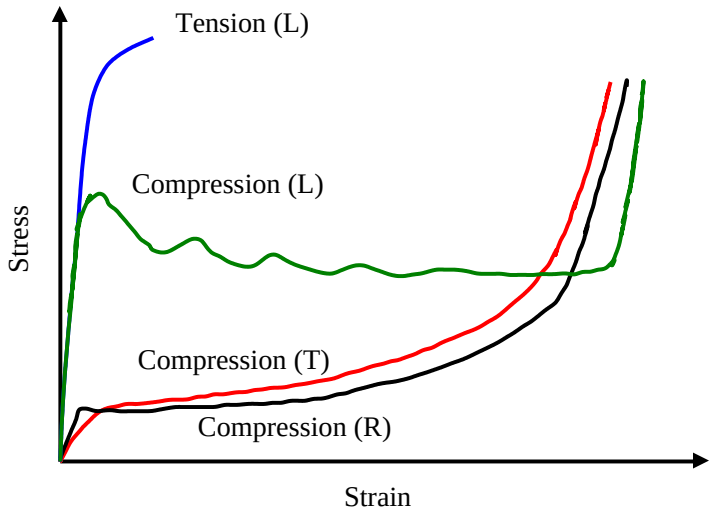

Figure 8: Typical stress-strain curves for timber [53].

Chen et al. [54] also described the behavior of timber in each direction. He mentioned that, for wood subjected to tension or shear, the stress-strain relationship is typically linear elastic, and the failure is quasi-brittle; for wood in compression, the stress-strain relationship is typically nonlinear, and the failure is ductile. The failure mode of wood is a complex problem which can be governed by rupture of tension fiber, delamination of fibers, buckling of the compression fiber, or combined of all mentioned failure modes [55]. Franke et al. [56] conducted a state of the art of failure modes in timber. For the timber in longitudinal direction and perpendicular to grain direction (transversal and radial directions), the compression failure can be described as a ductile behavior with plastic deformations. When the tensile capacity of the timber is exceeded, the failure of timber in either longitudinal direction or perpendicular to grain direction exhibits brittle behavior. According to Ehrhart et al. [57], the failure of the rolling shear occurs when the longitudinal grains roll off each other along the annual rings at either the tangential-longitudinal plane (TL) or the longitudinal-radial plane (LR) (see Figure 9). Due to low shear modulus perpendicular to grain direction, the rolling shear failure can be a critical concern, governing timber structural performances.

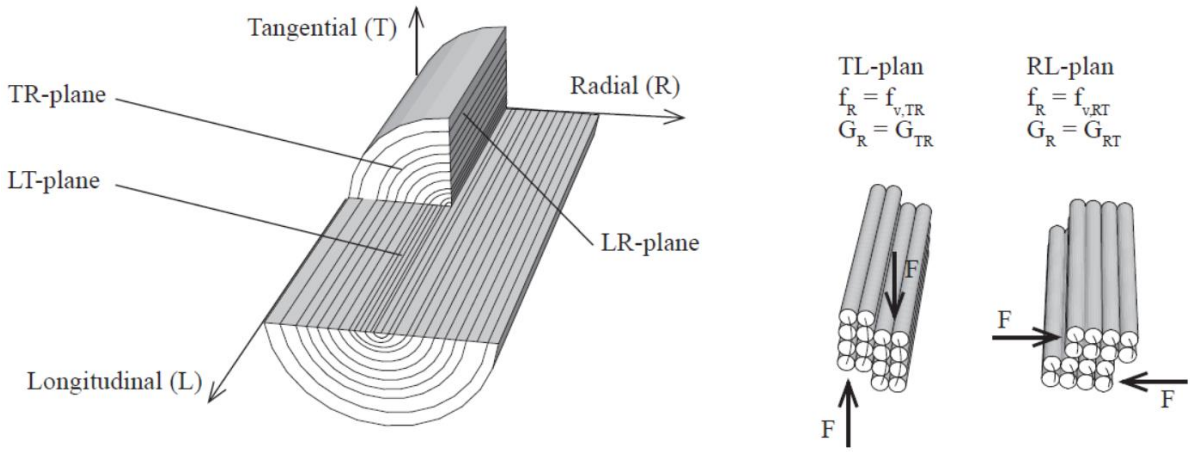

Figure 9: Rolling shear in wood based on Ehrhart et al. [58].

The elastic properties of timber are described by twelve elastic constants, including three elastic moduli, E, three shear moduli, G, and six Poisson ratios, v. The subscripts in elastic and shear moduli refer to the specific direction and plane of elastic and shear moduli. For the subscripts in Poisson ratios and strains, the first letter is the direction of applied stress while the second letter defines the direction of deformation. In the linear elastic behavior, stress σ and corresponding strain ε of timber can be described by Hooke's law as follow:

$$\varepsilon = C\sigma \tag{12}$$

$$\begin{Bmatrix} \varepsilon_L \\ \varepsilon_T \\ \varepsilon_R \\ \gamma_{TR} \\ \gamma_{RL} \\ \gamma_{LT} \end{Bmatrix} = \begin{bmatrix} \frac{1}{E_L} & \frac{-v_{TL}}{E_T} & \frac{-v_{RL}}{E_R} & & & \\ \frac{-v_{LT}}{E_L} & \frac{1}{E_T} & \frac{-v_{RT}}{E_R} & & 0 & \\ \frac{-v_{LR}}{E_L} & \frac{-v_{TR}}{E_T} & \frac{1}{E_R} & & & \\ & & & \frac{1}{G_{TR}} & 0 & 0 \\ & 0 & & 0 & \frac{1}{G_{LR}} & 0 \\ & & & 0 & 0 & \frac{1}{G_{LT}} \end{bmatrix} \begin{Bmatrix} \sigma_L \\ \sigma_T \\ \sigma_R \\ \tau_{TR} \\ \tau_{RL} \\ \tau_{LT} \end{Bmatrix} \tag{13}$$

where

ε_L, ε_T, ε_R	are normal strains in directions L, T, R;
σ_L, σ_T, σ_R	are normal stresses in directions L, T, R;
γ_{TR}, γ_{RL}, γ_{LT}	are shear strains in planes TR, RL, LT;
τ_{TR}, τ_{RL}, τ_{LT}	are shear stresses in planes TR, RL, LT.

In eq. (12), C is the compliance matrix. For the material matrix stiffness, it can be written as $D=C^{-1}$. In addition, Dias et al. [58] gives relations between elasticity and shear moduli in the following expressions.

$$E_0=E_L=30E_T=30E_R \tag{14}$$

$$G_{LT}=G_{LR}=\frac{1}{16}\times\frac{E_L+E_T}{2} \tag{15}$$

$$G_{TR}=\frac{1}{16}\times\frac{E_T+E_R}{2} \tag{16}$$

For Poisson ratios of timber, it can be determined relative to elastic moduli as follows:

$$\frac{v_{ij}}{E_i}=\frac{v_{ji}}{E_j} \tag{17}$$

where $i\neq j$, i,j=L, R, T.

Dias et al. [58] also conducted numerical simulations to study the sensitivity of the results to the elastic relationships as shown from eqs. (14) to (16), and to the Poisson ratios in eq. (17). Accordingly, the results of numerical simulations showed a little influence from the ratio between the elastic properties; however, the calculation became unstable if the value of elastic parameters were too low. For the variation of the Poisson ratios, the simulation obtained exactly the same results showing that the models did not depend on the values given for Poisson ratios.

The development of failure criterion to model the timber behavior is challenging since its mechanical properties depend on timber orientation and direction of loading. Hill [59] proposed a failure criterion which was adapted from the Von Mises criterion to deal with the anisotropic behavior of wood in plasticity. The yielding criterion of anisotropic material has the form of:

$$f(\sigma)=F(\sigma_{33}-\sigma_{22})^2+G(\sigma_{33}-\sigma_{11})^2+H(\sigma_{11}-\sigma_{22})^2+2L(\sigma_{23})^2+2M(\sigma_{13})^2+2N(\sigma_{12})^2 \tag{18}$$

where F, G, H, L, M, and N are constants obtained by tests of the material in different orientations. They are defined as follows:

$$F=\frac{1}{2}\left(\frac{1}{R_{22}^2}+\frac{1}{R_{33}^2}-\frac{1}{R_{11}^2}\right) \tag{19}$$

$$G=\frac{1}{2}\left(\frac{1}{R_{33}^2}+\frac{1}{R_{11}^2}-\frac{1}{R_{22}^2}\right) \tag{20}$$

$$H=\frac{1}{2}\left(\frac{1}{R_{11}^2}+\frac{1}{R_{22}^2}-\frac{1}{R_{33}^2}\right) \tag{21}$$

$$L=\frac{3}{2R_{23}^2} \tag{22}$$

$$M=\frac{3}{2R_{13}^2} \tag{23}$$

$$N = \frac{3}{2R_{12}^2} \tag{24}$$

where R is the yield stress ratio and subscriptions 1, 2, and 3 refer to the direction of the timber in longitudinal, tangential, and radial directions, respectively. The directional yield stresses are defined in relation to the strength of the timber as the following relationships [58]:

$$R_{11} = f_{c,0} / f_{eq} \tag{25}$$

$$R_{22} = R_{33} = f_{c,90} / f_{eq} \tag{26}$$

$$R_{12} = R_{13} = \sqrt{3} f_v / f_{eq} \tag{27}$$

$$R_{23} = \sqrt{3} f_r / f_{eq} \tag{28}$$

where $f_{c,0}$ is the compressive strength parallel to grain; $f_{c,90}$ is the compressive strength perpendicular to grain; f_v is the shear strength; f_r is the rolling shear strength; and f_{eq} is the equivalent yielding strength of the timber.

Glos [60] also studied the stress-strain relationship based on the experimental data of timber in compression parallel to grain (see Figure 10), which can be determined as follows:

$$\sigma(\varepsilon) = \frac{\varepsilon/\varepsilon_{c,0} + G_1(\varepsilon/\varepsilon_{c,0})^7}{G_2 + G_3(\varepsilon/\varepsilon_{c,0}) + G_4(\varepsilon/\varepsilon_{c,0})^7} \tag{29}$$

with

$$G_1 = \frac{f_s}{6E(1 - f_s/f_{c,0})} \tag{30}$$

$$G_2 = 1/E \tag{31}$$

$$G_3 = 1/f_s - 7/6E \tag{32}$$

$$G_4 = G_1/f_s \tag{33}$$

where σ is stress; ε is strain; E is modulus of elasticity; f_s is the residual stress; $f_{c,0}$ is the maximum compression stress; and $\varepsilon_{c,0}$ is the strain corresponding to maximum stress. The four parameters *G1* to *G4* that define the curve were determined using curvilinear regression techniques based on test results of Glos study.

Lau [61] highlighted the advantages of this model such as the stress does not drop to zero at the large strains, and it closely represents the true shape of actual stress-strain curve of timber. Additionally, derived from a comparative study, he also concluded that this model behaved more accurately than other models.

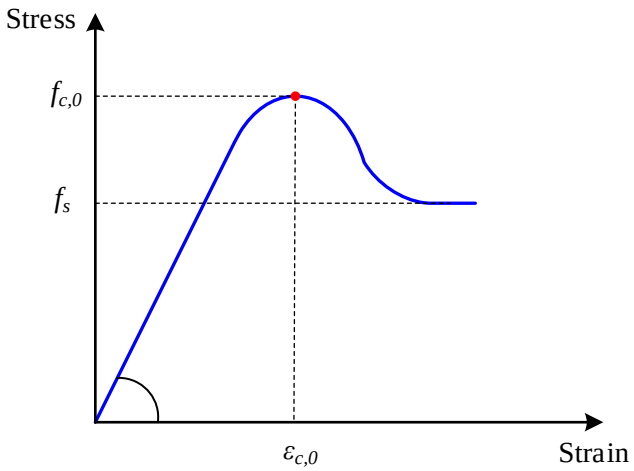

Figure 10: Model of stress-strain relationship in compression described by Glos [60] (reproduced by Lau [61]).

In addition, according to Eurocode 5 [62], the design for working life and durability at the different limit states should take into account the different time-dependent behavior of timber (duration of load, creep) and different climatic conditions (temperature, moisture variations). The change of environmental relative humidity affects the timber behavior by increasing the delayed strains under constant load, referred as the so-called mechanosorptive effect, which results in shrinkage/swelling and influences the Young's modulus [63]. But, as already stated, time effects won't be addressed in this work.

2.4.2 Cross-laminated timber

The limited diameter and strength of wooden logs raise a challenge in modern construction, which requires large section sizes and dimensional stability. To meet design criteria, engineered wood products with better physical and mechanical properties are then developed [64]. Engineered wood products can be lumber-based products such as glue-laminated timber (GLT or glulam), nail-laminated timber (NLT), dowel-laminated timber (DLT), and cross-laminated timber (CLT), or can be structural composite lumbers which are manufactured with wood veneers bonded together with adhesives such as laminated veneer lumber (LVL), laminated strand lumber (LSL), orientation strand lumber (OSL), and parallel strand lumber (PSL) [16]. Compared to traditional lumber logs, engineered wood products have advantages of a high strength to weight ratio [8], and inherent resistance due to the thermal barrier formed by the charring layer of the outer surface [65].

In TCC floors system, timber beams made of glue-laminated timber (GLT), laminated strand lumber (LSL), or laminated veneer lumber (LVL) are usually adopted for T-beam floors, while timber panels made of cross-laminated timber (CLT), laminated veneer lumber (LVL), dowel-laminated timber (DLT), and nail-laminated timber (NLT) are usually employed for flat slab floors [16]. For this research, cross laminated timber is adopted as the timber part in the TCC floor.

Cross-laminated timber was introduced in Germany by Professor Gerhard Schickhoferand in 1994 [66], with the first technical publication in 1998 [67]. Cross laminated timber is an engineered wood panel (see Figure 11) manufactured by laminating the timber boards in alternating arrangements at a precise angle, typically at 90 degrees, and gluing them together using hydraulic or vacuum press techniques [68]. The alternation or cross-wide arrangement of timber boards in the CLT panel minimizes the directional disparity, providing high strength and stiffness in both directions (two-way load bearing

floor). In addition, the CLT cross-section is laid up in uneven numbers, usually three, five, or seven layers, to ensure that the upper and lower layers are in the same grain direction in order to maintain the symmetry condition. Each timber board has a thickness, t_l, between 12 mm to 45 mm [69] while the width of the timber board, w_l, is at least four times the thickness of the timber board to withstand the rolling shear stress ($w_l \geq 4t_l$) [70]. The adhesive is typically applied to wide surfaces of the timber board and sometimes to side surfaces (narrow surfaces). It should be noted that the influence of side faces bonding on mechanical performance is little [67]. Over the past two decades, cross-laminated timber has been receiving attention globally, particularly in multi-storey buildings [71]. The success of the CLT in building applications results from its advantages in manufacturing, installation, mechanical performance, environmental impact, and cost competitiveness [71]. However, certain limitations are also realized from the CLT configuration, such as low rolling shear properties and strength variability of natural timber material due to natural defects in comparison to concrete [72].

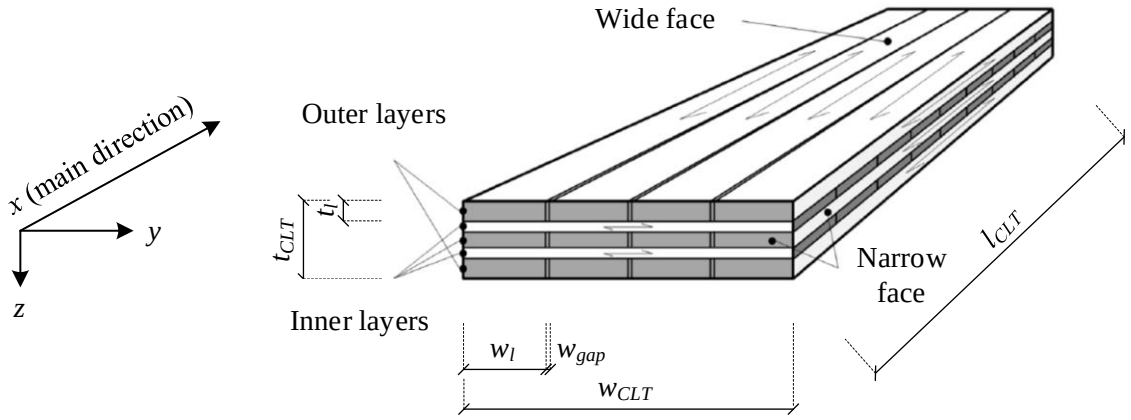

Figure 11: Cross Laminated Timber [70].

Design and guidelines for the CLT panel have been published and are available, such as the European guideline EN 16351 [73], the North American standard ANSI/APA PRG 320 [74], and the Canadian standard of Engineering Design in Wood CSA-O86:2014 [75].

2.5 TCC connection system

The connection system at the interface layer between concrete and timber panels is the critical component to ensure the structural efficiency of TCC floors [4]. In order to achieve high composite action in TCC floors, the connection system should have sufficient strength to transfer the horizontal shear force, enough stiffness to limit relative slip, and adequate ductility to allow load redistribution and to avoid brittle failure mechanism [1]. The three primary characteristics of the connection system, namely strength, stiffness, and ductility have a significant influence on the structural response of TCC floors. The strength of the connection system is determined by the maximum shear load transferred at the interface layer, while the stiffness is characterized by the slip modulus derived usually from the load-slip curve of experimental pushout tests. A high stiffness allows a reduction of the TCC thickness and controls the midspan deflection of the TCC floor due to an increase in bending stiffness of the TCC floor [2]. Some ductility is desirable since both timber and concrete behave relatively brittle in tension and compression, respectively, and the connection system is the only source of ductility for the TCC system [9].

To assess the mechanical properties of the connection system, various types of pushout test setup have been conceived by researchers including pure shear tests, double-shear tests, and asymmetric shear tests. Monteiro et al. [76] conducted a statistical analysis to establish a database for pushout test configurations based on 60 references in literature. Figure 12 illustrates the fractions of different pushout test configurations derived from the statistical analysis. The double shear tests appeared to be the most popular, accounting for 43 percent. For double shear tests, the center element could be concrete or timber. The database further indicated that concrete was considered as the center element for around 65 percent, whereas timber was considered as the center element for about 35 percent.

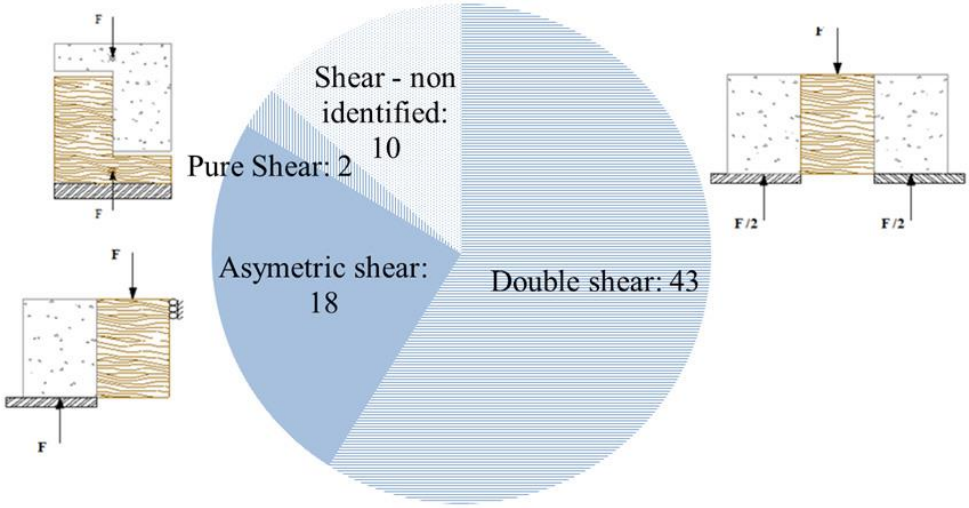

Figure 12: Contribution of different types of pushout test configurations [76].

Various standards for loading protocol have been adopted to perform pushout tests, for example EN 26891 [77] which is the standard for timber-timber joints, or Eurocode 4 [78] which is intended to address the composite concrete-steel connection system. Recently, the technical specification CEN/TS 19103 [79] allows to adopt the loading procedure given by EN 26891 [77] in order to perform pushout tests for concrete-timber connections.

However, limitations are observed in EN 26891 [77], relating to methods for the evaluation of the slip modulus. According to EN 26891 [77], the slip modulus depends on the estimation of the maximum force which can differ up to 20 percent compared to actual maximum force obtained from the experimental test. Along with the pronounced non-linear load slip behavior of the TCC connection system, the results may not represent the actual behavior of the tested connector. However, this standard EN 26891 has been commonly adopted by various researchers [1].

Besides the demand for mechanical properties, connection systems of the composite structure should be cost effective and practical (constructability of the connection system). The typical connection systems for TCC floors are self-tapping screws, coach screws, steel dowels, steel mesh plates (known as HBV connectors), notched connections, adhesives, and the combination of mentioned connectors [4], [5]. Based on mechanical properties of the connection system, Ceccotti [80] classified the most commonly used shear connector into four categories as shown in Figure 13a. The least rigid connectors were placed in group A, while the most rigid connectors were categorized in group D. From the load-slip curves in Figure 13b, a continuous connector with glue in group D provided the highest strength and stiffness, but with brittle behavior. For notch connectors combined with metallic elements, relatively large stiffness and ductility were obtained.

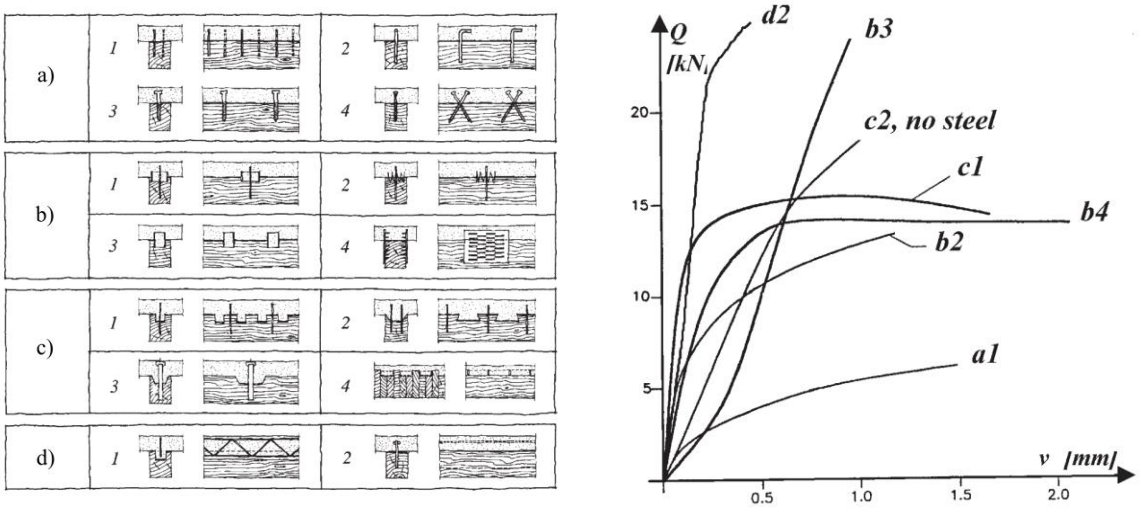

a. Connection system categories b. Load-slip curves

Figure 13: Various connection systems and their corresponding load-slip curves [80].

Additionally, the TCC connection system can also be categorized based on the connection typology. From the database established by Monteiro et al. [76] at the Civil Engineering Department of the University of Coimbra, Dias [1] classified connection systems into four groups: dowel type fasteners, notches, notches combined with steel fasteners, and other systems (glue, nail plates, steel meshes). Figure 14 presents the distribution of the development of TCC connection system. The statistics indicate that dowel type fasteners obtain the highest attention for researchers, which represents nearly half (45 percent) of the research on the connection system. The notches either alone or combined with steel fasteners claim a portion of about one-third (33 percent) of the research works, while the other connection systems, such as nail plates or system based on gluing, account for 22 percent of the studies.

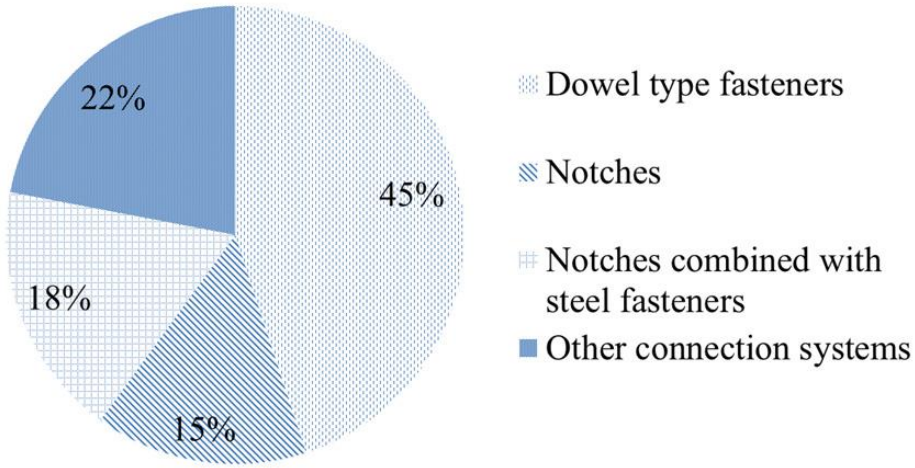

Figure 14: Distribution of the development of TCC connection system [1].

In overall, it can be seen that dowel type fasteners are the most flexible connection system with the lowest stiffness and the largest ductility. Steel mesh and adhesives are relatively stiff. Notch alone is also stiff but highly prone to sudden collapse compared to other connection systems. In response, notch is often combined with steel fasteners to add ductility to the connection system. Each category of the connection system is further investigated in the following subsections.

2.5.1 Dowel type fasteners and continuous metal connectors

The timber-concrete connection system was first adopted based on the background of timber-timber joints. Connection systems at that time focused on the low cost with high load-carrying capacity and ease of fabrication, which involved steel fasteners such as nails, bolts, dowels, and screws [1].

Research on dowel type fasteners is numerous. Schaub [24] used steel Z-profiles and I-profiles as connectors, McCullough [81] adopted metallic fasteners and pipe dowels in TCC structures, and Richart et al. [82] attempted to provide the full composite action in beam test using triangular plate-spikes. In the early 1990s, Meierhofer [83] introduced special timber-concrete connectors made of steel fasteners consisting of two heads as shown in Figure 15a. The lower 100 mm threaded part was screwed in the wood, and the upper 50 mm long part was anchored in the concrete. Shear tests (pullout tests) and four-point flexural tests were performed on timber-concrete composite specimens using these screws with several constructive connection arrangements as shown in Figure 15b in order to minimize the horizontal slip and to increase the stiffness of composite section. The results indicated that the arrangement type, in which screws were placed inclined at an angle of 45^0 cross each other, obtained the most satisfying results. Following studies of Van der Linden [21], Dias [84], and Mai et al. [85] also included this special screw in their research. They confirmed that, in order to obtain the desired characteristic of the connection and to improve the composite action, screws should be arranged with an inclination angle between 30^0 to 45^0.

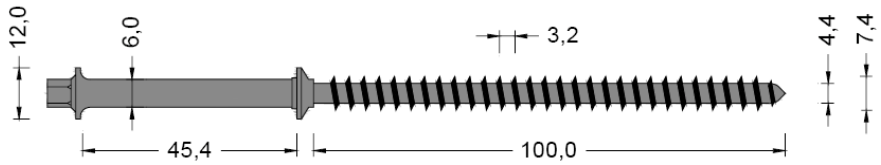

a. Screw adopted in TCC structure (dimensions in mm)

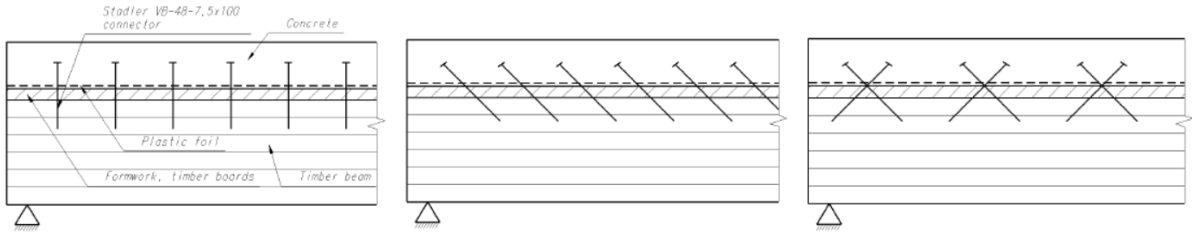

b. Arrangements of the connectors in bending tests

Figure 15: TCC connector and its arrangements in bending tests described by Meierhofer [83].

It should be noted that the steel fastener is embedded in the timber in one end and anchored to wet or prefabricated concrete in the other end. Thus, material properties of concrete and timber also influence the load-carrying capacity and stiffness of the connection system since its characteristic depends on the concrete strength and the embedment length of the steel fastener in the timber beam [84]. However, dowel type fasteners are considered as a semi rigid connection system which can limit the structural efficiency of the TCC floors.

Besides discrete steel fasteners, continuous steel connectors were also developed. Girhammar [86] investigated the characteristics of nail plates by conducting 50 pushout tests to evaluate load-slip curves and failure modes. After this first experimental study, many researchers such as Van der Linden [21] and Jacquier et al. [87] also adopted nail plates (see Figure 16) as the connection system in composite beams

to evaluate the maximum load-carrying capacity using four-point bending tests. The results showed that the performance of nail plates was satisfactory in terms of strength and stiffness and was able to provide a high composite action to the TCC system. However, the assembly process was relatively complicated and costly compared to the other connection systems.

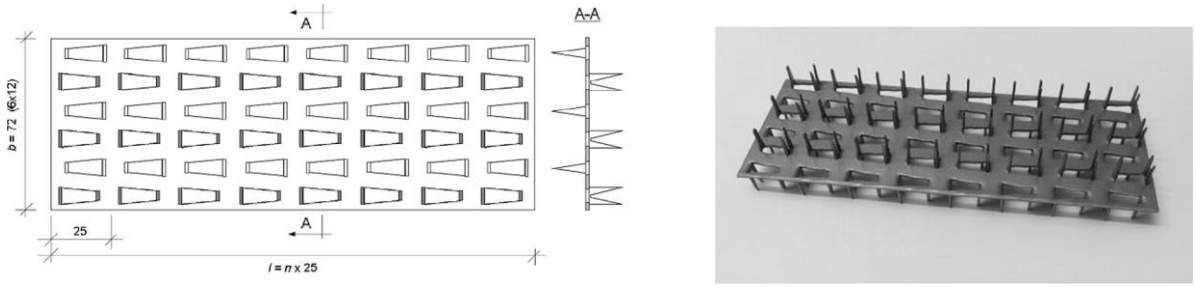

Figure 16: Nail plates as the connection system in TCC structure [87].

Following the finding in the mentioned literature, dowel type fasteners made of nails, screws, steel dowels, and bolts are commonly used connectors in the TCC structure due to their simplicity and high ductility. However, dowel type fasteners are considered as a semi rigid connection system which can limit the structural efficiency of the TCC floors. For continuous connectors, such as steel plates or nail plates, despite their capacity to offer high strength and stiffness, their complicated assembly process increases the production cost.

2.5.2 Adhesives and glued-in connectors

The glue connection can generate a very rigid behavior between timber and concrete. Pincus [88] tested 5 composite beams using epoxy resin to connect a wet concrete flange and timber beam together. As a result, a highly rigid connection with little relative slip was obtained until the failure of the specimen. However, the compatibility between concrete and epoxy was not described. In 2007, a similar approach was proposed by Brunner et al. [89] that connected a timber beam to wet concrete panel after coating the epoxy at the interface layer. The authors mentioned the high stiffness of the connection system but also raised an uncertainty due to the risk of mixing fresh concrete with wet epoxy. In 2010, Negrão et al. [90] conducted 18 pushout tests on TCC specimens using adhesive at the interface layer. Several factors were considered which involved the variation of the moisture content, adhesive film thickness, adhesive types, and surface of the interface layer. High shear strength was obtained due to the uniform transfer of shear force over the entire surface of the interface layer that was applied to the adhesive material. The failure was mostly governed by concrete in brittle behavior. In addition, the bonding system was optimized under steadily dry conditions. The author also stated that the application of adhesive material can cause delamination at the interface layer due to thermo-hygrometric behavior between adhesive and composite elements. Even if glue connection is a potential connection system, it is still under development to fulfill high requirement in quality control and long-term performance [9].

Dowel type fastener and metal continuous connectors can also be adopted along with the adhesive connection to withstand the brittle failure and uncertainty of adhesive behavior in long-term performance. Piazza et al. [91] tested glued-in dowel connectors and a continuous system made of steel sheet (see Figure 17). Two types of glued-in dowel connectors were tested, including the bend dowel fastener, which was glued to the timber in one end while the other end was bended at 90 degrees to connect with the concrete panel, and the concrete stocky connector, in which a straight dowel was

adopted into the round notch connector. The results of full-scale bending tests on beams demonstrated that the composite beams exhibited linear responses up to nearly half the maximum load level followed by a post elastic hardening stage. In addition, 70 percent and 85 percent of composite efficiency were achieved respectively for bend dowel and concrete stocky. Compared to the timber beam, using glued-in bend dowel and concrete stocky could improve the bending strength approximately 2 to 2.5 times as measured in the bending test.

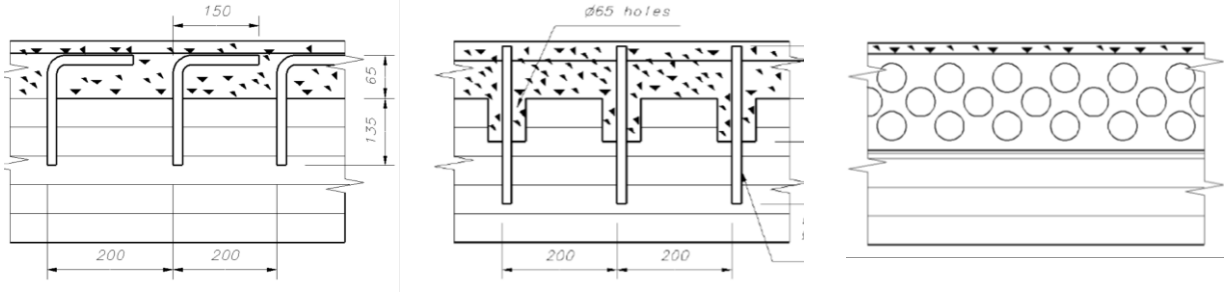

a. Bend dowel b. Concrete stocky c. Steel sheet

Figure 17: Glued-in dowel and steel sheet connection systems described by Piazza et al. [91].

In overall, using adhesive in the connection system or applying glued connection can provide various advantages over mechanical fasteners such as higher strength and stiffness. Furthermore, local force concentrations are avoided since the applied shear force is distributed uniformly over the entire surface. However, challenges associated with on-site application, quality control, and long-term performance have limited the use of these connection systems in practice and called for further development.

2.5.3 Notch connectors

A notch connector is an interlocking solution between concrete and timber which is fabricated by cutting a groove in the top of the timber surface and filling it with concrete afterward. With the facilitation of the Computer Numerical Control (CNC) machine to manufacture the desired shape of the notch, various shapes of the notched connection such as rectangle, round, dovetail, and trapezoid have been studied [16]. Figure 18 illustrates different shapes of notched connectors which are derived from the literature study of Zhang [16]. Among them, notches with rectangular and trapezoidal shapes are the most commonly adopted.

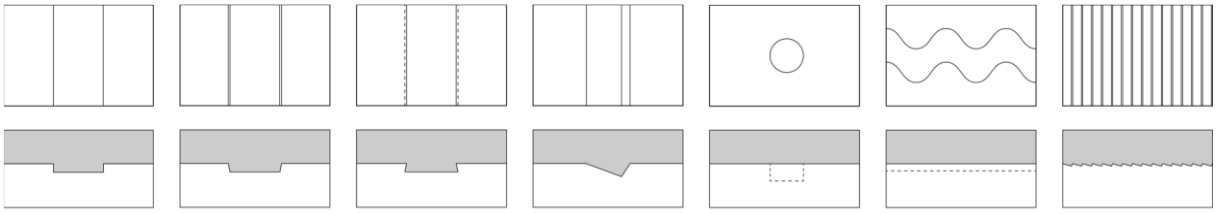

Figure 18: Different shapes of notched connectors [16].

Boccadoro [92] conducted a total of 28 asymmetrical shear tests on beech Laminated Veneer Lumber (LVL)-concrete connection without vertical steel reinforcements in order to investigate the influence of notches with different geometries and material properties on the strength and stiffness of the connection system as well as its post-peak behavior. Three failure modes were observed from the tests: a brittle shearing-off failure of the timber, a ductile compressive failure of the timber, and a brittle

shear failure of concrete. He also mentioned that the ductility of the notch in post-peak performance was slightly improved when notch connectors experienced compressive failure in the timber. In addition, Jiang et al. [93] studied the shear performance of notched connectors for glulam-lightweight concrete composite beams by 6 groups of pushout tests with varied concrete types, shear length of the timber, and the presence of inserted fasteners in the notches. They confirmed that low shear capacity and poor ductility were obtained when the failure was governed by shear fracture of concrete or timber.

As indicated in the literature above, when using notched connectors as the connection system in TCC structure, high strength and stiffness are achievable resulting from the bearing surface of timber or concrete (depth or width of the notch). Notch is often classified as the most effective solution for the TCC connection system due to the simplicity of the fabrication and its high performance. However, some drawbacks can be highlighted:

- a low uplift resistance,
- high stress concentration provoking sometimes a brittle behavior.

To address the issue of the brittle failure, the reinforcement of additional fasteners in the notch connection is suggested in order to improve the strength, ductility, and post-peak behavior of the connection system. Zhang [16] presents several reinforcing techniques found in literature which involved vertical screw or self-tapping screw embedded into timber in the notch or in front of the notch, double head steel dowel, post tensioned steel dowel, end to end steel rod, and steel rebar (see Figure 19).

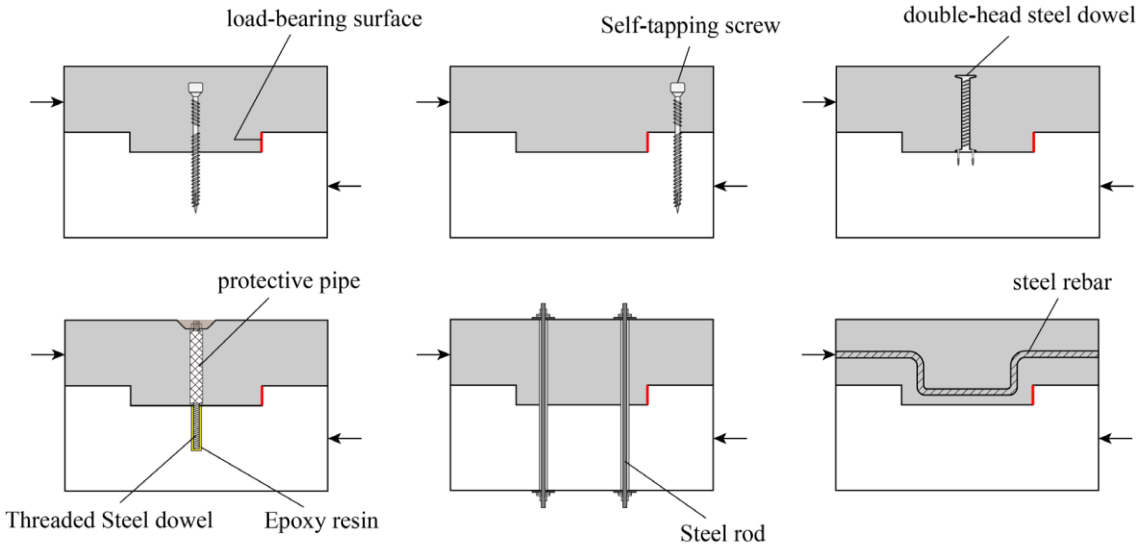

Figure 19: Reinforcing techniques in notched connectors [16].

Yeoh et al. [94] carried out a parametrical experimental study on symmetrical pushout tests on LVL-concrete connection specimens in order to investigate the effects of depth, length, and shape of the notch and of the presence, size, and penetration of lag screw reinforcement in the timber (see Figure 20). It was found out that the longer length of the notch increased the strength of the connection, whereas the strength, stiffness, and post peak performance of the connection were influenced by the presence of embedded coach screws. The size of the screw affected the strength but not the stiffness while the penetration depth influenced the stiffness but not the strength. Similar performance was observed between the rectangular and triangular shaped notches. On the other hand, Boccadoro et al. [3] later

performed a series of ten bending tests in order to evaluate the feasibility of timber-concrete composite members made of beech LVL with notched connections. The presence, the amount, and the mode of vertical embedded reinforcement (screws or fasteners) in the notches were studied. The results demonstrated that a ductile behavior of the composite member could be obtained if a compressive failure of the timber governed the mode of failure. The vertical embedded reinforcement in the notch was however indispensable to prevent gap opening and concrete failure.

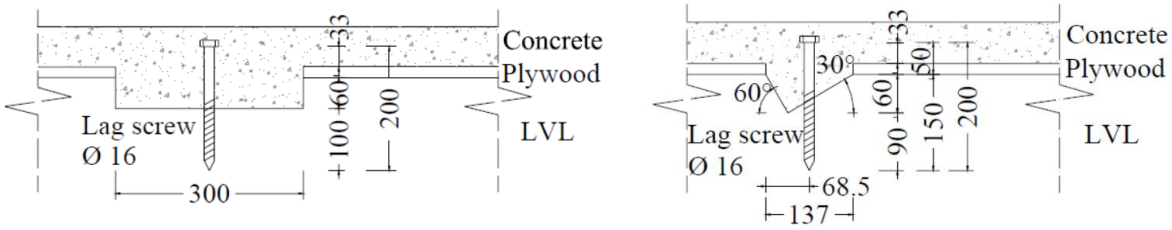

a. Rectangular notch b. Triangular notch

Figure 20: Notched connectors tested at UTS described by Yeoh et al. [94].

More recently, Zhang et al. [19] implemented shear tests on 60 specimens of notched connections in mass timber-concrete floor systems in order to study the influence of important factors on the performance of notched connections (see Figure 21a). The factors included the geometry of notches, orientation of the timber, and the presence as well as the position of the additional embedded steel fasteners (self-tapping screws). It was found that the timber orientation significantly affected the connection performance. They commented that such a huge disparity of the connection performance by the timber orientation made it challenging to use notched connection in two-way slabs. CLT panels are typical in this situation. However, the research (e.g., [95], [96], [97] among the few) on the behavior of the CLT-concrete notched connectors is still scarce. Lamothe et al. [95] developed a ductile notch connector between Glue Laminated Timber (GLT) panels and concrete slabs as well as between CLT panels and concrete slabs using special concretes. It was observed in their pushout tests that the notch connections with GLT panel were stiffer than those with CLT panel. As for the connection of the CLT panel, they recommended that the notch depth should be limited to remain within the first single layer of the CLT panel to avoid the rolling shear mechanism in the cross-layer of the CLT panel. It should be noted however that they used two or four steel screws inserted inside each notch. Thai [96] conducted a large number of pushout tests in order to study the performance of notched connectors in CLT-concrete composite floors with the focus on the influence of key parameters such as heel length, notch depth, concrete thickness, reinforced screw length, loading sequence, and moisture content of timber. Experimental results proved that the performance of the notched connector depended significantly but not linearly on the notch depth and the length of the loaded edge. The connector with a deeper notch and a shorter heel will be stiffer and more robust, but it also tends to have a brittle rupture. Additionally, Jiang et al. [97] investigated the structural behavior of CLT-concrete floors by conducting four pushout tests and two bending tests, complemented by numerical simulation and analytical model. High shear stiffness and capacity of the notched connectors were obtained in pushout tests, whereas the bending tests showed high composite action. They even proposed a modification of the so-called gamma method for composite floors with 5-layer-CLT panel. It was also discovered in their study that using the embedded vertical screws as vertical link between CLT and concrete at the two innermost-notched connectors was important to prevent the separation of the concrete part from the timber part, as it could lead to large deflections or even a premature failure of the composite floor.

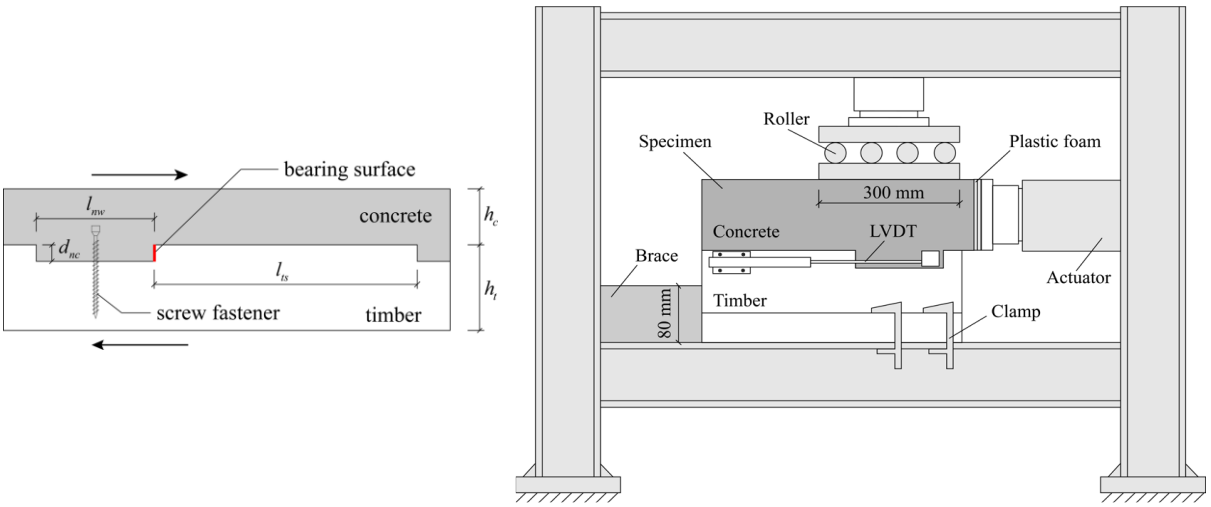

a. Notched connector configuration b. Pushout test setup

Figure 21: Notched connector and pushout test setup [19].

Based on the findings from the above studies, it can be concluded that the concrete notch can provide higher strength and stiffness, but usually with brittle behavior. To improve ductility and uplift resistance to the notched connector, metallic fasteners are usually added to the concrete notch. However, this enhancement requires higher cost and time of construction compared to the concrete notch alone.

In this context, to achieve a combination of high strength and stiffness while maintaining relative ductility and uplift resistance, an innovative notched connector is conceptualized by Thierry Soquet, an architect of the Architecture Plurielle agency and a designer of the Horizons Bois building in Rennes, France, in collaboration with INSA Rennes. A comprehensive description of this novel notched connector and its characterization will be presented in chapter 3 of this doctoral research. Furthermore, as presented in the literature, the influence of key parameters such as heel length, notch depth, notch length, concrete thickness, presence of reinforcement, and other parameters on the structural performance of the notched connector will also be identified in the parametric study.

2.6 Structural analysis and design methods

2.6.1 Composite action

The performance of the connector can affect the structural response of the TCC floor by generating relative slips at the interface layer. Figure 22 presents the strain distribution and internal forces of the TCC floor with various degrees of composite action. When a connection system is not adopted between the interface layer of the composite floor, there is no interaction between concrete and timber. In this case, the floor has non-composite action; therefore, individual parts of the TCC floor can act freely to each other. As a result, concrete and timber panels are subjected to pure bending generated from the applied loading and no axial force is developed in cross-section. Additionally, a large deflection of the composite floor is obtained.

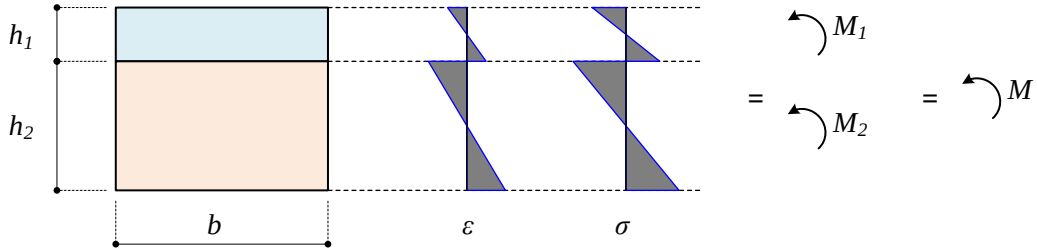

a. No composite action

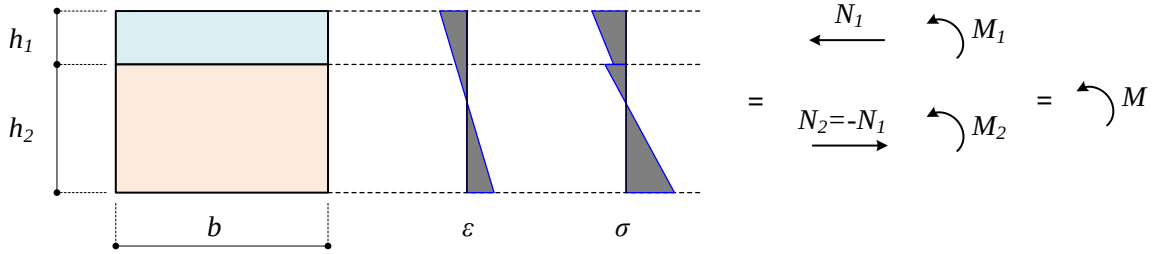

b. Full composite action

Figure 22: Strain distribution in the cross-sections of timber-concrete composite floors with different composite efficiencies.

When a connection system is implemented, relative slip is constraint, thus generating composite action. Therefore, higher stiffness and load-carrying capacity of the TCC floor are achieved, resulting in the improvement of structural efficiency of the floor system. If the floor has full-composite action, the connection is supposed to be perfectly rigid. The strain distribution is continuous at the timber-concrete interface, allowing the application of the transformed section method for stress analysis in the composite cross-section. However, when the connection system is semi-rigid, relative slip can be extended to some degree, and a partial composite action is obtained. The degree of composite action, *DCA*, which is usually defined as composite efficiency can be estimated by the equation below [27]:

$$DCA = \frac{EI_{test} - EI_0}{EI_\infty - EI_0} \tag{34}$$

where EI_∞ is the bending stiffness of a composite floor with a theoretical full-composite action, EI_0 is the bending stiffness of the composite floor with no composite action, and EI_{test} is the actual bending stiffness of the composite floor. The value of the degree of composite action has a tendency to approach 1 when shear connectors are very stiff, whereas it can reach a lower bound value of zero if shear connectors are very flexible. Van der Linden [21] addressed the relationship between the bending stiffness of the composite floor and the stiffness of the connection system. The influence of connectors on the bending stiffness of the composite floor was investigated for span lengths ranging from 3 m to 9 m. The results, as shown in Figure 23, indicated that composite floors with a shorter span required stiffer connectors compared to floors with a longer span. In addition, the difference in bending stiffness between a full-composite floor and a non-composite floor could reach up to four times.

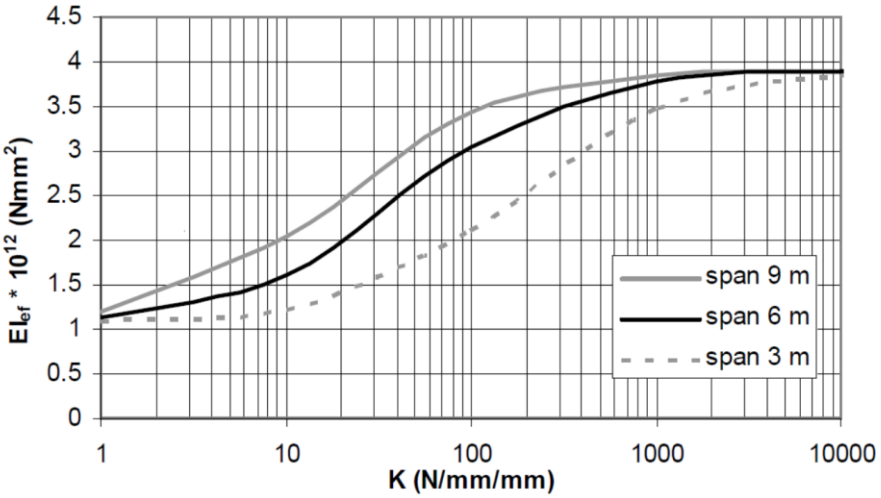

Figure 23: Relationship between bending stiffness of composite floor and stiffness of connection system on a logarithmic scale [19].

2.6.2 Bending stiffness computation

The design for timber concrete composite structure must satisfy both ultimate and serviceability limit states. The ultimate limit state is usually fulfilled by verifying the maximum stress in individual parts of the composite member such as the concrete, timber, and connection system using an elastic analysis [80]. The verification of the serviceability limit state requires, inter alia, to check the maximum midspan deflection. Stress and deflection can be computed depending on the bending stiffness of the composite member, indicating the significance of the bending stiffness in analytical analysis.

When no composite action is achieved, the composite floor system can be considered as two layers working in parallel (see Figure 22a) [98]. Therefore, the bending stiffness can be determined by the addition of bending stiffness of each part of the composite member. In the design for the composite floor with full composite action (see Figure 22b), the transformed section analysis is adopted to compute the bending stiffness of the composite floor.

Taking into account the connection flexibility, the composite member can be analyzed by assuming that each layer of the composite element is subjected to combined bending and axial stresses, and the connection system, supposed to have a constant spacing, is simplified as a continuous connector along the span of the member. From these assumptions, Newmark et al. [99] and Mohler [100] developed a method based on the differential equations of equilibrium for the partial composite action of the composite element, which was later adopted in the design code of Eurocode 5 [62]. This design method, called the gamma method, is developed for simply supported beam subjected to a sinusoidal load distribution. Figure 24 presents the distribution of stress and strain of a composite member cross-section under the applied loading described in Eurocode 5 [62].

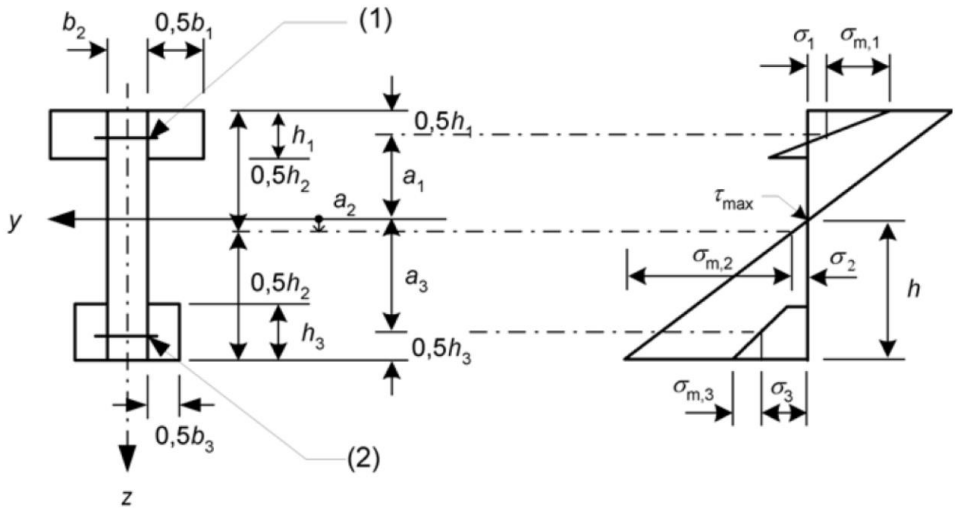

Figure 24: Cross-section and stress distribution of a composite section described in Eurocode 5 [62].

The effective bending stiffness of the composite member, which is determined by using the gamma method derived from the Annex B of Eurocode 5 [62], is given in eq. (35):

$$(EI)_{eff} = \sum_{i=1}^{3} (E_i I_i + \gamma_i E_i A_i a_i^2) \tag{35}$$

where the subscription 1 denotes the upper flange, 2 refers to the web, and 3 is the additional lower flange of the composite member as shown in Figure 24. The gamma factor, γ, indicates the effectiveness of the connection system ranged from zero (no connection) to one (rigid connection). The gamma factor can be computed as expressed in eq. (36) taking into account the shear stiffness of the connections system K, the modulus of elasticity of the composite parts E, the span of the composite member l, and the distances between the connectors, s. It should be noted that the value of the gamma factor in 2nd part of the composite member is taken equal to 1 (γ_2=1).

$$\gamma_i = \left[1 + \pi^2 E_i A_i s_i / \left(K_i l^2\right)\right]^{-1} \tag{36}$$

The inner lever arm, a, is the distance from the neutral axis of composite member to the neutral axis of part i, which can be determined using the expressions below.

$$a_2 = \frac{\gamma_1 E_1 A_1 (h_1 + h_2) - \gamma_3 E_3 A_3 (h_2 + h_3)}{2 \sum_{i=1}^{3} \gamma_i E_i A_i} \tag{37}$$

$$a_1 = (h_1 + h_2)/2 - a_2 \tag{38}$$

$$a_3 = (h_2 + h_3)/2 + a_2 \tag{39}$$

Based on experimental tests, Yeoh et al. [2], for example, confirmed that the simplified gamma method is accurate and can be adopted for predicting the structural performance of a composite floor when material properties of timber, concrete, and connection system remain in elastic range.

In terms of the connection system, the gamma method is more applicable for continuous and uniform connection systems such as adhesives and continuous steel mesh plates or closely spaced steel fasteners. When the notch is adopted as the connection system, the continuous behavior of the connection system may not be achieved since the transfer of shear force concentrates locally at the notch location. In order to maintain the continuous bond between concrete and timber, Niederer [101] recommends that the distance between discrete connectors should not exceed 5 percent of the span of the composite member. It should be noted that the technical specification CEN/TS 19103[79] also specifies a minimum requirement of four notched connectors to be distributed along the span. For the span less than 2 meters, the minimum number may be reduced to two notched connectors. However, this technical specification does not indicate whether these suggested minimum values are sufficient to maintain a continuous bond between materials or not.

For the CLT-concrete composite floor, the implementation of the gamma method faces a challenge due to orientation of the CLT panel. In a calculation of bending stiffness, the longitudinal layers of the CLT panel are assumed to carry flexural stresses, whereas the transversal layers are considered as a semi-rigid connection between the longitudinal layers [102]. It should be reminded that the gamma method is applicable to composite floors with a maximum of three load bearing layers. To address this restriction, modifications of the gamma method are proposed.

Jiang et al. [97] presents a theoretical calculation for 5-layer-CLT-concrete composite floors based on the gamma method. In their approach, the effective bending stiffness is the sum of two parts (see Figure 25). The first part consists of the concrete panel with the middle and bottom longitudinal layers of the CLT panel, while the second part is only the top longitudinal layer of the CLT panel. In addition, the combined stiffness of the shear connectors s/K, which is described in the calculation for the gamma factor in eq. (36), can be replaced by [102]:

$$s/K=\bar{h}/G_{90}b \tag{40}$$

where G_{90} is the shear modulus of the cross-layer of the CLT panel, b is the width of the CLT panel, $\bar{h}$ is depth of the cross-layer of the CLT panel.

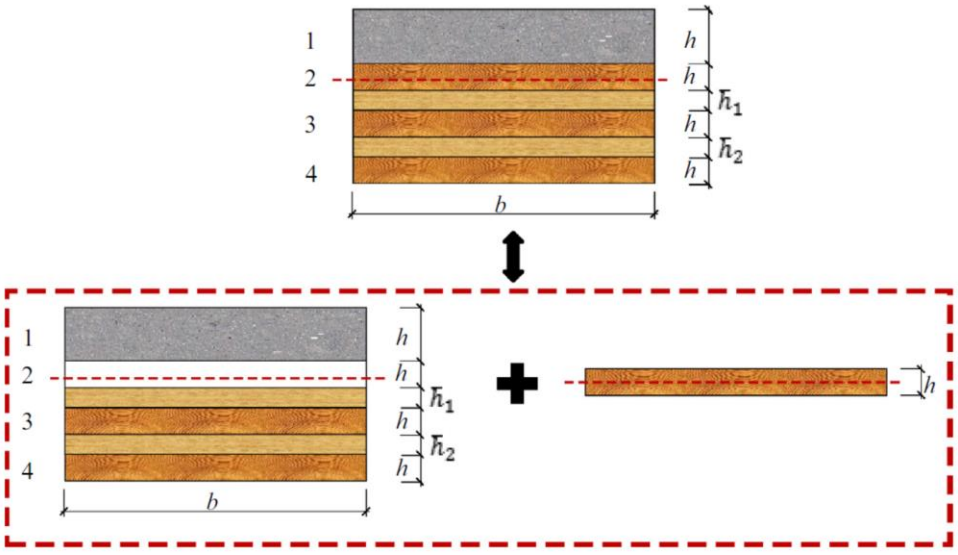

Figure 25: Calculation of 5-layer CLT-concrete composite floor [97].

2.6.3 Analytical methods for failure mechanisms of notched connectors

Initially, it is necessary to distinguish 2 types of failure modes in timber-concrete composite floors which are described as follows:

- Global failure modes: failures caused by internal forces in the composite floor governed by excessive traction in the lower part (timber panel) or excessive compression in the upper part (concrete panel).
- Local failure modes: failures mechanisms occurred locally in the notches. Possible failure mechanisms of the notched connection can be shear failure of the concrete notch, compressive failure of the concrete notch at the load-bearing area, shear failure of the timber in front of the notch, and crushing of timber at load-bearing area (see Figure 26) [9].

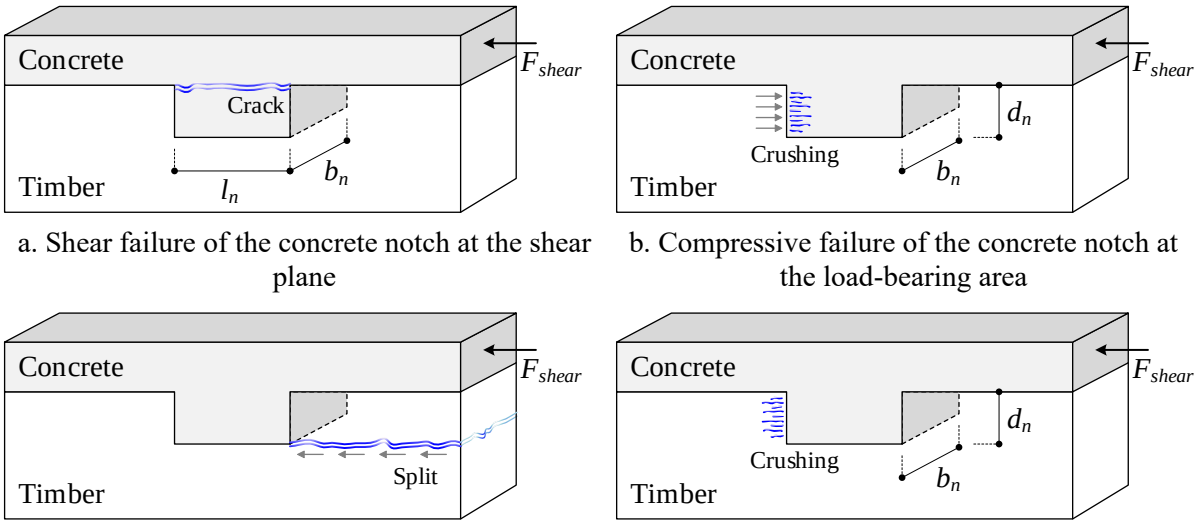

a. Shear failure of the concrete notch at the shear plane

b. Compressive failure of the concrete notch at the load-bearing area

c. Shear failure of timber in front of the notch

d. Crushing of timber at the load-bearing area

Figure 26: Typical failure mechanisms for a TCC notched connection [9].

The detailed descriptions of the analytical methods to determine the load-carrying capacity for each failure mechanism in timber and concrete parts of the notch connection are provided in the following sections. Additionally, several assumptions are made for the analytical methods which include [103]:

- Composite floor is subjected to a vertical load uniformly distributed over its entire length,
- Composite floor is dimensioned with sufficient thickness of concrete and timber parts in order to avoid global failures,
- Behavior of the notch connector is elastic in terms of strength and stiffness,
- Uplift phenomenon is neglected so that timber and concrete materials keep the same curvature.

2.6.3.1 Timber part

When notched connectors were adopted in the TCC floor, two prevalent failure modes were observed in the timber part, namely compressive failure of timber at the notch, and shearing-off failure of the timber [92] (see Figure 27).

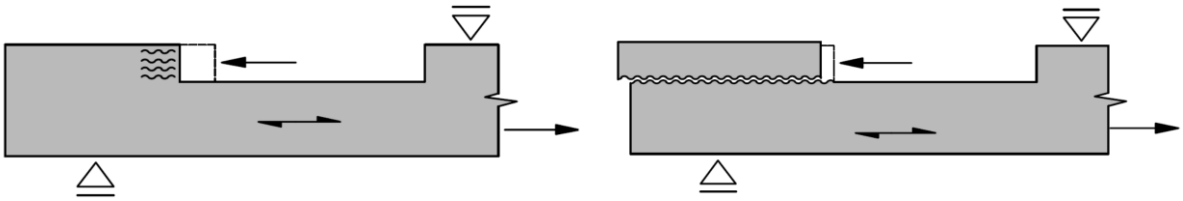

a. Compressive failure b. Shearing-off failure

Figure 27: Failure modes occurred in the timber part of TCC floor [92].

In the case of the compressive failure in the notch, the timber section of the notch is subjected to compression parallel to the grain. According to the technical specification CEN/TS 19103[79], an analytical formula to determine the timber crushing resistance is demonstrated in eq. (41):

$$F = f_{c,0} b_n d_n \tag{41}$$

where $f_{c,0}$ is the compressive strength parallel to grain, b_n is the width the notch, and d_n is the depth of the notch.

For the horizontal shearing-off failure mode, to estimate the failure load, Kaiser [104] determined the elastic shear stress distribution by adopting the strength theory. Figure 28 illustrates the elastic shear stress distribution of the shear plane. The stress applied to the timber part exhibited non-linear behavior with the highest stress at the edge of the notch and reached to zero at approximately eight times the notch depth ($8d_n$). Michelfelder [105], and the technical specification CEN/TS 19103[79] also confirmed the limited length of shear stress distribution in function of notch depth, $8d_n$. Therefore, the shear resistance of the timber part in TCC can be determined using the following eq. (42):

$$F = f_v b_n 8 d_n \tag{42}$$

where f_v is the shear strength of timber. When CLT panel is adopted as the timber panel, along with a notched connection, the failure induced by shear in timber is highly anticipated due to the low rolling shear strength of the cross-layer of the CLT panel [96].

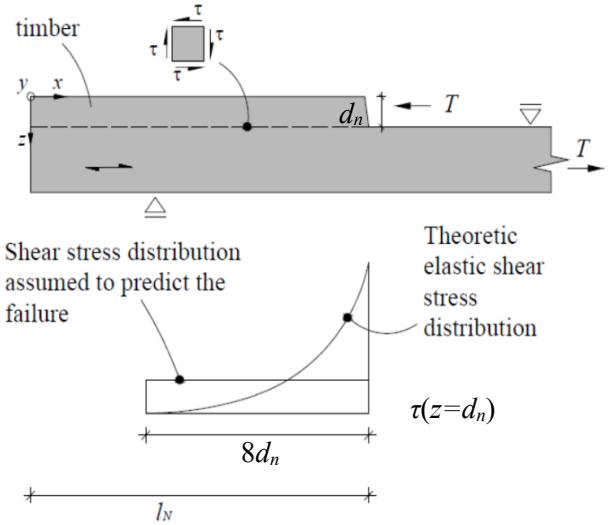

Figure 28: Shear stress distribution in the timber [92].

2.6.3.2 Concrete part

Two types of the concrete failure mechanisms can be observed in the concrete notch: the concrete shear failure at the shear plane and the concrete compressive failure at the load bearing surface (see Figure 26a,b). When notches are adopted as the connection system of TCC floors, force from concrete to timber is transferred locally through the notch border. Thus, concrete notch is subjected to high compressive and tensile stresses as well as shear stress [92]. If steel reinforcement is placed inside the concrete notch, it can be used to carry tensile and shear stresses. Concrete is commonly regarded as a compressive material owing to its high resistance in compression and its tensile strength is assumed to be approximately ten times lower than its compression strength [41]. Frequently, tensile strength of concrete is disregarded in calculations. According to Eurocode 2 [40], when concrete notch is subjected to a uniform distribution of compressive load, the concentrated resistance should be three times the design strength of concrete, f_{cd}, if appropriately confined.

The shear transfer of the concrete member can be studied by using various methods including the approach applied in conventional reinforced concrete, the shear friction theory at the shear plane between the concrete notch and concrete panel, and the strut-and tie model. For the approach applied in conventional reinforced concrete [92], the total shear resistance of the concrete part involves the combined shear resistance provided by concrete V_c and shear reinforcement within concrete part V_s as presented in eq. (43). The shear strength is assumed to be provided by concrete alone when the concrete member without shear reinforcement is adopted.

$$V_n = V_c + V_s \tag{43}$$

Baker et al. [106] and Kani et al. [107] for example developed the load transfer mechanism which participated in carrying shear load over cross-section as demonstrated in Figure 29. The shear contribution in reinforced concrete involves shear load of uncracked compression zone V_c, dowel-action of longitudinal rebars V_{do}, tensile stress over cracks in the fracture process zone V_{fpz}, crack friction τ_{cr}, and direct compression struts σ_{cr} (arching action) [108]. A comprehensive description regarding the residual tension at crack cross-section when tensile strain exceeds maximum strain, the contribution of aggregate interlock from the friction in a crack caused by crack surface, the dowel action from reinforcing rebars, and the arching action (compression struts) in shear transfer mechanism can be found in [109].

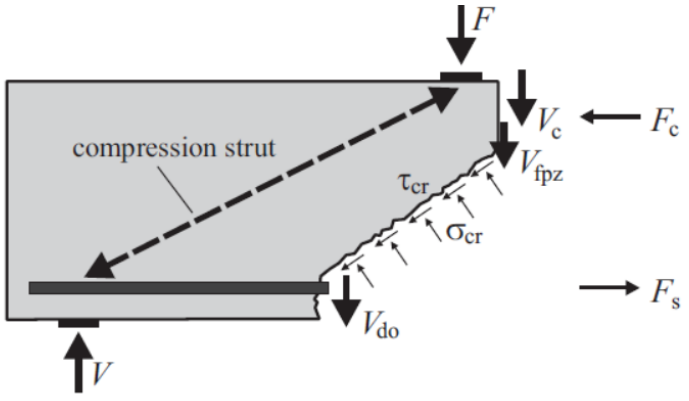

Figure 29: Load transfer mechanism in the reinforced concrete member [108].

The complex of internal forces which is represented in Figure 29 is treated differently in various models such as Modified Compression Field Theory (MCFT) [110], or Critical Shear Crack Theory [111]. Collins [110] developed the compression field theory using stress-strain relationship for the cracked concrete, assuming that the concrete did not carry tension after cracking. This MCFT model is adopted as the basis for the shear provision in FIB model design code [112] and AASHTO design code [113]. Muttoni et al. [111] described the development of the critical shear crack theory of a beam element under the flexural loading in order to determine the shear resistance of the concrete member, which is later introduced in Swiss standard [114].

In addition, empirical relations are also adopted to evaluate the shear capacity of the reinforced concrete. Eurocode 2 [40] provides a shear expression for reinforced concrete cross-section (clause 6.2.a) based on the experimental results conducted by Regan [115], which takes into account the effects of the longitudinal reinforcement ratio, the concrete compressive strength, and the size effect of cross-section. In ACI 318-14 [116], the expressions given in clause 22.5.5.1 to compute the concrete shear strength for members subjected to shear and flexural force are semi-empirical formulae, developed from the test results of 194 beams [117].

On the other hand, the shear capacity of concrete at the shear plane between concrete notch and concrete slab can be determined by adopting principles of shear friction theory at the interface which were presented for the first time by Mast [118]. Then, Birkeland et al. [119] described the shear friction theory in saw-tooth analogy where the crack was resulted from the displacement of both contact surfaces, and the interlocking of aggregate particles was counteracted by reinforcements crossing the joint (see Figure 30). The ultimate shear stress, τ_i, is presented in a general form as follows:

$$\tau_i = c + k_s.\rho.f_y + k_f.\sigma_n \tag{44}$$

where c is the coefficient reflecting adhesive forces, k_s is the coefficient of friction (for contribution of reinforcement), ρ is the ratio of the reinforcement crossing the shear plane, f_y is the yield strength of the reinforcing steel, and k_f is the coefficient of friction (for contribution of normal stress σ_n). In addition, factors affecting shear capacity of the interface, which involve the concrete strength, shear reinforcement, aggregate composition, and profiles of the surface, are discussed in the work of Gołdyn [120]. The principle of shear friction theory is adopted in current design codes including Eurocode 2 [40], ACI 318-14 [116], and AASHTO [113].

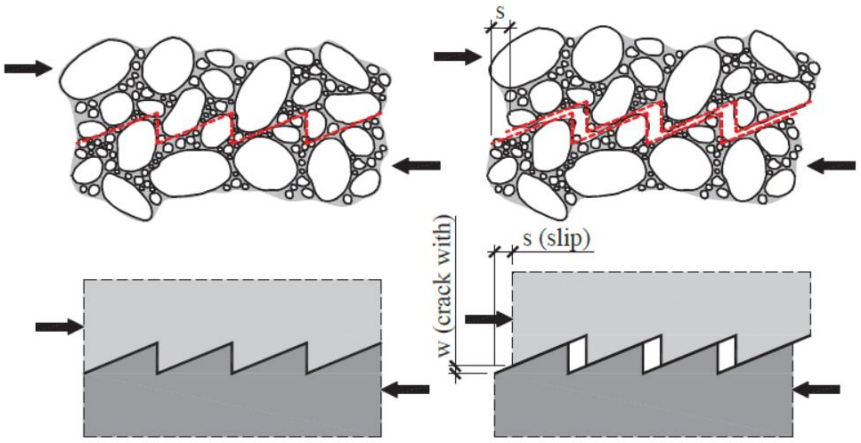

Figure 30: Concept of saw-tooth analogy to compute the shear capacity of beam element [119].

Besides formulae provided in the abovementioned design codes, the strut-and-tie model, which is particularly developed to design the concrete notched configuration, also has been developed. Michelfelder [105] developed a strut-and-tie model (see Figure 31) in order to consider the local behavior of the concrete notch based on the results obtained from the finite element analysis. The compressive struts act as compression chords while tensile ties serve as the tension chords in the truss mechanism. Internal forces are theoretically determined from truss analysis, while axial forces, shear forces, and bending moments can be computed using composite beam theories [16].

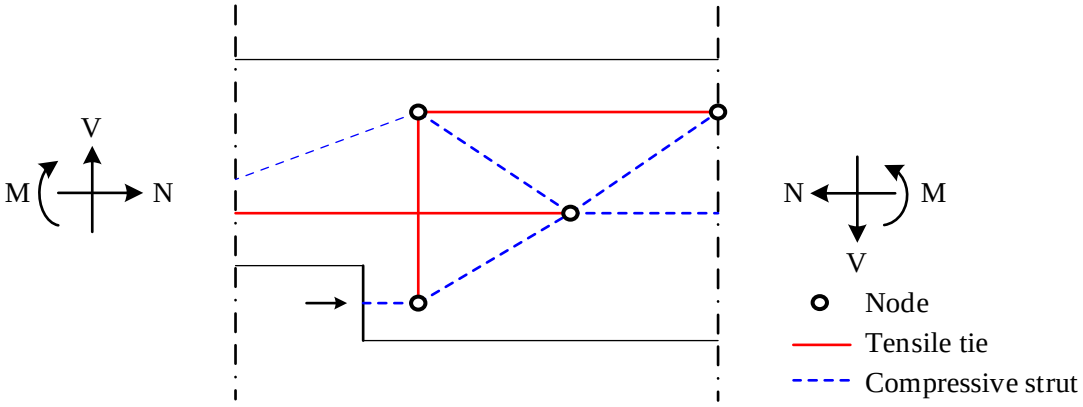

Figure 31: Strut-and-tie model for the notch connector developed by Michelfelder [105].

Furthermore, the technical specification CEN/TS 19103[79] also proposes a strut-and-tie model to investigate the failure mechanism of notched connector. The shear load-carrying capacity of the concrete notch is in function of the effective design shear strength of the concrete member, the notch width, and notch length. Figure 32 illustrates the notch configuration adopted in the technical specification CEN/TS 19103[79].

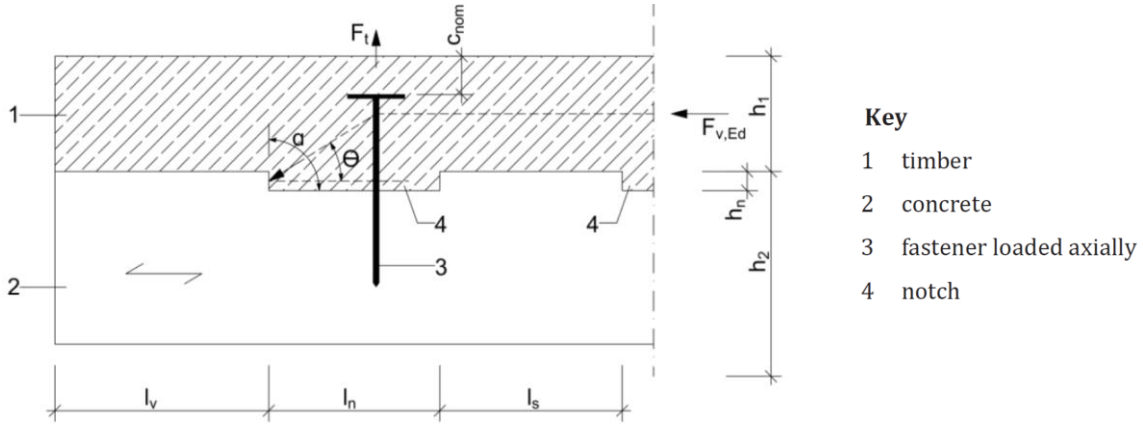

Figure 32: Notch connection system in the technical specification CEN/TS 19103 [79].

2.7 Numerical study

In parallel with the experimental tests and analytical methods, which can be time-consuming and require the continuity of support to analyze the behavior of the composite structure, the numerical study using finite element (FE) model can be developed to reproduce the behavior of the composite system. The FE model is a numerical modelling technique adopted to solve mathematical problems involving complex geometries, material properties, and physical behaviors of the structure. It describes the structural response of the structure by dividing a complex problem into smaller, simpler subdomains

called finite elements. This approach is preferable for engineers due to the cost-saving and efficiency compared to experimental tests or complex analytical methods. The level of accuracy of obtained results can be influenced by the quality of input data, including material properties, choice of element types, boundary conditions, interactions between elements, and mesh sizes.

Dias [58] presented a three-dimensional (3D) non-linear FE model which was developed to predict the behavior of the timber-concrete pushout test. Steel and concrete were considered as isotropic materials, and timber was treated as an orthotropic material. Geometrical properties, interactions between various elements, and configuration of the pushout test setup were also considered in the model. Comparing the load-slip curve of the FE model with the results obtained from the experimental shear tests, the developed 3D FE model showed the capacity to simulate the behavior of the composite member if material definitions were used properly.

More recently, a full 3D model of the notched connection has been developed by Bedon et al. [121]. They conducted a numerical investigation using an advanced 3D FE model on notched connections for TCC beam (concrete and LVL timber) (see Figure 33a). The proper calibration of the surface interaction and appropriate material constitutive behavior with damages model, were assigned to capture possible failure mechanisms of component materials in the connection system. The FE model results were compared with experimental pushout data from the literature and simplified analytical methods. It was shown that the FE model could provide a good correlation with the experimental tests and was capable of capturing the failure mechanism of the connection system as well as the load-carrying capacity.

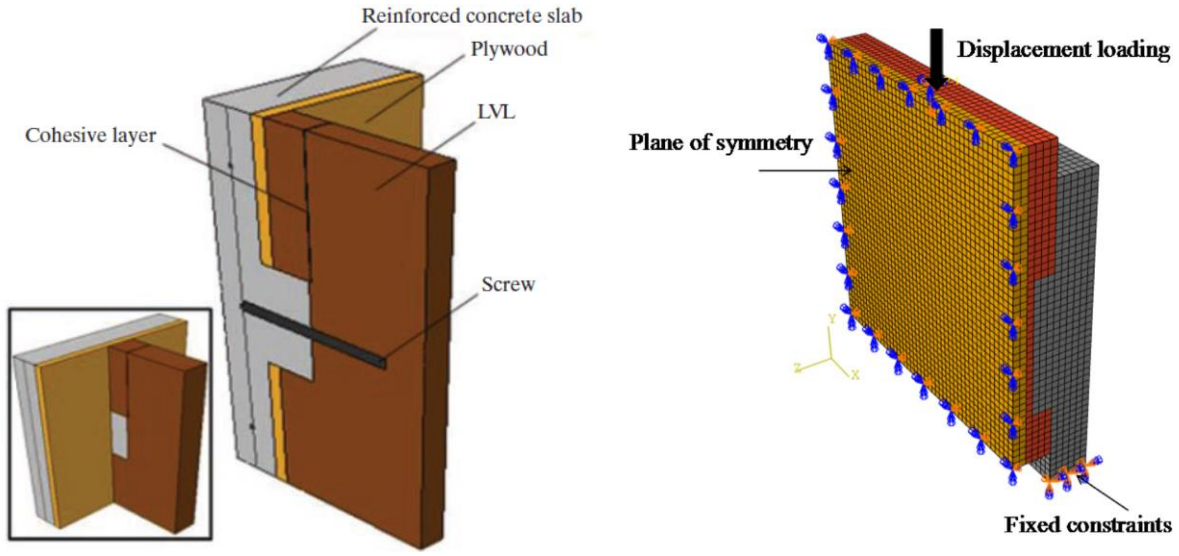

a. Bedon et al. [121]. b. Jiang et al. [93].

Figure 33: Three-dimensional FE models of the notched connection.

Additionally, a recent study through laboratory tests, analytical methods, and numerical modellings on the notched connection of TCC specimens using CLT panel has been carried out in the university of Wuxi, China. Jiang et al. [97] have developed a FE model for CLT-concrete notches to calibrate with experimental results before conducting a parametric study to investigate the behavior of the notched connector (see Figure 33b). The results of the proposed FE model show a close agreement with the experimental tests, and the parametric study that investigates the variations of the notch depth has a small influence on the load-deflection response of composite floors.

It is found that in most cases where FE models are developed, comparisons between FE models and experimental tests are made in order to calibrate the FE model to a desired level of accuracy. Then, the validated FE model is adopted to conduct a parametric study in order to achieve the objective of the study. Dias et al. [1] mentioned that this comparison is a one-way procedure to assure that the model is able to properly describe the structural response. The need for experimental verification is the major drawback for the FE model when experimental data are limited.

2.8 Conclusion

This chapter has presented a comprehensive literature review of timber-concrete composite (TCC) structures. Several aspects have been covered, including the background of TCC structures, material properties, connection systems, structural analysis and design methods, and numerical studies. This chapter highlights the following findings:

- The TCC solution is inspired by the advantages of timber in environmental sustainability and in structural performance, compared to pure timber or traditional reinforced concrete structures.
- For the concrete material in TCC structures, low-shrinkage and self-compacting concrete should be considered for onsite casting to prevent water absorption from wet concrete to timber.
- For the timber material in TCC structures, to address the limited diameter and dimensional stability of wooden logs in floor systems, engineered wood products with improved physical and mechanical properties are developed. Among available engineered wood products, cross-laminated timber (CLT) is adopted in this research due to its crosswise arrangement of timber boards in the CLT panel, resulting in two-way load bearing behavior (longitudinal and transversal directions).
- Regarding the concrete-timber connection system, it can be made of dowel fasteners, adhesives, and notched connectors. Dowel type fasteners made of nails, screws, steel dowels, and bolts are considered as a semi rigid connection system which can limit the structural efficiency of TCC floors. For continuous connectors, such as steel plates or nail plates, despite their capacity to offer high strength and stiffness, their complicated assembly process can increase the production cost. While adhesive use in the connection system can provide higher strength and stiffness, challenges associated with on-site application, quality control, and long-term performance have limited the use of these connection systems in practice and called for further development. Notch is often classified as the most effective solution for the TCC connection system due to the simplicity of the fabrication and its high performance. However, concrete notch alone exhibits brittle behavior. To improve ductility and uplift resistance, metallic fasteners are usually added to the concrete notch.
- For characterizing mechanical properties of the connection system, pushout tests are commonly performed. Besides experimental tests, analytical and numerical approaches can be adopted to determine the load-carrying capacity of the connection system.
- Regarding the global behavior of TCC structures, apart from experimental bending tests, the analytical uniaxial bending method, known as gamma method, is used for the estimation of

internal action, bending stiffness, and ultimate strength of the composite floor or beam. As an alternative to experimental tests and analytical methods, numerical studies using finite element models can be adopted for the further assessment or validation of the composite floor.

Following the findings from the literature, the understanding of the timber-concrete composite system can serve as a valuable reference point for the upcoming chapters. Then, several aspects are made as follows:

- While the literature suggests the use of low shrinkage concrete or the application of coatings or plastic films on the timber surface at the interface layer before casting, the initial phase of this research adopts normal concrete. This decision is driven by the reason that using high performance concrete or applying coating can be costly, time-consuming, and requires high quality control.
- Once again, cross-laminated timber (CLT) is chosen in this study due to its high mechanical performance in both directions, thanks to crosswise arrangement of timber boards.
- To achieve a combination of high strength and stiffness while maintaining relative ductility and uplift resistance, an innovative dovetail notched connector is proposed by Thierry Soquet, an architect of the Architecture Plurielle agency, in collaboration with INSA Rennes.

Therefore, this research aims to characterize the local behavior of the proposed dovetail notched connector and to assess the global performance of the TCC floor with dovetail notched connectors as the connection system. This notch is proposed due to the simple and fast assembly of the composite floor. The mechanical performance of the dovetail notched connector is presented in chapter 3, where a series of pushout tests are conducted, and the test results are then compared with those obtained from the finite element model and formulae found in design codes. Subsequently, the global behavior of composite floors with notched connectors is investigated in chapter 4 through a series of bending tests. Then, the test results are compared to those estimated from the gamma method and simplified engineering models. Finally, a proposed design guideline for CLT-concrete composite floors with dovetail notched connectors is formulated in chapter 5, relying on the validation from experimental tests, analytical developments, and numerical studies.

2.9 References

[1] Dias, A. (2018). Design of timber-concrete composite structures: A state-of-the-art report by COST Action FP1402/WG 4. Shaker Verlag.

[2] Yeoh, D., Fragiacomo, M., De Franceschi, M., & Heng Boon, K. (2011). State of the art on timber-concrete composite structures: Literature review. Journal of structural engineering, 137(10), 1085-1095.

[3] Boccadoro, L., Zweidler, S., Steiger, R., & Frangi, A. (2017). Bending tests on timber-concrete composite members made of beech laminated veneer lumber with notched connection. Engineering Structures, 132, 14-28.

[4] Dias, A. M. P. G., Skinner, J., Crews, K., & Tannert, T. (2016). Timber-concrete-composites increasing the use of timber in construction. European Journal of Wood and Wood Products, 74, 443-451.

[5] Boccadoro, L., & Frangi, A. (2014). Experimental analysis of the structural behavior of timber-concrete composite slabs made of beech-laminated veneer lumber. Journal of performance of constructed facilities, 28(6), A4014006.

[6] Jelusic, P., & Kravanja, S. (2017). Optimal design of timber-concrete composite floors based on the multi-parametric MINLP optimization. Composite structures, 179, 285-293.

[7] Müller, K. (2020). Timber-concrete composite slabs with micro-notches (Doctoral dissertation, ETH Zurich).

[8] Liang, S., Gu, H., Bergman, R., Kelley, S. 2020. Comparative life-cycle assessment of a mass timber building and concrete alternative. Wood and Fiber Science 52(2): 217-229.

[9] Yeoh, D. E. C. (2010). Behavior and design of timber-concrete composite floor system. (Doctoral dissertation, University of Canterbury).

[10] Aguaron-Fuente, E. (2012). Assessment of Carbon Storage by Sacramento's Urban Forest. University of California, Davis.

[11] Higgins, C., Barbosa, A.R., Blank, C. 2017. Structural Tests of Concrete Composite-Cross-Laminated Timber Floors. Report No. 17-01. Oregon State University, Corvallis, OR, USA.

[12] Ceccotti, A. (2002). Composite concrete-timber structures. Progress in structural engineering and materials, 4(3), 264-275.

[13] Martins, C., Santos, P., Almeida, P., Godinho, L., Dias, A. 2015. Acoustic performance of timber and timber-concrete floors. Construction and Building Materials 101: 684-691.

[14] Wymelenberg, K., Northcutt, D., Fretz, M., Stenson, J., Marks, E. 2019. Acoustic Lab Testing (ASTM E492-2016, ASTM E90-2016) of CLT and MPP Wall and Floor Assemblies for Multi-Family Residential Application. University of Oregon, Portland, Oregon, USA.

[15] Shephard, A.B., Fischer, E.C., Barbosa, A.R., Sinha, A. 2021. Fundamental Behavior of Timber Concrete-Composite Floors in Fire. Journal of Structural Engineering 147(2): 04020340.

[16] Zhang, L. (2022). Structural Performance of Mass Timber Panel-Concrete Composite Floors with Notched Connections. (Doctoral dissertation, University of Alberta).

[17] Crocetti, R., Sartori, T., & Tomasi, R. (2015). Innovative timber-concrete composite structures with prefabricated FRC slabs. Journal of Structural Engineering, 141(9), 04014224.

[18] Song, Y. J., Baek, S. Y., Lee, I. H., & Hong, S. I. (2021). Variations of moisture content in manufacturing CLT-concrete composite slab using wet construction method. BioResources, 16(1), 372.

[19] Lamothe, S. (2019). Développement d'un connecteur Rigide-Ductile-Économique pour dalles composites en bas lamellé-croisé et béton pour les bâtiments multiétages (Doctoral dissertation, Université Laval).

[20] Zhang, L., Chui, Y. H., & Tomlinson, D. (2020). Experimental investigation on the shear properties of notched connections in mass timber panel-concrete composite floors. Construction and Building Materials, 234, 117375.

[21] Van der Linden, M. L. (1999). Timber-concrete composite beams. HERON-ENGLISH EDITION-, 44(3), 215-236.

[22] Muller, P. (1922). Decke aus hochkantig stehenden Holzbohlen oder Holzbrettern und Betondeckschicht. Patentschau aus dem Betonbau und den damit verwandten Gebieten, Auszuge aus den Patentschriften, Beton und Eisen, 244.

[23] Schaub, O. Patent US1792040A: Wood Reenforced Concrete Structural Member, 1931.

[24] Schaub, O. Patent DE673556C: Verbunddecke aus Holzrippen und Betonplatte, 1939.

[25] Poštulka, J. (1997). Holz-Beton-Verbunddecken, 36 Jahre Erfahrang. Bautecknic 74.

[26] Godycki, T., Pawlica, J. and Kleszczewski, J. (1984). Concrete decks with wooden joists/Verbunddecke aus Holzrippen und Betonplatte. Bauingenieur, 59(12), pp. 477-483.

[27] Turrini, G. and Piazza, M. (1983a). Il comportamento statico della struttura mista legno calcestruzzo. Recuperare, 2(5), pp. 224-237.

[28] Blasi, C., Ceccotti, A., and Gambi, A. (1992). I solai misti legno lamellare-calcestruzzo. L'Edilizia, 6(2), pp. 39-45.

[29] Van der Linden, M. and Blass, H. J. (1996). Timber-concrete composite floor systems. Proc. International Wood Engineering Conference (IWEC), New Orleans, USA, 3, pp. 309-316.

[30] Natterer, J., Herzog, T., and Volz, M., (1998) Construire en Bois 2. 2nd edition, Presses polyechniques et universitaires romandes, Switzerland.

[31] Poutanen, T. (1987). Composite structure of Timber Joints and Concrete Slab. 20th CIB-W18 meeting, Bublin.

[32] Cook JP (1976). Composite construction methods. J construction Division, Proceedings of the American Society of Civil Engineers, 102(CO1), March 1976, pp21-27.

[33] Rodrigues, J., Dias, A. & Providência, P. 2013. Timber-concrete composite bridges: state-of-the-art review. BioResources, 8(4), pp. 6630-6649.

[34] Wacker, J. P., Dias, A. M. P. G., and Hosteng, T. K. 100-Year Performance of Timber-Concrete Composite Bridges in the United States. Journal of Bridge Engineering 25, 3 (2020), 04020006.

[35] Balogh, J., Fragiacomo, M., Gutkowski, R., Atadero, R. & Ivanyi, P. 2012. Fatigue behavior of notched connections in wood-concrete composites. Proc. of the 12th World Conference on Timber Engineering 2012.

[36] Cone, C. M. (1960). A composite timber-concrete bridge. New Zealand Forest Service, Forest Research Institute.

[37] Nauta, F. (1984). New Zealand Forest Service Timber Bridge. Proceedings of 1984 Pacific Timber Engineering Conference. Auckland, New Zealand.

[38] Tommola, J., Salokangas, L. & Jutila, A. 1999. Wood-concrete composite bridges: tests on shear connectors. Stockholm: Nordic Timber Council.

[39] Gagg, C. R. (2014). Cement and concrete as an engineering material: An historic appraisal and case study analysis. Engineering Failure Analysis, 40, 114-140.

[40] European standard EN 1992-1-1, Eurocode 2: Design of concrete structures - Part 1-1: General rules and rules for buildings, CEN, Brussels (2004).

[41] Isaksson, T., Martensson, A., & Thelandersson, S. (2010). Byggkonstruktion. Lund: Studentlitteratur AB.

[42] Timoshenko, S. P., & Gere, J. M. (1997). Mechanics of materials (p. 807).

[43] Idiart, A. E. (2013). Drying shrinkage and creep in concrete: a summary. Web. Sept.

[44] Lubliner, J., Oliver, J., Oller, S., & Oñate, E. (1989). A plastic-damage model for concrete. International Journal of solids and structures, 25(3), 299-326.

[45] Lee, J., & Fenves, G. L. (1998). Plastic-damage model for cyclic loading of concrete structures. Journal of engineering mechanics, 124(8), 892-900.

[46] Alfarah, B., López-Almansa, F., & Oller, S. (2017). New methodology for calculating damage variables evolution in Plastic Damage Model for RC structures. Engineering Structures, 132, 70-86.

[47] Borgstrom, E. & Karlsson, R. (2016). Design of Timber Structures volume 1. Stockholm: Svenskt Tra.

[48] Moutee, M. (2006). Modélisation du comportement mécanique du bois au cours du séchage (Doctoral dissertation, Université Laval).

[49] NF, B. 52-001: 2011 Règles d'utilisation du bois dans les constructions; Classement visuel pour employ en structure pour les principales essences résineuses et feuillues. AFNOR, Saint-Denis, 23.

[50] EN 14081-1. Timber structures - Strength graded structural timber with rectangular cross section - Part 1: General requirements. Brussels: European Committee for Standardization; 2013.

[51] EN 14080. Timber structures Glued laminated timber and glued solid timber Requirements. Brussels: European Committee for Standardization; 2013.

[52] EN 338:2009. Structural timber - Strength classes. Brussels: European Committee for Standardization; 2009.

[53] Holmberg, S., Persson, K., & Petersson, H. (1999). Nonlinear mechanical behavior and analysis of wood and fibre materials. Computers & structures, 72(4-5), 459-480.

[54] Chen, Z., Tung, D., & Karacabeyli, E. MODELLING OF TIMBER STRUCTURES.

[55] Bodig, J., & Jayne, B. A. (1982). Mechanics of wood and wood composites.

[56] Franke, S., Franke, B., & Harte, A. M. (2015). Failure modes and reinforcement techniques for timber beams–State of the art. Construction and Building Materials, 97, 2-13.

[57] Ehrhart, R. Brandner, G. Schickhofer, and A. Frangi. "Rolling Shear Properties of some European Timber Species with Focus on Cross Laminated Timber (CLT): Test Configuration and Parameter Study". 2nd Meeting of the International Network on Timber Engineering Research (INTER). Sibenik, Croatia, 2015, pp. 61–76. doi: 10.3929/ethza-010548168.

[58] Dias, A. M. P. G., Van de Kuilen, J. W., Lopes, S., & Cruz, H. (2007). A non-linear 3D FEM model to simulate timber–concrete joints. Advances in Engineering Software, 38(8-9), 522-530.

[59] Hill, R. (1950). The mathematical theory of plasticity, Clarendon. Oxford, 613, 614.

[60] Glos, P. (1978). Reliability Theory for Timber Structures: Determination of Compression Strength Behavior of Glulam Components From Interaction of Material Properties. Heft 34/1978.

[61] Lau, W. W. S. (2000). Strength model and finite element analysis of wood beam-columns in truss applications (Doctoral dissertation, University of British Columbia).

[62] European standard EN 1995-1-1, Eurocode 5: Design of timber structures- Part 1-1: General — Common rules and rules for buildings, CEN, Brussels (2004).

[63] Fragiacomo, M., & Ceccotti, A. (2006). Long-term behavior of timber–concrete composite beams. I: Finite element modeling and validation. Journal of structural engineering, 132(1), 13-22.

[64] Gong, M. 2019. Lumber-Based Mass Timber Products in Construction. Timber Buildings and Sustainability. IntechOpen.

[65] Harte, A.M. 2017. Mass timber-the emergence of a modern construction material. Journal of Structural Integrity and Maintenance 2(3): 121-132.

[66] Harris, R. (2015). Cross laminated timber. In Wood composites (pp. 141-167). Woodhead Publishing.

[67] Brandner, R., Flatscher, G., Ringhofer, A., Schickhofer, G., & Thiel, A. (2016). Cross laminated timber (CLT): overview and development. European Journal of Wood and Wood Products, 74, 331-351.

[68] Brandner, Reinhard. (2013). Production and Technology of Cross Laminated Timber (CLT): A state-of-the-art Report. Paper presented at the Focus Solid Timber Solutions - European Conference on Cross Laminated Timber (CLT), Graz.

[69] EN 16351:2015, CEN/TC 124-Timber structures,Timber structures - Cross laminated timber - Requirements, 2015.

[70] Falk, A., Dietsch, P., & Schmid, J. (2016). Proceedings of the Joint Conference of COST Actions FP1402 & FP1404 Cross Laminated Timber: A competitive wood product for visionary and fire safe buildings. In Joint Conference of COST Actions FP1402 & FP1404 Cross Laminated Timber. KTH Royal Institute of Technology.

[71] Crespell, P. and Gaston, C. 2011. The Value Proposition for Cross-Laminated Timber. FPInnovations, Pointe-Claire, Quebec City, Canada.

[72] Franzoni, L., Lebée, A., Lyon, F., and Foret, G. 2016. Influence of orientation and number of layers on the elastic response and failure modes on CLT floors: modeling and parameter studies. European Journal of Wood and Wood Products 74: 671-684.

[73] EN 16351:2021, EN 16351:2021. Timber structures. Cross laminated timber. Requirements. European Committee for Standardization (CEN), 2021.

[74] ANSI/APA PRG-320-2019, Standard for performance-rated cross-laminated timber. APA - The Engineered Wood Association, 2019.

[75] Canadian Standards Association, CSA-O86:19. Engineering design in wood. 2019.

[76] Monteiro, S., Dias, A. M. P. G., & Negrao, J. H. J. D. (2010). Experimental and numerical evaluation of notched timber-concrete joints mechanical behavior. 11th WCTE, Riva del Garda, Trentino, Italy, 20-24.

[77] European standard EN 26891, Timber Structures - Connections Made With Mechanical Fasteners General Principles for the Determination of Strength and Deformation Characteristics, CEN, Brussels (1991).

[78] European standard EN 1994-1-1, Eurocode 4: Design of composite steel and concrete structures - Part 1-1: General rules and rules for buildings, CEN, Brussels (2004).

[79] CEN/TS 19103 :2021. Eurocode 5 : Design of Timber Structures - Structural design of timber-concrete composite structures – Common rules and rules for buildings. European Committee for Standardization (CEN): Brussels, Belgium, 2021.

[80] Ceccotti, A. Timber Engineering STEP2: Composite Structures. STEP / Eurofortech, Centrum Hout, Almere, 1995.

[81] McCullough, C. B.: Oregon Tests on Composite (Timber-Concrete) Beams. Journal of the American Concrete Institute, No. 14, pp. 429-440, 1943.

[82] Richart, F. E.; Williams, C. B.: Tests of Composite Timber And Concrete Beams. University of Illinois Bulletin 40, p. 62, 1943.

[83] Meierhofer, U.: A Timber/Concrete Composite System. Structural Engineering International, No. 3(2), pp. 104-107, 1993.

[84] Dias, A. M. P. G. (2005). Mechanical behavior of timber-concrete joints. Faculty of Civil Engineering and Geosciences, Netherlands. (Doctoral dissertation, Delft University of Technology)

[85] Mai, K. Q., Park, A., & Lee, K. (2018). Experimental and numerical performance of shear connections in CLT–concrete composite floor. Materials and Structures, 51, 1-13.

[86] Girhammar, U. A. (1984). Composite timber and concrete components for walls. In IABSE 12 Congress. Vancouver. Article.

[87] Jacquier, N., & Girhammar, U. A. (2015). Evaluation of bending tests on composite glulam–CLT beams connected with double-sided punched metal plates and inclined screws. Construction and Building Materials, 95, 762-773.

[88] Pincus, G. (1969). Bonded wood-concrete T-beams. Journal of the Structural Division, 95(10), pp. 2265-2279.

[89] Brunner, M., Romer, M. and Schnüringer, M. (2007). Timber-concrete-composite with an adhesive connector (wet on wet process). Materials and structures, 40(1), pp. 119-126.

[90] Negrão, J. H. J. D. O., Leitão de Oliveira, C. A., Maia de Oliveira, F. M., & Cachim, P. B. (2010). Glued composite timber-concrete beams. I: Interlayer connection specimen tests. Journal of Structural Engineering, 136(10), 1236-1245.

[91] Piazza, M. and Ballerini, M. (2000). Experimental and numerical results on timber-concrete composite floors with different connection systems. 6th World Conference on Timber Engineering WCTE 2000, Whistler Resort, British Columbia, Canada.

[92] Boccadoro, L. (2016). Timber-concrete composite slabs made of beech laminated veneer lumber with notched connection. IBK Bericht, 371.

[93] Jiang, Y., Hu, X., Hong, W., Zhang, J., & He, F. (2020). Experimental study on notched connectors for glulam-lightweight concrete composite beams. BioResources, 15(2), 2171-2180.

[94] Yeoh, D., Fragiacomo, M., Buchanan, A., & Gerber, C. (2009). Preliminary research towards a semi-prefabricated LVL–concrete composite floor system for the Australasian market. Australian Journal of Structural Engineering, 9(3), 225-240.

[95] Lamothe, S., Sorelli, L., Blanchet, P., & Galimard, P. (2020). Engineering ductile notch connections for composite floors made of laminated timber and high or ultra-high performance fiber reinforced concrete. Engineering Structures, 211, 110415.

[96] Thai, M. V. (2021). Évaluation du comportement en vibration et optimisation de la conception des planchers composite en bois lamellé collé croisé-béton (Doctoral dissertation, Université du Québec à Chicoutimi).

[97] Jiang, Y., & Crocetti, R. (2019). CLT-concrete composite floors with notched shear connectors. Construction and Building Materials, 195, 127-139.

[98] Piazza, M., Tomasi, R., & Modena, R. (2005). Strutture in legno. Materiale, calcolo e progetto secondo le nuove normative europee (Wooden structures. Material, calculation and design according to the new European regulations). Biblioteca Tecnica Hoepli Milano, Milano, 512-558.

[99] Newmark, N. M. (1951). Test and analysis of composite beam with incomplete interaction. Proc. of the society for experimental stress analysis, 9(1), 75-92.

[100] Möhler, K. (1956). Über das Tragverhalten von Biegeträgern und Druckstäben mit zusammengesetzten Querschnitten und nachgiebigen Verbindungsmitteln (Doctoral dissertation).

[101] Niederer, A: Grenzen der Anwendung des γ-Verfahrens, HTWG Konstanz, Bachelor-thesis, 2008

[102] Gagnon S, Pirvu C. CLT handbook: cross-laminated timber. FPInnovations, 2011.

[103] de Suraÿ, Julien ; Raynal, Antoine (2020). Développement d'un connecteur pour plancher mixte bois-béton. Ecole polytechnique de Louvain, Université catholique de Louvain.

[104] Kaiser, H. (2010). Wind-Ertüchtigung statisch ausgenutzter Holzdächer zur Aufnahme angestellter Solarpaneele mittels in Schlitze geklebter CFK-Lamellen. epubli.

[105] Michelfelder, B. C. (2006). Trag-und verformungsverhalten von kerven bei brettstapel-beton-verbunddecken.

[106] Baker ALL, Abeles PW, Ashdown AJ et al. (1969) The Shear Strength of Reinforced Concrete Beams: A Report. Institution of Structural Engineers, London, UK, pp. 1–170.

[107] Kani MW, Huggins MW and Wittkopp RR (1979) Kani on Shear in Reinforced Concrete. Department of Civil Engineering, University of Toronto, Toronto, Canada, pp. 1–225.

[108] Rombach, G. A., Kohl, M., & Nghiep, V. H. (2011). Shear design of concrete members without shear reinforcement—A solved problem?. Procedia engineering, 14, 134-140.

[109] Lantsoght, E. O., van der Veen, C., Walraven, J. C., & de Boer, A. (2015). Transition from one-way to two-way shear in slabs under concentrated loads. Magazine of Concrete Research, 67(17), 909-922.

[110] Collins MP (1978) Towards a rational theory for RC members in shear. Journal of the Structural Division, ASCE 104(4): 649–666.

[111] Muttoni, A., & Fernández Ruiz, M. (2008). Shear strength of members without transverse reinforcement as function of critical shear crack width. ACI Structural Journal, 105(ARTICLE), 163-172.

[112] fib (2012) Model Code 2010: Final Draft. International Federation for Structural Concrete, Lausanne, Switzerland, pp. 1–676.

[113] AASHTO LRFD Bridge Design Specifications. Washington, DC: Association of State Highway and Transportation Officials, 2012.

[114] Swiss Standards Association, SIA 262 - Concrete Structures", Swiss Society of Engineers and Architects, Zurich, Switzerland, 2003.

[115] Regan PE (1987) Shear Resistance of Members without ShearReinforcement; Proposal for CEB Model Code MC90. Polytechnic of Central London, London, UK, pp. 1–28.

[116] Building code requirements for structural concrete and commentary. (2014). ACI 318-14, American Concrete Institute, Farmington Hills, Mich.

[117] Bresler B and MacGregor JG (1967) Review of concrete beams failing in shear. Journal of the Structural Division, ASCE 93(1): 343–372.

[118] Mast, R. F. (1968). Auxiliary reinforcement in concrete connections. Journal of the Structural Division, 94(6), 1485-1504.

[119] Birkeland, P. W., & Birkeland, H. W. (1966, March). Connections in precast concrete construction. In Journal Proceedings (Vol. 63, No. 3, pp. 345-368).

[120] Gołdyn, M. (2022). Shear capacity of the interface between concretes cast at different time in the light of experimental investigations and codes of practice. Archives of Civil Engineering, 68(1).

[121] Bedon, C., & Fragiacomo, M. (2017). Three-dimensional modelling of notched connections for timber–concrete composite beams. Structural Engineering International, 27(2), 184-196.

CHAPTER 3

The local behavior of notched connection system

This page is intentionally left blank.

Contents

3.1 Introduction

As reported in literature review of chapter 2, a novel notched connector is proposed for the use as the connection system of CLT-concrete composite floors (referred as the HOBOA system). It is important to determine the load-carrying capacities and the effectiveness of the proposed configuration of the notched connector prior to its full-scale implementation onsite. In this chapter, the description of the dovetail notched connection is presented in section 3.2. Then, the behavior of notched connectors is first investigated by conducting an experimental program of three symmetrical pushout tests, which is described in section 3.3. The results from these tests allow to determine the shear resistance, the stiffness, the deformation capacity, and the failure mode of the notched connectors. Next, section 3.4 presents the development of a three-dimensional finite element (FE) model of the pushout tests and its validation by comparison with the experimental results. In section 3.5, the validated FE model is used to further understand the load-transfer mechanisms at the connection system and to conduct a parametric study in order to investigate the influence of important parameters relating to material properties and geometries of the pushout test on the behavior of the connection system. The results of the parametric study serve to analyze the optimization process. Lastly, in section 3.6, design formulae from different standards are afterwards tested to estimate the strength of the current connection corresponding to failure modes and verified against the results from the parametric study. Then, a strut-and-tie model is developed following the results of the FE model in order to estimate the strength of the current connection system if the failure mode is governed by the concrete shear failure.

3.2 Description of the dovetail notched connection system

Different types of shear connectors in timber-concrete composite structures have been studied in the past, ranging from the most flexible (simple nails or screws) to the most rigid (notches or continuous connectors with glue) [1], [2], [3]. Among all the existing connection types discussed in the literature above, the notch connector is often highlighted as the highest performing type in terms of shear stiffness and resistance, while maintaining simplicity of on-site application and quality control. However, despite its advantages of high strength and stiffness, the notched connector exhibits very brittle behavior at failure if no metallic stiffeners are used, as confirmed by experimental tests in the study of Ceccotti [1] and Boccadoro [4].

To improve ductility in post-peak performance, additional fasteners embedded in the notches (penetrated in the timber) were added and studied by many researchers [3], [5], [6], [7], [8]. The results indicated that embedded fasteners enhanced the strength, and the post-peak behavior by limiting the uplift between the timber and the concrete, and by providing an additional dowel action.

However, the installation of these steel elements requires tools and skills and slows down the construction process. In this study, the novel notched connection system proposed by Thierry Soquet, with a dovetail shape for CLT-concrete composite floors, as shown in Figure 1, is investigated. The particular shape of the notch is able to limit the separation (uplift) between the concrete and the CLT panels. Furthermore, the V-shape rebar cage inside the notch improves the uplift resistance and provides an additional dowel action to the concrete notch and is expected to avoid the brittleness of the connection. Consequently, this connection system should avoid the use of anchored steel screws or fasteners, thus facilitating onsite erection.

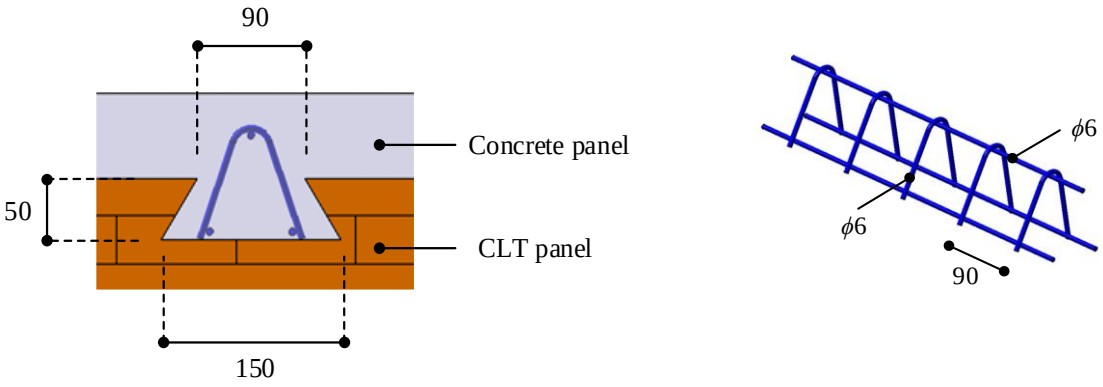

a. Notched connector b. V-shape rebar cage

Figure 1: Dovetail-shape notched connector (unit in mm).

3.3 Experimental pushout test

The mechanical performance of a shear connection system between composite members can be characterized by means of standard pushout tests. Three common types of pushout tests exist, including symmetrical or double shear test, asymmetric shear test, and pure shear test [9]. According to Thai et al. [10], the asymmetrical test configuration can be cheaper, but it tends to result in higher stiffness and strength than the symmetrical one by the increase of friction effect between the two materials due to the eccentricity moment. In this study, the symmetrical configuration of pushout test is adopted.

3.3.1 Test specimen

Three specimens (namely 1B-1, 1B-2, and 1B-3) were fabricated. Each specimen was made of two CLT panels (each composed of a symmetrical lay-up of 5 layers of 33-mm thick timber planks), glued to each other and placed between two 80 mm thick reinforced concrete panels (see Figure 2). Each reinforced concrete panel was connected to the CLT panel by two notched connectors. This notched connector was obtained by cutting a notch with the dimensions given in Figure 1a from the CLT panel. A V-shape rebar cage with a diameter of 6 mm (see Figure 1b) was then placed in the notch, and the concrete was cast. In the specimen fabrication process, the concrete was poured on each CLT panel separately using the same concrete on the same day. After the concrete was hardened, the two pieces were glued to each other at the free surface of the CLT panels (see Figure 2) using polyurethane glue. This process avoids the inconvenience of casting the concrete at a different time for each concrete panel and ensures the same age and properties of the concrete. It is worth noting that the concrete was cast directly on the CLT panel without laying plastic films nor applying any paint.

The dimensions of the three specimens as illustrated in Figure 3 were identical except for the width. After testing 1B-1, the width of specimens 1B-2 and 1B-3 was adjusted from 500 mm to 400 mm in order to have a bigger margin between the capacity of the force jack and the maximum load to be applied to the specimen. Reinforcement mesh ST15 was also placed inside and at the middle of the concrete panel to conform with real construction details.

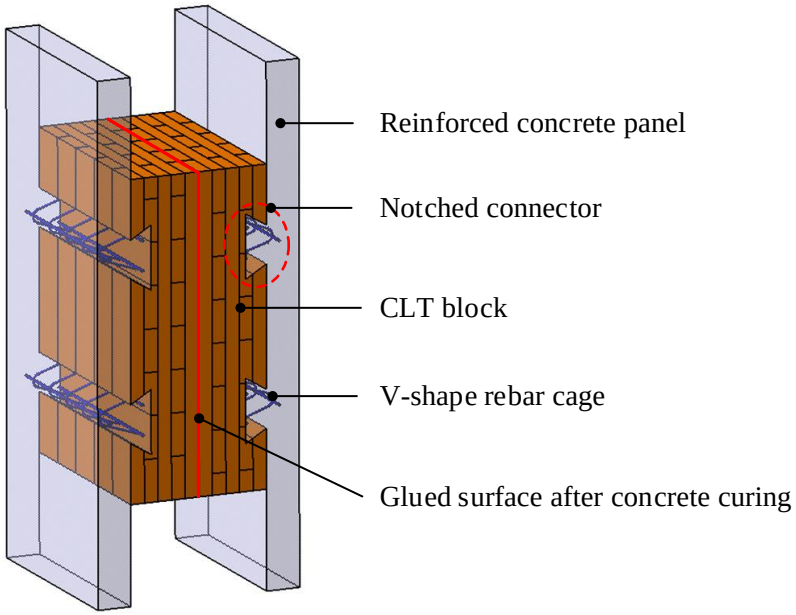

Figure 2: Description of pushout specimens.

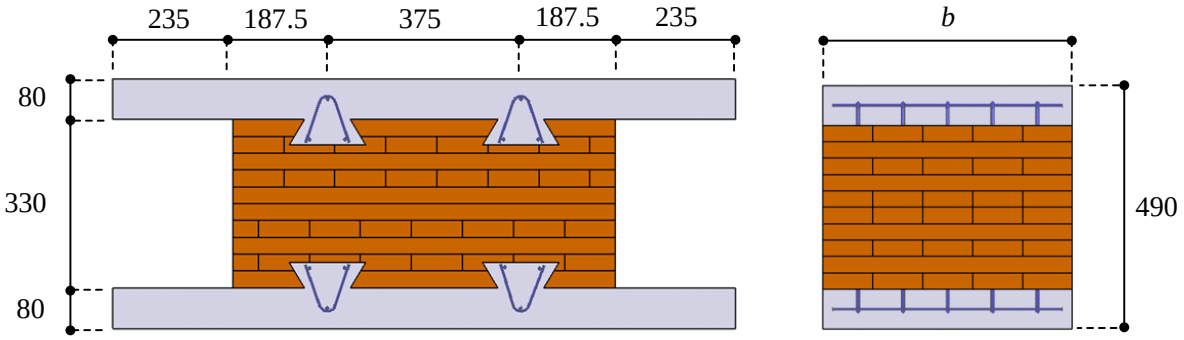

Figure 3: Dimension of pushout specimens (unit in mm).

3.3.2 Test setup and loading procedure

The standard EN 26891 [11] can be adopted in order to determine the stiffness and strength of timber-timber connections. This standard is commonly accepted for characterizing the behavior of the timber-concrete connections, because there is no specific standard yet. However, in this study, the effect of friction between the concrete and the CLT was not removed or reduced by means of plastic films or paint. Therefore, the test setup and the loading procedure were made to conform to Annex B of Eurocode 4 [12] with adjustment to fit with the configuration of the CLT-concrete composite floor.

The load was thus applied according to the test procedure described in Annex B of Eurocode 4 [12]. With a loading rate of 1 mm/min, 25 loading/unloading cycles between 5 percent and 40 percent of the expected failure load were initially applied to the specimen in order to remove the friction between the concrete and CLT surfaces. The load was then monotonically increased up to failure with a loading rate of 1 mm/min. For the first pushout test (specimen 1B-1), the expected maximum load was estimated supposing a shear failure of concrete in the notched connector for a loading of 400 kN. After testing specimen 1B-1, the expected failure load was updated to 650 kN for specimens 1B-2 and 1B-3.

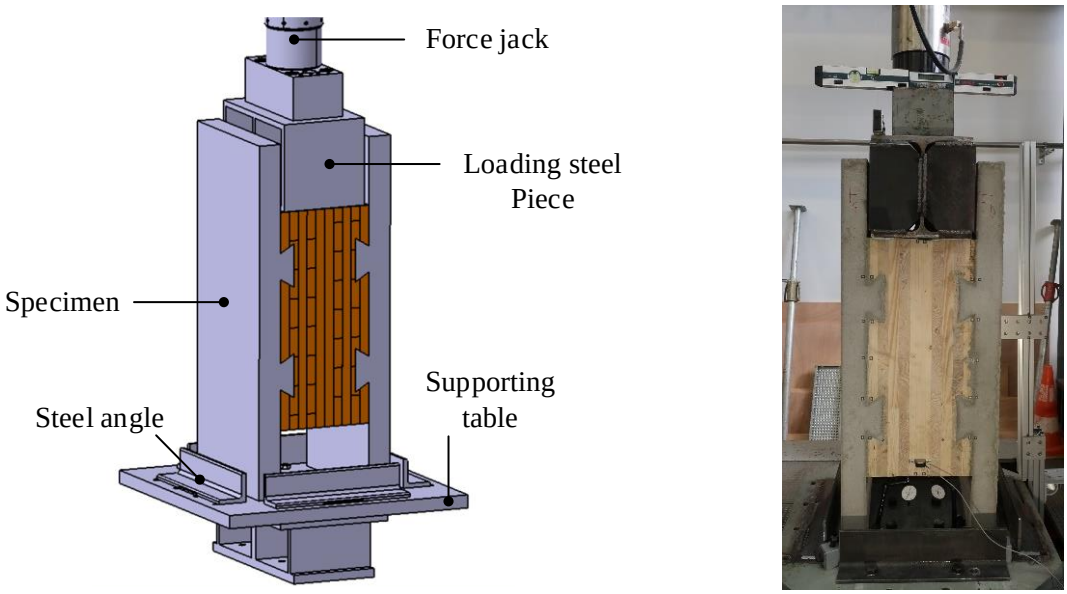

Figure 4: Description of pushout test setup.

Illustrated in Figure 4, the test setup consisted of a force jack with a capacity of 1500 kN, a loading HEB-300 steel piece, a specimen, and a supporting steel table. The specimen was placed vertically on the supporting table. On the top surface of the CLT block of the specimen, the force jack applied a uniform vertical load via the HEB-300 profile while the supporting steel table provided a reaction to the reinforced concrete panels. The width of this HEB profile (300 mm) almost covered the width of the CLT panel (330 mm) so that the loading could be as uniform as possible. Four steel angles placed around the four faces of the specimen were fixed on top of the supporting steel plate for security purposes. These angles were however not in contact with the pushout specimen.

3.3.3 Material

3.3.3.1 Concrete

In this research, a concrete with a strength class of C35/45 was used and formulated according to the norm EN 206-1 [13], having the class of environment XF1. Two series of three-cylinder specimens with a dimension of 11×22 cm were tested on the day of each pushout test using standard compressive tests for compressive strength and using Brazilian tests for tensile strength. The results are reported in Table 1. f_{ct} and f_{ctm} are concrete tensile strength of each specimen and their mean value, respectively. f_c and f_{cm} are concrete compressive strength and their mean value, respectively. It is worth mentioning that the specimens of pushout tests were tested at early ages in order to have a concrete strength on the testing day ranged from 60 percent to 80 percent of concrete characteristic strength, as required by Eurocode 4 [12]. In this case, the concrete with strength class of C35/45 is expected to achieve a compressive resistance ranging between 21 MPa and 28 MPa on the testing day. However, the data obtained from Table 1 indicates that the initial objective of minimizing the concrete resistance is not fully realized.

Table 1: Concrete strength of pushout specimens.

Test	Age (days)	f_{ct} [MPa]	f_{ctm} [MPa]	f_c [MPa]	f_{cm} [MPa]
1B-1	6	3.16	3.20	33.82	34.51
		3.50		34.46	
		2.94		35.25	
1B-2	3	2.80	2.56	29.31	29.12
		2.35		28.70	
		2.53		29.36	
1B-3	7	3.72	3.39	39.73	39.51
		3.21		38.95	
		3.23		39.84	
Average			3.04		34.38

3.3.3.2 Timber and rebar

The CLT panel was made of massive wooden boards with a minimum class of C24 and a mean density of 420 kg/m^3, specified in the technical specification of the product TOT'm X [14]. On the other hand, the steel rebars for the concrete panel and the notch connector have a nominal yield strength of 500 MPa.

3.3.4 Instrumentation

The force generated by the hydraulic jack was measured with a force sensor. Relative displacements between the CLT and concrete panels (slips and uplifts) during the test were measured using Digital Image Correlation (DIC) method. In this method, a series of photos were captured during the course of the test at each increment of loading by two high-resolution cameras (one at the front surface and the other at the back surface of the specimen). Points were marked on the concrete and the first layer of the CLT panels (see Figure 5); the change of the positions of these points was tracked and measured in order to compute the slips and uplifts. The precision determined for this test is currently ± 0.1 mm.

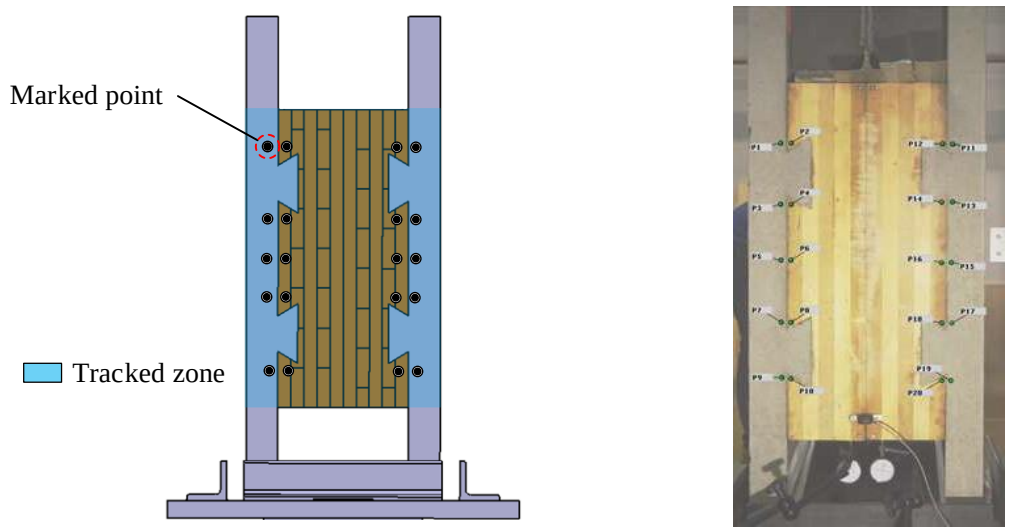

Figure 5: Zones for Digital Image Correlation measurement of pushout tests.

3.3.5 Results

3.3.5.1 Observations and failure mode

Figure 6 shows the evolution of the applied force in function of the elongation of the force jack for all the three pushout tests. In overall, the curves exhibited a linear behavior until the failure was attained at a load level of 840 kN, 685 kN and 742 kN for specimens 1B-1, 1B-2 and 1B-3, respectively. It is reminded here that the specimen 1B-1 was 500 mm wide, while specimens 1B-2 and 1B-3 were 400 mm wide. The equivalent forces per connector per meter linear width were 420 kN/m, 428 kN/m, and 464 kN/m for tests 1B-1, 1B-2, and 1B-3, respectively.

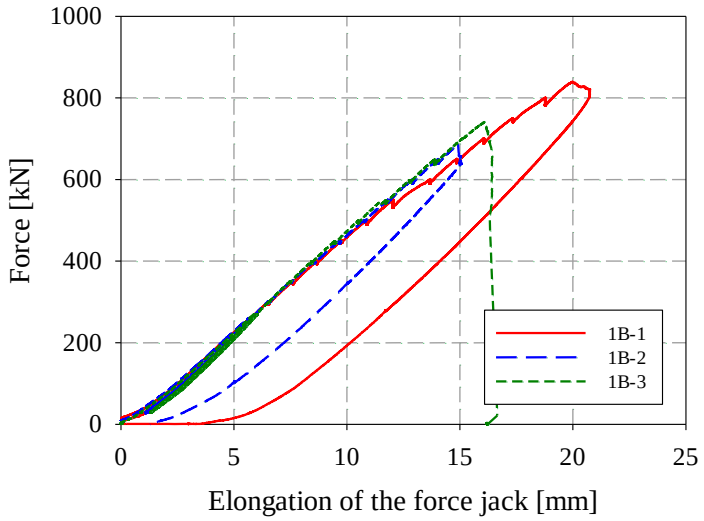

Figure 6: Force-elongation curves of the force jack in pushout tests.

For the test 1B-1, during the initial 5 cycles of loading, there was no sign of cracks in the concrete panels nor in the wood. Cracks first started in the concrete panel near the connector (see Figure 7a) and in the timber panel (see Figure 7b) at a load level of 300 kN and 350 kN, respectively. No further crack was noticed until the loading reached 700 kN, when a fine crack was observed on the width of the concrete panel below the bottom connector, caused by the bending stress (see Figure 7c). The loading was stopped after hearing a loud noise associated with the extension of cracks in the wood and a rupture

in the most outer cross-layer of the CLT panel at a load level of 840 kN, as shown in Figure 7d. For the test 1B-2, cracks were noted in the concrete notch during the first cycle of loading at a load level of 150 kN (see Figure 8a). They developed further during the third cycle of loading, at a load level of 260 kN (see Figure 8b). Similar to the test 1B-1, a horizontal crack was noticed in the concrete panel at a load level of 650 kN, due to the bending stresses (see Figure 8c). No crack in the timber panel could be observed until sudden cracks of the cross-layer of the CLT panel and brutal noises were observed at the load level of 685 kN (see Figure 8d). In the test 1B-3, the appearance of some cracks started in the wood and concrete at the load level of 270 kN and 420 kN, respectively (see Figure 9a,b). Unlike tests 1B-1 and 1B-2, no horizontal crack due to bending stresses appeared in the concrete panel in test 1B-3. However, severe cracks of the most outer cross-layer of CLT panel were observed in this test at the load level of 690 kN (see Figure 9c). The loading continued until the full collapse of the specimen at a load level of 742 kN, as illustrated in Figure 9d.

In all the three tests, the failure mode was governed by a brittle shear rupture of one of the most outer cross-layer of the CLT panel. After the experimental tests, the rebars in the notches were made visible by removing concrete with a jackhammer (see Figure 10). No excessive deformations could be observed in the rebars.

(a) (b) (c) (d)

Figure 7: Crack observations and failure mode of the specimen 1B-1.

(a) (b) (c) (d)

Figure 8: Crack observations and failure mode of the specimen 1B-2.

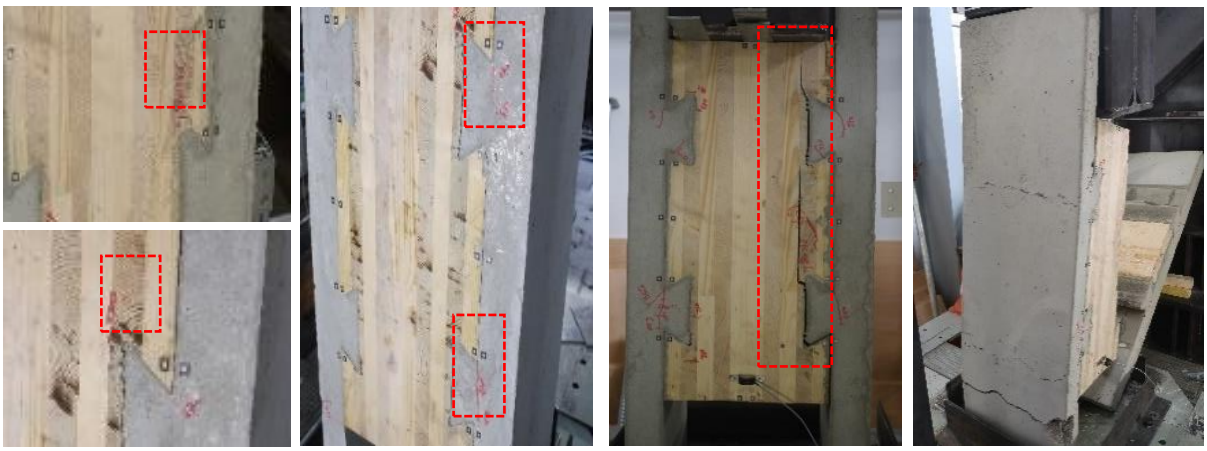

(a) (b) (c) (d)

Figure 9: Crack observations and failure mode of the specimen 1B-3.

Figure 10: Steel rebars in the concrete notched connectors after collapse (concrete was removed by a jackhammer).

3.3.5.2 Experimental test interpretation

Figure 11 illustrates the evolution of the mean slips and the mean uplifts in function of the force per connector per meter width derived from the digital image correlation method. The horizontal plateaus can be related to the pauses that were made during the loading in order to observe the evolution of the damages in the specimens. The maximum value obtained from the three tests ranged between 0.8 mm and 1.6 mm for the slip and between 0.7 mm and 1 mm for the uplift. The maximum loads attained per connector per meter width (F_{max}) were 420 kN/m, 428 kN/m and 464 kN/m for tests 1B-1, 1B-2 and 1B-3, respectively. The corresponding mean slips ($\delta_{F_{max}}$) and uplifts ($g_{F_{max}}$) are listed in Table 2. The average maximum force is 437 kN/m with a coefficient of variation of 5 percent, indicating the small experimental dispersion of the connection strength of the three tests. Due to the significant variation of the timber strength caused by natural characteristics or defects, it is surprising that such a small dispersion of the forces was observed, as the failure was governed by shear rupture of the transversal layer of CLT panel in all the three pushout tests.

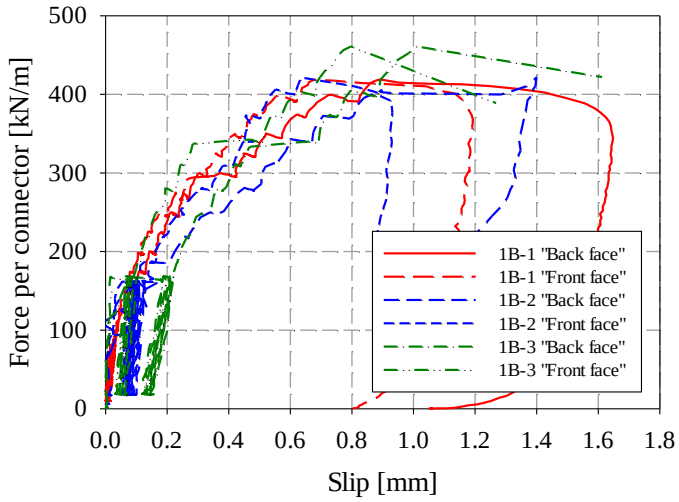

a. Force per connector versus slips

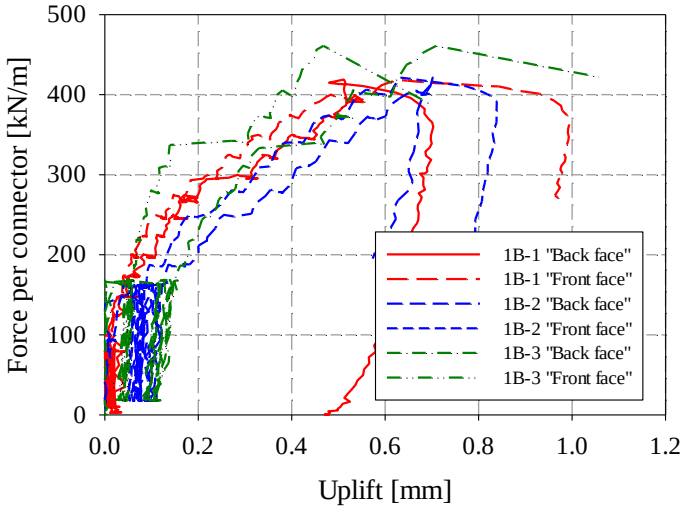

b. Force per connector versus uplifts

Figure 11: Slip and uplift curves of all three pushout tests.

Table 2: Shear strength for one connector with corresponding slip and uplift of pushout tests.

Test	F_{max} [kN/m]	$\delta_{F_{max}}$ [mm]	$g_{F_{max}}$ [mm]
1B-1	420	0.79	0.57
1B-2	428	1.02	0.67
1B-3	464	0.9	0.59
Avg. (CoV)	437 (5%)	-	-

3.3.5.3 Design value

The design value of the strength of the connector is required in the design procedure of timber-concrete composite members at the ultimate limit state. The three specimens tested had the same configuration, and the failure mode was governed by the brittle shear rupture of the most outer cross-layer of the CLT panel. Hence, the design value under static loads is determined based on the values of

the maximum forces obtained from the three experimental tests in accordance with Annex D, Eurocode 0 [15]. The design resistance value can then be defined as:

$$X_d = \eta_d \frac{X_{k(n)}}{\gamma_m} = \frac{\eta_d}{\gamma_m} m_x (1 - k_n V_x) \quad (1)$$

where n is the sample size, equal to 3, X is the studied variable, m_x is the mean value of the results, V_x is the coefficient of variation of X, η_d=1 is the design value of the possible conversion factor, k_n is the characteristic fractile factor, equal 3.37 in case of V_x unknown and $n=3$ given in Table D1 of Eurocode 0 [15], γ_m is the partial factor for materials (concrete: $\gamma_{m,c}$ = 1.5, timber: $\gamma_{m,t}$ = 1.3). Using the values of maximum load attained per connector per meter width (F_{max}) from the Table 2, the design value of the shear connection resistance R_d is computed and reported in Table 3.

Table 3: Design values of the shear connection resistance.

m_x [kN/m]	V_x	γ_m	R_d [kN/m]
437	0.053	1.5	239
		1.3	276

It is worth to remind that the failure mode of the pushout tests was governed by the rolling shear resistance in one of the transversal layers of the CLT panel. For other possible collapse mechanisms, as for example the concrete shear failure, it can only be inferred that they happen for a larger load. Anyway, a sufficient safety for those unknown modes must be ensured. For that reason, in the perspective of a conservative design, the design values presented in Table 3 take into account the safety factor of each composite member (timber and concrete).

3.3.5.4 Computation of slip modulus

In the design of timber-concrete composite beams and slabs, the strength and stiffness of the connection are required. At the serviceability limit state, the stiffness of the connection is taken equal to the slip modulus, noted by K_s in EN 26891 [11] and by K_{ser} in Eurocode 5 [16]. This stiffness can be quantified experimentally by standarsd pushout tests. If the tests are performed in accordance with EN 26891[11], the slip modulus K_s can be determined in function of the estimated maximum force F_{est} as follows:

$$K_s = \frac{0.4 F_{est}}{\frac{4}{3}(\delta_{04} - \delta_{01})} \quad (2)$$

where δ_{04} and δ_{01} are the slips corresponding to 40 percent and 10 percent of the estimated maximum load F_{est}, respectively. At the ultimate limit state, the slip modulus is denoted by K_u and taken equal to two thirds of K_s according to Eurocode 5 [16]. However, the computation of K_s in Eq. (2) is based on the estimated maximum load F_{est} and not on the actual maximum load F_{max} obtained from the pushout tests. Based on the definition in EN 26891 [11], the value of F_{est} can be replaced by the value of F_{max} only if the deviation between the values of F_{est} and F_{max} is more than 20 percent. As indicated by Dias [17] and Manthey [18], such a difference of maximum force can lead to a non-negligible difference of the slip modulus. As a consequence, this method is disregarded.

Ceccotti [1] proposed an effective approach for computing slip modulus using direct relation with the actual maximum force obtained from the tests. The slip modulus to be used at serviceability limit state and at ultimate limit state can be defined as follows:

$$K_s = 0.4F_{max}/\delta^*_{0.4} \quad (3)$$

$$K_u = 0.6F_{max}/\delta^*_{0.6} \quad (4)$$

where $\delta^*_{0.4}$ and $\delta^*_{0.6}$ are the slips corresponding to 40 percent and 60 percent of the actual maximum load, respectively. In this study, the slip modulus of notched connector is therefore computed using the method proposed by Ceccotti [1] for all the three pushout tests. Table 4 provides the values of slip modulus for one notched connector per one meter width at serviceability limit state (K_s) and ultimate limit state (K_u) as well as the ratio of K_u/K_s.

Table 4: Shear strength and slip moduli values for one connector per one meter width.

Test	0.4 F_{max} [kN/m]	$\delta^*_{0.4}$ [mm]	0.6 F_{max} [kN/m]	$\delta^*_{0.6}$ [mm]	K_s [N/mm/m]	K_u [N/mm/m]	K_u/K_s
1B-1	167	0.09	251	0.22	1.81×10^6	1.14×10^6	0.63
1B-2	169	0.12	253	0.23	1.38×10^6	0.85×10^6	0.61
1B-3	184	0.14	277	0.27	1.29×10^6	1.10×10^6	0.85
Avg. (CoV)	-	-	-	-	1.49×10^6 (19%)	1.03×10^6 (25%)	0.69 (19%)

The stiffnesses have a large deviation compared to the deviation of the maximum applied forces (5 percent). This large deviation of stiffness might come partially from the precision of the measurement of the slips by DIC method at small values. It should be reminded that the precision of this technique in these tests was ±0.1 mm, which is approximately 10 percent of the maximum slips.

The average value of the ratio K_u/K_s is around 0.69, giving a good agreement with the recommendation by Eurocode 5 [16] for computing K_u being equal to two thirds of K_s. Figure 12 presents the synthetic force-slip curves drawn based on a limited number of load levels ($0.2F_{max}$, $0.4F_{max}$, $0.6F_{max}$, $0.8F_{max}$, and F_{max}).

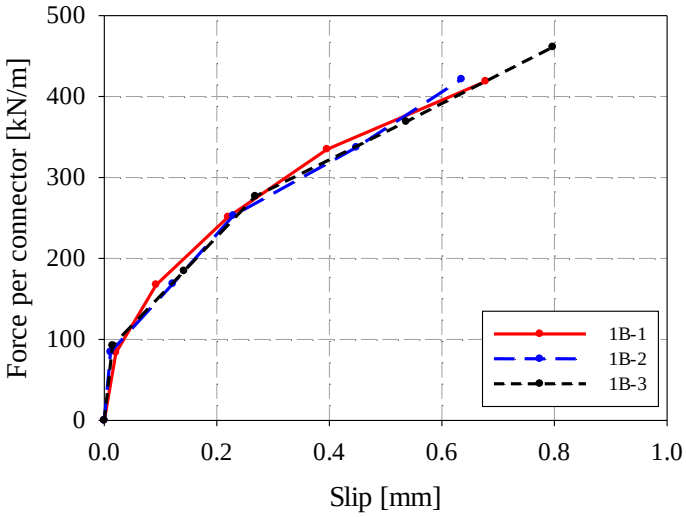

Figure 12: Force-slip curves at different load levels of pushout tests.

3.3.6 Comparison and discussion

In order to get some insight into the efficiency of the tested connection, a comparison to similar notched connections [19], [20], [21] is presented in this section. First, the LVL-concrete notched connection (S3.2.2) studied by Boccadoro [19] is considered. The LVL timber consisted of 13 veneers with 3 cross-layers while the concrete with strength of C50/60 was used (see Figure 13a). The notched connection had a rectangular shape with a width of 530 mm, a length of 100 mm and a depth of 15 mm. The maximum force was limited at 726 kN/m by the rolling shearing-off failure of the middle cross-layer of LVL timber. Despite a similar mode of failure by rolling shear action in the timber panel, the maximum load was nearly twice larger than the value obtained in this research, see Table 5. For a comparable rolling shear plane in the two cases, such a difference in load-carrying capacity was due to the different rolling shear resistances, being 3.66 MPa for the LVL timber in the specimen S3.2.2 in [19] and 1.49 MPa in the specimens tested in the present study. The SLS stiffness K_S was also nearly twice larger, at 2290 kN/mm/m. The difference in stiffness might be accounted by the different shear modulus, being 433 MPa for the LVL timber in the specimen S3.2.2 in [14] and 133 MPa in the specimens tested in the present study.

Next, the LVL-concrete notched connector studied by Monch et al. [20] is compared (see Figure 13b). The strength class of the LVL was GL24h and the concrete grade was C30/37. The notch had a rectangular shape with a width of 200 mm, a length of 160 mm, a depth of 20 mm and was complemented by a head screw with a diameter of 8 mm and a length of 160 mm. The test showed a ductile behavior with a compression failure of the wooden fiber. The maximum load attained was 549 kN/m, and the SLS stiffness K_S was 1320 kN/mm/m. Although the failure mode obtained in [20] and the one in the present study were different, the maximum force and the stiffness are comparable.

The last reference examined in this section is the CLT-concrete notched connector tested by Jiang et al. [21] (see Figure 13c). The CLT panel had 5 layers with a strength class of C24 and the concrete grade was C30/37. The notched connector had a rectangular shape with a width of 450 mm, a length of 200 mm, and a depth of 25 mm and was supplemented by two lag screws with a diameter of 7 mm and a length of 120 mm. The maximum load was governed by the shear failure of the concrete in the notch at 502 kN/m. This was again close to the value obtained for the connection presented in this study, despite of the different failure modes and the larger dimensions of the notch. The stiffness K_s was 1790 kN/mm/m, and was also comparable with the value obtained in tests in the present study.

Table 5: Comparison between the notched connector tested in this research and other research with values for one connector per one meter width.

Connection type (Length [mm] × depth [mm])	F_{max} [kN/m]	K_s [kN/mm/m]	Failure mode	Ref.
1B: Dovetail notch (90 × 50)	437	1490	Rolling shear of cross-layer of CLT	This study
S3.2.2: Rectangular notch (100 × 15)	726	2290	Rolling shear of cross-layer of LVL	[19]
PO-M1: Rectangular notch (160 × 20)	549	1320	Compression failure of LVL	[20]
N180-1: Rectangular notch (200 × 25)	502	1730	Shear failure of concrete at notch	[21]

All results are summarized in Table 5. The resistance and the stiffness of the notched connection are thus similar to the ones obtained for usual notched connections, if considering the differences in wood strength. A high value of K_s and K_u indicates that the notch connector proposed in this study can be considered as a stiff connection system; however, its behavior should be verified in a global full-scale TCC floor system which is conducted later in chapter 4.

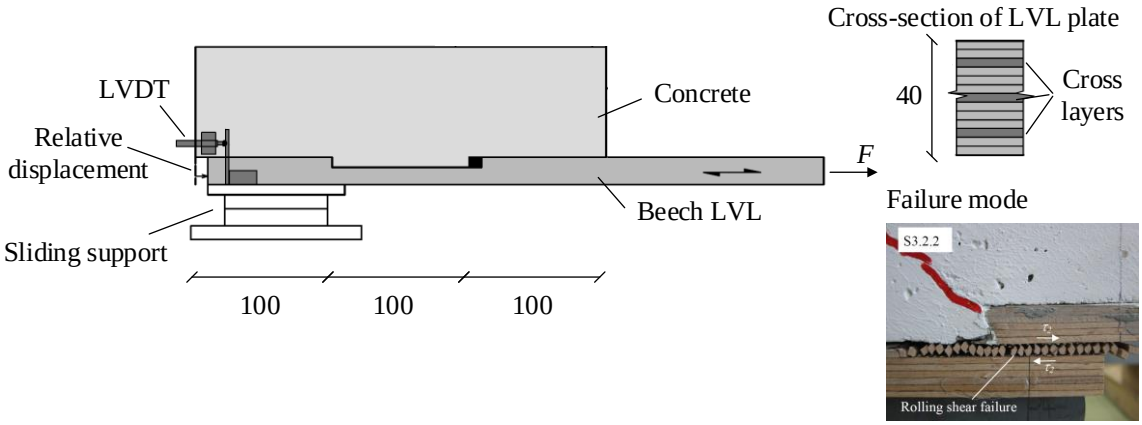

a. Test S.3.2.2 by Boccadoro [19]

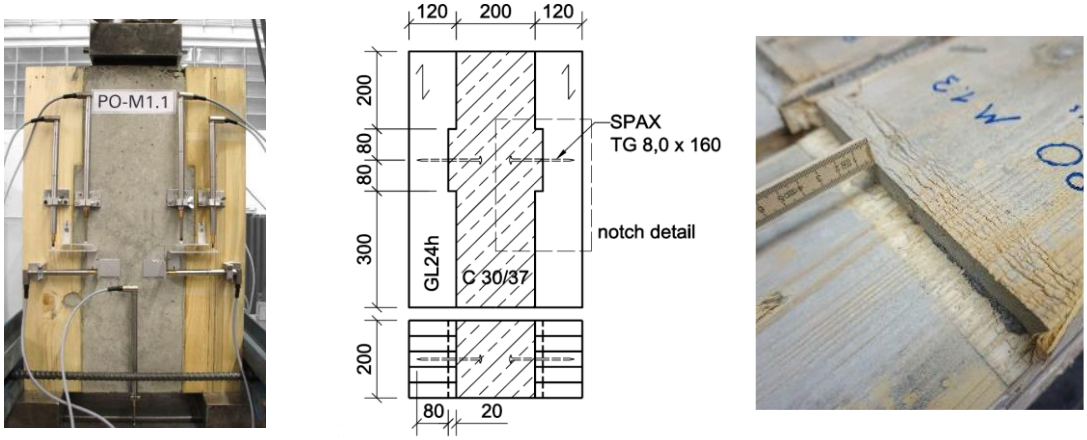

i. Test specimen PO-M1 ii. Front and top view iii. Failure mode

b. Test PO-M1 by Monch et al. [20]

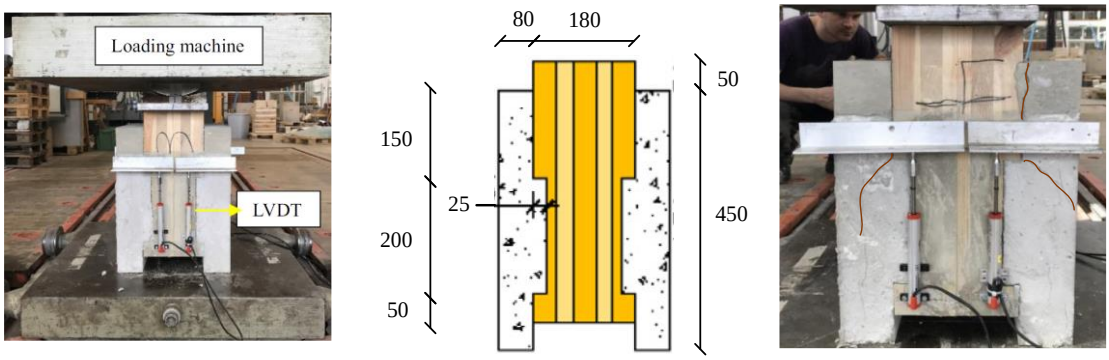

i. Test specimen N-180-1 ii. Front view iii. Failure mode

c. Test N-180-1 by Jiang et al. [21]

Figure 13: Configurations and failure modes in different pushout tests.

3.4 Numerical study

The results obtained from the experimental tests are limited in assessing the full mechanical behavior of the dovetail notched connector. As a response, a numerical study is carried out using a full three-dimensional finite element program, ABAQUS/EXPLICIT [22], in order to further investigate the notched connector behavior including the load transfer mechanism, distribution of the normal or shear stresses, and strains of each component. After validating and assessing the behavior of the notched connector in the FE model, a parametric study is then carried out in order to study the influence of different parameters such as material properties and geometries of pushout tests. This parametric study aims to provide further insight and optimized choices of the notched connectors. The establishment and the validation of the FE model, and the parametric study are described in the following sections.

3.4.1 Model establishment

In order to develop a comprehensive 3D FE model to represent the actual pushout tests, the behavior of materials, and rigorous contact definition between CLT and concrete panel are taken into account. In terms of material behavior, concrete is considered to exhibit non-linear behavior including softening and damage in compression and tension, whereas the CLT panel is considered to exhibit orthotropic behavior. To address all difficulties from considered material and rigorous contact definition, and to obtain convergences in numerical simulation, the explicit analysis was adopted in ABAQUS program [22].

3.4.1.1 Geometry and element modelling

To reduce the computational cost and simulation time, only one quarter of the pushout test configuration was considered by taking advantages of the symmetric disposition. All components of the specimen and the steel loading block were modelled according to the actual configuration and dimension of the experimental test. Figure 14 depicts the configuration of the FE model and the test setup of the experimental tests.

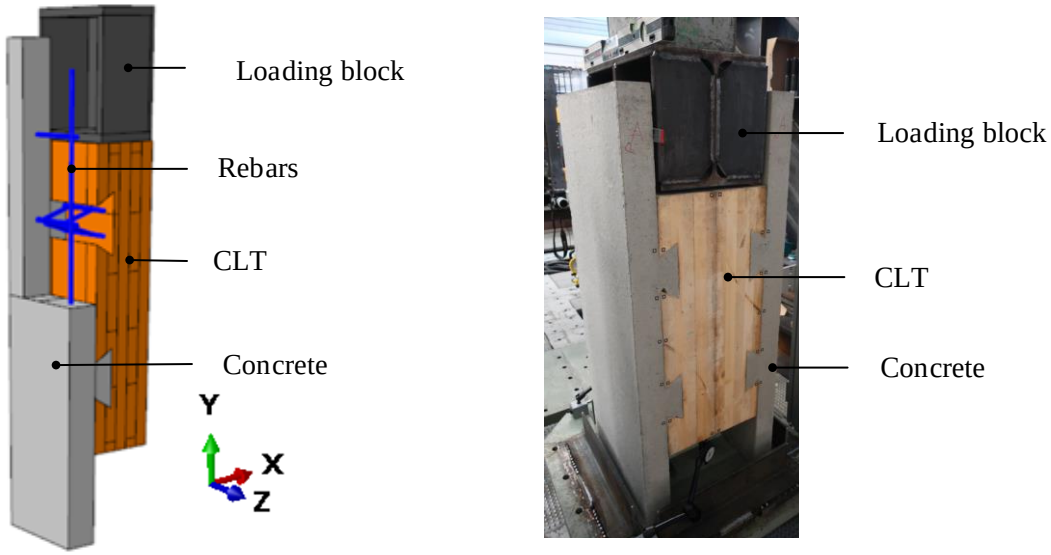

a. FE Model b. Experimental test setup

Figure 14 : Configuration of pushout test setup in FE model and experimental test.

In the FE model, timber boards were made as separate parts and then combined together in order to model a CLT panel. Regarding the contact between timber boards, common nodes were shared with each other creating a rigid contact. Furthermore, the orientation of timber boards as orthotropic materials was also modelled in the CLT part. Figure 15 illustrates the orientation of longitudinal and cross-layer of timber boards in the CLT panel.

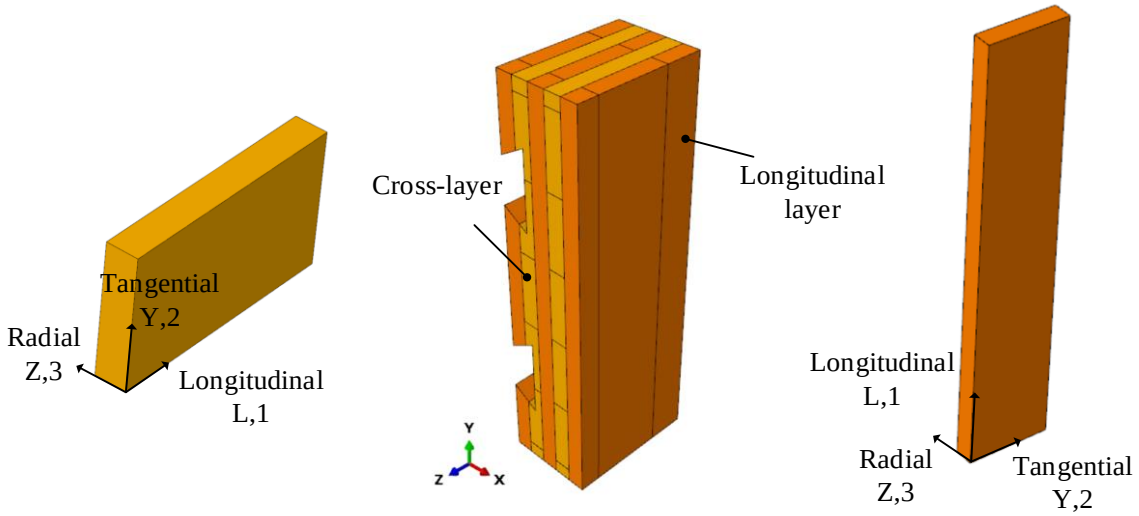

Figure 15: Orientation of the CLT panel in FE model.

3.4.1.2 Materials modelling

In order to accurately capture the behavior of the specimen, proper material properties should be defined by taking into account the non-linearity. The constitutive law of materials including concrete, timber and steel are described in the following subsections.

A. Constitutive model for concrete

Concrete can be considered as a non-linear isotropic material [23]. The concrete damaged plasticity (CDP) model available in Abaqus/Explicit [22] was adopted based on the uniaxial concrete behavior provided in [24] to reproduce properly the two main behaviors of concrete (compression crushing and tensile cracking). Moreover, the parameters to define the flow potential and the yield surface, including the dilatation angle Ψ, the eccentricity ϵ, the ratio of biaxial compressive strength to uniaxial compressive strength f_{b0}/f_{c0}, the shape factor for yield surface K_c, and the viscosity parameter υ which were adopted from the recommendation in ABAQUS user manual [22], are reported in Table 6.

Table 6: Parameters of concrete damaged plasticity model.

Ψ [^{0}]	ϵ	f_{b0}/f_{c0}	K_c	υ
40	0.1	1.16	0.67	0

The compressive concrete strength obtained experimentally using cylinder specimens from the previous pushout tests (see section 3.3.3.1) was used in the FE model while the concrete tensile strength was computed in relation to the compressive concrete strength in accordance with Eurocode 2 [25]. The mean value of the compressive strength f_{cm} and the tensile strength f_{ctm} were thus 35 MPa and 2.71 MPa, respectively. The Poisson ratio of concrete was assumed to be equal to 0.2 while the strain at compressive strength ε_{cm} was taken as 0.0022, as proposed in [26]. Figure 16 describes the stress-strain

and damage-strain curves for the non-linear behavior of concrete in compression and tension. It should be noted that the construction process of the concrete compressive and tension curves presented below is extensively described in section 2.3 of Chapter 2.

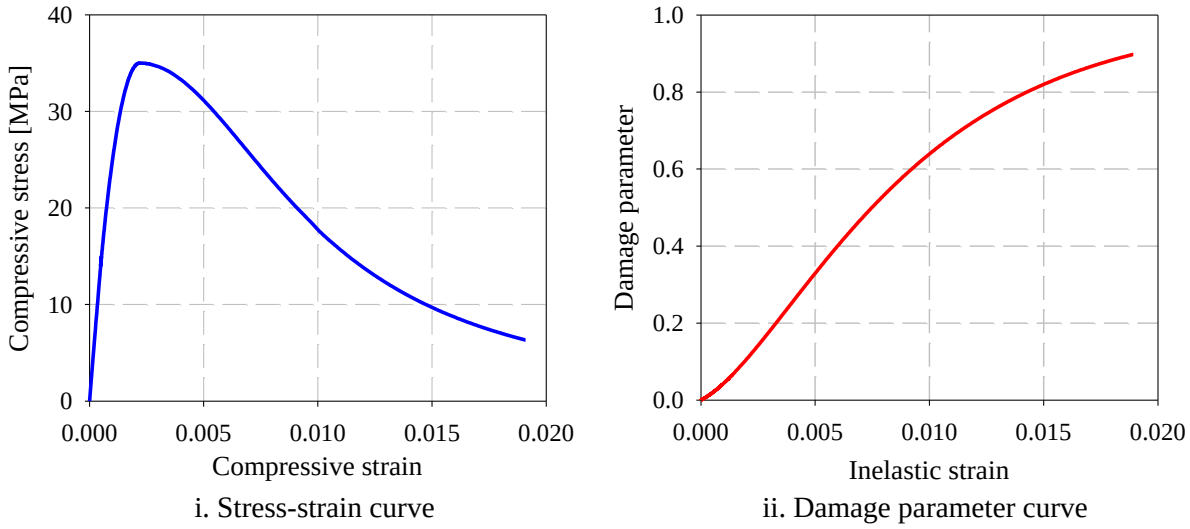

i. Stress-strain curve ii. Damage parameter curve

a. Compressive behavior

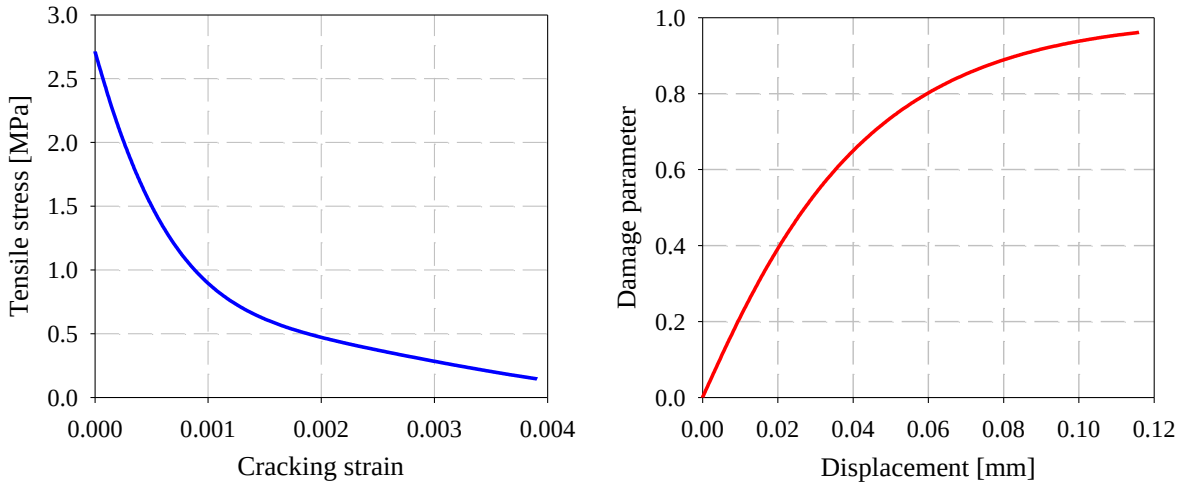

i. Stress-strain curve ii. Damage parameter curve

b. Tensile behavior

Figure 16: Constitutive concrete model in the numerical simulation.

B. Constitutive model for timber

The timber was considered as an orthotropic material using the assumption that the stiffness and strength of timber in radial and in tangential directions were identical. The mechanical elastic parameters are given in Table 7. The subscriptions 1, 2, and 3 of parameters in Table 7 represent the orientation of timber in longitudinal, tangential, and radial directions, respectively. The Young's modulus E and shear moduli G_{12}, G_{13} were obtained from standard EN 338 [27] for the timber grade C24 whereas the rolling shear modulus G_{23} was obtained experimentally from the rolling shear tests. The detailed description of these tests and test procedures can be found in chapter 4 in section 4.2.2.2. In addition, the Poisson ratios were set to zero in accordance with Eurocode 5 [28]. As indicated by Dias et al [29], the Poisson ratios should not have significant influences on the results of the numerical simulation. However, the effect of this parameter will be discussed in the following section.

Table 7: Elastic material properties of the timber used in the FE model.

E_1 (MPa)	$E_2=E_3$ (MPa)	$G_{12}=G_{13}$ (MPa)	G_{23} (MPa)	$v_{12}=v_{13}=v_{23}$
11000	370	690	127	0

The plasticity of the timber was defined using the orthotropic yield criterion proposed by Hill [30]. This criterion is an extension of Von-Mises yield criterion taking into account the orthotropy of the material and its stress potential. The directional yield stress ratios or stress potentials are defined in a relation to the strength of the timber as the following relationships:

$$R_{11}=f_{c,0}/f_{eq} \quad (5)$$

$$R_{22}=R_{33}=f_{c,90}/f_{eq} \quad (6)$$

$$R_{12}=R_{13}=\sqrt{3}f_v/f_{eq} \quad (7)$$

$$R_{23}=\sqrt{3}f_r/f_{eq} \quad (8)$$

where $f_{c,0}$ is the compressive strength parallel to grain; $f_{c,90}$ is the compressive strength perpendicular to grain; f_v is the shear strength; f_r is the rolling shear strength; and f_{eq} is the equivalent yielding strength of the timber.

From compressive tests (see chapter 4 in section 4.2.2.2), the compressive strength of timber in longitudinal ($f_{c,0}$) and transversal directions ($f_{c,90}$) were found to be 31 MPa, and 3 MPa, respectively. The rolling shear resistance (f_r) was 1.49 MPa, obtained from the rolling shear tests. The equivalent yield strength f_{eq} was assumed to correspond to the value of $f_{c,0}$ [29], while the shear strength of the timber f_v was taken as 4 MPa according to EN 338 [27]. Therefore, the input parameters in ABAQUS [22] associated with the stress potentials were determined and are presented in Table 8. In addition, the yield stress-plastic strain relationship in the FE model was adopted using the stress and strain curve obtained from compression tests on timber in longitudinal direction (see Figure 17).

Table 8: Stress potentials or directional yield stress ratios in Hill criterion.

R_{11}	R_{22}	R_{33}	R_{12}	R_{13}	R_{23}
1	0.0965	0.0965	0.22	0.22	0.084

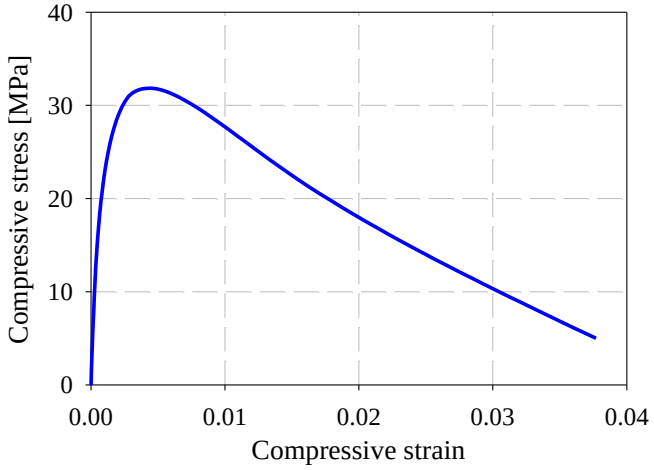

Figure 17: Stress-strain curve of timber parallel to grain under compression test.

C. Constitutive model for steel

Steel was considered to be an isotropic material and to exhibit a bilinear elastic-plastic behavior in the FE model. Its properties based on the experimental tests from literature [31] were used in this study. The material properties including yield stress f_y, ultimate stress f_u, Young's modulus E, yield strain ε_y, and ultimate strain ε_u were obtained in the form of engineering stress and strain. They were then converted to true stress and strain values using the following expressions [32]:

$$\sigma_{True}=\sigma_{Eng}(\varepsilon_{Eng}+1) \quad (9)$$

$$\varepsilon_{True}=ln(\varepsilon_{Eng}+1) \quad (10)$$

In equations (9) and (10), the subscripts "True" and "Eng" refer to true and engineering, respectively. Table 9 and Figure 18 present the steel properties and stress-strain curve adopted in the FE model, respectively.

Table 9: Tensile properties of steel reinforcements [31].

f_y (MPa)	f_u (MPa)	E (GPa)	ε_y [-]	ε_u [-]	v
500	635	200	0.00317	0.14559	0.3

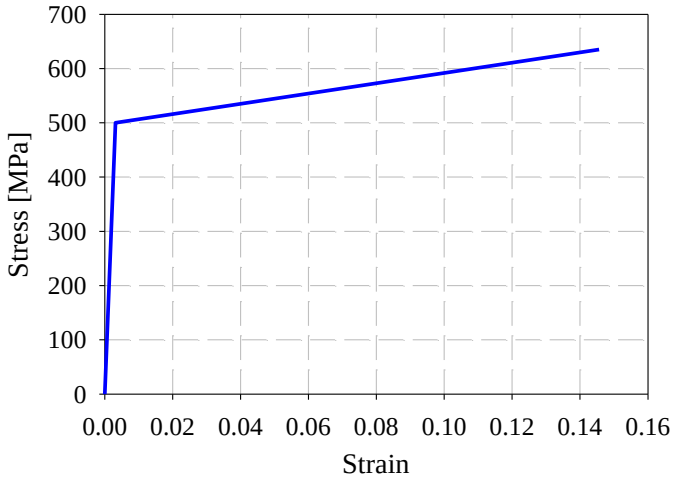

Figure 18: Stress-strain curve of steel reinforcement adopted in the FE model.

3.4.1.3 Mesh definition and contact interaction

The concrete panel, the CLT panel, and the HEB-300 loading block were meshed using hexahedral element with reduced integration and hourglass control (C3D8R) while the steel rebars were modelled using two-node beam element, B31. Figure 19 presents the identification of mesh definition of each component in the FE model. In addition, the partitions were adopted to generate more surfaces inside the model components for the proper and consistent mesh size and pattern. For the concrete panel, a finer mesh of 5 mm was generated in the neighboring region of the connection system in order to better predict the evolution of damage under the applied loading. The rest of the concrete panel had a size of 10 mm. The CLT panel was defined with a mesh of 7.25 mm, which corresponds to one-fourth of the thickness of each timber layer. The loading block and rebar reinforcement were defined with a mesh of

10 mm and 5 mm, respectively. In total, the one-quarter configuration of the FE model consisted of 95457 elements including 94172 elements of C3D8R and 1285 elements of B31.

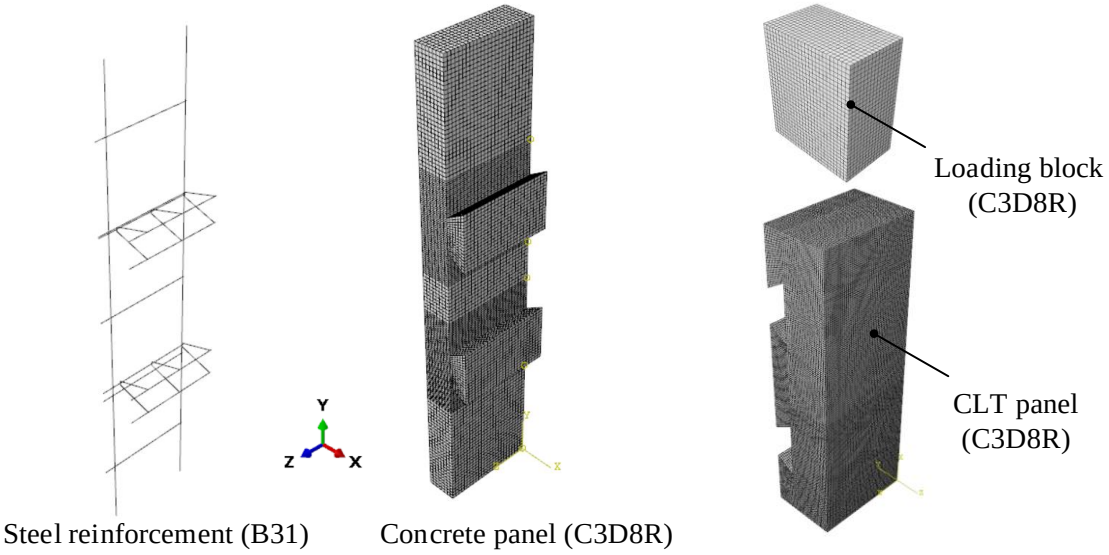

Figure 19: Mesh definition of each component in FE model.

The mechanical interaction at contact interfaces between model components is important to obtain an accurate response of the numerical simulation. Surface-to-surface contacts between concrete panel and CLT panel as well as between loading block (HEB-300) and CLT panel were considered. Figure 20 presents surfaces of the contact interaction highlighted in red color for all model components. The contact properties were defined by hard contact and friction penalty formulations for the normal and tangential behaviors, respectively. In this study, the friction coefficient for the contacts between concrete and timber, and between steel and timber were 0.62 [33] and 0.50 [34], respectively. Apart from that, an embedded constraint was adopted for the interaction between the steel reinforcement and the concrete panel.

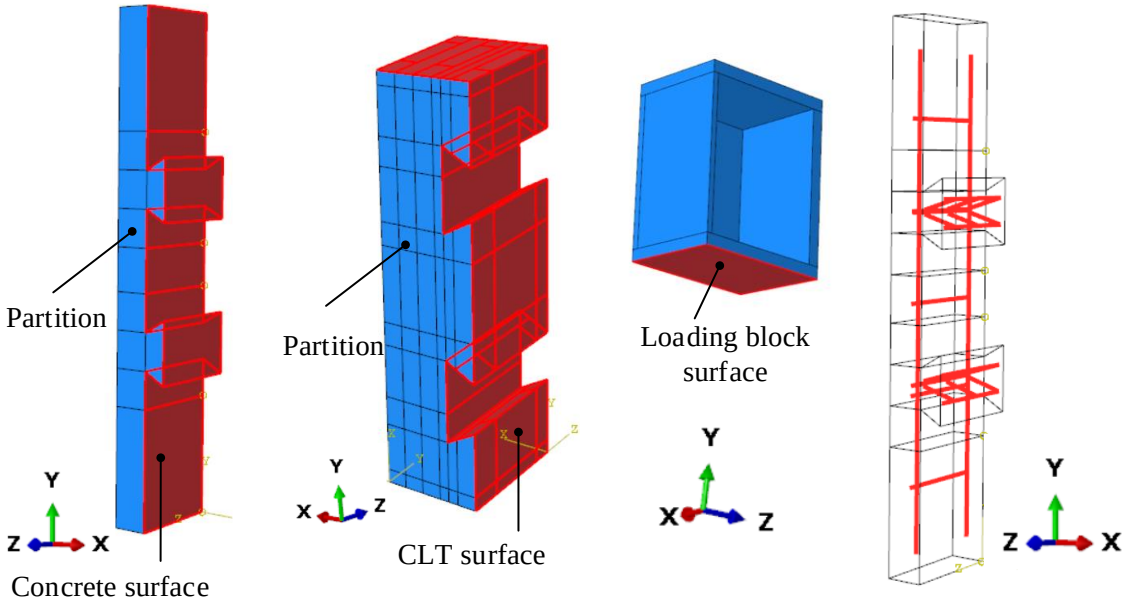

a. Concrete panel b. CLT panel c. Loading block d. Steel reinforcement

Figure 20: Contact surfaces of each model component in the FE model.

3.4.1.4 Boundary conditions and loading

The symmetry boundary conditions were applied at the highlighted surfaces in red and in blue color in Figure 21a, constraining the displacements in X-direction and Z-direction, respectively. The support was modelled by applying a rigid constraint to the bottom surface of the concrete panel that rigidly followed the movement of a reference point (see Figure 21b). This reference point was fixed in all degrees of freedom. In addition, the loading was simulated by applying an imposed displacement to another reference point that governed a rigid displacement of the top flange of the loading block HEB-300 (see Figure 21c). In the simulation, the loading was increased slowly in accordance with the assigned smooth amplitude function to reduce the dynamic effect over the course of loading and to obtain a quasi-static solution from the explicit dynamic analysis [35]. To achieve a computationally economical solution, the mass scaling method was adopted. However, attention had to be paid in order to obtain a compromise between the running time and the stability as well as the accuracy as the change of the mass-scaling was proportional to the kinetic energy of the model. It was verified that the kinetic energy was lower than 5 percent of the strain energy in order to achieve a quasi-static response [36]. In this study, a semi-automatic mass scaling was adopted with a target time increment of Δt=0.00005 in the time period of 15 seconds.

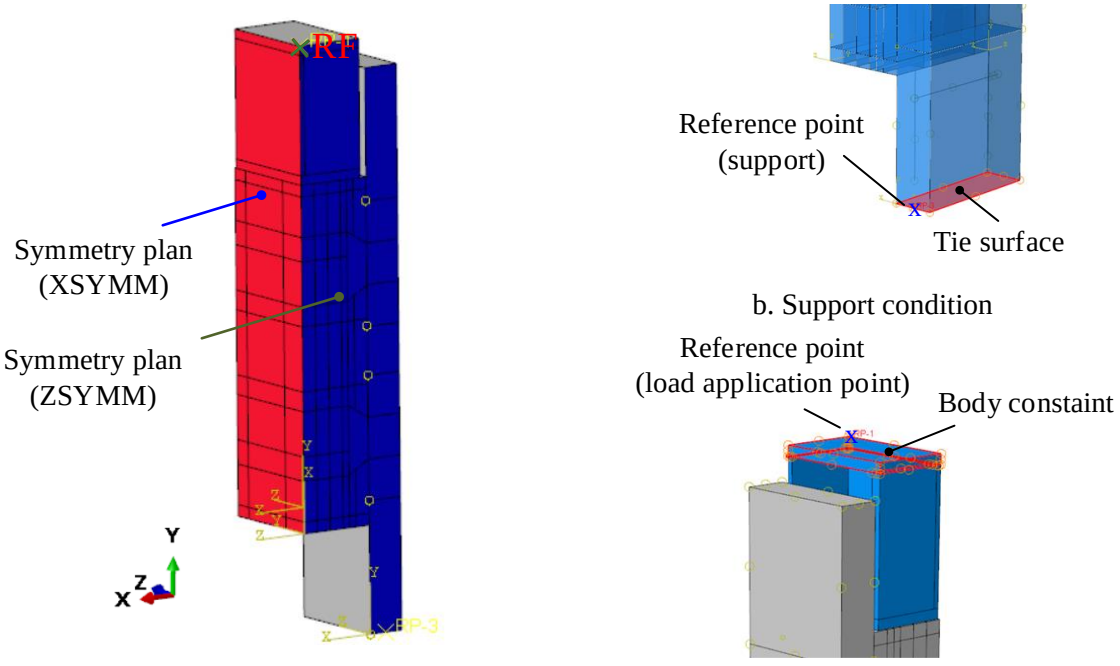

a. Applied symmetry plane

b. Support condition

c. Loading condition

Figure 21: Boundary conditions, support condition, and loading of the pushout test in the finite element program.

3.4.2 Finite element model validation

In order to validate the model, results such as the crack propagation, the maximum load level, the failure mode, the force-slip curve, and the slip moduli were compared with the experimental results. Through the FE model, estimations of unobservable information during the experimental tests including the load transfer mechanism and the stress distribution on the concrete and CLT panel were accessible and were then analyzed to gain a comprehensive understanding of the behavior of the notched connection system. In addition, the effect of variations of unknown data, including the friction

coefficient at the interface between the concrete and timber panel, the Poisson ratios of timber, and the loading block configuration are discussed in the following subsections.

3.4.2.1 Comparative discussion between FE model and experimental tests

The failure mode from the simulation was governed by the rolling shear failure of the CLT panel, reproducing the same failure mode as in experimental tests. Figure 22 illustrates the deformed shape and the rolling shear stress at the maximum load level obtained in the FE model as well as the failure mode obtained in experimental tests. The deformed shape in Figure 22a was scaled to approximately 20 times to enhance the visual presentation of the rolling shear failure in the CLT panel. In addition, a high rolling stress (blue color) of approximately 1.49 MPa was obtained, which corresponded to the rolling shear strength assigned as input value in the FE model (see Figure 22b).

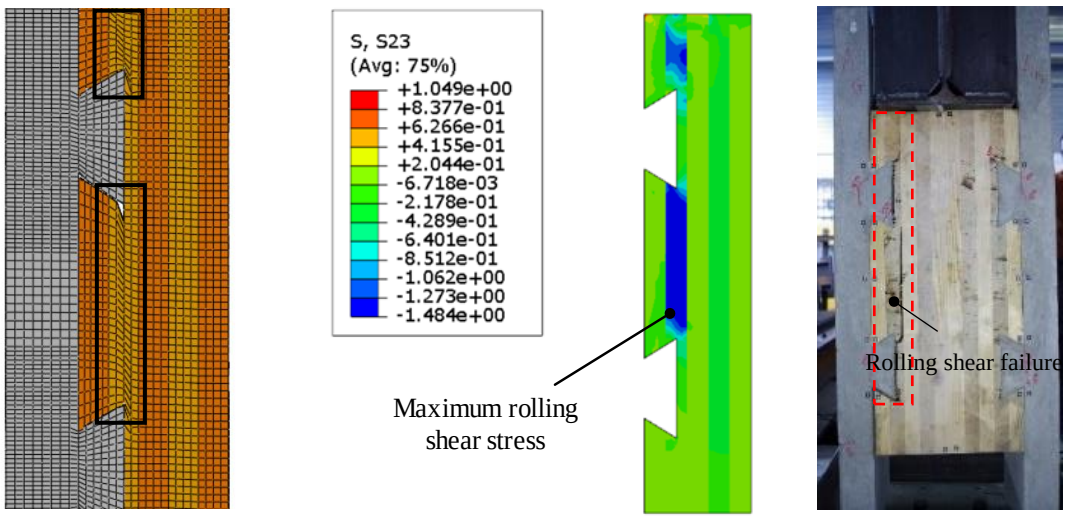

a. Deformed shape in FE model b. Rolling shear stress in FE model c. Failure mode in experiments

Figure 22: Rolling shear failure of the CLT panel in the numerical simulation and experimental tests.

In terms of force-slip curves, relative slips of both experimental tests and FE model were extracted from the same location along the interface layer between the concrete panel and the first layer of the CLT panel (see Figure 23). Figure 24a presents the comparison of force-slip curves obtained from the FE model and the experimental tests. It can be seen that a peak load of around 431 kN was obtained in the FE model, which is in good agreement with the experimental value with an approximately 2 percent difference. However, the behavior of the notched connector in the FE model is stiffer, as a smaller slip was obtained at the peak load compared to the experimental results. In fact, during the experimental tests, several cyclic loadings were applied, and rather frequent pauses were taken to observe the cracks in the concrete panel. This has generated additional slips that might come from the creep effect. In order to be able to compare the experimental results with the ones from the FE model, the slips caused by the cyclic loadings and by the pauses were removed from the results, obtaining the new force-slip curves illustrated in Figure 24b. It should be noticed that the modified curves of pushout tests are the mean curves of the “back face” and “front face” curves in Figure 24a. A better agreement of the curves was obtained. The comparison between the results obtained from the FE model and the ones from experimental tests are summarized in Table 10. The differences of maximum force F_{max} and corresponding slip $\delta_{F_{max}}$ were respectively 2 percent and 3 percent while higher discrepancies of slip modulus were noticed with 22 percent and 8 percent for the values at SLS and at ULS, respectively. It

is reminded that the precision of the Digital Image Correlation technique adopted in the pushout tests was 0.1 mm. Hence, the comparison was limited by this imprecision, as the connection was very stiff.

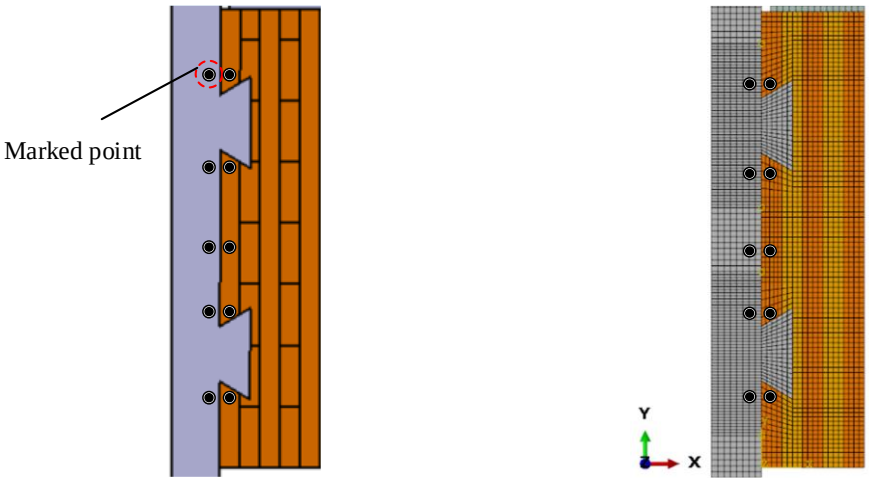

a. Experimental test b. FE model

Figure 23: Location of marked points to define the relative slip in experimental tests and FE model.

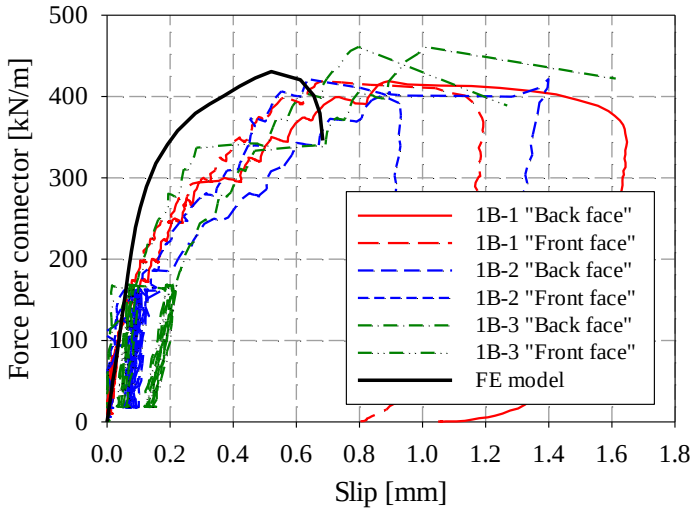

a. Original experimental force-slip curves

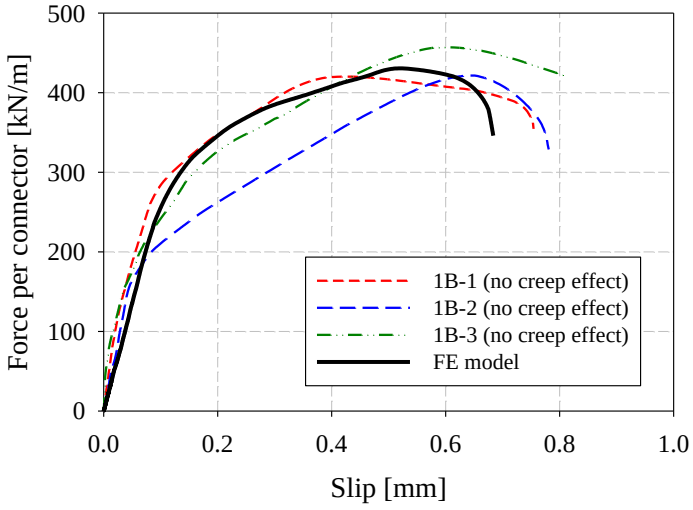

b. Modified force-slip curves

Figure 24: Comparisons of force-slip curves.

Table 10: Results of FE model and experimental tests (no creep effect).

Test	F_{max} [kN/m]	$\delta_{F_{max}}$ [mm]	K_s [N/mm/m]	K_u [N/mm/m]
1B-1	419	0.39	3.92×10^6	3.22×10^6
1B-2	421	0.65	3.13×10^6	1.40×10^6
1B-3	456	0.50	3.38×10^6	2.08×10^6
Test average	437	0.54	3.48×10^6	2.24×10^6
FEM	431	0.52	2.72×10^6	2.43×10^6
Difference	0.02	0.03	0.21	0.08

Note: Difference = |FEM-Test average|/test average.

In the FE model, concrete tensile damages were initiated at both notched connectors at a load level of approximately 350 kN (see Figure 25a). Subsequently, the damage gradually propagated from the upper to lower corner of both notched connectors when the load increased (see Figure 25b). At the maximum load level, the damages of the concrete developed around the notched connectors were consistent with cracks observed in experimental tests (see Figure 25c).

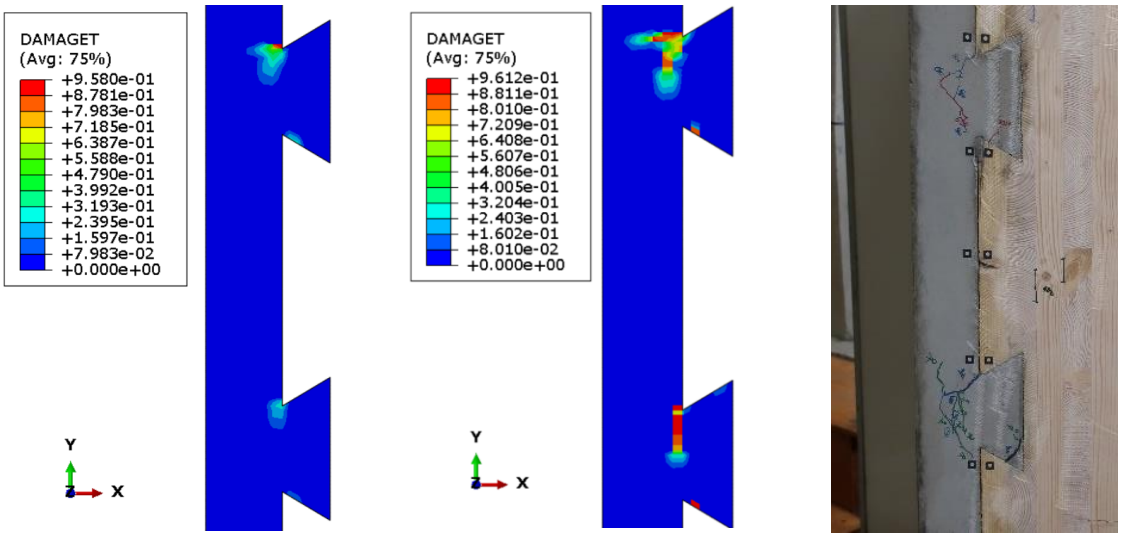

a. Tensile damage at a load level of 350 kN

b. Tensile damage at a maximum load level

c. Cracks in experimental tests

Figure 25: Tensile damage evolution of the concrete panel in the FE model and cracks observed in experimental tests.

Figure 26a depicts the principal stress map of the concrete panel. The load was transferred to the concrete slab via the top oblique surfaces of both notched connectors with the highest compressive stress concentrated at the support of the concrete panel and at the lower corners between both notches and concrete slab. The maximum stress obtained in compression was 45 MPa, and in tension, it was 2.6 MPa, respectively. The maximum stress in compression was found at the lower corner of the lower notched connector, while maximum stress in tension was located at the shear plane of the notched connector where damage was initiated.

The longitudinal and V-shape reinforcements placed inside the concrete panel were also investigated. The results indicated that the longitudinal reinforcements remained in an elastic behavior with a maximum stress of approximately 90 MPa in compression and 60 MPa in tension at the maximum

load level (see Figure 26b). In contrast, the V-shape rebars placed inside notched connector were subjected to higher stresses. The highest tensile stresses of the V-shape rebars (see Figure 26c) were approximately 167 MPa and 221 MPa for the upper and the lower notched connectors, respectively, while the compressive stresses were little compared to the tensile stress.

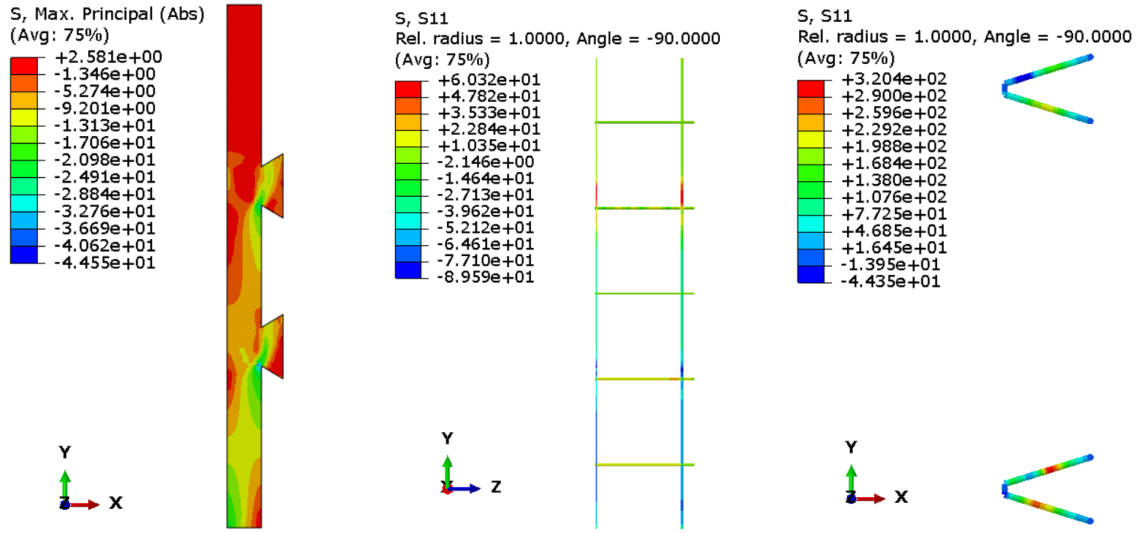

a. Principal stress map in concrete panel

b. Stresses on longitudinal reinforcement

c. Stresses on V-shape reinforcements

Figure 26: Principal stress map in the concrete panel and stresses in reinforcements inside the concrete panel at a maximum load level.

In the lower notched connector, more tensile damage was observed. When the damage in concrete was initiated, a portion of load was then transferred by means of V-shape rebars (placed inside the lower notched connector) in order to maintain the structural performance of the connection system. This resulted in higher tensile stresses of the V-shape rebars as more tensile damage was exhibited, as illustrated in Figure 25b and Figure 26c.

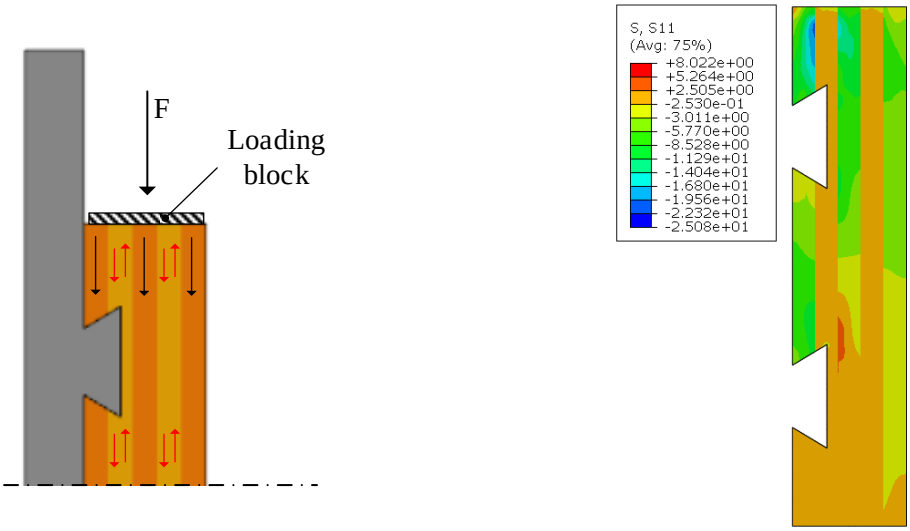

a. Load transfer mechanism from loading block to the concrete panel

b. Compressive normal stress in longitudinal direction of the CLT panel

Figure 27: Load transfer mechanism in the pushout test and compressive normal stress of longitudinal timber at a maximum load level.

Concerning the loading block in the pushout test setup, covering almost the entire top surface of the CLT panel, a portion of the load was directly transferred from the loading block to the concrete notch in form of compressive force through the outer longitudinal timber, while the remaining load was transmitted via rolling shear action of the cross-layers of the CLT panel. Thus, the whole load is not transferred to the notch by rolling shear action of the second layer of the CLT panel. Figure 27 illustrates the load transfer mechanism from the loading block and timber parallel to grain that acts directly on the upper notched connector. The effect of the configuration of steel loading block is investigated in the following section.

3.4.2.2 Effect of steel loading block configuration

To better understand the rolling shear effect in the load transfer mechanism, the experimental loading block was adjusted as presented in Figure 28. This new loading block configuration, which covered only the three middle layers of the CLT panel is denoted as “middle loading block”. The establishment of a new FE model including material properties, contacts, and boundary conditions was consistent with the pushout test model made in section 3.4.1 except for the loading block geometry. To facilitate the presentation of the finding, “Exp.” and “Mid.” refer to the configuration of experimental loading block and the middle loading block, respectively. Additionally, cases “C-Ref” and “C-Ref.M” denote the pushout test simulation with Exp. and Mid. loading configurations, respectively.

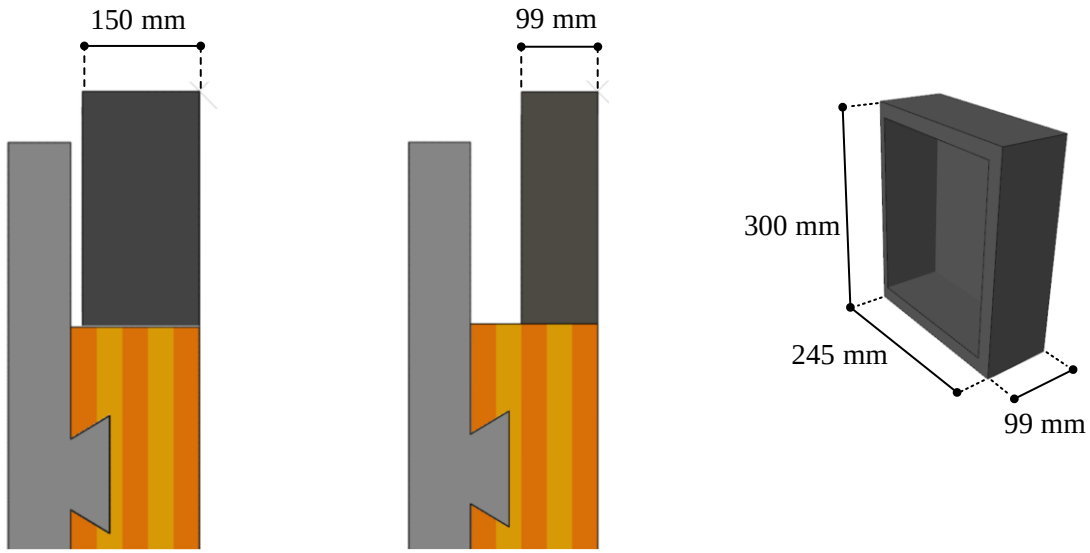

a. Experimental loading block (Exp. block, C-Ref case)

b. Middle loading block (Mid. block, C-Ref.M case)

c. Dimensions of middle loading block

Figure 28: A new FE model with middle loading block configuration.

From the numerical simulation of case C-Ref.M, it was seen that the failure mechanism of the specimen was governed by the rolling shear resistance of the cross-layer of the CLT panel (see Figure 29) at a maximum load level of 269 kN with a corresponding slip of 0.29 mm. Compared to the case C-Ref, the maximum force and corresponding slip were reduced by about 38 percent and 45 percent, respectively, whereas the slip modulus was decreased by 37 percent at both SLS and ULS. Besides, little ductility was obtained with an ultimate slip of approximately 0.9 mm at the end of the FE simulation corresponding to 74 percent of F_{max} (see Figure 29a). Table 11 summarizes numerical results of C-Ref and C-Ref.M cases.

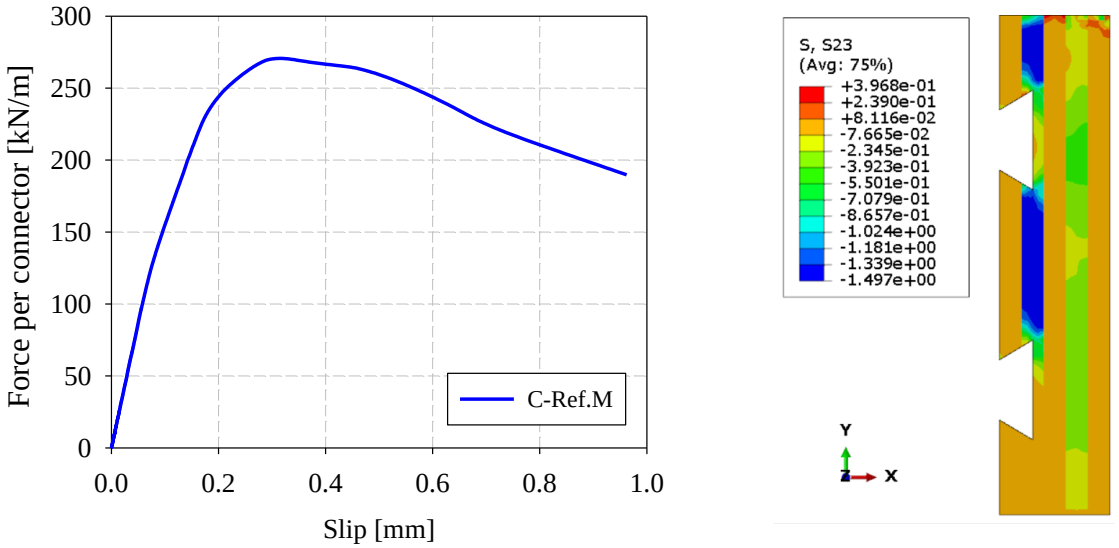

a. Force-slip curve b. Rolling shear stress of CLT panel

Figure 29: Force-slip curve and rolling shear stress obtained in the FE model of the case C-Ref.M.

Table 11: Results of FE model between C-Ref and C-Ref.M cases.

Case	F_{max} [kN/m]	$\delta_{F_{max}}$ [mm]	K_s [N/mm/m]	K_u [N/mm/m]
C-Ref	431	0.52	2.72×10^6	2.43×10^6
C-Ref.M	269	0.29	1.71×10^6	1.52×10^6
Difference	0.38	0.45	0.37	0.37

Note: Difference = | C-Ref.M – C-Ref |/ C-Ref

High tensile damage of the concrete and high tensile stresses of the V-shape rebars were observed only in the lower notched connector while the upper notched connector remained undamaged at the maximum load level (see Figure 30). The V-shape rebars were subjected to the maximum tensile stress of approximately 173 MPa and 5 MPa in the lower and upper notched connectors, respectively.

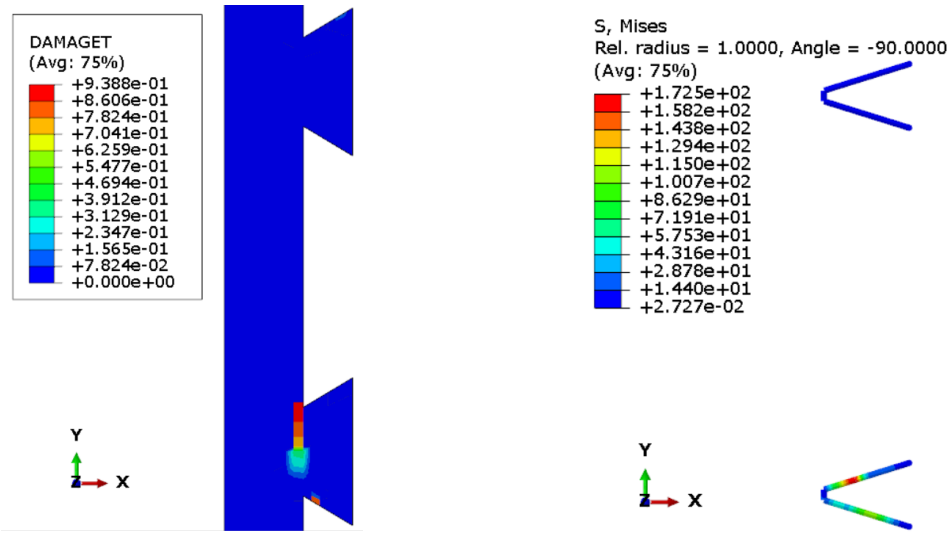

a. Tensile damage b. Tensile stresses of V-shape rebars

Figure 30: Tensile damage and tensile stresses of V-shape rebars at a maximum load level.

In conclusion, when adopting the middle loading block configuration in the C-Ref.M case for the investigation of rolling shear effect, the maximum force was limited by the rolling shear failure at a load level of 269 kN, accounting for 38 percent decrease compared to the C-Ref case. The slip moduli at both SLS and ULS were also decreased by 37 percent in comparison to the C-Ref case. No ductility was observed in the post-peak loading as the failure mode was governed by the rolling shear resistance of the CLT panel. It should be noted that, when loading is applied to the CLT-concrete composite floor, the whole CLT section will be subjected to the applied load, resulting in transferring a portion of load via a longitudinal layer of the CLT panel and the rest by rolling shear. Therefore, the resistance and stiffness obtained in C-Ref case with experimental loading configuration should be adopted to define the bending stiffness of the CLT-concrete composite floor.

3.4.2.3 Effect of timber Poisson ratios

In this study, the Poisson ratios of timber in all directions were assumed to be zero as recommended in Eurocode 5 [9]. However, various values of Poisson ratios were reported in the literature [37], [38], [39]. Xu et al. [37] conducted a numerical simulation of the embedding strength of glued laminated timber (resistance class GL28h). This glulam had Poisson ratios of v_{12}= v_{13}=0.41 and v_{23}=0.02. In addition, Guan et al. [38] studied and modelled an anisotropic elasto-plastic timber using the finite element program. Timber in tension and in compression were modelled as linear orthotropic elastic and elasto-plastic material, respectively. In their study, the timber Poisson ratios were taken as 0.47, 0.37, and 0.25 for v_{12}, v_{13}, and v_{23} respectively. A good agreement between experimental results and FE simulations was obtained by adopting the value of mentioned Poisson ratios. Furthermore, Oudjene et al. [39] investigated the elasto-plastic behavior of the spruce wood under the compression loading by adopting Poisson ratios obtained from the uniaxial compression tests on the specimens of timber parallel to grain. From the experimental data, the material parameters for orthotropic elastic properties (E_1, E_2, v_{12}, v_{21}) were determined. The value of v_{12} was equal to 0.29, while the value of v_{13} and v_{23} were determined using the relation below:

$$E_i v_{ji} = E_j v_{ij} \tag{11}$$

where $i \neq j$; and i,j=1,2,3. According to eq. (11), Poisson ratios v_{13} and v_{23} were found to be 0.29 and 0.036, respectively. It should be noted that no distinction of material parameters between radial and tangential directions due to the assumption in orthotropic behavior of the timber.

Table 12 summarizes the parameters of the timber Poisson ratios derived from the literature [37], [38], [39] and their results obtained from the model of C-Ref case. The value in brackets is the ratio between the maximum force of different Poisson ratios and that of Poisson ratios of zero. The maximum forces obtained from the FE model ranged from 412 kN to 428 kN with the failure mode in all cases governed by the rolling shear failure of the cross-layer of the CLT panel. Compared to the C-Ref case, a maximum difference regarding the maximum force was around 4 percent, indicating a small influence of the timber Poisson ratios on the behavior of the notched connection. The case with higher values of the Poisson ratio in tangential-radial plane v_{23} (Guan et al. [38]) resulted in lower maximum forces compared to the cases with close-to-zero values of the Poisson ratio in that direction. In terms of the trend of force-slip curves (Figure 31), no changes were noticed until reaching the onset of the failure at the load level of approximately 400 kN. From this study, when the value of the timber Poisson ratio in

tangential-radial plane v_{23} was taken almost zero, a little influence was observed in comparison to the C-Ref case. Such an influence was linked to the fact that the failure of the model was governed by the rolling shear failure mechanism, generating high deformation in the tangential-radial plane. However, a limited difference of only around 4 percent was observed.

Table 12: Result obtained from using different Poisson ratios in numerical study.

Case	Wood type	v_{12}	v_{13}	v_{23}	F_{max} [kN]
C-Ref	--	0	0	0	431 (1.00)
Xu et al. [37]	GLT	0.41	0.41	0.02	428 (0.99)
Guan et al. [38]	--	0.47	0.37	0.25	412 (0.96)
Oudjene et al. [39]	Spruce wood	0.29	0.29	0.036	428 (0.99)

Note: 1, 2, and 3 refer to longitudinal direction, tangential direction, and radial direction, respectively.

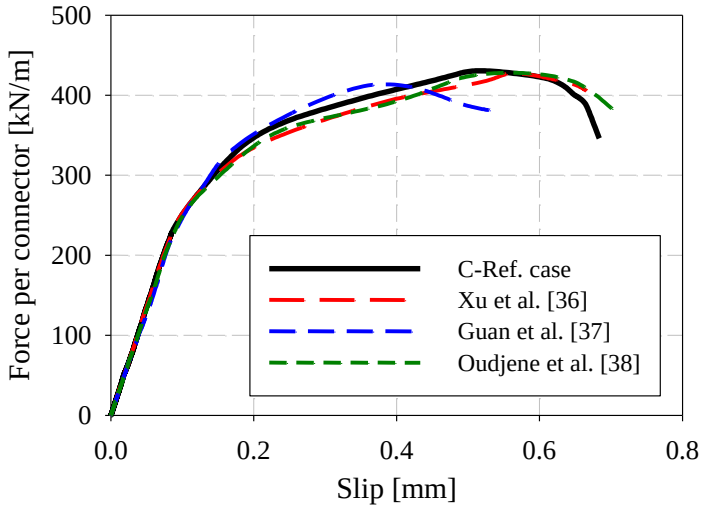

Figure 31: Slip-force curves for cases with different values of Poisson ratios.

3.4.2.4 Effect of friction coefficient at the interface layer

During the specimen fabrication, the concrete was cast directly onto the CLT panel without any painting or plastic film at the interface layer to reduce the friction. Consequently, it could be expected that a portion of loads could be transferred from the timber to the concrete panel by the friction effect. To investigate this effect, a finite element (FE) model of the C-Ref case was employed. The friction coefficient was taken as 0.62, which was the value obtained from experimental friction tests by Aira et al. [33]. This value was adopted by many studies such as [40], [41], and [42]. The results obtained from the numerical simulation of the C-Ref case were found to be in close agreement with the experimental test results. However, according to Eurocode 5 [28], the design value of static friction coefficient between wood and concrete layers should be taken as μ=0.4. Accordingly, a new numerical simulation was made with this value (μ=0.4). For the further investigation of the friction effect, a case with no friction behavior (μ=0) was also included.

Table 13 summarizes the results obtained from the numerical simulations and Figure 32 shows the force-slip curves of the FE model under the influence of different friction coefficients. The value shown

in brackets in Table 13 is the ratio of the results obtained in each study to those of the C-Ref case while RS and CS denote the rolling shear of the CLT panel and concrete shear of the concrete notched connector.

Table 13: Result obtained from the numerical study of different friction coefficients.

Case	Friction Coef.	F_{max} [kN/m]	g_{Fmax} [mm]	K_s [N/mm/m]	K_u [N/mm/m]	Failure mode
C-Ref	0.62	431	0.52	2.73×10^6	2.43×10^6	RS
Eurocode 5	0.40	421 (0.98)	0.78	2.31×10^6 (0.85)	1.90×10^6 (0.78)	RS+CS
No friction	0	339 (0.79)	1.80	1.40×10^6 (0.51)	0.81×10^6 (0.33)	CS

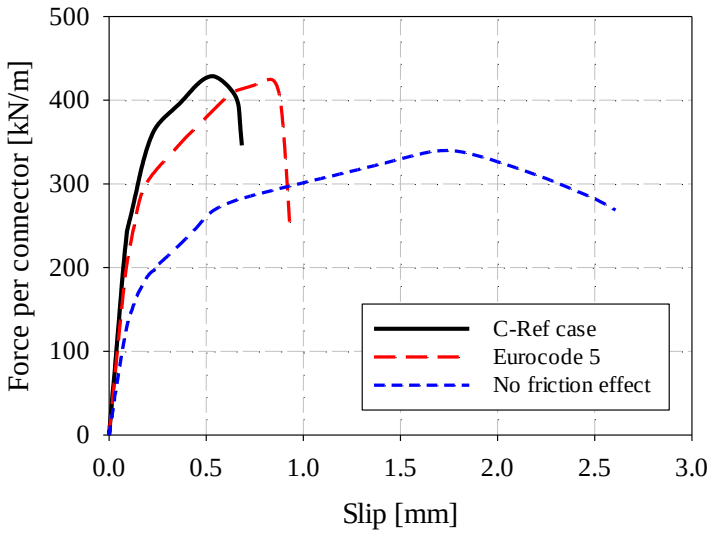

Figure 32: Force-slip curves of numerical simulations under different friction coefficients.

In overall, the findings indicated that a lower friction coefficient led to lower strength and stiffness of the connection system. The use of a friction coefficient of 0.4 recommended in Eurocode 5 showed only a 2 percent decrease in connection resistance compared to the C-Ref case with a friction coefficient of 0.62. However, the slip modulus was reduced by 15 percent at the serviceability limit state and 22 percent at the ultimate limit state. The failure mode was governed by the rolling shear failure of the CLT panel, followed by the shear failure of the concrete notch in the lower notched connection. Figure 33a presents the rolling shear stress of the CLT panel and the tensile damage of the concrete panel as well as the stresses in V-shape rebars placed inside the lower notch. On the other hand, when a zero-friction coefficient was adopted, a significant drop in strength by 21 percent was obtained. In addition, slip moduli at the serviceability and the ultimate limit states decreased by 49 percent and 71 percent, respectively. The failure mode was limited by the concrete shear resistance at the maximum load level of 339 kN. Figure 33b presents the tensile damage of the concrete panel at the maximum load level and tensile stresses in V-shape rebars at both notched connectors.

In terms of ductility, the case without any friction exhibited better post-peak performance, with a total slip of approximately 2.5 mm at the end of the simulation corresponding $0.93F_{max}$, while cases with the friction coefficient of 0.62 and 0.4 showed limited ductility. This could be explained by the obtained failure mechanism of the connection system. The failure mode induced by the rolling shear resistance of the cross-layer of the CLT panel limited the ductility in the post-peak loading stage as a sudden

collapse of the specimen was experienced. In contrast, when the failure mode was governed by the concrete shear at the shear plane of the concrete notch, better ductility was observed.

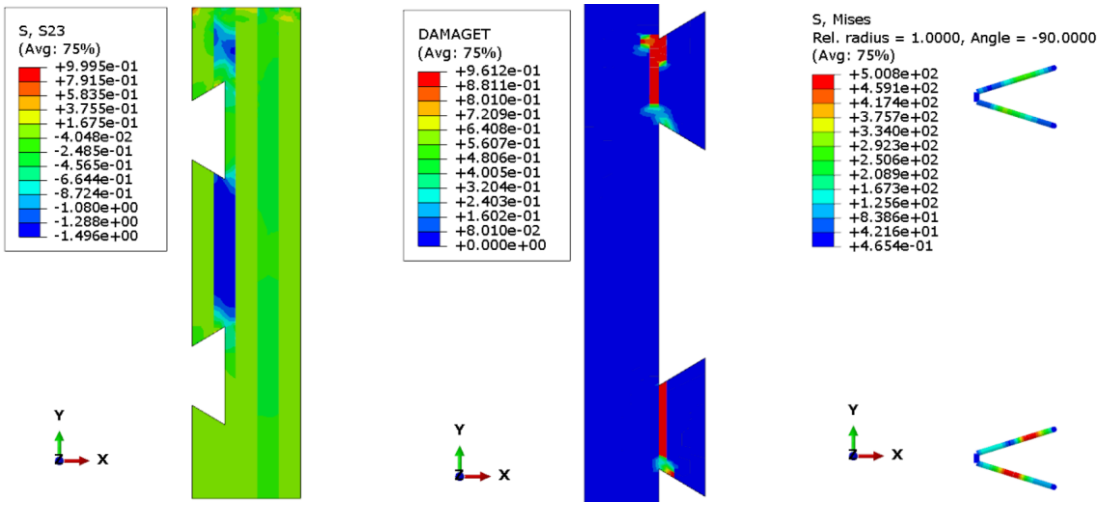

i. Rolling shear stress of the CLT panel

ii. Tensile damage of the concrete panel

iii. Tensile stresses of V-shape rebars

a. Friction coefficient of 0.4

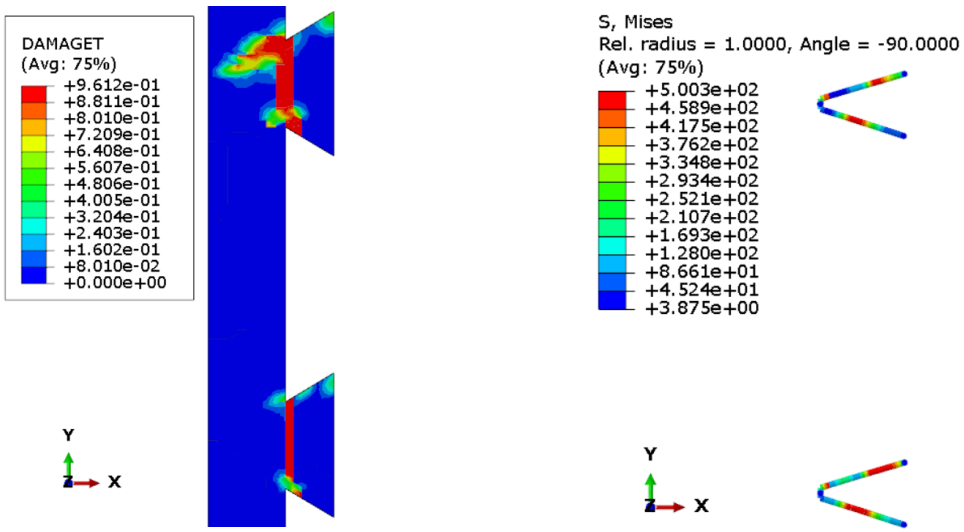

i. Tensile damage of the concrete panel

ii. Tensile stresses of V-shape rebars

b. Friction coefficient of zero

Figure 33: Failure mode and stress of components in FE models under various friction coefficients at a maximum load level.

Figure 34 illustrates the contact area at the interface between the concrete and the CLT panels, where the load was distributed in the form of contact normal force (Figure 34a) and contact friction force (Figure 34b) on the concrete panel. In the case of no friction effect (coefficient of zero), as expected, no contact friction force was applied to the concrete surface between concrete and CLT panels, and the contact normal forces appeared only on the top and lateral surfaces of both concrete notches. By applying friction coefficients, new contact areas on the concrete panel above the top of the upper concrete notch were exposed.

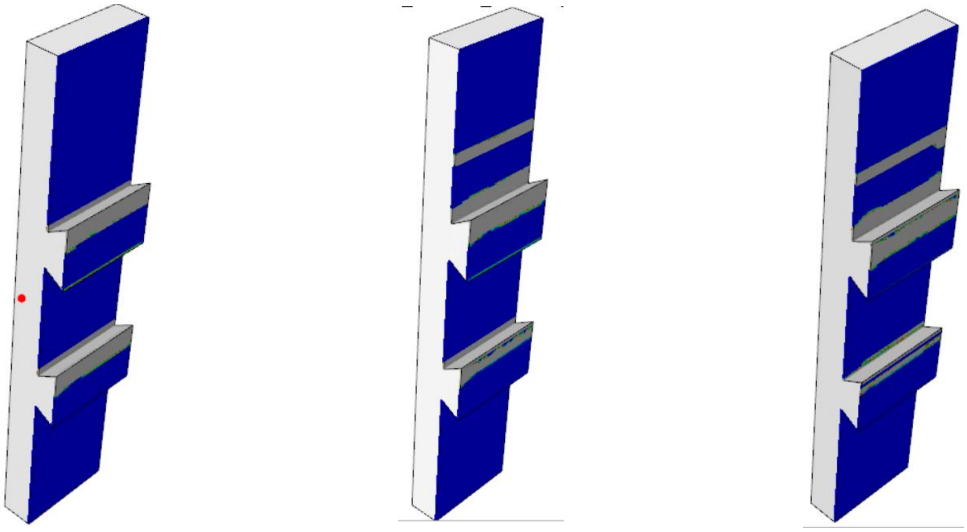

i. Friction coefficient of zero ii. Eurocode 5 iii. Exp. case

a. Contact normal force

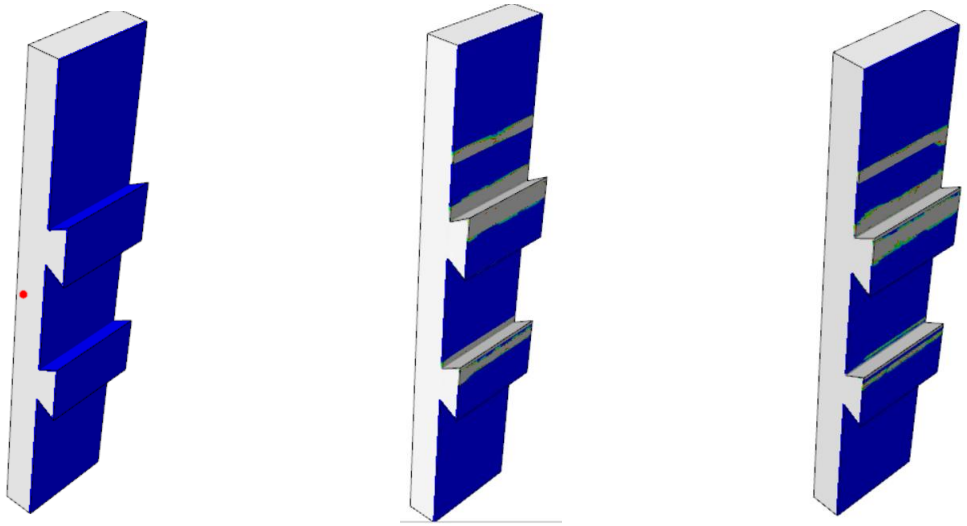

i. Friction coefficient of zero ii. Eurocode 5 iii. Exp. case

b. Contact friction force

Figure 34: Contact areas on the concrete panel for cases with different friction coefficients at a maximum load level.

In this study, the results of the numerical simulation with the friction coefficient of 0.62 [33] corresponded well to the experimental results. However, when using the value of friction coefficient of 0.4 recommended in Eurocode 5 [28], a small difference of 2 percent was obtained in terms of maximum force, and 15 percent lower in the slip modulus in comparison to the case with coefficient of 0.62.

3.4.2.5 Conclusion on the validation of finite element model

The developed FE model was successfully validated against the experimental pushout tests with a close correlation of the maximum load level, force-slip curve, failure mechanism, and slip moduli. In the FE model, the friction coefficient between concrete and timber of 0.62 recommended in the literature [33] and value of Poisson ratios of zero in accordance with Eurocode 5 [28] were adopted. Various other values of Poisson ratios of timber and friction coefficient at the interface from the literature were also considered in the FE model in order to study the effect of these parameters. The changes of timber

Poisson ratios had a small influence on the results of the numerical simulation. Differently, the study of the friction effect demonstrated that using a lower friction coefficient led to lower strength and slip moduli. With the friction coefficient of 0.40 in accordance with Eurocode 5 [28], the FE model provided similar results in terms of maximum force and 15 percent lower in the slip modulus in comparison to the C-Ref case. However, a better correlation with experimental tests was obtained when adopting the friction coefficient of 0.62, using in C-Ref case.

Even if the failure of the specimen was caused by the rolling shear resistance of the cross-layer of the CLT panel, the whole load was not transferred by the cross-layer as a portion of the loading was contributed from the loading block to the concrete notch through the outer longitudinal layer of the CLT panel in form of the compressive stress. Consequently, a new model of pushout test with configuration of middle loading block (C-Ref.M case) was made in order to study the load transfer mechanism from the timber to the concrete panel by pure rolling shear action. The findings showed that, by adopting the middle loading block, the maximum force decreased by 38 percent while the slip modulus at SLS and ULS decreased by 37 percent in comparison to the C-Ref case. However, the resistance and stiffness obtained in C-Ref case with experimental loading configuration should be adopted to define the bending stiffness of the CLT-concrete composite floor due to the actual behavior of load transfer mechanism from CLT panel to concrete panel.

3.5 Parametric study

The parametric study was conducted using the FE model with friction coefficient between concrete and timber panels of 0.62 and timber Poisson ratios of zero, for both Exp. and Mid. cases, to gain a thorough understanding of the mechanical behavior and to predict the possible failure mechanisms of the notched connection system under the influence of various parameters. In addition, the results of the parametric study provide useful information for the optimization of the connection system with regard to geometries and material properties. The determined parameters and the obtained results as well as the summary of the parametric study are described in the following subsections. For a better comparison, the pure rolling shear-carrying capacity of the parametric study of Mid. cases (pushout model with the middle loading block configuration) are discussed and compared in the summary section (section 3.5.8).

3.5.1 Studied parameters

In the parametric study, six different parameters were considered, including the concrete strength f_c, the thickness of the concrete panel h_c, the heel length of the CLT panel l_t, the notch length l_n, the notch depth d_n, and the cross-sectional area of the V-shape rebars reinforcement inside the notched connection system A_s (see Figure 35). The material properties and geometries of the CLT panel (mechanical properties and thickness) were not changed, as they were fixed in the industrial process. Additionally, the notched angle of 59.04^0 was kept unchanged to maintain the notched shape, while the V-shape rebars were adjusted to fit inside the notched connector.

As a reminder, in the parametric study, “C-Ref” case was used as the reference case for the study of Exp. cases, while “C-Ref.M” case was used as the reference case of the study of Mid. cases. The values of the parameters are detailed in Table 14.

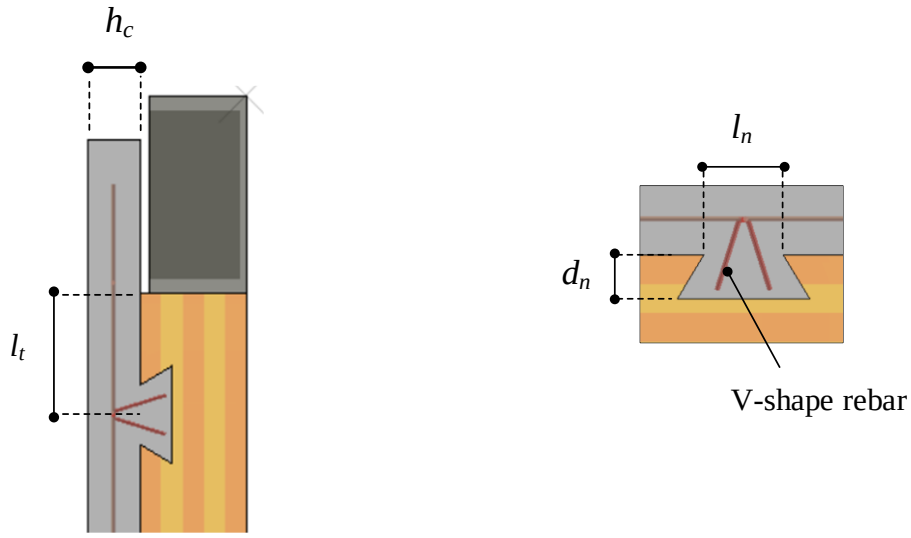

Figure 35 : Studied parameters in the FE model of the pushout specimen.

Table 14: Summary of the studied parameters.

Parametric study			f_c [MPa]	h_c [mm]	l_t [mm]	l_n [mm]	d_n [mm]	A_s [mm^2]
Case	Exp.	Mid.						
Reference	C-Ref	C-Ref.M	35	80	187.5	90	50	141.37
C1	C1-1	C1-1M	25	80	187.5	90	50	141.37
	C1-2	C1-2M	45					
C2	C2-1	C2-1M	35	50				
	C2-2	C2-2M		100				
C3	C3-1	C3-1M		80	375			
C4	C4-1	C4-1M			187.5	40		
	C4-2	C4-2M				140		
C5	C5-1	C5-1M				90	25	
C6	C6-1	C6-1M					50	0
	C6-2	C6-2M						56.55

The case series C1 investigated the influence of concrete strength taking a value of 25 MPa (case C1-1) and 45 MPa (case C1-2) in addition to the value in experimental tests (f_c=35MPa). The thickness of the concrete panel was varied between 50 mm (case C2-1) and 100 mm (case C2-2) in the second case series C2. In case series C3, the heel length of 375 mm (case C3-1) was adopted, corresponding to the spacing of the notched connector to compare with the reference case having a value of 187.5 mm. The investigations of notch lengths of 40 mm (case C4-1) and 140 mm (case C4-2) were conducted in case series C4. The case with the notch length of 40 mm was expected to develop a failure mode caused by concrete shear, as the shear resistance of the concrete notch should be reduced with a smaller notch length. In case series C5, a notch depth of 25 mm was adopted, so that the notch was found located

solely in the first layer of the CLT panel. This case should increase the rolling shear resistance, as the whole rolling shear cross-section will contribute to transferring the applied force to the connectors. Finally, the influence of the cross-sectional area of V-shape reinforcement in the notched connector (case series C6) was investigated. Based on experimental tests, none of the rebars placed inside the notched connector experienced yielding when the connection system failed. Therefore, the parametric study of case series C6 was set to decrease the number of V-shape rebars in order to provoke the yielding of shear reinforcement. The number of V-shape rebars was decreased from 5 rebars with a cross-sectional area of 141.37 mm^2 in reference case to 2 rebars with a cross-sectional area of 56.55 mm^2 in case C6-1 and to zero rebar (0 mm^2) in case C6-2. It should be noted that cases with "M" refers to the cases with middle loading configuration of Mid. cases.

3.5.2 Influence of concrete strength

To evaluate the influence of concrete strength on the notched connector behavior, normal concrete with strength of 25 MPa and 45 MPa were adopted for the case series C1. The tensile strength, as well as the modulus of elasticity were determined in relation to the value of the adopted concrete strength as described in Eurocode 2 [25].

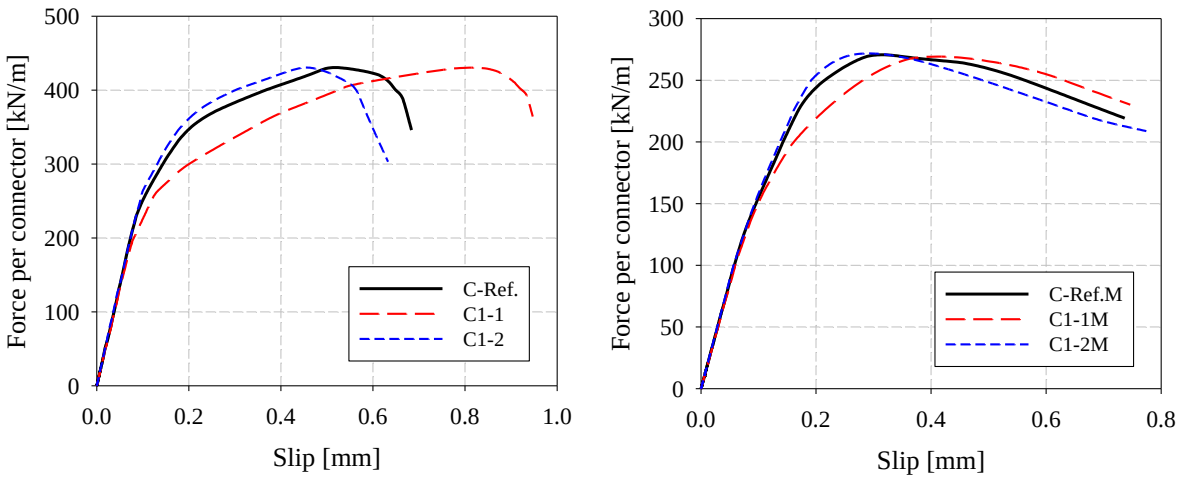

a. Exp. cases b. Mid. cases

Figure 36: Force-slip curves of case series C1.

Table 15: Results obtained from case series C1 for Exp. cases.

Case	f_c [MPa]	f_t [MPa]	F_{max} [kN]	δ_{Fmax} [mm]	σ_{Rebar} [MPa]	K_s [N/mm/m]	K_u [N/mm/m]	Failure mode
C-Ref	35	1.99	431	0.52	321	2.73×10^6	2.43×10^6	RS
C1-1	25	2.71	429 (1.00)	0.78	365	2.58×10^6 (0.95)	2.03×10^6 (0.84)	RS
C1-2	45	3.35	430 (1.00)	0.45	202	2.73×10^6 (1.00)	2.63×10^6 (1.08)	RS

Force-slip curves of case series C1 in the experimental loading configuration (Exp. cases) are presented in Figure 36a. It can be inferred from these results that concrete strength had a little effect on the resistance of the composite specimen, as the failure mode was governed by rolling shear failure of CLT panel. In Table 15, the results obtained from numerical simulations are summarized. The value in

brackets indicates the ratio of the results obtained from the parametric study to the ones of the reference case (C-Ref case). A difference of the maximum force of about 1 percent was obtained by changing the concrete strength from 25 MPa to 35 MPa or from 35 MPa to 45 MPa. In addition, the slip moduli at SLS and ULS were reduced by 5 percent and 16 percent, respectively, comparing case C1-1 to case C-Ref, and were improved by around 1 percent and 8 percent, respectively, comparing case C1-2 to case C-Ref. From Figure 36a, all curves exhibited a similar initial slope from the beginning to the load level of approximately 200 kN, whereas cases C-Ref and C1-2 continued a similar behavior until reaching the maximum force. The influence of concrete strength on the stiffness of the connection system can be explained by the intensity of tensile damage that happened in the concrete notch as shown in Figure 37. It was found that higher concrete strength generated less damage in the concrete notch at the maximum load level. Higher tensile stresses of V-shape rebars were also observed in more severe damage location of the notched connector. The maximum tensile stresses of V-shape rebars ranged from 202 MPa to 365 MPa at the maximum load level. As failures were governed by rolling shear of CLT panel, the ductility in post-peak performance was limited.

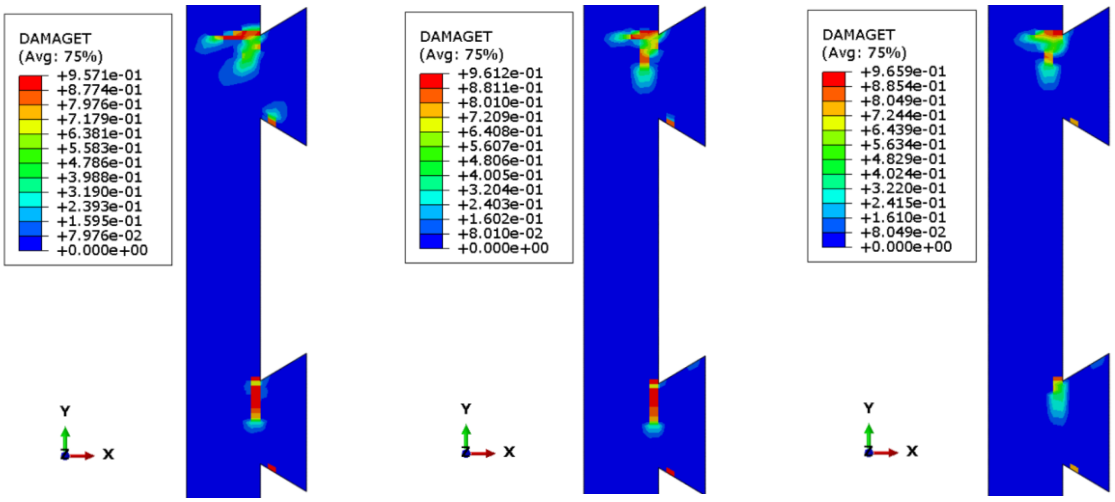

a. Case C1-1 b. Reference case (C-Ref) c. Case C1-2

Figure 37: Tensile damage of the concrete panel in case series C1 at the maximum load level.

The results of case series C1 for the middle loading configuration are summarized in Figure 36b and Table 16. The maximum force in all cases was approximately 269 kN with a failure mode governed by the rolling shear resistance of the cross-layer of the CLT panel. The difference in slip moduli was minimal with a maximum difference of 4 percent. In Figure 36b, all curves were comparable in the initial stiffness until reaching the load level of 150 kN. The use of the lower concrete strength resulted in higher slip. In overall, the differences were small when adopting the middle loading block configuration to study the influence of concrete strength.

Table 16: Results obtained from case series C1 for Mid. cases.

Case	f_c [MPa]	f_t [MPa]	F_{max} [kN]	δ_{Fmax} [mm]	σ_{Rebar} [MPa]	K_s [N/mm/m]	K_u [N/mm/m]	Failure mode
C-Ref.M	35	1.99	269	0.29	173	1.71×10^6	1.52×10^6	RS
C1-1M	25	2.71	268 (0.99)	0.36	232	1.66×10^6 (0.97)	1.45×10^6 (0.96)	RS
C1-2M	45	3.35	270 (1.00)	0.26	66	1.73×10^6 (1.01)	1.56×10^6 (1.03)	RS

From numerical results, the variation of concrete strength had limited influence on maximum force, as rolling shear failure was still obtained in the CLT panel. However, when using lower concrete strength, higher damage in concrete notches was observed, resulting in higher slip at the maximum load level and lower stiffness of the notched connection system.

3.5.3 Influence of concrete thickness

Concrete slab thicknesses of 50 mm and of 100 mm were adopted in case series C2. It should be noted that the concrete thickness of 50 mm was the practical lower bound while the concrete thickness of 100 mm was the practical upper bound found in practice of timber-concrete composite floor [43].

Figure 38a and Table 17 present the results obtained from case series C2 for Exp. cases. Once again, the failure mode in this series was governed by rolling shear failure of CLT panel, obtained at a maximum force in a range of 3 percent difference in comparison to the C-Ref case. For slip moduli at SLS and ULS, the difference ranged from 21 percent lower to 8 percent higher compared to the C-Ref case. When the concrete slab thickness was changed from 80 mm to 50 mm in case C2-1, the notched connector behaved less stiff by approximately 21 percent and 19 percent at SLS and ULS, respectively. However, the increase of the thickness of the concrete slab from 80 mm to 100 mm in case C2-2 resulted in higher slip moduli for about 5 percent and 8 percent at SLS and ULS, respectively. It should be noted that early damage in concrete and higher tensile stress of V-shape rebars were typically observed in the lower notched connector in all cases. In addition, no ductility in post-peak performance was noticed as the failure was controlled by rolling shear resistance of CLT panel.

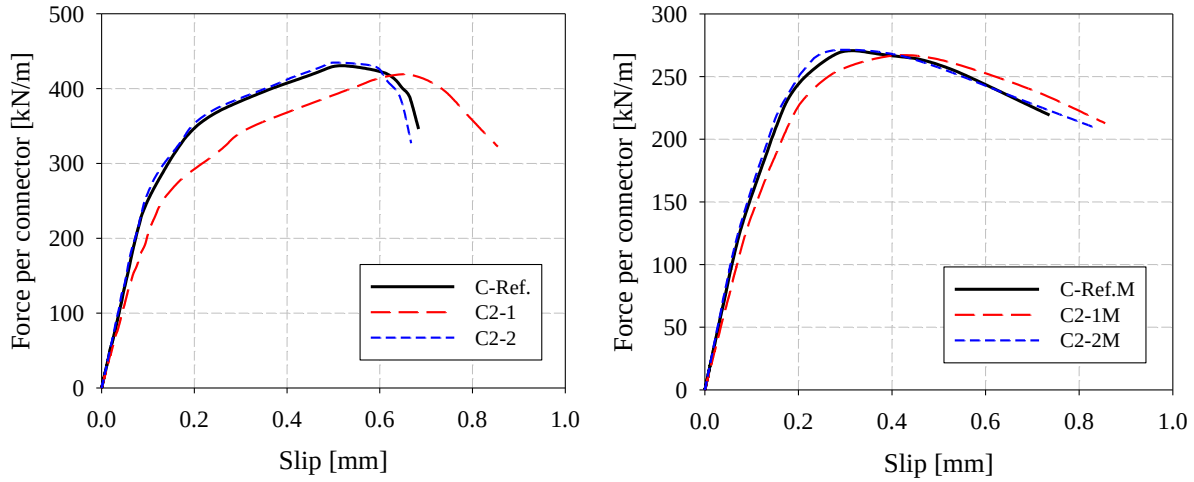

a. Exp. cases b. Mid. cases

Figure 38: Force-slip curves of case series C2.

Table 17: Results obtained from case series C2 for Exp. cases.

Case	h_c [mm]	F_{max} [kN]	δ_{Fmax} [mm]	σ_{Rebar} [MPa]	K_s [N/mm/m]	K_u [N/mm/m]	Failure mode
C-Ref	80	431	0.52	321	2.73×10^6	2.43×10^6	RS
C2-1	50	419 (0.97)	0.66	355	2.17×10^6 (0.79)	1.96×10^6 (0.81)	RS
C2-2	100	435 (1.01)	0.48	285	2.87×10^6 (1.05)	2.62×10^6 (1.08)	RS

Figure 38b and Table 18 report the results of case series C2 for Mid. cases. Comparable force-slip curves and failure mode were obtained in comparison to the C-Ref.M case. Similar to results obtained in simulations of Exp. cases, the curve of case C2-1M exhibited a lower slope than the other cases (C-Ref.M and C2-2M) which was contributed by the earlier damage of the concrete slab. A marginal deviation in slip moduli of approximately 15 percent and 13 percent lower was noticed at SLS and ULS, respectively. For case C2-2M, when the concrete thickness was increased, slip moduli were also increased by 5 percent at both limit states. As the failure occurred in the cross-layer of the CLT panel, no ductility was noticed in post-peak performance. In addition, the highest tensile stresses were observed in the lower notched connector of all cases, ranging from 154 MPa to 181 MPa.

Table 18: Results obtained from case series C2 for Mid. cases.

Case	h_c [mm]	F_{max} [kN]	δ_{Fmax} [mm]	σ_{Rebar} [MPa]	K_s [N/mm/m]	K_u [N/mm/m]	Failure mode
C-Ref.M	80	269	0.29	173	1.71×10^6	1.52×10^6	RS
C2-1M	50	267 (0.99)	0.40	181	1.45×10^6 (0.85)	1.32×10^6 (0.87)	RS
C2-2M	100	272 (1.01)	0.28	154	1.79×10^6 (1.05)	1.59×10^6 (1.05)	RS

From the numerical simulations of case series C2, the finding indicated that the variation of the concrete thickness had minor implication on the maximum force as the failure mode remained governing by limited rolling shear resistance in the cross-layer of the CLT panel. On the other hand, the increase of the concrete thickness resulted in higher slip moduli in a range of 20 percent compared to reference cases (C-Ref and C-Ref.M cases).

3.5.4 Influence of heel length of the CLT panel

Case series C3 investigated the influence of the heel length of the CLT panel. The increase of the heel length from 187.5 mm to 375 mm resulted in an increase in rolling shear resistance due to the enlarged cross-layer area of the CLT panel that transferred the applied load to the connectors. For Exp. cases, the failure was primarily governed by the concrete shear in the lower notched connector at the maximum load level of 526 kN and followed by the upper one, despite the rolling shear stress being high in the cross-layer of the CLT panel.

Figure 39 depicts the tensile damage in the concrete panel, rolling shear stress of the CLT panel, and V-shape rebars stresses at the maximum load level. The damage in the critical shear plane in the concrete was close to 1.0, while the V-shape rebars were experiencing the yielding stress (of 500 MPa) in the lower notched connector at the maximum load level. It can be inferred that the simulation of case C3-1 provided an estimation of the connection resistance on the concrete side with a 22 percent increase (see Table 19) in the maximum force compared to the C-Ref case.

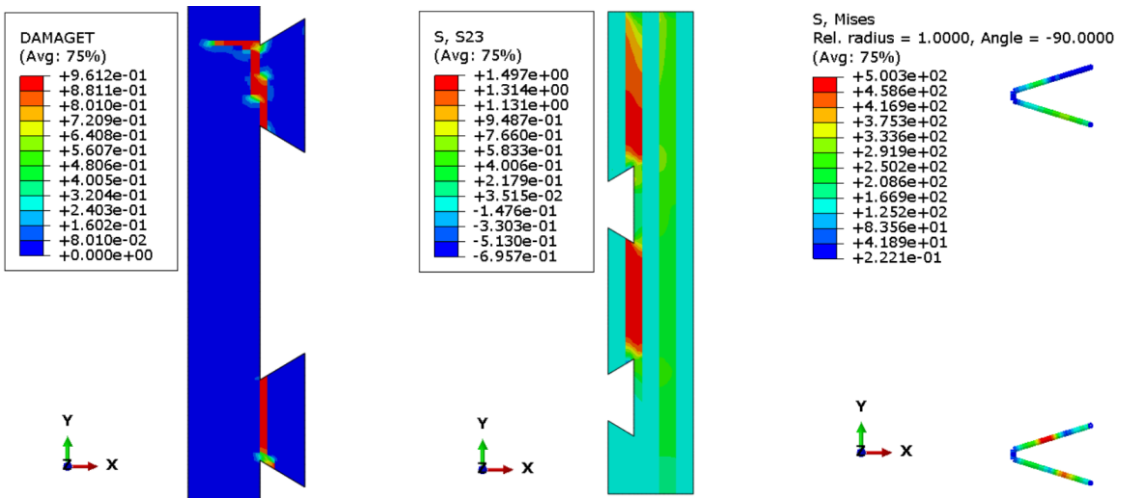

a. Tensile damage b. Rolling shear stress c. Stress of V-shape rebars

Figure 39: Tensile damage of the concrete panel, rolling shear stress of the CLT panel, and tensile stress of V-shape rebars in case C3-1 at a maximum load level.

Table 19: Results obtained from case series C3 for Exp. cases.

Case	l_t [mm]	F_{max} [kN]	δ_{Fmax} [mm]	σ_{Rebar} [MPa]	K_s [N/mm/m]	K_u [N/mm/m]	Failure mode
C-Ref	187.5	431	0.52	321	2.73×10^6	2.43×10^6	RS
C3-1	375	526 (1.22)	0.72	501	2.51×10^6 (0.92)	1.95×10^6 (0.80)	CS

The force-slip curves of cases C-Ref and C3-1 (see Figure 40a) exhibited a good agreement up to a load level of approximately 350 kN. Then, case C3-1 demonstrated stiffer behavior compared to the C-Ref case. A plateau of force-slip curve in case C3-1 was noticed, starting from 0.72 mm of slip, where the first failure of the lower notched connector was obtained and ending at 0.99 mm of slip, where the other connector failed. At this point, V-shape rebars in both notches experienced the yielding stress. It was seen that an improved ductility was noticed, as the failure was governed by the concrete shear in the notched connector. In terms of slip moduli, a decrease was noticed for Exp. cases with 8 percent and 20 percent at SLS and ULS, respectively, even if a close correlation of the force-slip curves was obtained in the initial stage. This decrease resulted from the computation method of slip moduli adopted from Cecotti [1] which considered the proportion of forces and corresponding slips at 40 percent and 60 percent of the maximum load attained. From Figure 40a, the corresponding points (40 percent and 60 percent of maximum force, F_{max}) on the force-slip curve in case C3-1 lay on more inclined curve in comparison to those of C-Ref curve, resulting in lower value of slip moduli.

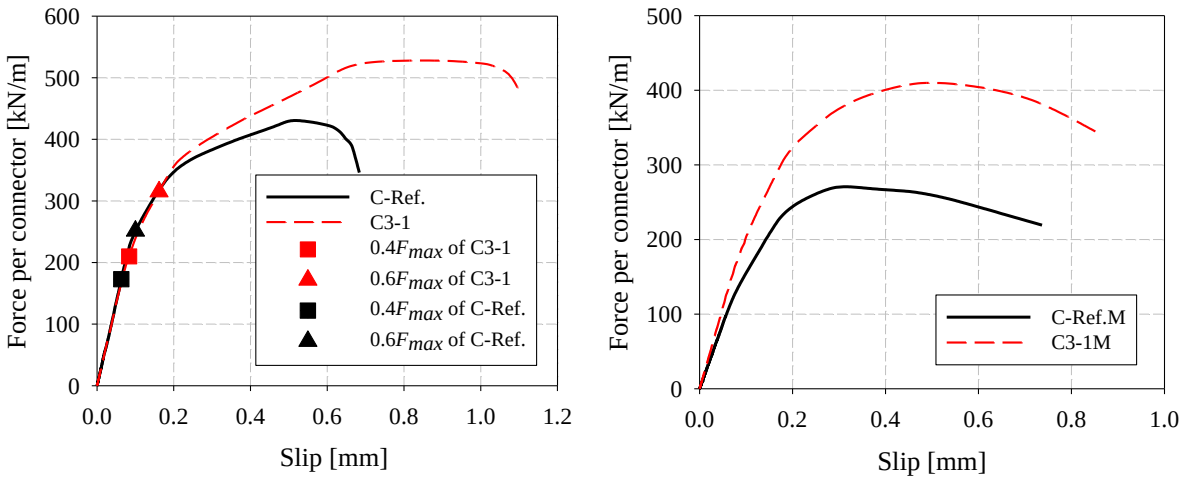

a. Exp. cases b. Mid. cases

Figure 40: Force-slip curves of case series C3.

The results of case series C3 for Mid. cases are summarized in Figure 40b and Table 20. The failure mode was governed by the rolling shear resistance of the CLT panel at a maximum load level of 410 kN at corresponding slip of 0.40 mm. Furthermore, the increase by 26 percent and 23 percent of the slip modulus at both limit states was computed.

Table 20: Results obtained from case series C3 for Mid. cases.

Case	l_t [mm]	F_{max} [kN]	δ_{Fmax} [mm]	σ_{Rebar} [MPa]	K_s [N/mm/m]	K_u [N/mm/m]	Failure mode
C-Ref.M	187.5	269	0.29	173	1.71×10^6	1.52×10^6	RS
C3-1M	375	410 (1.52)	0.40	181	2.15×10^6 (1.26)	1.87×10^6 (1.23)	RS

In conclusion, an increase in heel length of the CLT panel was able to induce the shear failure of the concrete notch at a load level 22 percent higher than the maximum force obtained from pushout tests. The ductility was also improved when the notch experienced concrete shear failure.

3.5.5 Influence of notch length

In case series C4, the change of notch length resulted in modifying the area of the cross-layer of the CLT panel. Figure 41a presents the force-slip curves obtained from numerical simulations for Exp. cases. The decrease in notch length from 90 mm to 40 mm in case C4-1 contributed to higher rolling shear resistance of the CLT panel and to the lower shear resistance and stiffness in the concrete panel. In this case, the failure was governed by the shear failure of concrete in the notched connector with a maximum force of 425 kN at a corresponding slip of 0.85 mm. At this point, tensile damage of the concrete panel was propagated entirely at the shear plane of the concrete notch and yielding stresses of V-shape rebars were noticed, as shown in Figure 42.

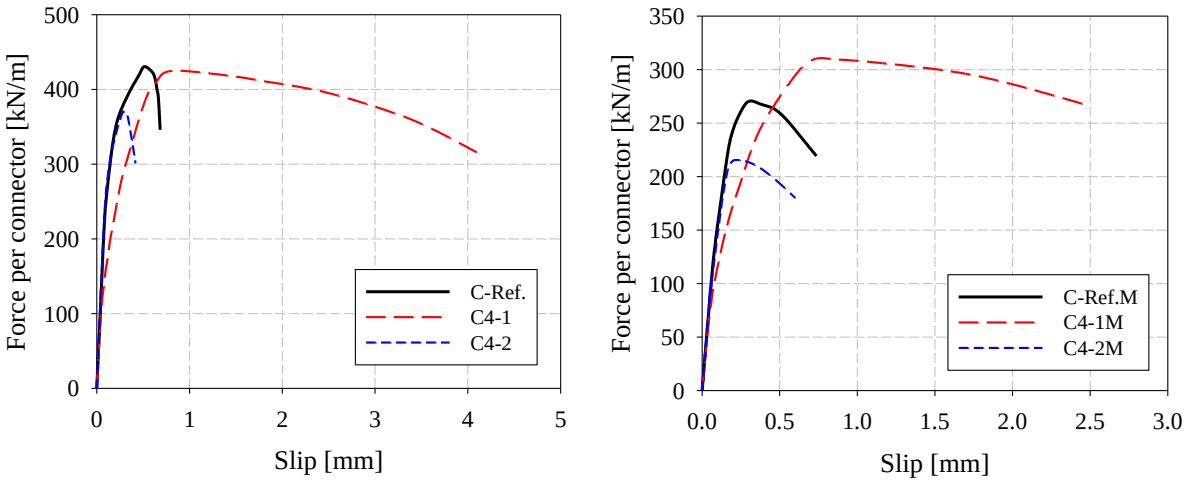

a. Exp. cases b. Mid. cases

Figure 41: Force-slip curves of case series C4.

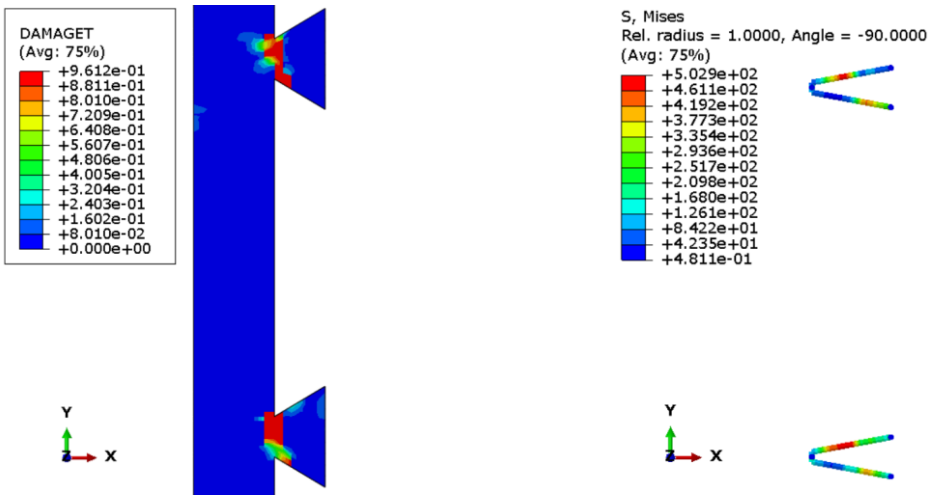

a. Tensile damage b. Stress of V-shape rebars

Figure 42: Tensile damage in the concrete panel and tensile stress of V-shape rebars at the maximum load level in case C4-1.

Even if slip moduli were decreased more than 50 percent compared to the C-Ref case (see Table 21), the notched connector in case C4-1 could still be considered as stiff, as its stiffness was higher than the suggested value of the design slip modulus of 1.00×10^6 N/mm/m proposed in the recommendations for the design of TCC beams with notched connectors given in the technical specification CEN/TS 19103 [44]. In addition, a better ductility in post-peak performance was observed in this case with an ultimate slip of approximately 4 mm at the end of the simulation corresponding to $0.73F_{max}$.

Table 21: Results obtained from case series C4 for Exp. cases.

Case	l_n [mm]	F_{max} [kN]	δ_{Fmax} [mm]	σ_{Rebar} [MPa]	K_s [N/mm/m]	K_u [N/mm/m]	Failure mode
C-Ref	90	431	0.52	321	2.73×10^6	2.43×10^6	RS
C4-1	40	425 (0.99)	0.85	504	1.51×10^6 (0.55)	1.11×10^6 (0.45)	CS
C4-2	140	370 (0.86)	0.30	30	2.88×10^6 (1.05)	2.80×10^6 (1.15)	RS

Besides, in case C4-2, the increase of notch length (140 mm) resulted in rolling shear failure at the maximum force of 370 kN accounted for 86 percent of that of C-Ref case. As expected, when cross-layer area of the CLT decreased due to the increase of notch length, the rolling shear resistance of case C4-2 was also limited. As shown in force-slip curve (see Figure 41a), the behavior of the notched connector remained in the elastic region when the brittle failure was obtained in the cross-layer of the CLT panel. Compared to the C-Ref case, an increase of 5 percent and 15 percent in slip moduli were observed at SLS and ULS, respectively.

For Mid. cases, similar failure modes were found in comparison to Exp. cases. In case C4-1M, the failure mode occurred at the lower notched connector at a maximum load level of 312 kN, accounting for 15 percent higher than the C-Ref.M case (see Table 22). Although the failure was governed by concrete shear, considerable differences in maximum forces between case C4-1 (425 kN) and C4-1M (312 kN) were noticed. It should be noted that the upper notched connector in case C4-1M only experienced partial failure. This resulted from the configuration of the loading block. For the numerical simulation of Mid. case, the upper notched connector was subjected to a limited portion of load while most of the remaining load was transferred to the lower notched connector. As shown Figure 43, only the lower notched connector failed with yielding stress in V-shape rebars at the maximum load level and at the ultimate slip, while the upper notched connector remained subjected to the limited load. It can be inferred that the failure load in case C4-1M should be comparable to that in case C4-1 if both notched connectors failed by concrete shear.

Table 22: Results obtained from case series C4 for Mid. cases.

Case	l_n [mm]	F_{max} [kN]	δ_{Fmax} [mm]	σ_{Rebar} [MPa]	K_s [N/mm/m]	K_u [N/mm/m]	Failure mode
C-Ref.M	90	269	0.29	173	1.71×10^6	1.52×10^6	RS
C4-1M	40	312 (1.15)	0.78	501	1.10×10^6 (0.65)	0.81×10^6 (0.54)	CS
C4-2M	140	215 (0.80)	0.20	20	1.73×10^6 (1.01)	1.50×10^6 (0.98)	RS

Additionally, an ultimate slip of 2.5 mm corresponding to $0.85F_{max}$ was achieved in the post-peak loading stage. At this slip, tensile stress of V-shape rebars experienced a stress of 568 MPa whereas rebars in upper notched connector remained in elastic region, with a stress of 305 MPa. A tensile damage with a horizontal line pattern was noticed at the end of concrete slab near the lower notched connector, which might be caused by bending in concrete.

When the notch length was increased to 140 mm in case C4-2M, the maximum force was obtained at 215 kN, 20 percent lower compared to the C-Ref.M case, due to the decrease of the cross-layer area of the CLT panel. No significant difference in slip moduli, and no ductility in post-peak loading stage were obtained.

In conclusion, the variation of the notch length had a significant influence on the rolling shear resistance of the cross-layer of the CLT panel. When the notch length was decreased from 90 mm to 40 mm, the failure was provoked by the concrete notch. The slip modulus decreased nearly twice-fold in comparison to the C-Ref case. Little ductility was obtained in the post-peak loading. On the other hand, an increase of the notch length from 90 mm to 140 mm resulted in a failure due to typical rolling shear stress in the cross-layer of the CLT panel. In addition, a slight difference in slip moduli was observed when the connection system was characterized by the rolling shear failure.

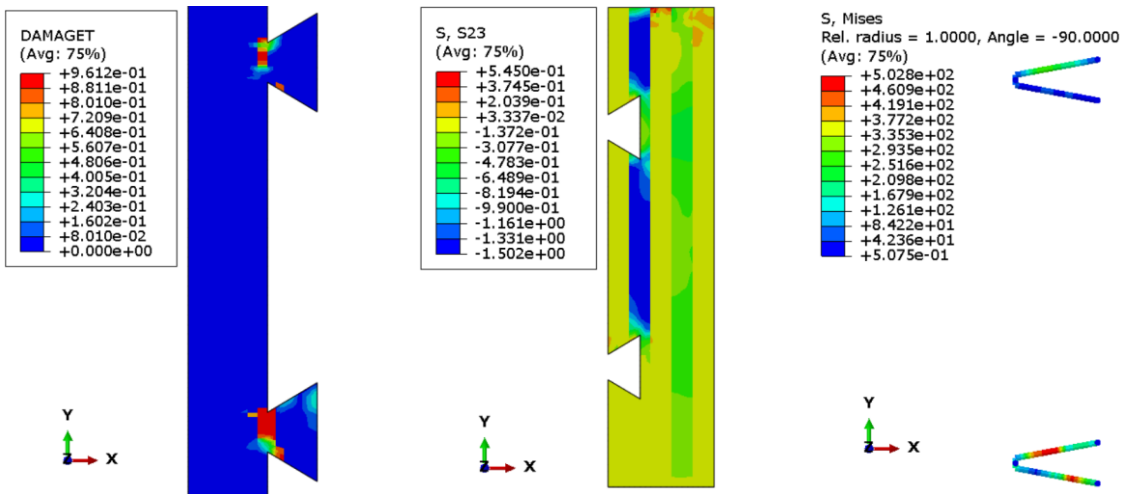

i. Tensile damage ii. Rolling shear stress iii. Stress of V-shape rebars

a. At the maximum load level

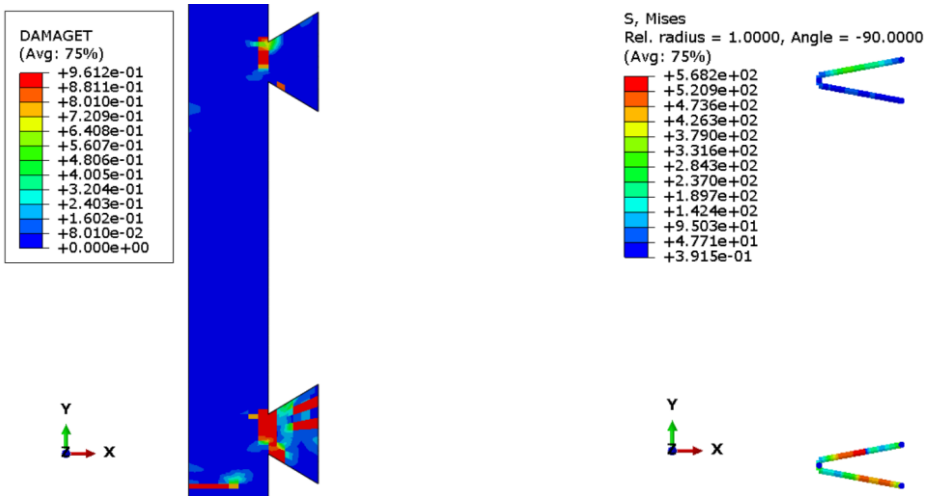

i. Tensile damage ii. Stress of V-shape rebars

b. At the ultimate slip

Figure 43: Tensile damage in concrete panel and tensile stress of V-shape rebars at the maximum load level and at the ultimate slip in case C4-1M.

3.5.6 Influence of notch depth

The influence of the notch depth was investigated in case series C5. Figure 44a presents the force-slip curves obtained from numerical simulations of Exp. cases. In case C5-1, by decreasing the notch depth from 50 mm to 25 mm, which was smaller than the first longitudinal layer's thickness (33 mm), the rolling shear resistance of the CLT panel was increased due to larger cross-layer section. As a result, the connection system remained in elastic behavior until a load level of 350 kN before the failure was induced by the concrete shear at a maximum force of 516 kN with a corresponding slip of 0.65 mm (see Figure 44a). It can be seen that the load-carrying capacity was increased by 20 percent compared to that in the C-Ref case as summarized in Table 23.

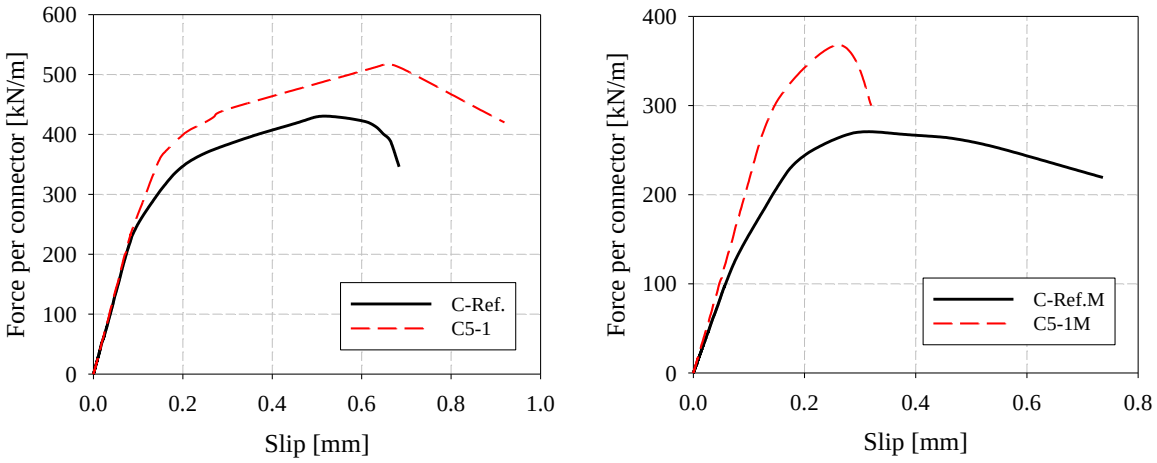

a. Exp. cases b. Mid. cases

Figure 44: Force-slip curves of case series C5.

Table 23: Results obtained from case series C5 for Exp. cases.

Case	d_n [mm]	F_{max} [kN]	δ_{Fmax} [mm]	σ_{Rebar} [MPa]	K_s [N/mm/m]	K_u [N/mm/m]	Failure mode
C-Ref	50	431	0.52	321	2.73×10^6	2.43×10^6	RS
C5-1	25	515 (1.20)	0.65	500	2.78×10^6 (1.04)	2.54×10^6 (1.14)	CS

The failure of case C5-1 started from the lower notched connector, followed by the upper one as shown in Figure 45a. At the maximum load level, high rolling shear stresses were found from the top surface of the CLT panel to the lower notched connector (blue color) with a maximum rolling shear stress of approximately 1.50 MPa (see Figure 45b), while V-shape rebars in the lower notched connector were experiencing yielding stress. Despite being governed by the concrete shear, case C5-1 exhibited no ductility with an ultimate slip of only 0.9 mm, possibly due to the short anchorage length of V-shape rebars. It should be noted that the steel reinforcement placed in the concrete notch was also decreased to fit into new configuration of the notch with the depth of 25 mm. Therefore, the anchorage length of the reinforcement was also limited. On the other hand, relative differences of slip moduli were obtained with 4 percent and 14 percent higher for SLS and ULS, respectively, compared to the C-Ref case.

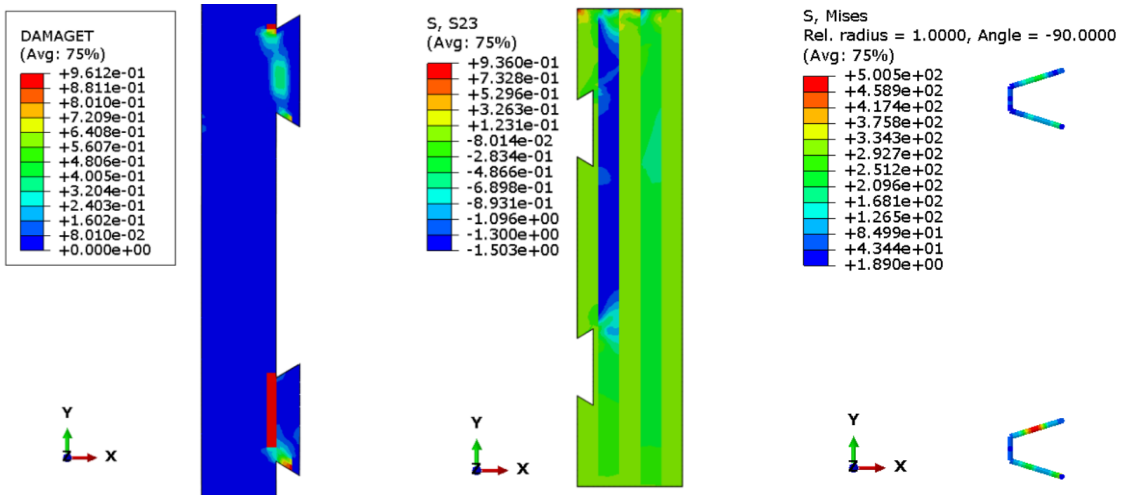

a. Tensile damage b. Rolling shear stress c. Stress of V-shape rebars

Figure 45: Tensile damage in the concrete panel, rolling shear stress of the CLT panel, and tensile stress of V-shape rebars at the maximum load level in case C5-1.

For numerical simulations of Mid. cases, case C5-1M experienced a sudden collapse which was governed by the rolling shear failure of cross-layer of the CLT panel at a maximum force of 368 kN, 37 percent higher than that of the C-Ref.M case. In comparison to C-Ref.M case, less slip was observed in case C5-1M for the same load levels as shown in force-slip curves (see Figure 44b). Consequently, higher stiffnesses were computed, 25 percent and 49 percent at SLS and ULS, respectively.

Table 24: Results obtained from case series C5 for Mid. cases.

Case	d_n [mm]	F_{max} [kN]	δ_{Fmax} [mm]	σ_{Rebar} [Mpa]	K_s [N/mm/m]	K_u [N/mm/m]	Failure mode
C-Ref.M	50	269	0.29	173	1.71×10^6	1.52×10^6	RS
C5-1M	25	368 (1.37)	0.26	181	2.31×10^6 (1.25)	2.27×10^6 (1.49)	RS

In overall, the decrease of the notch depth to the value smaller than the thickness of the first layer of the CLT panel provoked the failure on the concrete side at a load level of 516 kN, about 20 percent higher than the maximum force obtained from the C-Ref case. However, no improvement on ductility was observed, which might be due to insufficient anchorage length of V-shape rebars. Additionally, no significant difference in slip moduli was noticed in comparison to the C-Ref case.

3.5.7 Influence of the cross-sectional area of V-shape rebars

The influence of the number of V-shape rebars was investigated in case series C6. The obtained force-slip curves for Exp. cases are illustrated in Figure 46a. The results indicated that the maximum force decreased when the amount of V-shape rebars was reduced.

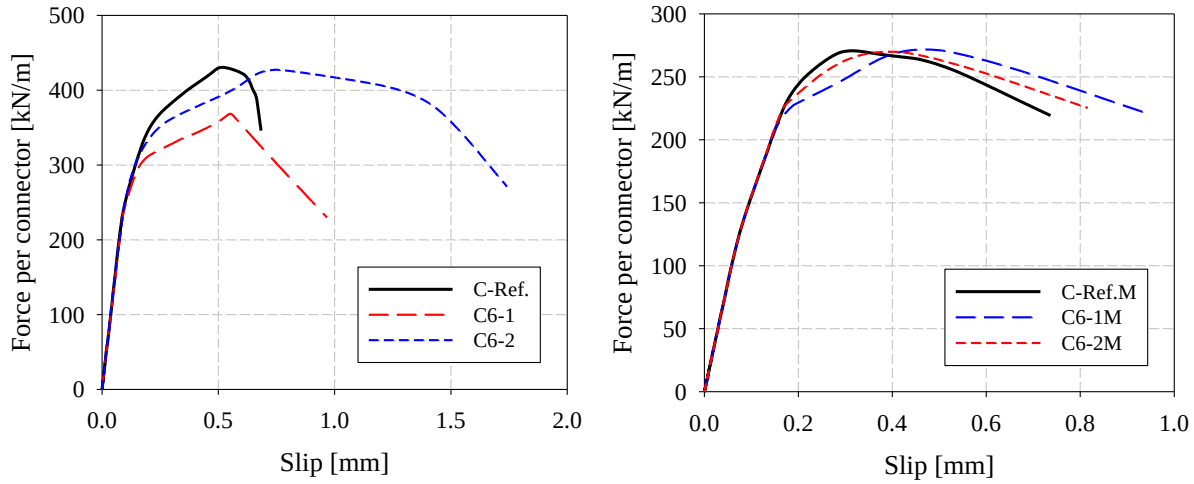

a. Exp. cases b. Mid. cases

Figure 46: Force-slip curves of case series C6.

In case C6-1, when no shear reinforcement was adopted, the failure mode was governed by the concrete shear resistance at the maximum force of 364 kN with a corresponding slip of 0.53 mm. At the maximum load level, the upper notched connector failed first and was followed by the lower one. Compared to the C-Ref case, the load-carrying capacity decreased by 16 percent. However, the influence on the slip modulus of the connection system was little with a 3 percent lower and 7 percent higher value at SLS and ULS, respectively (see Table 25). This resulted from a close correlation of the force-slip curve in elastic stage and the adoption of the computation method proposed by Ceccotti [1]. The

connection system of case C6-1 reached the nonlinear stage earlier, at a load level of approximately 300 kN compared to the C-Ref curve (see Figure 46a). For the CLT panel, the highest rolling shear stress obtained was approximately 1.43 MPa (see Figure 47a). Despite failing in concrete shear, no improvement on ductility was noted, which can be associated with the absence of shear reinforcements in notched connectors.

Table 25: Results obtained from case series C6 for Exp. cases.

Case	A_s [mm^2]	F_{max} [kN]	δ_{Fmax} [mm]	K_s [N/mm/m]	K_u [N/mm/m]	Failure mode
C-Ref	141.37	431	0.52	2.73×10^6	2.43×10^6	RS
C6-1	0	364 (0.84)	0.53	2.63×10^6 (0.97)	2.60×10^6 (1.07)	CS
C6-2	56.55	427 (0.99)	0.75	2.68×10^6 (0.87)	2.36×10^6 (0.97)	RS+CS

In case C6-2, the failure was initiated by concrete shear failure of the notched connector. The maximum force was obtained, when the upper notched connector failed, at a load level of 427 kN with a corresponding slip of 0.75 mm. At this point, although certain regions of the cross-layer of the CLT panel reached shear strength, a complete failure by rolling shear was not observed based on the deformed configuration in the FE model. The V-shape rebars were subjected to a tensile stress of 478 MPa at the maximum load level and experienced the yielding stress shortly after the concrete of the upper notched connector failed. The tensile damage of the concrete and the rolling shear stress of the CLT panel can be visualized in Figure 47b. Compared to the C-Ref case, a decrease in stiffnesses by 13 percent and 3 percent was computed at SLS and ULS, respectively. An improvement of ductility in post-peak loading was obtained with an ultimate slip of 1.75 mm.

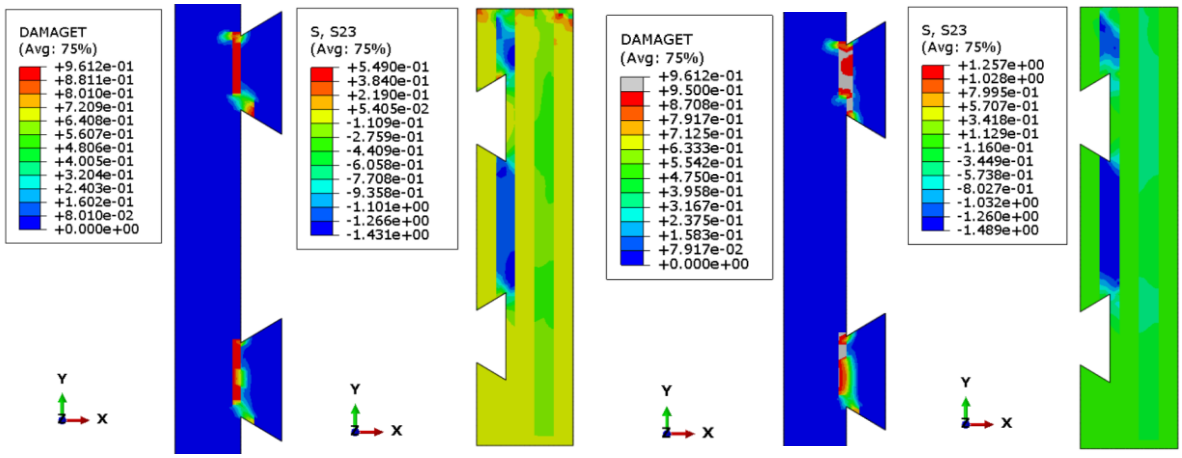

i. Tensile damage ii. Rolling shear stress i. Tensile damage ii. Rolling shear stress

a. Case C6-1 b. Case C6-2

Figure 47: Tensile damage in the concrete panel and rolling shear stress of the CLT at the maximum load level in cases C6-1 and C6-2.

For numerical simulations of Mid. cases, force-slip curves are shown in Figure 46b and the summary of obtained results are reported in Table 26. It was found that the influence of V-shape rebars was limited as, in all cases, the failure was governed by limited rolling shear resistance of the CLT panel. In all cases, at the maximum load level of 269 kN, the cases with less V-shape rebars experienced higher

slips ranging from 0.29 mm (5 rebars) to 0.42 mm (no rebars). In terms of slip modulus, no difference was noticed in either SLS or ULS.

Table 26: Results obtained from case series C6 for Mid. cases.

Case	A_s [mm^2]	F_{max} [kN]	δ_{Fmax} [mm]	K_s [N/mm/m]	K_u [N/mm/m]	Failure mode
C-Ref.M	141.37	269	0.29	1.71×10^6	1.52×10^6	RS
C6-1M	0	269(1.00)	0.51	1.71×10^6 (1.00)	1.52×10^6 (1.00)	RS
C6-2M	56.55	269 (1.00)	0.42	1.71×10^6 (1.00)	1.53×10^6 (1.00)	RS

In conclusion, the influence of V-shape rebars was observed only when adopting the experimental loading block configuration. For Exp. cases, reducing the rebar cross-section resulted in a reduction of the connection strength and a higher chance of experiencing shear failure at the concrete notch. However, varying the cross-sectional area of V-shape rebars caused only a slight difference in slip moduli. On the other hand, when adopting the middle loading block configuration for Mid. cases, no change was observed for the maximum load and slip moduli, as the failure mode was governed by the rolling shear resistance of the CLT panel.

3.5.8 Summary and conclusion on the parametric study

The influence of geometries and material properties of pushout model on the behavior of the notched connectors was investigated using the pushout model with Exp. and Mid. block configurations. The mechanical resistances and stiffness, and the failure mechanisms of cases in the parametric study are summarized in Table 27. The value in brackets refers to the ratio between results of each case and those of the C-Ref case. The following main results can be highlighted as follows:

- The concrete strength had no impact on the load-carrying capacity of the specimen. However, when using lower concrete strength, higher damage in concrete notches was observed, resulting in higher slip at the maximum load level. Thus, lower stiffness was obtained in this case. No ductility was observed in the post-peak loading as the failure was governed by rolling shear resistance of the cross-layer of the CLT panel.
- The thickness of the concrete panel had a slight influence on the strength of the specimen, as the collapse was governed by the rolling shear failure in cross-layer of the CLT panel. A change of slip moduli was noticed in a range of 20 percent value compared to the reference case (C-Ref). Higher tensile damage of the concrete notch was observed when adopting lower thickness of the concrete panel.
- The increase of heel length of the CLT panel from 187.5 mm to 375 mm was sufficient to obtain the failure from the concrete side of the notch connector with an increase of maximum force of approximately 22 percent value compared to the reference case (C-Ref). A small improvement in the post-peak behavior was obtained. In terms of slip moduli, a decrease in the range of 20 percent value was observed in comparison to the C-Ref case.
- The variation of the notch length resulted in a change of the load-carrying capacity of the specimen. When the notch length decreased from 90 mm to 40 mm, the failure was obtained by concrete shear of the notch. The slip moduli decreased nearly two times in comparison to

that of the C-Ref case, which was due to the early damage of the concrete notch. A little ductility was also obtained in the post-peak loading. In contrast, when the notch length increased, the collapse of the specimen was governed by the rolling shear failure of the CLT panel. In this case, higher slip moduli were observed in a range of 15 percent difference compared to the C-Ref case.

- A reduction of the notch depth to a value smaller than the thickness of the first longitudinal layer of the CLT panel resulted in an increase of the cross-layer area of the CLT panel. As a result, higher strength and stiffness of about 20 percent value were obtained in comparison to the C-Ref case. Even though the shear failure of the connection system occurred on the concrete side, no improvement on the ductility was noticed, which was possibly due to the insufficient anchorage length of V-shape rebars.
- A higher amount of V-shape rebars increased the strength of the notched connection. When no shear reinforcement was used, the specimen was governed by the shear failure of the concrete notch. No ductility in the post-peak loading was noticed.

It should be noted that numerical simulations of the pushout specimen with the middle loading block (Mid. cases) were also made in order to determine the behavior for pure rolling shear action. From Table 27, when the rolling shear failure was obtained, the maximum ranged from 35 percent to 38 percent lower than those of the C-Ref case. Lower slip moduli were also noticed, ranging from 47 percent value lower to 7 percent value lower in comparison to the C-Ref case.

In conclusion, following the results of numerical simulations of the parametric study, high strength and high slip moduli of the connection system were still obtained under the influence of the investigated parameters. Thus, it is possible to improve the ductility of the notched connection by prioritizing the shear concrete failure of the notch, if a sufficient number of V-shape rebars are placed inside the notch. This prioritization can be obtained by increasing the spacing between the connectors, in order to increase the rolling shear resistance of the CLT panel. The concrete failure should happen for a load 22 percent larger than the experimental resistance obtained by pushout tests. However, these conclusions need to be confirmed by additional experimental investigations.

Table 27: Summary of results obtained from the parametric study.

Parametric study	F_{max} [kN]	K_s [N/mm/m]	K_u [N/mm/m]	Failure mode
C-Ref	431	2.73×10^6	2.43×10^6	RS
C1-1	429 (1.00)	2.58×10^6 (0.95)	2.03×10^6 (0.84)	RS
C1-2	430 (1.00)	2.73×10^6 (1.00)	2.63×10^6 (1.08)	RS
C2-1	419 (0.97)	2.17×10^6 (0.79)	1.96×10^6 (0.81)	RS
C2-2	435 (1.01)	2.87×10^6 (1.05)	2.62×10^6 (1.08)	RS
C3-1	526 (1.22)	2.51×10^6 (0.92)	1.95×10^6 (0.80)	CS
C4-1	425 (0.99)	1.51×10^6 (0.55)	1.11×10^6 (0.45)	CS
C4-2	370 (0.86)	2.88×10^6 (1.05)	2.80×10^6 (1.15)	RS
C5-1	515 (1.20)	2.78×10^6 (1.04)	2.54×10^6 (1.14)	CS
C6-1	364 (0.84)	2.63×10^6 (0.97)	2.60×10^6 (1.07)	CS
C6-2	427 (0.99)	2.68×10^6 (0.87)	2.36×10^6 (0.97)	RS+CS
C-Ref.M	269 (0.62)	1.71×10^6 (0.63)	1.52×10^6 (0.63)	RS
C1-1M	268 (0.62)	1.66×10^6 (0.61)	1.45×10^6 (0.60)	RS
C1-2M	270 (0.63)	1.73×10^6 (0.63)	1.56×10^6 (0.64)	RS
C2-1M	267 (0.62)	1.45×10^6 (0.53)	1.32×10^6 (0.54)	RS
C2-2M	272 (0.63)	1.79×10^6 (0.66)	1.59×10^6 (0.65)	RS
C3-1M	410 (0.95)	2.15×10^6 (0.79)	1.87×10^6 (0.77)	RS
C4-1M	312 (0.72)	1.10×10^6 (0.40)	0.81×10^6 (0.33)	CS
C4-2M	215 (0.50)	1.73×10^6 (0.63)	1.50×10^6 (0.62)	RS
C5-1M	368 (0.85)	2.31×10^6 (0.78)	2.27×10^6 (0.93)	RS
C6-1M	269 (0.62)	1.71×10^6 (0.63)	1.52×10^6 (0.62)	RS
C6-2M	269 (0.62)	1.71×10^6 (0.63)	1.53×10^6 (0.63)	RS

3.6 Analytical evaluation of the notched connection strength

As stated in the literature review of chapter 2 (see section 2.6.3), the strength of the timber-concrete connection system can be determined by four possible failure mechanisms. In this section, the assessment of different analytical approaches to estimate the load-carrying capacities of the notched connection system is investigated. Following the two failure modes with their corresponding resistances obtained experimentally and numerically, analytical methods are adopted to estimate the shear resistance of the concrete notch and the rolling shear resistance of the CLT panel. In addition, the formulae to define the remaining failure modes, including the compressive resistances of concrete and timber, are also provided.

3.6.1 Shear resistance of concrete notch

For the estimation of the shear resistance of the concrete notch, different expressions provided in current design codes were adopted and verified against the results from various cases in the parametric study. For the verification, the results from the FE simulations of Exp. cases, in which the failure was governed by concrete shear resistance of the notch, were considered. They were cases C3-1, C4-1, C5-1, and C6-1. It should be noted that case C4-1M also experienced a concrete shear failure, but the failure occurred only in the lower notched connector. For this reason, case C4-1M was disregarded.

3.6.1.1 Evaluation of concrete shear resistance based on expressions in design codes

From the results of the FE model, concrete shear failure occurred in the shear plane between the concrete slab and the notched connector (see Figure 48a,b). In a first attempt, the notched connection was assumed to be a short beam subjected to a distributed load F. This short beam had a width b, a thickness l_n, and a length h_c+d_n (see Figure 48c).

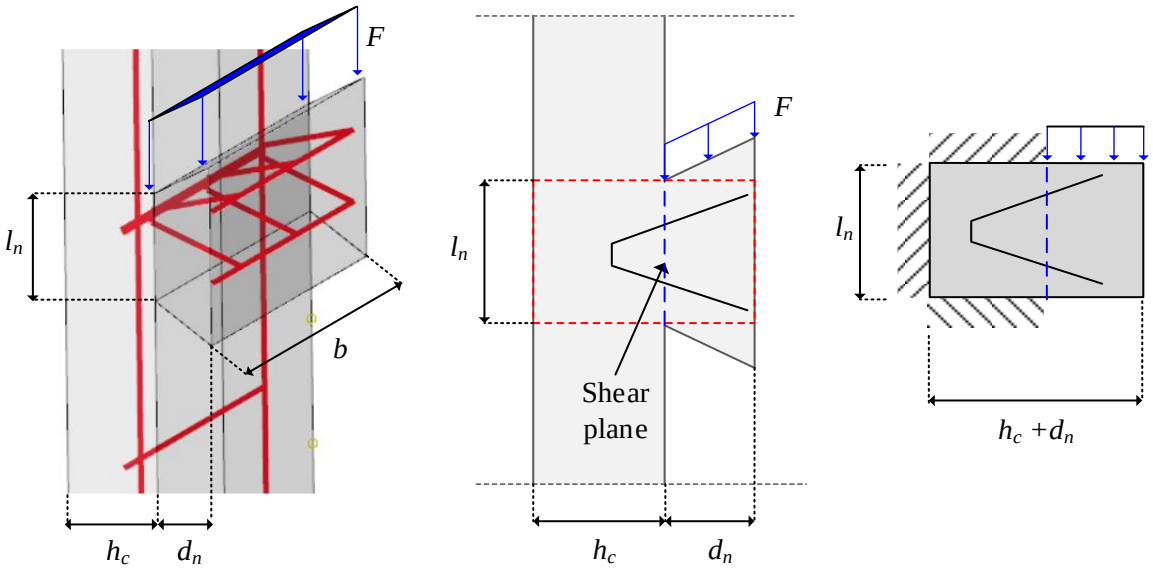

a. Notched connector in 3D b. Notched connector in 2D c. Assumed short beam

Figure 48*:* Assumption of the notched connector as a short beam.

The shear resistance V can be defined as an addition of shear resistances provided by the reinforcement V_s and by the concrete panel V_c:

$$V=V_s+V_c \tag{12}$$

For the shear resistance contributed by the rebar reinforcement, a simplified analytical method was employed. To facilitate the calculation, the V-shape rebars were regarded as two separated inclined rebars as shown in Figure 49.

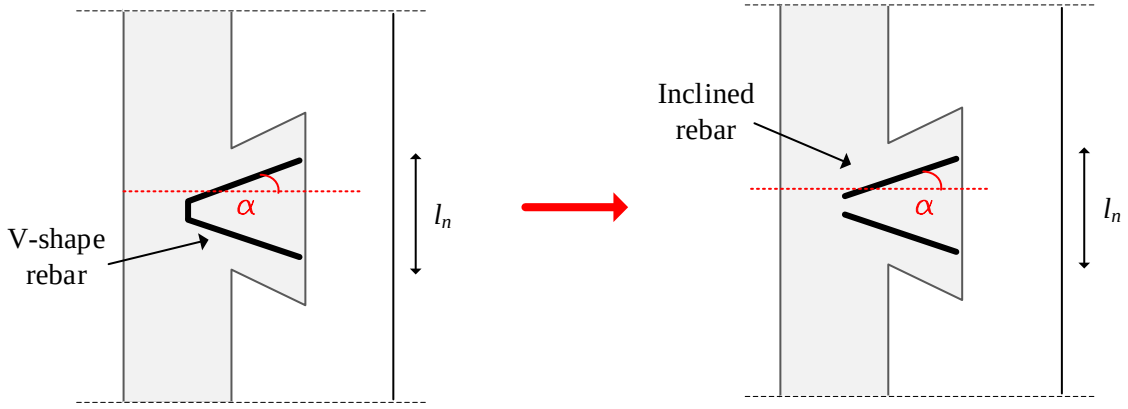

Figure 49: Simplicity of V-shape rebars as two separated inclined rebars.

The shear resistance of the inclined rebars can be determined using eq. (13) depending on the tensile yield strength of the rebar f_y, the number of the inclined rebars n, the cross-sectional area of rebars A_s, and the angle between the inclined rebar and horizontal axis α. The yield strength of the rebar was taken as 500 MPa, which was consistent with that in the FE model.

$$V_s=nf_yA_s\sin\alpha \tag{13}$$

On the other hand, the shear resistance contributed by the concrete part was computed following different design codes, including Eurocode 2 [25], ACI 318-14 [45], and AASHTO [46].

According to Eurocode 2 [25], the design value for the concrete shear resistance V_c, eq. (14), is in function of the minimum shear stress v_{min} which can be assessed using eq. (15). The parameter k_1 is taken as 0.15, while the axial force σ_{cp} is disregarded in this study. The parameter k in minimum stress v_{min} is given in eq. (16). The parameters f_{ck}, b, and l_n denote the characteristic compressive strength of the concrete, the width of the beam, and notch length respectively. In addition, the value of f_{ck} was replaced by the value of f_c which equal to 35 MPa for the evaluation of the concrete shear resistance.

$$V_c=\left(v_{min}+k_1\sigma_{cp}\right)bl_n \tag{14}$$

$$v_{min}=0.035k^{3/2}f_{ck}^{\ 1/2} \tag{15}$$

$$k=1+(200/l_n)^{1/2} \tag{16}$$

According to ACI 318-14 [45], the shear resistance for the concrete panel can be assessed by eq. (17) and depends on the modification factor λ, the specific compressive strength of the concrete f'_c which can be taken as f_c, the width of the beam b, and the notch length l_n. In this study, the value of λ is equal to 1 for the normalweight concrete.

$$V_c = 2\lambda \sqrt{f'_c} b l_n \tag{17}$$

The AASTSHO design code [46] provides a design method for the shear resistance of the concrete panel based on eq. (18). It is governed by the factor indicating the ability of diagonally cracked concrete to transmit tension and shear β, the compressive strength of concrete for use in design f'_c (taken as f_c), the width of the beam b, and the notch length or depth of beam cross-section l_n. Having the overall depth of the cross-section less than 16 inch, the value of β was recommended to be 2.

$$V_c = 0.0316\beta \sqrt{f'_c} b l_n \tag{18}$$

Table 28 reports the comparison between the results of the shear resistance (provided by concrete and by reinforcement) obtained from design codes and the parametric study. The unit of the shear resistance is considered in one meter width, and the value in brackets shows the difference of shear resistance obtained from design codes to the one obtained from the parametric study.

Table 28: Comparison of the shear resistance of the concrete panel obtained from standard codes and from the parametric study.

Case	Shear resistance [kN/m]			
	Eurocode 2 [25]	ACI 318-14 [45]	AASHTO [46]	FE model
C3-1	137 (0.26)	173 (0.33)	173 (0.33)	526
C4-1	76 (0.19)	91 (0.22)	91 (0.22)	408
C5-1	105 (0.20)	173 (0.33)	173 (0.33)	516
C6-1	53 (0.14)	88 (0.24)	88 (0.24)	364

The results indicated that the concrete shear resistance obtained from the analytical methods were substantially underestimated, ranging from 67 to 86 percent values lower than the maximum forces obtained in the numerical results. Eurocode 2 [25] provided the lowest concrete shear resistance while the results obtained from ACI 318-14 [45] and AASHTO [46] were identical. It can be concluded that the assumption of the notched connector as a short beam was not applicable to estimate the shear resistance of the concrete notch.

3.6.1.2 Evaluation of concrete shear resistance based on expressions for shear at the interface between concrete cast at different times

In the second attempt, the concrete notch was considered as an additional concrete part cast along the concrete slab, connected together using the shear reinforcement (see Figure 50). The shear resistance can be defined using the shear friction theory that was adopted in design codes. Three design codes were adopted, including Eurocode 2 [25], ACI 318-14 [45], and AASHTO [46]. For simplicity in the computation, the V-shape rebars were regarded as two separated inclined rebars.

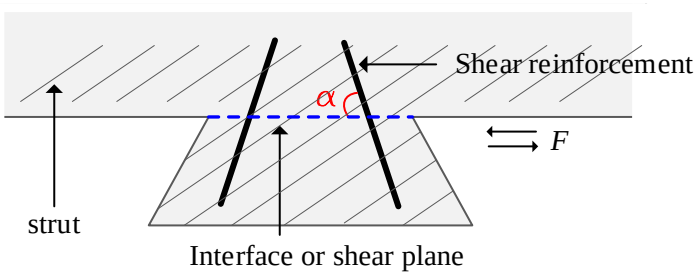

Figure 50: Assumptions of the notched connector as the concrete cast at different time.

In Eurocode 2 [25], the design shear strength at the interface v_c (considered in MPa) is dependent on the adhesion, friction, and the dowel action of the reinforcement, which can be computed using the eq. (19). The factors c and μ are determined by the roughness of the interface. Parameters f_{ctd}, σ_n, ρ are the tensile strength, the stress acting perpendicular to the shear plane, and the shear reinforcement ratio, respectively. The angle α between shear reinforcement and beam axis, perpendicular to the shear force, should be between 45^0 and 90^0. However, the design shear strength should not exceed $0.5vf_{cd}$ in which, v is the reduction factor, and f_{cd} is the design compressive strength of the concrete. In this computation, parameters corresponding to indented surface at the interface layer are chosen with the values: c=0.50 and μ=0.9. In addition, the values of parameters f_{cd}, f_{ctd}, f_{yd}, and σ_n are assumed to be 35 MPa, 2.7 MPa, 500 MPa, and 0, respectively. It should be noted that the values of f_{cd} and f_{ctd} are taken equal to the values of f_c and f_t in the numerical simulation. The shear resistance can be computed as $V_c=v_c b_n l_n$.

$$v_c = cf_{ctd} + \mu\sigma_n + \rho f_{yd}(\mu \sin\alpha + \cos\alpha) \le 0.5vf_{cd} \tag{19}$$

The ACI 318-14 [45] adopts the shear friction theory, in which the shear resistance can be evaluated using eq. (20). The equation is governed by several parameters, including the angle between shear-friction reinforcement and the shear plane α, the coefficient of friction μ, the yield stregnth of the shear reinforcement f_y, and the area of reinforcement A_{vf}. It is important to note that this design formula is applicable only when shear reinforcement is under tension. Additionally, the concrete resistnce in eq. (20) only depends on the contribution of shear reinforcement. For this study, a cofficient of friction μ is equal to 1.4 where concrete is assumed to be placed monolithically.

$$V_c = A_{vf} f_y (\mu \sin\alpha + \cos\alpha) \tag{20}$$

The design formula for the shear resistance based on the friction theory can also be found in AASHTO [46] expressed in eq. (21). This method is dependent on adhesion c, friction coefficient μ, area of concrete section resisting shear transfer A_{cv}, yield strength of reinforcing bars f_y, area of

reinforcement for interface shear A_{vf}, and permanent net compressive force P_c considered as zero in this study. Based on the cohesion and friction factors, the shear resistance should not exceeded the value derived from eq. (22) which is in function of the surface condtion, types of concrete, and casting process. For the concrete placed monothically, cohesion factor c and friction factor μ are taken as 0.4 ksi and 1.4, respectively.

$$V_c = cA_{cv} + \mu\left(A_{vf}f_y + P_c\right) \tag{21}$$

$$V_{c,max} = \min\left(k_1 f'_c A_{cv},\ k_2\right) \times A_{cv} \tag{22}$$

The results of the shear resistance obtaiend from the aforementioned design codes and from numerical simulations of the parametric study cases C3-1, C4-1, C5-1, and C6-1 are summarized in Table 29. In overall, design codes underestimated the concrete shear resistance, varying from 32 percent to 67 percent lower in comparison to the shear resistance obtained from the parametric study. It should be noted that the concrete shear resistance in accordance to ACI design code [45] was not computed in case C6-1 since no reinforcement was placed inside the concrete notch. Based on the results presented in Table 29, it can be concluded that these expressions were again not applicable to determine the concrete shear resistance of the concrete notch.

Table 29: Comparisons of the results obtained from analytical method based on interface shear resistance and from the parametric study.

Test	Shear resistance [kN/m]			
	Eurocode 2 [25]	ACI 318-14 [45]	AASHTO [46]	FE model
C3-1	249 (0.47)	231 (0.44)	307 (0.58)	526
C4-1	181 (0.44)	221 (0.54)	147 (0.36)	408
C5-1	249 (0.48)	231 (0.45)	307 (0.60)	516
C6-1	122 (0.33)	N/A	248 (0.68)	364

3.6.1.3 Evaluation of concrete shear resistance of the notched connection based on expressions in the technical specification CEN/TS 19103

In accordance with the technical specification CEN/TS 19103 [44], a design method for usual notch connection system of timber-concrete composite members is proposed (see Figure 51a). This method is then adapted to the configuration of the notched connector in this study (see Figure 51b). For the concrete part, the shear resistance at shear plane of the notched connection V_c can be assessed using eq. (23):

$$V_c = f_{v,c,d}\, b l_n \tag{23}$$

with

$$f_{v,c,d} = v f_{cd} / (\cot\theta + \tan\theta) \tag{24}$$

$$v=0.6(1-f_{ck}/250) \quad (25)$$

$$\theta=\arctan(d_n/l_n) \quad (26)$$

where $f_{v,c,d}$ is the effective design shear strength, b is the notch width, l_n is the notch length, v is the reduction factor, θ is the angle of the compression strut, respectively. In this computation, f_{cd} and f_{ck} are taken equal to f_c =35 MPa.

However, the notched connection should also be designed to withstand a minimum vertical component by using eq. (27):

$$V_t=\max(V_c\tan\theta\,;\,0.1V_c) \quad (27)$$

where V_t is the design tensile force between timber and concrete at the shear plane and can be determined under two conditions:

- without reinforcement (rebars) $V_t=f_t b l_n$ (28)
- with reinforcement (rebars) $V_t=f_y A_s\cos\alpha$ (29)

where f_t and f_y are tensile strength of concrete and yield strength of reinforcement, respectively. As a result, it was verified that the tensile stress provided by V-shape rebars inside the concrete notched was higher than 10 percent of the maximum shear force V_c. Thus, the requirement for the minimum tensile force to withstand the uplift was satisfied.

Table 30 presents the results of the shear resistance obtained from the design formula of the technical specification CEN/TS 19103 [44] and from the parametric study. In overall, a high discrepancy of the concrete shear resistance at the the shear plane was obtained, ranging from 19 percent lower to 90 percent higher in comparison to that of numerical results. When no V-shape rebars were adopted (case C6-1), the technical specification CEN/TS 19103 [44] overestimated the shear resistance by almost two times (90 percent higher). If sufficient rebars were adotped in the notched connection, a certain level of similarities in concrete shear resistance was observed between the design code and FE models, in a range of 30 percent difference. The limitaion in assessing the load-carrying capacity provided by the techincal specification CEN/TS 19103 [44] can result from the calculation method of the techincal specification, which is developed for steel fasteners embedded in timber panels, while in our research, V-shaped rebars are placed entirely inside the concrete notch.

Table 30: Comparisons of the results obtained from CEN/TS 19103 [44] and FE models.

Approach	Shear resistance [kN/m]			
	C3-1	C4-1	C5-1	C6-1
FE model	526	408	516	364
CEN/TS 19103 [44]	690 (1.31)	352 (0.86)	419 (0.81)	690 (1.90)

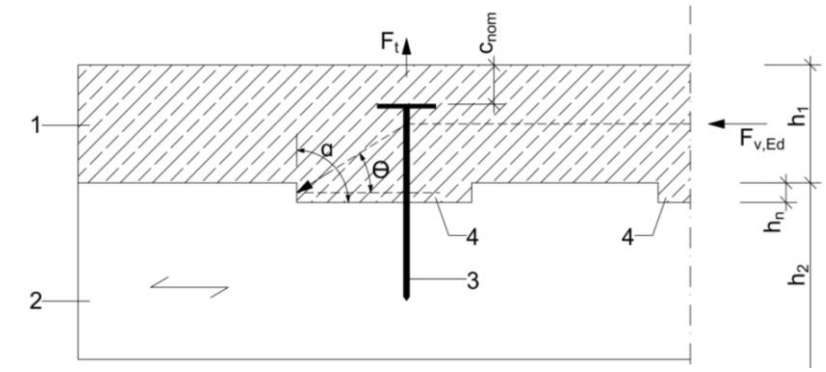

a. In the technical specification CEN/TS 19103 [44]

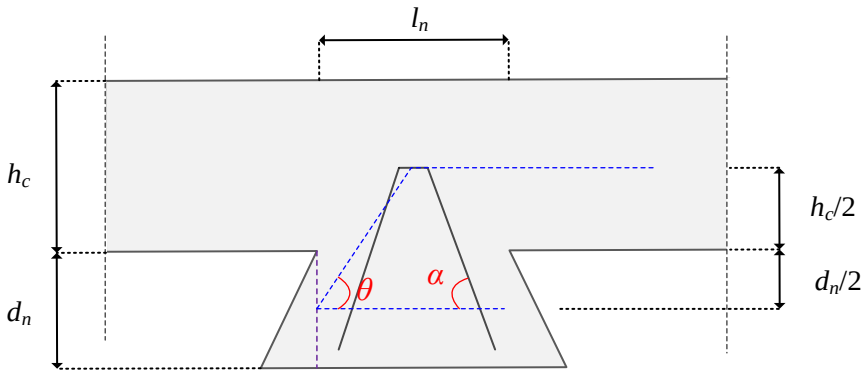

b. In this study

Figure 51: Configuration of the notched connection in the technical specification CEN/TS 19103 [44] and in this study.

3.6.1.4 Strut-and-tie model

As a conclusion drawn from sections 3.6.1.1 to 3.6.1.3, it can be affirmed that the design codes were not able to provide accurate shear resistance of the concrete notch. As an alternative, a strut-and-tie model was developed in this section. This method is generally developed based on the truss analogy method to represent the flow of the stress paths within the member (see [47], [48]).

The strut-and-tie model of the concrete panel was developed based on the contact forces and the principal stress map obtained from the FE model of the experimental test (C-Ref case). However, certain parameters were modified, including the number of V-shape rebars, and the friction coefficient in order to obtain a shear failure in concrete. The friction coefficient of 0.4 between the concrete panel and the CLT panel was adopted in accordance with the value recommended by the Eurocode 5 [28], while the number of V-shape rebars was reduced from five rebars (141.37 mm^2) to three rebars (56.55 mm^2).

The first attempt of the strut-and-tie model was initiated to determine the shear resistance of the concrete notch at the maximum load level. However, it is not satisfactory since V-shape rebars were not experiencing yield stresses. Then, the strut-and-tie model was developed again at post-peak load level when yield stresses were observed in V-shape rebars.

A. Proposed model of strut-and-tie at maximum load level

Figure 52 presents the force-slip curve, tensile damage, and tensile stress of V-shape rebars at the maximum load level obtained from the numerical simulation. The failure mode of the connection system was governed by the shear resistance of the concrete notch at a maximum force of 406 kN per one meter width with a corresponding slip of 1.15 mm. The failure initiated at the lower notched connector, before developing in the upper one.

For the development of the strut-and-tie model on the whole concrete panel of the pushout specimen, the contact forces applied to the concrete panel as well as the reaction forces on the concrete panel were required. These details could be obtained from the FE model by extracting the resultant forces of the contact normal forces and the contact friction forces at the contact surface between the concrete and the CLT panels. Figure 53a shows the areas subjected to the contact forces (black and red color) and force diagrams in the FE model. Figure 53b,c show the numbering of the resultant forces on the upper and lower notch connectors, respectively. The values of the contact forces as well as of the angle of the force orientations to the vertical axis are reported in Table 31. It was found that the contact forces were concentrated in the neighboring region of both notched connectors.

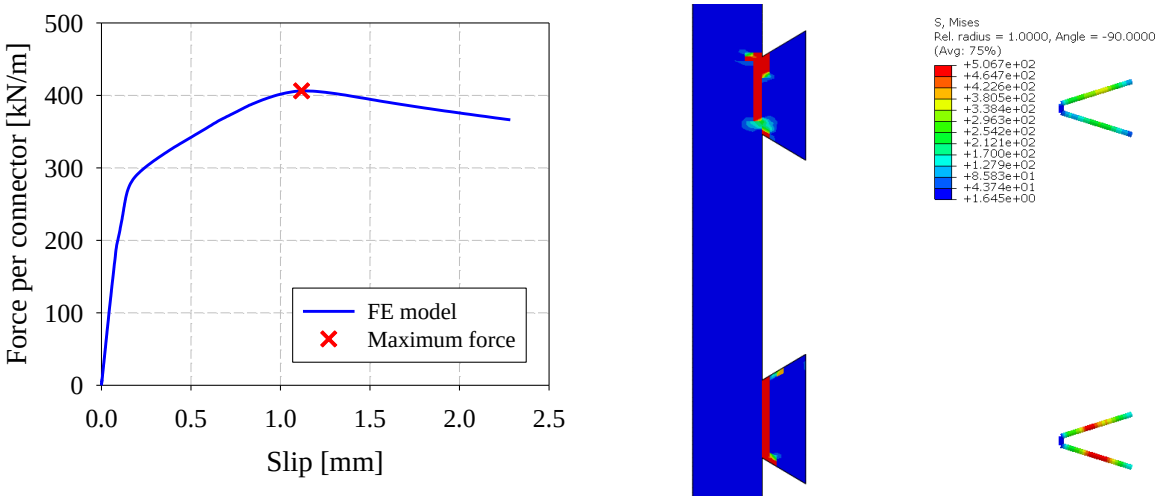

a. Force-slip curve of the FE model b. Tensile damage c. Stress of rebars

Figure 52: Force-slip curve, tensile damage of the concrete panel, and V-shape rebars stress at the maximum load level of the FE model.

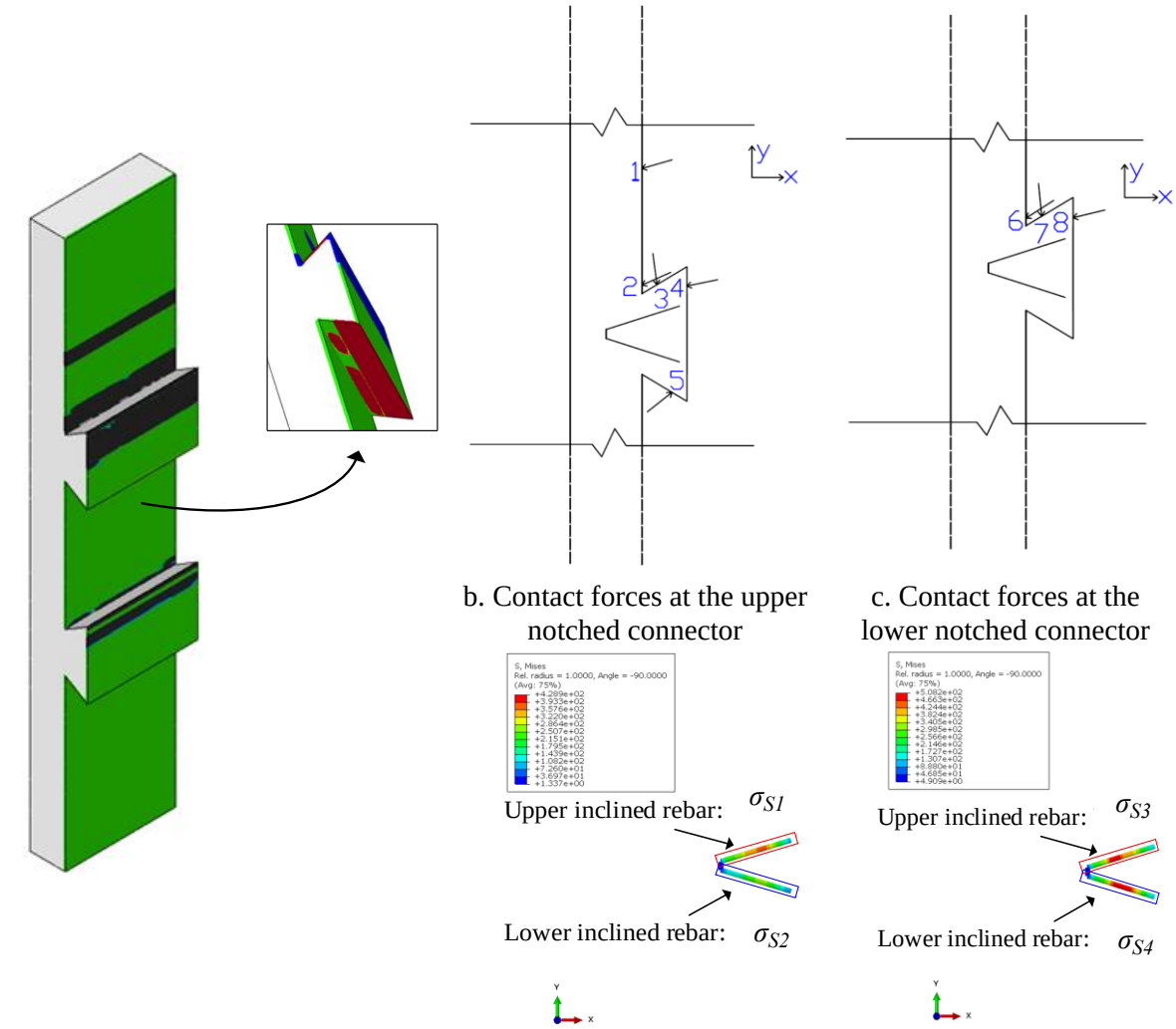

a. Areas subjected to contact forces

b. Contact forces at the upper notched connector

c. Contact forces at the lower notched connector

d. V-shape rebars stresses at the upper notched connector

e. V-shape rebars stresses at the lower notched connector

Figure 53: Contact forces and tensile stress of V-shape rebars obtained from the FE model at the maximum load level.

Table 31: Contact forces and its orientation at each location along the interface layer of the concrete panel at the maximum load level.

Location	1	2	3	4	5	6	7	8
F_x [kN/m]	-7.75	-65.29	54.66	-59.22	28.33	-17.45	33.70	-56.49
F_y [kN/m]	-2.25	-29.09	-416.65	-12.21	22.45	-11.17	-346.59	-13.51
θ [^{0}]	73.79	65.98	-7.47	78.35	51.61	57.39	-5.55	76.55

Table 32 summarizes the reaction forces in horizontal and vertical directions, the reaction moment, as well as the tensile stress of V-shape rebars. σ_{S1} and σ_{S2} denote the stress in upper and lower inclined rebar of the upper notched connector, respectively, while σ_{S3} and σ_{S4} represent the stress in upper and lower inclined rebar of the lower notched connector, respectively (Figure 53d,e). At the maximum load level, only V-shape rebars in the lower notched connector experienced yielding stress while those in upper connector were subjected to a tensile stress of 429 MPa (see Figure 52).

Table 32: Reaction forces of the concrete panel and tensile stresses of V-shape rebars of the FE model obtained at the maximum load level.

RF_x [kN/m]	RF_y [kN/m]	M_z [kN.m/m]	σ_{S1} [MPa]	σ_{S2} [MPa]	σ_{S3} [MPa]	σ_{S4} [MPa]
93	812	21	429	280	501	508

Figure 54a presents the proposed strut-and-tie model based on the principal stress map and the applied external forces derived from the FE model. A total of 25 nodes were adopted in the strut-and-tie model. The compressive struts and tensile ties, denoted by $C_{i\rightarrow j}$ and $T_{i\rightarrow j}$ connecting node *i* to node *j*, were drawn in dash black lines and continuous black lines, respectively. The dash red lines represent the extension of struts from the surfaces of the concrete panel to the nodes of the strut-and-tie model. The choice of strut and tie dispositions (see Figure 54b) was given as following:

- Nodes 1, 3 and 13 were fixed in position with regard to the position and the orientation of the applied external forces F_1, F_2, and F_6, respectively.
- Ties $T_{4\rightarrow 5}$ and $T_{4\rightarrow 6}$ in the upper notched connector as well as ties $T_{14\rightarrow 15}$ and $T_{14\rightarrow 16}$ in the lower notched connector were positioned with respect to the angle of the V-shape rebars.
- For simplicity, external force F_5 was distributed to node 5 and node 6. From Figure 54d, the green lines represent the scheme used with account of equilibrium to distribute the load from force F_5 to node 5 and node 6.

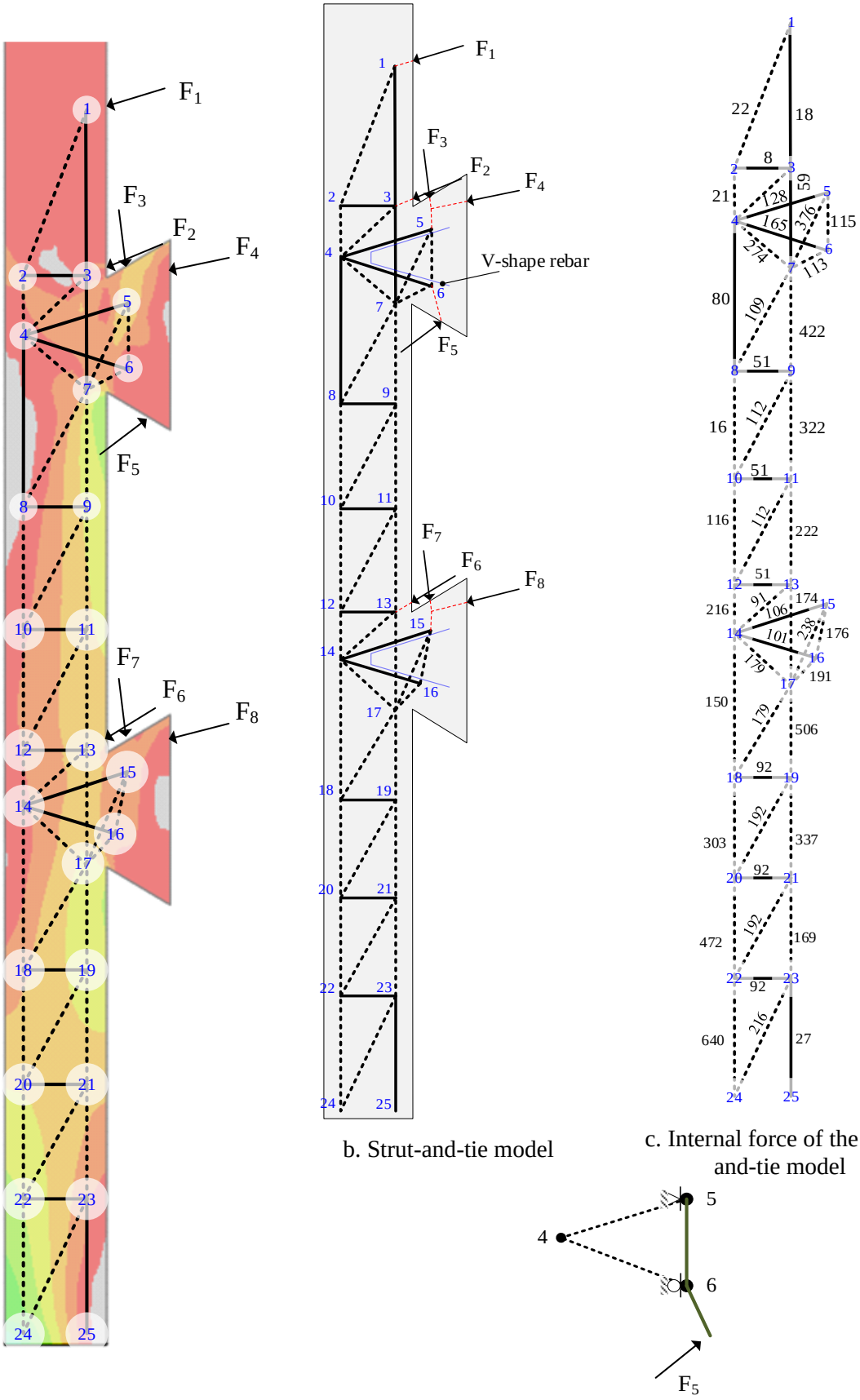

a. Stress map and external applied force

b. Strut-and-tie model

c. Internal force of the strut-and-tie model

d. Force transfer from F_5 to node 5 and node 6

Figure 54: Proposed strut-and-tie model deduced from the principal stress map of the FE model and the obtained internal force of the strut-and-tie model at the maximum load level.

By solving the nodal equilibrium equations of all nodes, the internal forces of the strut-and-tie model were determined and are presented in Figure 54b. In overall, according to the principal stress map, the strut-and-tie model demonstrated high accuracy in predicting the compressive and tensile regions in the concrete panel as well as the concentration region of the compressive force. For the validation of the strut-and-tie model, tensile forces T_{ij} deduced from FE model are computed as follows:

$$T_{ij}=f_{T_{ij}}A_s \tag{30}$$

where $f_{T_{ij}}$ is the tensile stress of the tie $T_{i\rightarrow j}$, and A_s is the cross-sectional area of the V-shape rebars. In the FE model, a total of six V-shape rebars with a diameter of 6 mm were adopted per meter linear. For the verification of ties $T_{4\rightarrow5}$, $T_{4\rightarrow6}$, $T_{14\rightarrow15}$, and $T_{14\rightarrow16}$, the stresses in the V-shape rebars deduced from the FE model, which was reported in Figure 53d,e and Table 32, were used. Comparisons of the results between the strut-and-tie model versus the FE model are summarized in Table 33. The parameter "Diff." represents the ratio of the strut-and-tie model results to the FE model results. Except for V-shape rebars, the finding indicates a good agreement of the horizontal and vertical reaction forces, as well as the bending moment with a maximum difference of four percent value. It should be reminded that in the FE model, only V-shape rebars in the lower notched connector experienced yielding stress at the maximum load level while the concrete and V-shape rebars were still able to resist more loads in the upper notched connector. As the contribution in tension and shear of the concrete in the upper notch is not presented in the strut-and-tie model, a non negligible discrepancy is inevitable.

Table 33: Comparison of the results between the strut-and-tie model and the FE model.

Test	RF_x [kN/m]	RF_y [kN/m]	M_z [kN.m/m]	T_{45} [kN/m]	T_{46} [kN/m]	$T_{14,15}$ [kN/m]	$T_{14,16}$ [kN/m]
FE model	93	812	21	73	48	85	86
Strut-and-tie	90	809	22	128	165	106	101
Diff.	0.96	1.00	1.02	1.76	3.46	1.25	1.18

B. Proposed model of strut-and-tie at yield stress of rebars

A new strut-and-tie model was developed using the results from the numerical simulation where V-shape rebars in both notched connectors were experiencing yielding stress (see Figure 55). At a load level of $0.92F_{max}$ corresponding to a slip of 1.6 mm, all the V-shape rebars in the notches of the FE model experienced yielding stress of around 500 MPa (see Figure 55). In this section, the strut-and-tie model was adjusted with regard to the new principal stress map and the applied contact forces.

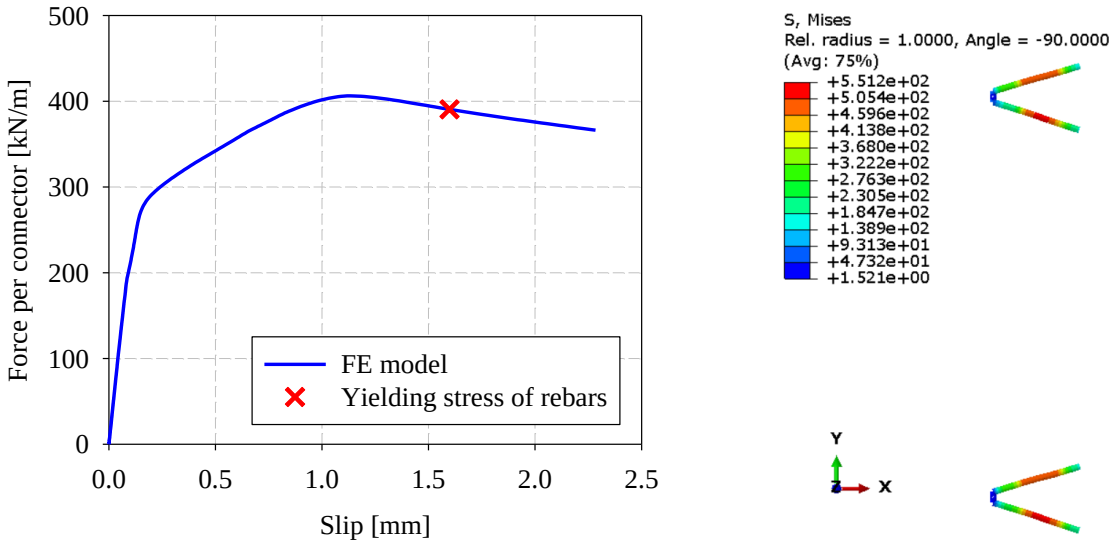

a. Force-slip curve of the FE model b. Yielding stress of rebars

Figure 55: Force-slip curve and yielding stress of V-shape rebars at post-peak loading stage.

Minor changes in the contact forces on the concrete panel were derived and are reported in Table 34. The positions of contact forces (F_1 to F_8) are displayed in Figure 56. The reaction force and bending moment as well as the stress on the V-shape rebars are summarized in Table 35.

Table 34: Contact forces and its orientation at each location along the interface layer of the concrete panel at the maximum load level.

Location	1	2	3	4	5	6	7	8
F_x [kN/m]	-2.30	-42.05	49.37	-68.46	27.80	-21.11	44.82	-88.09
F_y [kN/m]	-0.79	-18.52	-370.88	-9.82	59.52	-11.28	-376.39	-11.98
θ [^{0}]	71.08	66.23	7.58	81.84	25.03	61.88	6.79	82.26

Table 35: Reaction force of the concrete panel and V-shape rebars stress obtained at yield stress point of V-shape rebars.

RF_x [kN/m]	RF_y [kN/m]	M_z [kN.m/m]	σ_{S1} [MPa]	σ_{S2} [MPa]	σ_{S3} [MPa]	σ_{S4} [MPa]
102	743	24	505	539	511	551

The strut-and-tie model was redrawn as illustrated in Figure 56a, following the principal stress map and contact forces of the concrete panel, when the V-shape rebars in both notched connectors experienced yielding stress. As stated in the previous strut-and-tie model, certain nodes including node 1, node 3, node 5, node 6, node 13, and node 15 were positioned based on the orientation of contact forces, while ties $T_{4\rightarrow5}$, $T_{4\rightarrow6}$, $T_{14\rightarrow15}$, and $T_{14\rightarrow16}$ represented V-shape rebars. The disposition of strut-and-tie nodes and orientation of the contact forces in the upper and lower notched connectors at post-peak loading stage are detailed in Figure 56b.

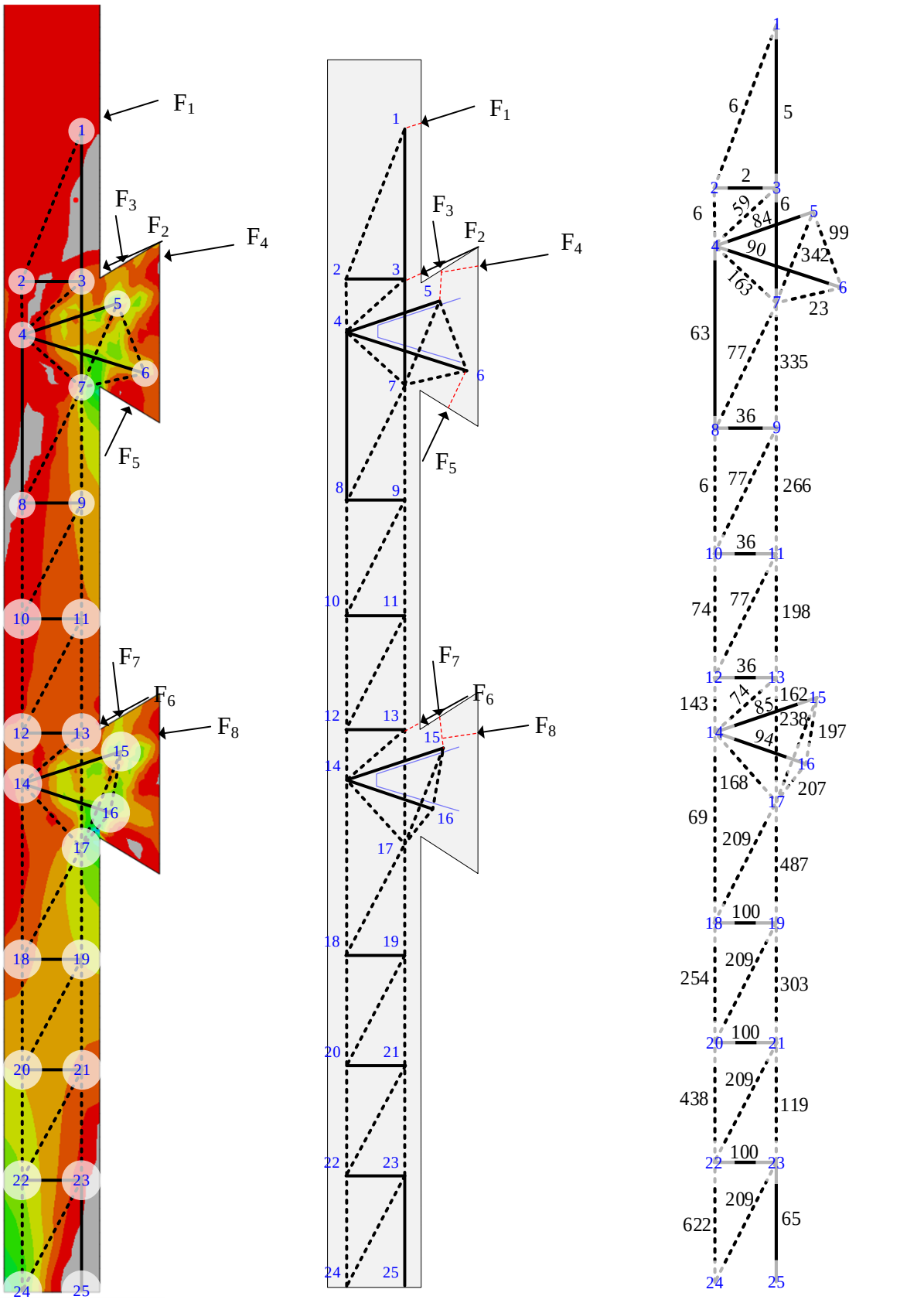

a. Stress map and external applied force

b. Strut-and-tie model

c. Internal force of the strut-and-tie model

Figure 56: Proposed strut-and-tie model deduced from principal stress map of FE model and the obtained internal forces of the strut-and-tie model at yielding stress of rebars.

By solving the equilibrium equations, the results of the internal forces of each compressive strut and tensile tie were obtained and are described in Figure 56c. To verify the proposed strut-and-tie model, the comparisons between the results obtained from the strut-and-tie model and those of the FE model are summarized in Table 36. In overall, it was observed that a better agreement between the strut-and-tie and the FE models was established when rebars experienced yielding stresses in both notched connectors at the post-peak loading stage. Except for the bending moment at the support, the highest difference was only two percent in reaction forces and tensile stresses of V-shape rebars. For the bending moment, the FE model exhibited 8 percent higher than the strut-and-tie model, which might be due to the inaccurate position of obtained contact forces. Besides, it was also necessary to check the capacity of the compressive struts and tensile ties as well as the connecting nodes in the notched connector zones to fully validate the strut-and-tie model.

Table 36: Comparison of the results between the strut-and-tie model versus the FE model.

Test	RFx [kN/m]	RFy [kN/m]	Mz [kN.m/m]	T_{45} [kN/m]	T_{46} [kN/m]	$T_{14,15}$ [kN/m]	$T_{14,16}$ [kN/m]
FE model	102	743	24	86	91	87	94
Strut-and-tie	100	740	22	84	90	85	94
Diff.	0.98	1.00	0.92	0.98	0.98	0.98	1.00

C. Verification of strut and tie capacities for the strut-and-tie model

In concrete, based on the study of Michelfelder [49], the failure at the notch typically occurs due to the excessive compressive stress on the top surface of the notch, the failure of the compressive struts, or the tensile failure of the tension tie. Figure 57 presents the compressive nodes, compressive struts, and tensile ties, which are then susceptible to failing in the concrete notch. It was necessary to verify nodes 5 and 15 against the applied compressive stress on the top surface of notch connectors, and to verify compressive struts $C_{5\rightarrow6}$, $C_{5\rightarrow7}$, $C_{15\rightarrow16}$, and $C_{15\rightarrow17}$ against the concrete strength. Furthermore, tensile ties $T_{4\rightarrow5}$, $T_{4\rightarrow6}$, $T_{14\rightarrow15}$, $T_{14\rightarrow16}$ were verified against the strength of the V-shape rebars.

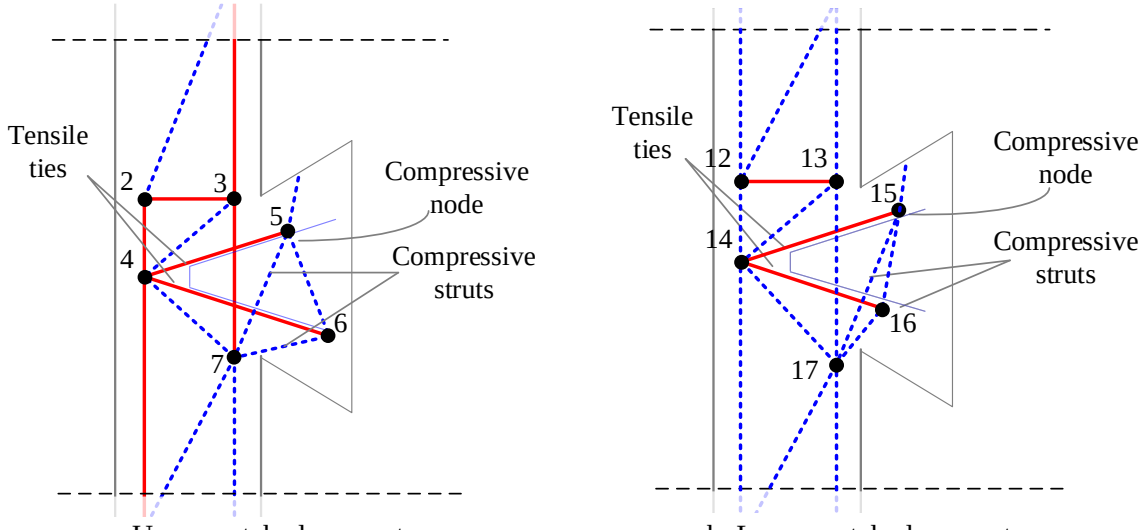

a. Upper notched connector b. Lower notched connector

Figure 57: Compressive node, compressive strut, and tensile tie of the strut-and-tie model subjected to possible failure mechanisms based on the study of Michelfelder [49].

In accordance with Eurocode 2 [25], the design value for the compressive stress resistance, σ_{Rd}, within nodes can be determined by:

$$\sigma_{Rd}=kv'f_{cd} \quad (31)$$

with

$$v'=1-f_{ck}/250 \quad (32)$$

where k is the parameter accounting for multi-axial stress, v' is a reduction factor, and f_{cd} and f_{ck} are the design value (f_{cd} = 23.33 MPa) and characteristic value of concrete compressive strength (f_{ck} = 35 MPa), respectively. In this study, the parameter accounting for multi-axial stress, k, was taken as 0.85 as one anchored tie of the V-shape rebar provided tension in one direction (see Figure 57). From eq. (31), the design value of compressive node was found to be σ_{Rd} = 17.61 MPa.

Additionally, the actual stress on the top surface of both notched connectors, which was distributed to node 5 and node 15, can be determined by $\sigma=F/A$ where F is the applied compressive force, and A is the corresponding area subjected to compressive force. From the diagram of the strut-and-tie model (see Figure 56a) and contact forces applied on concrete panel (see Table 34), node 5 was subjected to contact forces F_3 and F_4 corresponding to 381 kN, while node 15 was subjected to contact forces F_7 and F_8 corresponding to 388 kN. For the area A, it is assumed equal to $A=b\times h_{l,CLT}$, where b is the width of the specimen and $h_{l,CLT}$ is the thickness of the first longitudinal layer of the CLT panel. Therefore, the compressive stress subjected to node 5 and node 15 were found to be $\sigma_{Node,5}$ = 11.55 MPa and $\sigma_{Node,15}$ = 11.76 MPa, respectively.

For the verification of compressive nodes 5 and 15, it was found that the compressive stress acting on node 5, $\sigma_{Node,5}$ = 11.55 MPa, and on node 15, $\sigma_{Node,15}$ = 11.76 MPa, were lower than the design value of compressive node, σ_{Rd}=17.61 MPa; therefore, indicating a sufficient capacity of the compressive node to withstand with the applied compressive force.

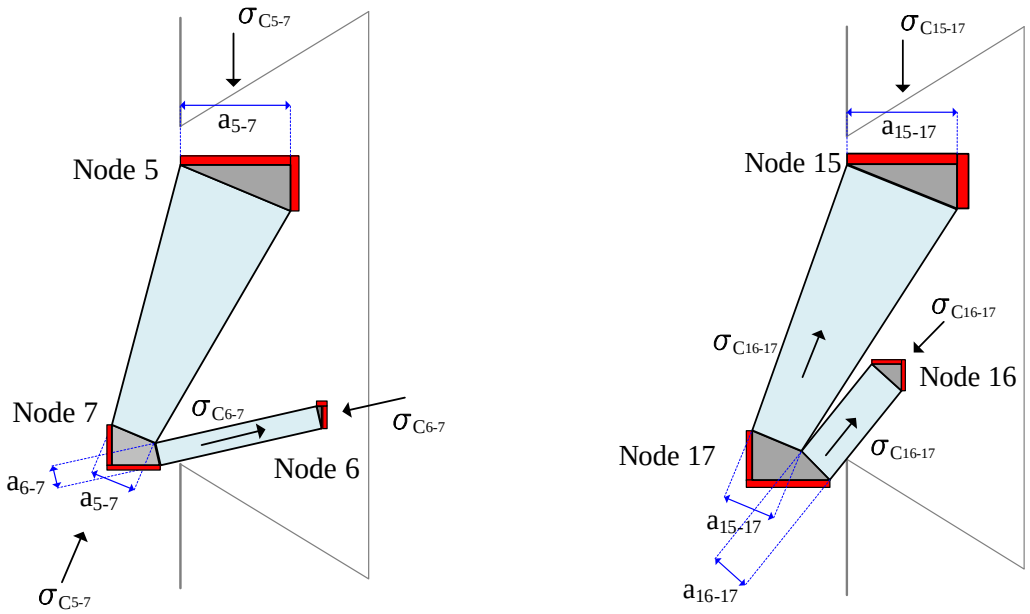

a. Upper notched connector b. Lower notched connector

Figure 58: Verification of compressive strut members.

For the strut member, the compressive stress, $\sigma_{C_{ij}}$, should not be higher than the concrete strength f_{cd} which can be computed using the eq. (33) [25]:

$$\sigma_{C_{ij}} = C_{ij}/A_{ij} \leq f_{cd} \tag{33}$$

where C_{ij} is the force subjected to the compressive strut $C_{i\rightarrow j}$, while A_{ij} is the cross-sectional area of the compressive strut $C_{i\rightarrow j}$. The cross-sectional area of the compressive strut A_{ij} was considered in rectangular shape with the dimension of the width of the pushout model, b, and width of strut, a_{ij}. The width of strut member is defined in Figure 58. Table 37 presents the details for the computation of compressive strut members. With the design compressive strength of concrete f_{cd} = 35/1.5= 23.33 MPa, the compressive stress of struts $C_{6\rightarrow 7}$, $C_{5\rightarrow 7}$, $C_{6\rightarrow 7}$, and $C_{5\rightarrow 7}$ obtained from eq. (33) as shown in Table 37 remained in the allowable limits of compressive strength of the concrete. Therefore, the compressive strut members in both notched connectors were able to transfer the force between nodes.

Table 37: Verification of the compressive struts in the strut-and-tie model.

Strut $C_{i\rightarrow j}$	a_{ij} [mm]	b_{ij} [mm]	C_{ij} [kN]	$\sigma_{C_{ij}}$ [MPa]	f_{cd} [MPa]
$C_{5\rightarrow 7}$	15.23	1000	342	22.46	23.33
$C_{6\rightarrow 7}$	6.74		23	3.40	
$C_{15\rightarrow 17}$	13.77		238	17.07	
$C_{16\rightarrow 17}$	12.38		207	16.72	

Furthermore, the tensile ties obtained from the strut-and-tie model in the notched connector zone were verified against the tensile stress in V-shape rebars in the FE model. The tensile stress $f_{T_{ij}}$ of the tensile tie $T_{i\rightarrow j}$ can be determined using eq. (30). Table 38 reports the comparison of the tensile stress between the strut-and-tie model and the FE model. The value in brackets refers to the ratio of obtained tensile stress between the strut-and-tie model and the FE model. It was found that tensile stress in V-shape rebars higher than rebar resistance $f_{T_{ij}} \geq f_s$=500 MPa, which indicated that the FE model took into account the hardening behavior of rebar reinforcements.

Table 38: Verification of tensile ties in the strut-and-tie model.

Tie $T_{i\rightarrow j}$	T_{ij} [kN]	A_s [mm^2]	$f_{T_{ij}}$ [MPa]	f_s [MPa]
$T_{4\rightarrow 5}$	84	54π	493	500
$T_{4\rightarrow 6}$	90		530	500
$T_{14\rightarrow 15}$	85		499	500
$T_{14\rightarrow 16}$	94		552	500

From the sufficient strength of the compressive nodes and strut members in notched connectors, as well as the verification of the tensile ties, the proposed strut-and-tie model was validated for this studied notched connector and can be used to evaluate the connection strength and stress distribution in the concrete panel.

3.6.2 Rolling shear resistance of the CLT panel

Based on the results of both experimental tests and the parametric study, rolling shear behavior of the cross-layer of the CLT panel was seen as the primary cause of the failure of the pushout specimen. To evaluate the rolling shear resistance of the cross-layer of the CLT panel, a simple analytical formula is adopted as given in eq.(34).

$$F_r = f_r b l_{eff} \tag{34}$$

where f_r is the characteristic rolling shear strength; b is the width of the specimen; l_{eff} is the effective length of the cross-layer subjected to shear loading. For a better comparison, the characteristic rolling shear strength f_r = 1.49 MPa was taken as the rolling shear strength obtained in the characterization tests, which was consistent with the shear strength adopted in the FE model. Additionally, the results were compared to the maximum force obtained from the parametric study of Mid. cases, where rolling shear failure was observed.

The effective length of the cross-layer, as given in eq. (34), was computed by measuring the length of timber subjected to high rolling shear stress in the FE model at the maximum load level. Figure 59 depicts the diagram of the effective length of the cross-layer, along with the examples of the effective length in the C-Ref.M case and case C5-1M. Except for case C5-1M, the effective length included the length on the top of the upper notched connector l_1 and the length between both notched connectors l_2 (see Figure 59b). In case C5-1M, due to the short notch depth, the effective length of the cross-layer l was considered from the top surface to the upper corner of the lower notched connector (see Figure 59c).

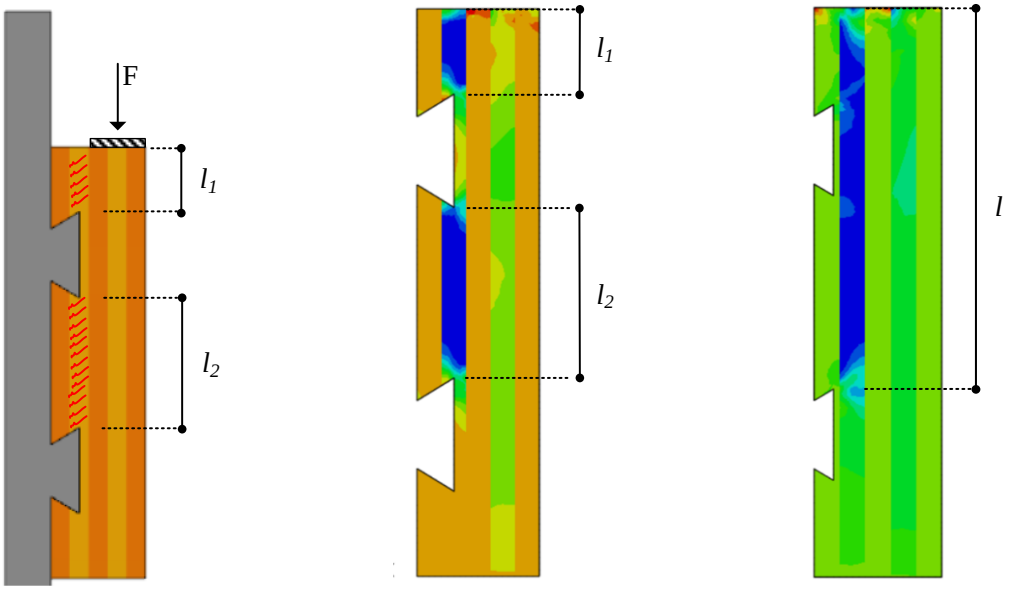

a. Diagram of effective length b. C-Ref.M case c. Case C5-1M

Figure 59: Effective length subjected to loading on the CLT panel.

Comparisons of rolling shear resistance obtained from eq. (34) with the FE model results are summarized in Table 39. The value in brackets indicates the difference between the resistance of the analytical method and the FE model. The rolling shear resistance obtained from the analytical formula showed a good agreement, ranging from 93 percent to 99 percent, compared to the maximum force in

the FE model. This indicated that a simple analytical method could be adopted to estimate the rolling shear resistance of the cross-layer of the CLT panel, although a slight underestimation should be expected.

It should be reminded that that rolling shear resistance obtained from eq.(34) considers only the failure of the cross-layer of the CLT panel. A higher rolling shear resistance should be obtained when a rolling shear failure occurs in CLT-concrete composite floors. Based on simulation results obtained from C-Ref and C-Ref.M cases (see 3.4.2.2), the connection resistance governed by the rolling shear failure in the CLT panel should be equal to 1.38 times the value obtained from eq.(34). However, this suggestion needs experimental validations.

Table 39: Comparisons of the shear strength derived from the computation using eq. (34) and obtained from the FE model.

Case		Parameter	F_r [kN/m]	F_{max} [kN/m]
C-Ref.M			251 (0.93)	269
C1	C1-1M	f_c=25 MPa	251 (0.94)	268
	C1-2M	f_c=45 MPa	251 (0.93)	270
C2	C2-1M	h_c=50 mm	251 (0.94)	267
	C2-2M	h_c=100 mm	251 (0.93)	272
C3	C3-1M	l_t=375 mm	391 (0.96)	410
C4	C4-2M	l_n=140 mm	207 (0.96)	215
C5	C5-1M	d_n=25 mm	363 (0.99)	368
C6	C6-1M	A_s=0 mm^2	251 (0.93)	269
	C6-2M	A_s=56.55 mm^2	251 (0.93)	269

3.6.3 Compressive resistance of the concrete and timber in the notched connection

In this section, the concrete and timber compressive resistances of the notched connection were determined and were compared with maximum forces of cases obtained in the parametric study. Figure 60 illustrates the failure mechanism of concrete and timber crushing in notched connection. First, the compressive resistance of the concrete notch $F_{c,con.}$ can be assessed using eq. (35) [44]:

$$F_{c,con.}=f_c b d_n \tag{35}$$

where f_c is the compressive strength of the concrete, b is the width of the specimen, and d_n is the notch depth.

For the timber crushing in the notch connection, only the longitudinal layer of the CLT is assumed to transfer the load. Accordingly, the compressive resistance $F_{c,tim.}$ can be determined in the following expression [44]:

$$F_{c,tim.}=f_{c,0}bh_{l,CLT} \quad (36)$$

where $f_{c,0}$ is the compressive strength of the timber parallel to grain, while $h_{l,CLT}$ is the thickness of the longitudinal layer of the CLT panel.

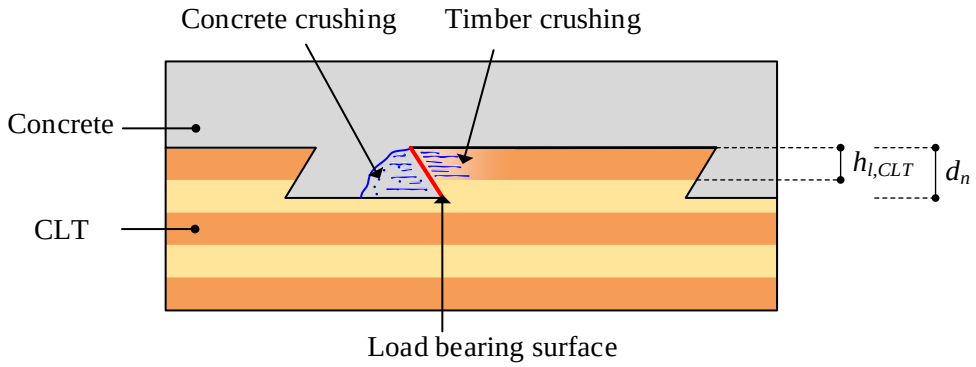

Figure 60: Compressive failure mechanisms in concrete and timber of the notched connection in case C-Ref.

Table 40 summarizes the compressive resistance of concrete and timber in the notched connection. Furthermore, the maximum forces obtained from the parametric study were also presented for the comparison. It was found that the compressive resistance of concrete and timber in all cases was higher than the maximum forces obtained from the parametric study, confirming that the failure mechanism was not governed by the concrete or timber crushing.

Table 40: Compressive resistances of concrete and timber in the notched connection obtained from the computation of eqs. (35) and (36).

Case	Parameter	$F_{max,FEM}$ [kN/m]	$F_{c,con.}$ [kN/m]	$F_{c,tim.}$ [kN/m]
C-Ref		431	1750	1023
C1-1	f_c=25 MPa	429	1250	1023
C1-2	f_c=45 MPa	430	2250	1023
C2-1	h_c=50 mm	419	1750	1023
C2-2	h_c=100 mm	435	1750	1023
C3-1	l_t=375 mm	526	1750	1023
C4-1	l_n=90 mm	425	1750	1023
C4-2	l_n=140 mm	370	1750	1023
C5-1	d_n=25 mm	515	875	775
C6-1	A_s=0 mm^2	364	1750	1023
C6-2	A_s=56.55 mm^2	427	1750	1023

3.6.4 Conclusion on analytical methods

Different analytical methods provided in standards were adopted to evaluate the resistance of possible failure mechanisms of the TCC pushout specimen and verified against the results from the parametric study. Two failure modes were obtained from the parametric study, including the shear failure of the concrete notch and the rolling shear failure of the cross-layer of the CLT panel.

For the concrete shear resistance at the shear plane of the concrete notch, various methods provided in design codes such as Eurocode 2 [25], ACI 318-14 [45], AASHTO [46], and the technical specification CEN/TS 19103 [44] were first tested. High discrepancies of the concrete shear resistance were obtained, ranging from 86 percent lower to 90 percent higher values in comparison to maximum forces in FE simulations. As an alternative, a strut-and-tie model, which was based on the principal stress map and contact forces in the concrete panel obtained from the validated FE model, was developed to estimate the maximum force. In this model, the concrete shear resistance was determined when V-shape rebars experienced yielding stresses. It was shown that the strut-and-tie model was able to indicate a close correlation with the numerical simulation in terms of internal forces and stress paths in the concrete panel.

For the rolling shear resistance of the CLT panel, a simple analytical formula could give a good estimation in comparison to FE models. Besides, the remaining two possible failure mechanisms, i.e. compressive failure in concrete and compressive failure in timber at the load bearing surface of the notched connection, were also estimated by the expression proposed in the technical specification CEN/TS 19103 [44]. The estimated resistance of concrete and timber in compressive failure was higher than the maximum force of cases observed in the parametric study, confirming that no crushing of concrete or timber in the specimen occurred in the simulation.

In conclusion, to estimate the connection strength, which is governed by various failure mechanisms, the analytical strut-and-tie model can be employed to determine the concrete shear resistance of the concrete notch while simple formulae are sufficient to predict the CLT rolling shear resistance of the CLT panel, and the compressive resistances of the concrete notch and timber at the load-bearing surface of the notched connection.

3.7 Conclusion

This chapter has presented the study of the dovetail notched connector as the connection system for the CLT-concrete composite floor. This notched connector featured dovetail shape configuration and was reinforced by V-shape rebars placed inside the concrete notch. The behavior of the notched connector was initially investigated by conducting a series of three symmetrical pushout tests on large-scale specimens. The test results showed the high shear resistance and stiffness of the connectors. However, the ductility of the connectors was low, as the failure mode of all specimens was governed by the limited rolling shear resistance of the cross-layer of the CLT panel. To gain further insight into the efficiency of the tested connection system, a comparison of mechanical properties was made with other notched connection systems found in literature. The comparison indicated that the notched connector in this study had similar performance in comparison to usual notched connections, indicating the efficiency of this dovetail notched connector in the TCC system.

Subsequently, a numerical study based on experimental pushout test results was carried out using ABAQUS/EXPLICIT [22], to fully understand the notched connector behavior including the load transfer mechanism, and stress distribution at each component. The actual geometry corresponding to the experimental test setup, the interface interactions between each component, the assigned material properties, and the boundary conditions of the model were taken into account to simulate the actual behavior of pushout tests. The FE model was capable of reproducing the same failure mode and giving a good agreement of the force-slip curve compared to that of pushout tests. In the FE model, the timber Poisson ratios of zero and the friction coefficient between concrete and CLT panels of 0.62 were adopted. In order to investigate the effect of these two parameters, various other values taken from the literature, were tested in the FE model. For the Poisson ratio, a little effect was observed. For the friction coefficient, the FE model with the friction coefficient of 0.62, which was adopted from tests by Aira et al. [33], resulted in a good outcome in comparison to the experimental tests. When using the friction coefficient of 0.40, which was recommended by Eurocode 5 [28], the FE model yielded a similar maximum force, but 15 percent lower value in comparison to the case with friction coefficient of 0.62.

The results of the pushout test model also highlighted that, by adopting the experimental loading steel block, the whole load was not transferred by the cross-layer of the CLT panel when rolling shear failure occurred. This was due to the contribution of load transfer from the loading block to the notched connector via the outer longitudinal layer of the CLT panel. In order to investigate the behavior of pure rolling shear action in the load transfer mechanism from timber to concrete panels, a new simulation of pushout test with the configuration of middle loading block (C-Ref.M case) was made. The findings showed that the maximum force decreased by 38 percent value, while slip moduli at SLS and ULS decreased by 37 percent value in comparison to that of the validated model with the configuration of experimental loading block (C-Ref case). Since the whole CLT section will be subjected to the applied load when loading is applied to the CLT-concrete composite floor, the resistance and stiffness obtained in C-Ref case with experimental loading configuration should be adopted to define the bending stiffness of the CLT-concrete composite floor.

The validated pushout model with experimental loading configuration (C-Ref case) and pushout model with middle loading configuration (C-Ref.M case) were then adopted to conduct a parametric study with variations in geometry and material properties to provide further insight and optimized choices of the connection system. From the numerical results of the parametric study, high strength and stiffness of the connection system were still obtained in most cases. Thus, it was possible to improve the ductility of the proposed notched connection by prioritizing the shear failure of the concrete notch, if a sufficient number of V-shape rebars was placed inside the notch. This prioritization could be obtained by increasing the spacing between the connectors. The concrete failure should happen for a load 22 percent larger than the experimental resistance obtained by pushout tests. This numerical conclusion calls for an experimental validation.

Furthermore, analytical methods derived from design codes such as Eurocode 2 [25], ACI 318-14 [45], AASHTO [46], and the technical specification CEN/TS 19103 [44], were tested to evaluate the load-carrying capacity of the pushout specimen for four possible different failure mechanisms. The results were then compared with those from experimental tests and from parametric study. For the shear resistance of the concrete notch, a limited correlation between design codes and the parametric study was obtained. As an alternative, a strut-and-tie model was developed, taking into account the principal stress map and contact forces of the concrete panel obtained from the FE simulation. Accordingly, it

was found that the strut-and-tie model was able to produce a close result compared to the numerical simulation in terms of internal forces and stress paths in the concrete panel. For the rolling shear resistance of the CLT panel, a simple analytical equation was applicable. Moreover, based on simulation results obtained from C-Ref and C-Ref.M cases, the connection resistance governed by the rolling shear failure in the CLT panel should be equal to 1.38 times the value obtained from such a mentioned equation. The remaining two possible failure mechanisms in the notched connection, including the compressive failures in concrete and in timber, were also estimated by the expression proposed in the technical specification CEN/TS 19103 [44].

In conclusion, following extensive studies in experimental tests, numerical studies, and analytical approaches, it is found that the dovetail notched connection system exhibits high strength and stiffness; however, its ductility is limited if the failure is governed by sudden collapse induced by rolling shear failure of the cross-layer of the CLT panel. Based on the developed FE model of the pushout test, it is shown that the ductility of the notched connection system can improve by inducing a shear failure in the concrete notch with sufficient shear reinforcements (V-shape rebars). Additionally, a developed strut-and-tie model can be used to illustrate the load transfer mechanism in concrete slab and to predict the concrete shear failure of the concrete notch, while a simple expression of analytical method is able to determine the rolling shear resistance of the CLT panel.

3.8 References

[1] Ceccotti, A. (2002). Composite concrete-timber structures. Progress in structural engineering and materials, 4(3), 264-275.

[2] Dias, A. M. P. G. (2005). Mechanical behavior of timber–concrete joints. Doc-toral Thesis. Civil Engineering, University of Coimbra, Portugal.

[3] Yeoh, D., Fragiacomo, M., De Franceschi, M., & Heng Boon, K. (2011). State of the art on timber-concrete composite structures: Literature review. Journal of structural engineering, 137(10), 1085-1095.

[4] Boccadoro, L. (2016). Timber-concrete composite slabs made of beech laminated veneer lumber with notched connection. IBK Bericht, 371.

[5] Van der Linden, M. (1999). Timber concrete composite floors. PhD. Delft University of Technology, The Netherlands.

[6] Gutkowski, R. M., Brown, K., Shigidi, A., & Natterer, J. (2004). Investigation of notched composite wood–concrete connections. Journal of Structural Engineering, 130(10), 1553-1561.

[7] Deam, B. L., Fragiacomo, M., & Buchanan, A. H. (2008). Connections for composite concrete slab and LVL flooring systems. Materials and Structures, 41, 495-507.

[8] Boccadoro, L., Zweidler, S., Steiger, R., & Frangi, A. (2017). Bending tests on timber-concrete composite members made of beech laminated veneer lumber with notched connection. Engineering Structures, 132, 14-28.

[9] Monteiro, S. R. S., Dias, A. M. P. G., & Negrão, J. H. J. O. (2013). Assessment of timber—concrete connections made with glued notches: Test set-up and numerical modeling. Experimental Techniques, 37, 50-65.

[10] Thai, M. V., Ménard, S., Elachachi, S. M., & Galimard, P. (2020). Performance of notched connectors for CLT-concrete composite floors. Buildings, 10(7), 122.

[11] European standard EN 26891, Timber Structures - Connections Made With Mechanical Fasteners General Principles for the Determination of Strength and Deformation Characteristics, CEN, Brussels (1991).

[12] European standard EN 1994-1-1, Eurocode 4: Design of composite steel and concrete structures - Part 1-1: General rules and rules for buildings, CEN, Brussels (2004).

[13] EN 206, B. S. (2013). Concrete-Specification, performance, production and conformity. British Standards Institution, Her Majesty Stationery Office, London, United Kingdom.

[14] Avis-Technique. 3.3/17-925 v1, Panneaux bois `a usages structurel – mur et plancher, Wood structural panels, 2017.

[15] European standard EN 1990-1-1, Eurocode — Basis of structural design, CEN, Brussels (2004).

[16] European standard EN 1995-1-1, Eurocode 5: Design of timber structures- Part 1-1: General — Common rules and rules for buildings, CEN, Brussels (2004).

[17] Dias, A. M. P. G. (2012). Analysis of the nonlinear behavior of timber-concrete connections. Journal of structural engineering, 138(9), 1128-1137.

[18] Manthey, M. (2015). Comportement des poutres mixtes bois-béton sous sollicitations accidentelles (Doctoral dissertation, Rennes, INSA).

[19] Boccadoro, L. (2016). Timber-concrete composite slabs made of beech laminated veneer lumber with notched connection. IBK Bericht, 371.

[20] Mönch, S. & Kuhlmann, U. (2018): Investigations on the effect of geometry in timberconcrete composite pushout tests with notched connections. In: Seoul National University (Ed.): WCTE 2018, World Conference on Timber Engineering, Seoul (Republic of Korea), 20.08.-23.08.2018

[21] Jiang, Y., & Crocetti, R. (2019). CLT-concrete composite floors with notched shear connectors. Construction and Building Materials, 195, 127-139.

[22] Dassault Systems Simulia Corporation, ABAQUS Analysis User's Manual 6.10-EF, Dassault Systems Simulia Corporation, Providence, RI, USA, 2010.

[23] Cedolin, L., Dei Poli, S., & Crutzen, Y. R. (1977). Triaxial stress-strain relationship for concrete. Journal of the Engineering Mechanics Division, 103(3), 423-439.

[24] Alfarah, B., López-Almansa, F., & Oller, S. (2017). New methodology for calculating damage variables evolution in Plastic Damage Model for RC structures. Engineering structures, 132, 70-86.

[25] European standard EN 1992-1-1, Eurocode 2: Design of concrete structures - Part 1-1: General rules and rules for buildings, CEN, Brussels (2004).

[26] CEB-FIP. Model Code 2010. London: Thomas Telford; 2010.

[27] European standard EN 338, Structural Timber—Strength Classes, CEN, Brussels (2003).

[28] European standard EN 1995-2, Eurocode 5: Design of timber structures- Part 2: Bridges, CEN, Brussels (2004).

[29] Dias, A. M. P. G., Van de Kuilen, J. W., Lopes, S., & Cruz, H. (2007). A non-linear 3D FEM model to simulate timber–concrete joints. Advances in Engineering Software, 38(8-9), 522-530.

[30] Hill, R. (1998). The mathematical theory of plasticity (Vol. 11). Oxford university press.

[31] T. Kartheek, T. V. Das, 3D modelling and analysis of encased steel-concrete composite columnusing ABAQUS. Materials Today: Proceedings, 27, 1545-1554. using ABAQUS. Materials Today: Proceedings, 27 (2020), 1545-1554.

[32] Faridmehr, I., Osman, M. H., Tahir, M. M., Nejad, A. F., & Azimi, M. (2015). Seismic and progressive collapse assessment of new proposed steel connection. Advances in Structural Engineering, 18(3), 439-452.

[33] Aira, J. R., Arriaga, F., Íñiguez-González, G., & Crespo, J. (2014). Static and kinetic friction coefficients of Scots pine (Pinus sylvestris L.), parallel and perpendicular to grain direction. Materiales de Construcción, 64(315), e030-e030.

[34] Van de Kuilen, J. W. G. (2004). 3D-numerical modelling of DVW-reinforced timber joints. In 8th World Conference on Timber Engineering (pp. 137-142). WCTE 2004 Secretariat.

[35] Lotfollahi M, Alinia MM, Taciroglu E. Inelastic buckling simulation of steel braces through explicit dynamic analyses. In: Num anal & appl math, ICNAAM 2011, AIP conf proc, vol. 1389; 2011. p. 2012–5.

[36] Prior, A. M. (1994). Applications of implicit and explicit finite element techniques to metal forming. Journal of Materials Processing Technology, 45(1-4), 649-656.

[37] Xu, B. H., Bouchaïr, A., Taazount, M., & Racher, P. (2013). Numerical simulation of embedding strength of glued laminated timber for dowel-type fasteners. Journal of wood science, 59, 17-23.

[38] Guan, Z. W., & Zhu, E. C. (2009). Finite element modelling of anisotropic elasto-plastic timber composite beams with openings. Engineering Structures, 31(2), 394-403.

[39] Oudjene, M., Khelifa, M., Segovia, C., & Pizzi, A. (2010). Application of numerical modelling to dowel-welded wood joints. Journal of adhesion science and technology, 24(2), 359-370.

[40] Bedon, C., & Fragiacomo, M. (2017). Three-dimensional modelling of notched connections for timber–concrete composite beams. Structural Engineering International, 27(2), 184-196.

[41] Mirdad, M. A. H., & Chui, Y. H. (2020). Stiffness prediction of Mass Timber Panel-Concrete (MTPC) composite connection with inclined screws and a gap. Engineering Structures, 207, 110215.

[42] Zhang, L., & Chui, Y. H. (2019). Numerical study of the geometry effect of notched connections in mass timber panel-concrete composite floors. Modular and Offsite Construction (MOC) Summit Proceedings, 587-596.

[43] Mirdad, M. A. H., Daneshvar, H., Joyce, T., & Chui, Y. H. (2021). Sustainability design considerations for timber-concrete composite floor systems. Advances in Civil Engineering, 2021, 1-11.

[44] CEN/TS 19103 :2021. Eurocode 5 : Design of Timber Structures - Structural design of timber-concrete composite structures – Common rules and rules for buildings. European Committee for Standardization (CEN): Brussels, Belgium, 2021.

[45] Building code requirements for structural concrete and commentary. (2014). ACI 318-14, American Concrete Institute, Farmington Hills, Mich.

[46] AASHTO LRFD Bridge Design Specifications. Washington, DC: Association of State Highway and Transportation Officials, 2012.

[47] Ritter, W. (1899). The Hennebique construction method. Die Bauweise Hennebique"), Schweizerische Bauzeitung, 33(7), 41-61.

[48] Schlaich, J., Schafer, K., & Jennewein, M. (1987). Towards a consistent design of reinforced concrete structures. PCI Journal, 32(3), 74-150..

[49] Michelfelder BC. Trag- und Verformungsverhalten von Kerven bei Brettstapel-Beton-Verbunddecken, Dissertation, Universität Stuttgart, 2006.

CHAPTER 4

The global behavior of CLT-concrete composite floor

This page is intentionally left blank.

Contents

4.1 Introduction

Timber-concrete composite floors have been increasingly studied for medium-to-large span structures due to the eco-friendly benefits of timbers, as demonstrated in various papers (e.g., [1], [2], [3], among many others). The idea is to combine concrete with timber in order to improve performances to meet the serviceability criteria such as deflection, acoustic, and vibration requirements that are hardly fulfilled using timber alone. This composite floor technique consists of a timber deck (made of solid or engineered timber) in the predominant tensile zone, a relatively thin layer of concrete cast above the timber members in the compression zone, and a system of shear connection between the two layers. The global behavior of such composite structures depends on an efficient connection system to transfer shear forces between the concrete and the timber panels with limited slips and uplifts. Indeed, the composite action ensured by the connection leads to significant improvements in bending stiffness, load-carrying capacity, sound insulation, and vibration performance when compared to simple timber floors [4], [5], [6].

The shear capacities (resistance and stiffness) of the proposed notched connection system have been studied in chapter 3. The results showed that the dovetail notched connection has high resistance and stiffness. In this chapter, the global behavior of CLT-concrete composite floors (HOBOA system) with studied connection system is assessed. First, a series of two full-scale bending tests is conducted with different assumptions of support condition. The experimental results are then compared with the estimations obtained from analytical and simple numerical calculations. The structure of this chapter is divided into the following sections. Section 4.2 describes the full-scale experimental tests on the HOBOA composite floor by two bending tests. Then, section 4.3 presents an numerical application of the gamma method to the present CLT-concrete floor and the comparison between the results obtained from the experimental tests and those of the gamma method. In order to assess the behavior of the CLT-concrete composite floor, section 4.4 reports the description of two simple engineering models: beam grid model and orthotropic plate model in engineering program [7]. In addition, a discussion on bi-dimensional behavior using the orthotropic plate model is also conducted to optimize and provide an accurate model to represent the actual two-way floor (bi-dimensional effect) under different assumptions of support system, loading configuration, and mechanical properties of the composite floor cross-section in transversal direction.

4.2 Experimental flexural test

4.2.1 Introduction

Experimental flexural tests were conducted to assess the global mechanical performance of the CLT-concrete floors with the dovetail notched connection system. Two large-scale composite specimens (HBF1 and HBF2) were subjected to four-point bending tests in order to validate the effectiveness of the new connectors. In bending test setups, linear support system and point support system were considered and implemented to represent the actual behavior of the floor system. Furthermore, the bending stiffness determined from the experimental tests was compared to the results of other TCC floors in previous studies in order to determine the performance of the HOBOA system in comparison to other TCC systems with usual notched connection in the literature.

4.2.2 Specimen and test setup

Two identical slab specimens were designed and fabricated. Each specimen had a dimension of 3200×6710×245 mm and was composed of a 5-layer-CLT panel with a thickness of 165 mm connected to a reinforced concrete panel with a thickness of 85 mm by a series of 13 notched connectors (see Figure 1). The concrete slab was reinforced with a rebar mesh type ST15. Notch configurations are shown in Figure 1a. For rebar steel cages placed inside concrete notches, the shape and dimensions are consistent with those adopted in pushout specimens as described in chapter 3. The concrete was cast directly on the CLT panels without laying plastic films nor applying any paint. Figure 2 shows the specimen before the casting of concrete.

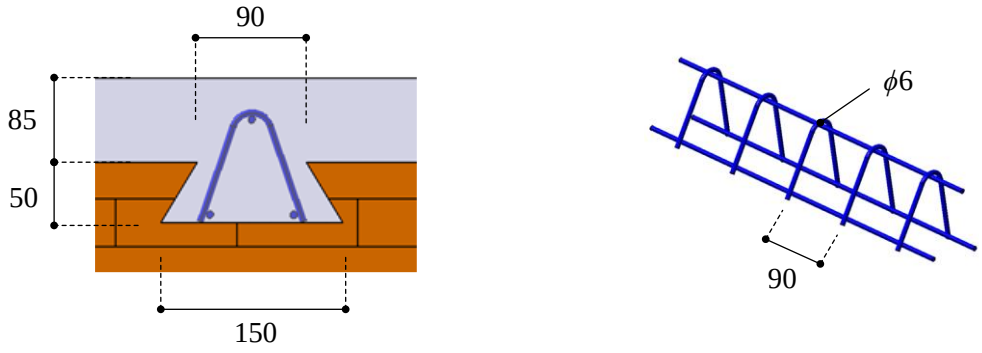

i. Notched configuration ii. V-shape rebar cage

a. Dovetail notched connection system

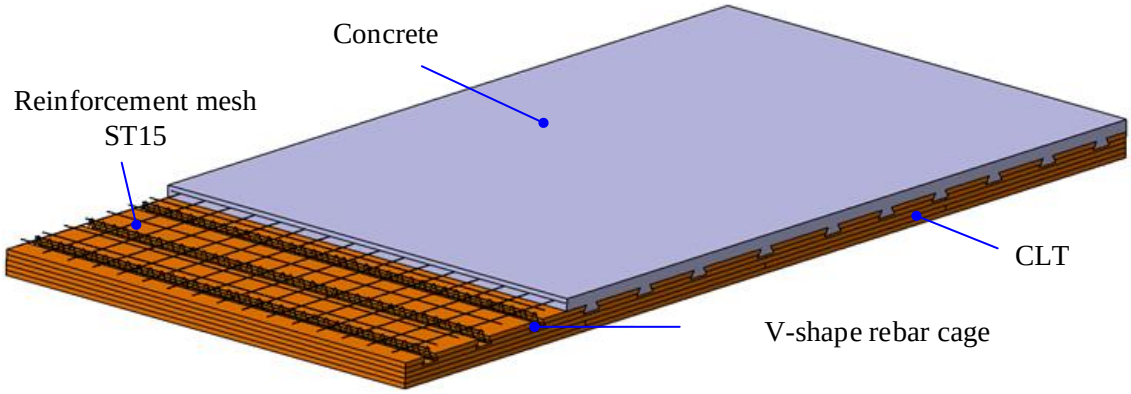

b. CLT-concrete composite floor

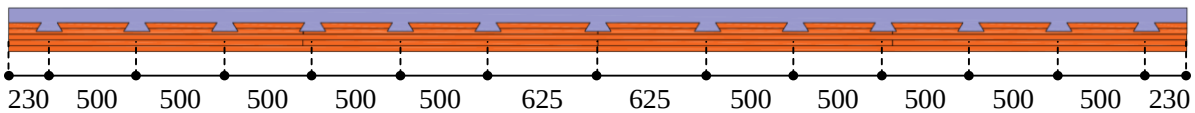

c. Spacing of connectors

Figure 1: Configuration of the specimen in flexural tests (unit in mm).

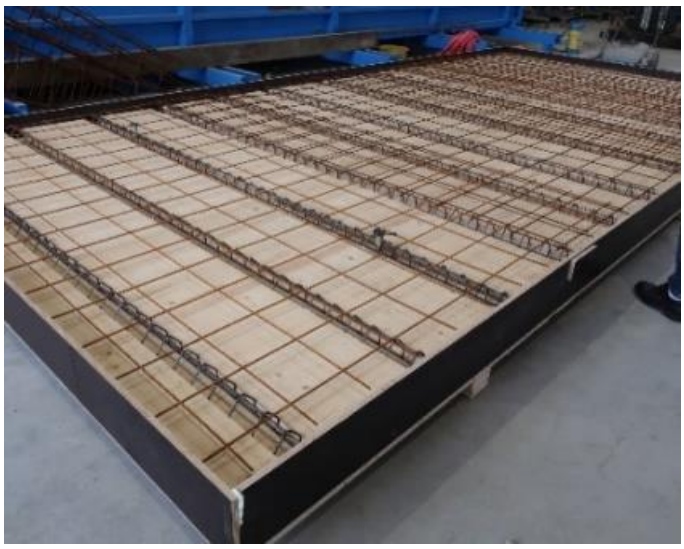

Figure 2: Photo of the specimen before the casting of concrete.

The test setup consisted of a slab specimen, two supports, a force jack with a capacity of 1500 kN, and a loading system to apply a four-point loading on the specimen (see Figure 3). In this test setup, the specimen was simply supported on two supports with a span of 6440 mm for the test HBF1 and 6540 mm for the test HBF2. Support 2 (conceptualized for supporting walls) was a linear support that gave a contact to the entire width of the specimen for both tests (see Figure 4). At this linear support, the longitudinal displacement of the specimen was restrained by fixing steel angles to the CLT panel that were fixed to UPN-300 columns by a bolt in an oblong hole (see Figure 4b).

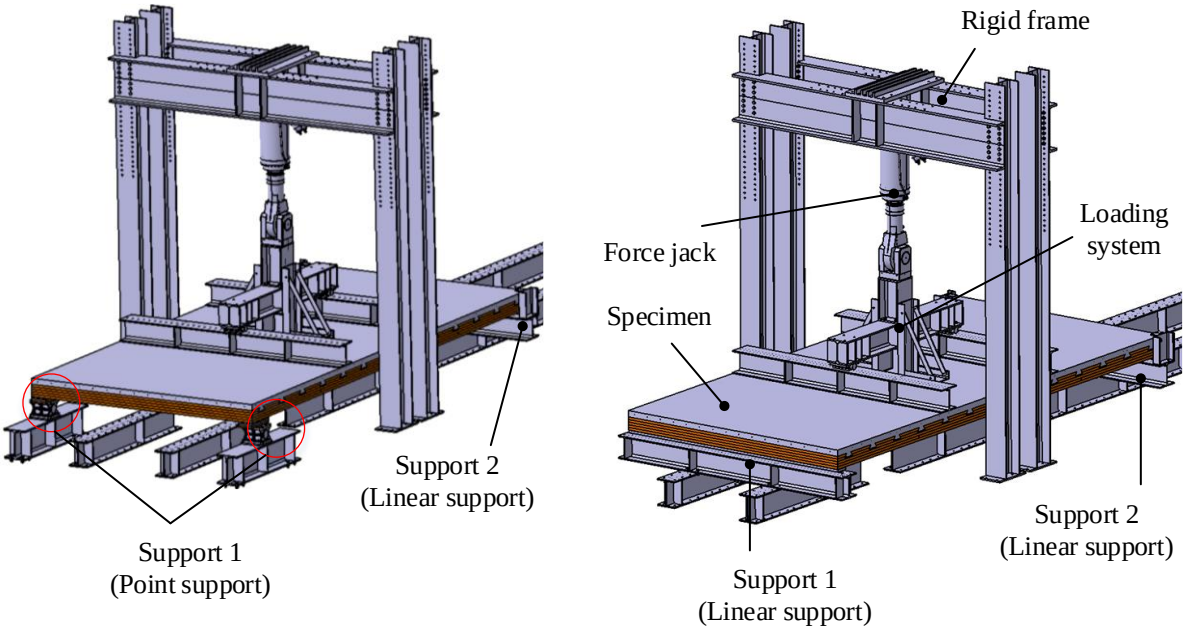

a. HBF1 test setup b. HBF2 test setup

Figure 3: Flexural test setups.

Support 1 of the test HBF1 consisted of two point supports (see Figure 5a) placed at corners below the specimen, conceptualized to represent the supporting columns. Alternatively, a linear support (see Figure 5b) was adopted for support 1 in the test HBF2. In order to minimize the friction between the support and the CLT panel, two PTFE layers were used for supports 1 and 2 of the two tests.

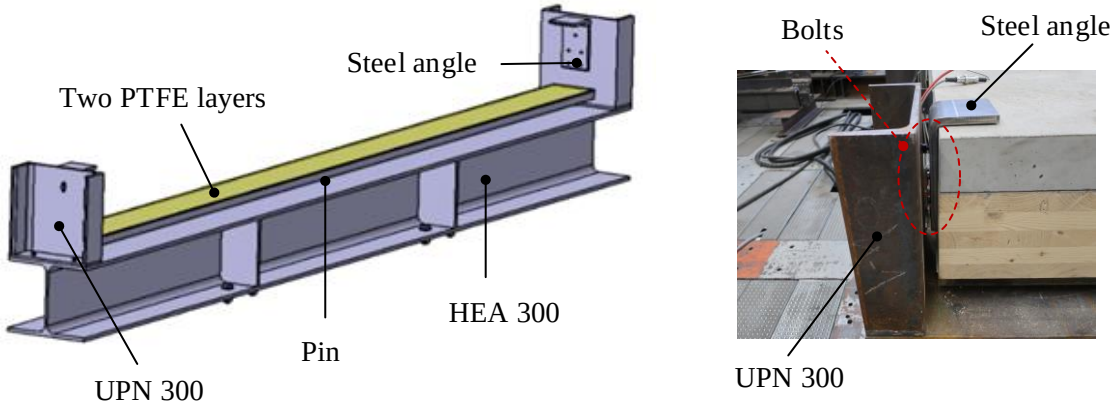

a. Detail of support 2 b. Attachment point of bolts to specimen

Figure 4: Support 2 of flexural tests

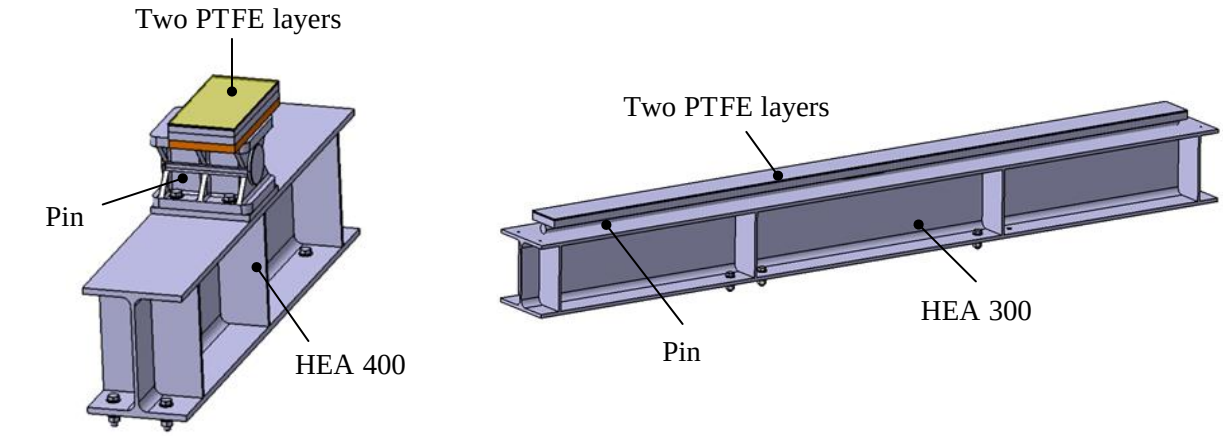

a. Details of point support in the test HBF1 b. Details of linear support in the test HBF2

Figure 5: Support 1 of flexural tests

In this test setup, the load was applied vertically from the force jack onto the specimen through the loading system. It consisted of two transversal HEA-300 beams, a longitudinal HEA-300 beam, two bracing systems, and a steel block connecting the force jack and the crossing beam. A pin mechanism was used between the HEA-300 longitudinal and transversal beams (see Figure 6a). The lateral displacement of the force jack was restrained by two bracing systems fixed on the concrete slab (see Figure 6b). Two PTFE layers were used between the bracing systems and the steel block to reduce friction. Figure 6c provides the photo of the test setup for test HBF2.

(a) (b) (c)

Figure 6: Photo of the flexural test setup (HBF2).

4.2.3 Material properties

4.2.3.1 Concrete

For both tests, a concrete with a strength class of C35/45 was used and formulated according to the norm EN 206-1 [8], having the class of environment XF1. Two series of three-cylinder specimens with a dimension of 11×22 cm were tested on the day of each test and at 28 days using standard compressive tests for compressive strength. The results are reported in Table 1.

Table 1: Concrete strength of flexural test specimens.

Test	Age [days]	f_{cm} [MPa]			
		Cylinder 1	Cylinder 2	Cylinder 3	Avg.
HBF1	28	52.0	52.3	52.8	52.4
	120	56.5	56.3	57.0	56.6
HBF2	29	49.8	47.3	51.4	49.5
	147	56.6	53.3	56.2	55.4

4.2.3.2 Timber

CLT panels TOT'm X [9] were used and constituted of wooden planks made from dry and calibrated massive timbers with a strength class of C24. The planks, having a thickness of 33 mm each, were stacked in crossed layers at 90° and glued together over their entire surfaces (except the edge surfaces).

As being presented in experimental pushout tests, the failure of all the pushout specimens was caused by the rolling shear failure of the cross-layer of the CLT panel. The variation of the mechanical properties of the timber can significantly influence the structural response of the connection system. In order to determine the actual properties of the timber, small samples were cut from the uninfluenced

part of the specimen of the flexural test HBF2 after the test. These samples were tested for longitudinal compression, transverse compression, and rolling shear properties.

The samples for compression tests were extracted from individual planks of the CLT panel without glued joints. These samples had a cross-section of 32×32 mm and 25×25 mm for longitudinal and transverse compression tests, respectively, and a height of 145 mm and 125 mm for longitudinal and transverse compression tests, respectively (see Figure 7). The compression tests were carried out in accordance with EN 408 [10] on 12 samples for longitudinal compression and 8 samples for transverse compression. The force was measured by a force sensor, whereas the relative displacement was determined as the mean value of the four LVDT displacement sensors. The modulus of elasticity (E_L for longitudinal compression and E_T for transverse compression) is defined by:

$$E_L \text{ or } E_T = \frac{L_0(F_{0.4}-F_{0.1})}{A_0(w_{0.4}-w_{0.1})} \quad (1)$$

where L_0 and A_0 are the initial length of the sample and the initial area of the sample, respectively. $w_{0.4}$ and $w_{0.1}$ are the relative displacements corresponding to 40 percent of maximum force $F_{0.4}$ and 10 percent of maximum force $F_{0.1}$, respectively. The relative displacements were computed as an average value of the four displacement sensors. The results obtained from these tests are reported in Table 2, in which $\bar{x}$ and s denote the mean value and the standard deviation, respectively. The values of modulus of elasticity parallel to the grain (longitudinal compression) show a significant variation, caused by natural defaults of the wood samples. The obtained mean value of modulus of elasticity is much smaller than the mean value of the modulus of elasticity under edgewise bending given in the technical document TOT'm X [9] following EN 338 [11]. It is known that the bending modulus of elasticity is different from its tensile and compressive moduli, as being noted by Kim et al [12]. They performed a study to predict the tensile and compressive moduli from dynamic and static bending moduli of elasticity of major softwood structural lumber in Korea. It was found that the compression modulus was one-half of the tensile modulus and two-thirds of the bending modulus for the same specimen. Such a difference between tensile and compression moduli was also supported by other studies [13]-[17]. It was concluded by Shim et al. [17] that the difference might be caused by grain angle deviation, which is induced by defects.

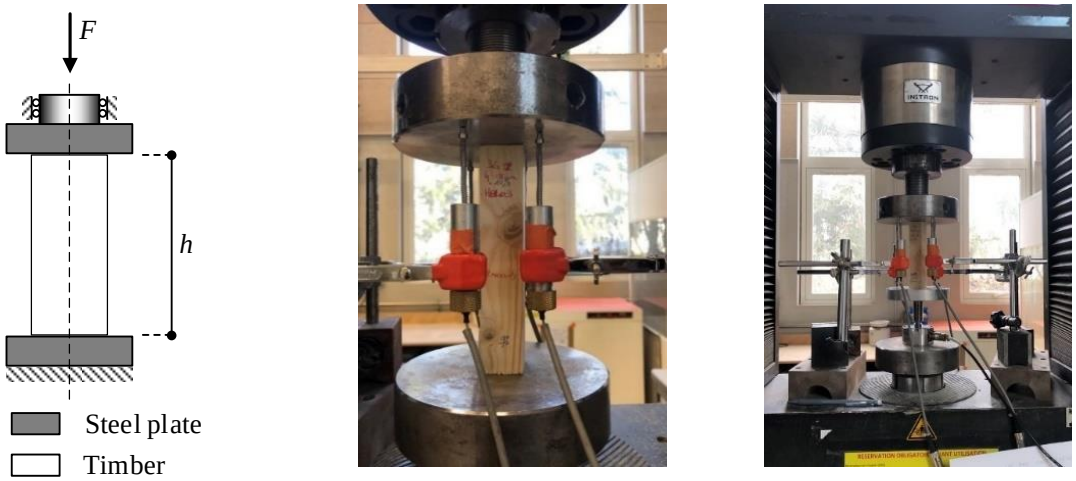

a. EN 408 [10] b. Longitudinal compression c. Transverse compression

Figure 7: Test setup for timber compression tests.

Table 2: Material properties of timber under compression.

Test	Number of specimens	Moisture content [%]	Modulus of elasticity		Strength	
			$\bar{x}$ [MPa]	s [MPa]	$\bar{x}$ [MPa]	s [MPa]
Long. compression	12	10.2	5317	1325	31.3	5.3
Trans. compression	8	9.6	162	26	3	0.2

In order to determine rolling shear properties, different test configurations can be used. One of the test methods is the four point out-of-plane bending test (EN 16351 [18]). However, this configuration seems to require high efforts and costs. Direct shear tests, described in EN 408 [10], EN 16351 [18], and EN 789 [19], can also be used to evaluate the rolling shear stiffness and strength of single lamination segments. Test setup consists of one cross-layer glued between two steel plates for the configurations in EN 408 [10] and EN 789 [19], as illustrated in Figure 8.

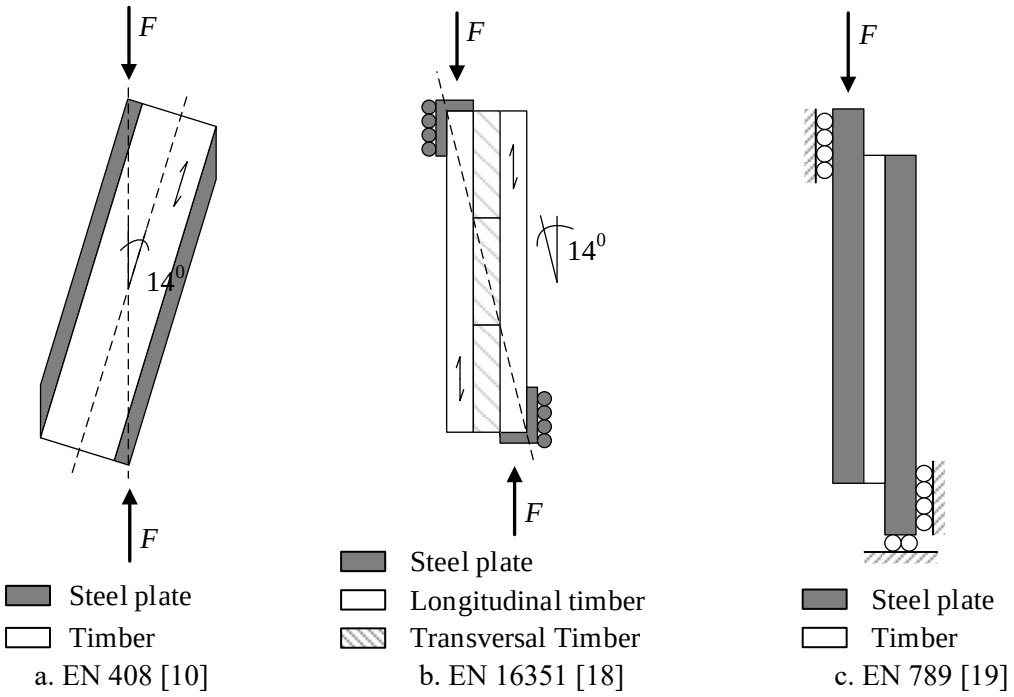

Figure 8: Direct shear test setups.

Nevertheless, it was criticized by Brandner et al. [20] that all configurations based on these three test configurations incur the presence of stresses perpendicular to the grain, supported by the study of Ehrhart et al [21]. In order to solve this problem, the modified shear tests with a reference to EN 408 [10], were developed by Mestek [22] (see Figure 9a) and by Gong et al. [23] (see Figure 9b), respectively. These modified configurations are claimed to provide uniform shear stress in the cross-layer and guarantee the rolling shear failure. The test setup by Gong et al. [23] was adopted in this study (see Figure 9c), as it was simpler to perform. However, an angle of around 14 degrees was assured in order to be in accordance with EN 408 [10]. Five samples with three lamination layers (one cross-layer sandwiched by two longitudinal layers) were extracted from the CLT panel. These samples had dimensions of 99 mm thick by 140 mm large by 269 mm long. The force was measured by a force sensor, whereas the relative displacements were determined as the mean value of two LVDT

displacement sensors. The rolling shear strength f_r and the rolling shear modulus G_R were respectively computed by:

$$f_r = \frac{F_{max} \times \cos\alpha}{L_R \times w} \tag{2}$$

$$G_R = \frac{t_c}{L_R \times w} \times \frac{F}{\Delta} \times \cos\alpha \tag{3}$$

where F_{max} is the maximum force. L_R and w are the height and the width of the specimen, respectively. t_c is the thickness of the cross-layer. α is the inclination angle of the specimen. F/Δ is the slope of the load-deformation curve between 20 percent and 50 percent of the maximum force. The results of the shear stiffness and shear strength are reported in Table 3.

The force-displacement curves and results obtained from timber characterization tests are detailed in ANNEX A.

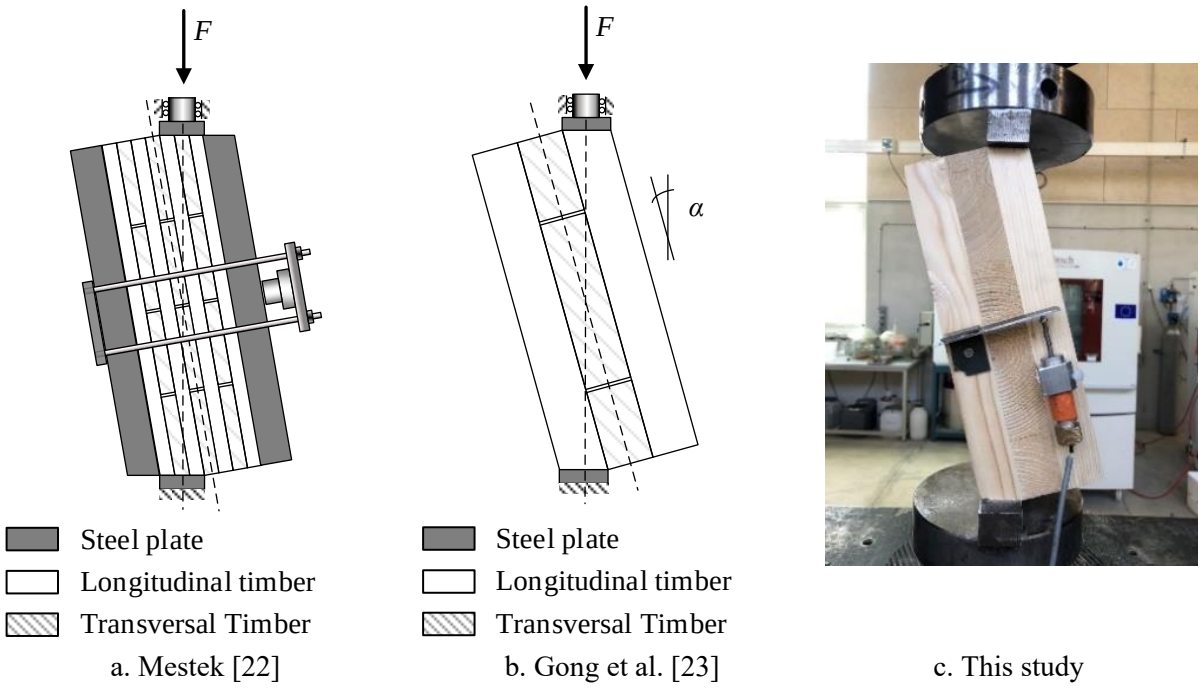

a. Mestek [22] b. Gong et al. [23] c. This study

Figure 9: Modified shear test setups.

Table 3: Mechanical properties of the timber used in flexural tests.

Number of specimens	Moisture content [%]	Rolling shear modulus		Rolling shear strength	
		$\bar{x}$ [MPa]	s [MPa]	$\bar{x}$ [MPa]	s [MPa]
5	9.25	133	25	1.49	0.17

4.2.4 Instrumentation and loading procedure

The force generated by the hydraulic force jack was measured by integrated double force sensors (± 500 kN and ± 1500 kN). The slips between the CLT and the concrete panels in horizontal direction were determined by 8 LVDT sensors (4 at each face along the specimen) noted by CG1 to CG8 with a capacity of ± 2.5 mm. In addition, the settlement of the supports in vertical direction were determined using 4 LVDT sensors (one at each corner of the specimen) noted by CD1 to CD4 with a capacity of ± 25 mm. The positions of the sensors are given in Figure 10.

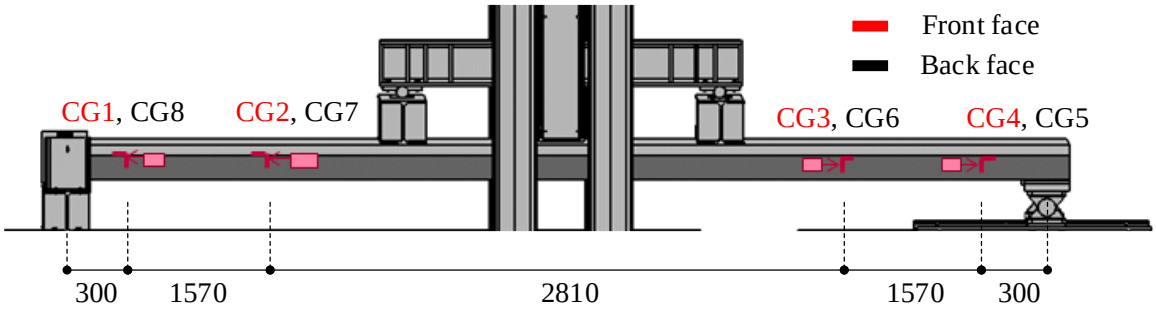

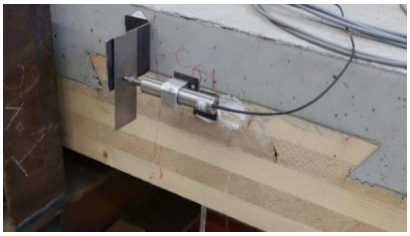

Photo of CG1

Photo of CG8

a. LVDT for slip measurement along the interface layer of the specimen

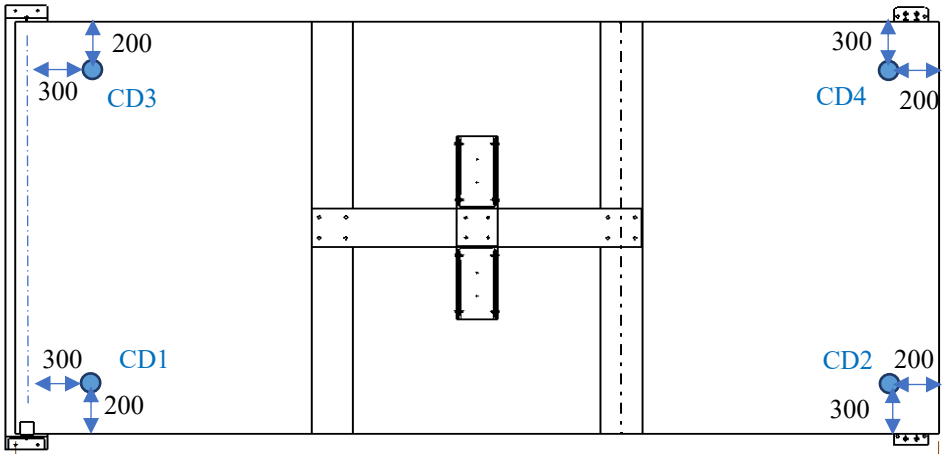

Photo of CD1

Photo of CD2

b. LVDT for support settlements in vertical direction

Figure 10: Positions of sensors LVDT for flexural tests (unit in mm).

Apart from the analogue sensors, three high resolution photo cameras were also installed on the front face of the specimen for an alternative measurement using Digital Image Correlation technology (DIC). The deflection of the specimen was determined by recording the evolution of points on steel boards fixed below the CLT at mid width (noted by C1 to C5). The uplifts (U1 and U2) were obtained from points on the recording areas. The measuring positions of the areas for the DIC are presented in Figure 11.

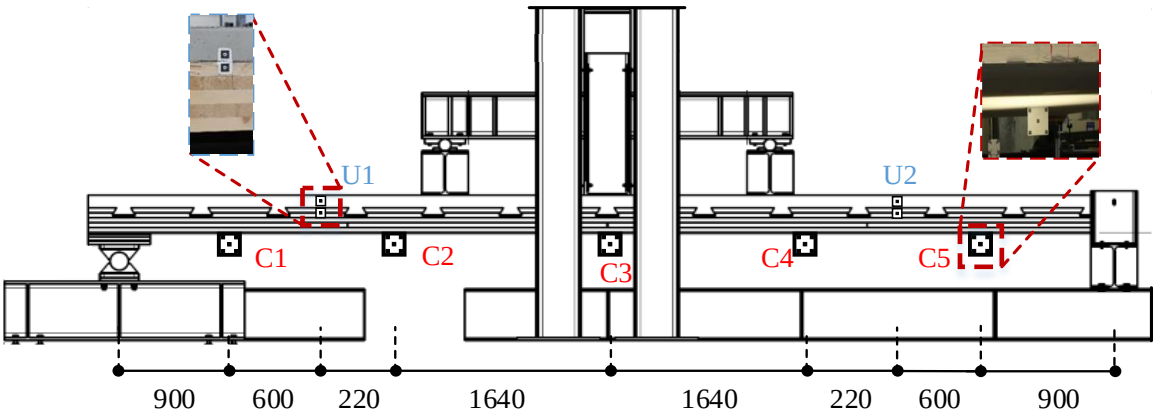

Figure 11: Measurements by digital image correlation (DIC) in flexural tests (unit in mm).

The loading procedures were conducted in accordance with Eurocode 4 [24]. 25 initial loading/unloading cycles between 5 percent and 40 percent of the estimated failure load were applied to the specimen in order to remove the friction with a loading rate of 1 mm/min. The failure load was estimated at 403 kN. One more cycle at a load level of the estimated ultimate limit state was then performed before the load was monotonically increased up to failure with a loading rate of 1 mm/min.

A uniformly distributed load combination case at the serviceability state Q_{sls} and the ultimate limit state Q_{uls} were considered in the design load cases and can be found according to EN 1990 [25]:

$$Q_{SLS}=G_k+Q_k \tag{4}$$

$$Q_{ULS}=\gamma_G G_k+\gamma_Q Q_k \tag{5}$$

where G_k is a permanent load and Q_k is a service load, and combination design load factors γ_G and γ_Q are 1.35 and 1.5, respectively. In this study, uniformly distributed load combination cases with a permanent load of 4 kN/m^2 and a live load of 2.5 kN/m^2 were considered in the design load cases. The uniformly distributed loads are then converted to the corresponding load levels of the flexural test based on the equivalent bending moment criterion, as presented in eq. (6):

$$F=2BQc \tag{6}$$

where B is the width of the specimen, Q is the load combination case, and c is the distance between a support and a loading point of bending test setup. For a width of 3.2 m of the cross-section of the specimen, the load levels corresponding to the design load for SLS and ULS are 98 kN and 138 KN, respectively.

4.2.5 Influence of shrinkage effects on the deflection

The first flexural test (HBF1) was performed four months after the concrete casting of the specimen. This delay was due to the first period of lockdown imposed by the French government during the Covid-19 crisis. During storage, many concrete cracks (see Figure 12) were observed on the concrete panel of the specimen, due to an improper position of the temporary supports at factory, that magnified the effects of shrinkage of concrete. However, it was not possible to quantify the deflection caused by this effect.

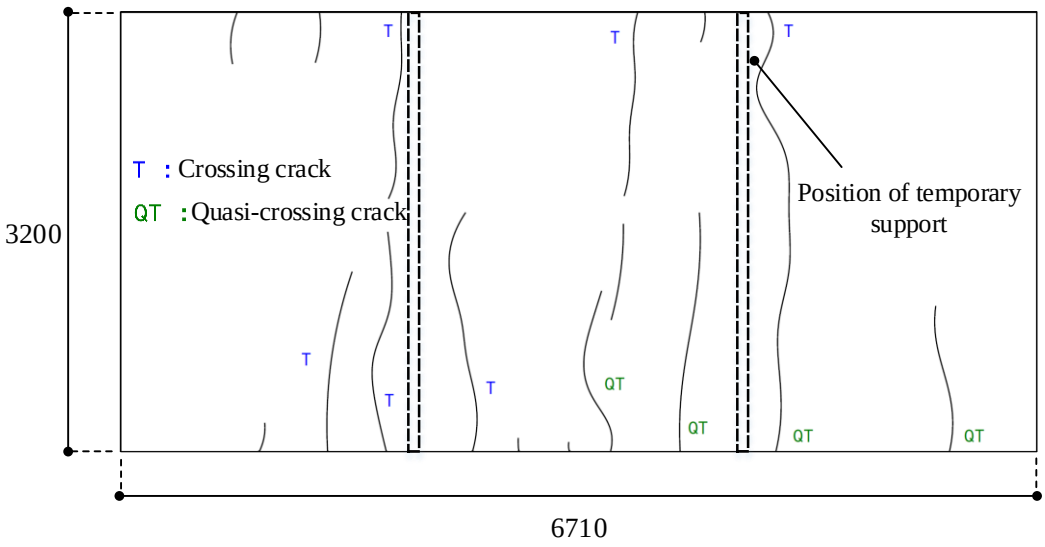

a. Diagram of cracks (dimensions in mm)

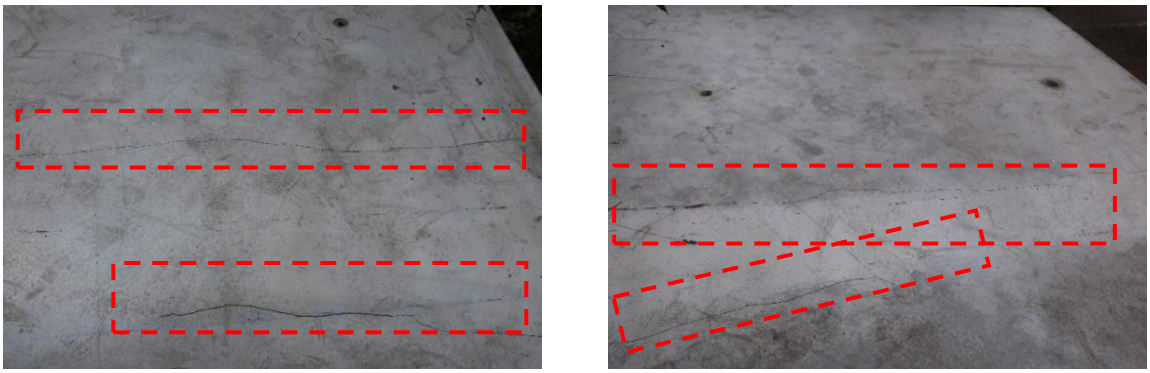

b. Photo of cracks on the concrete surface of the specimen

Figure 12: Cracks due to shrinkage effects of the specimen HBF1.

In order to evaluate qualitatively the effects of shrinkage, it was decided later to measure the evolution of the deflection of the specimen HBF2 during around three months. The specimen was placed on the supports of the flexural test setup with only the self-weight of the specimen applied on it. A laser sensor was installed at the midspan below the specimen in order to measure the evolution of deflection over time. The specimen HBF2 was cast with an initial imposed positive deflection of the wood at the midspan of 19 mm. Figure 13 shows the evolution of the midspan deflection over time. The imposed positive deflection dropped off immediately from 19 mm to 8 mm after placing the specimen on the supports of the flexural test setup, due to self-weight. No extra load was applied over a period of 100 days. During this time, as illustrated in Figure 13, the midspan deflection dropped gradually from +8 mm of positive deflection to -11 mm of negative deflection. The difference of vastly 16 mm between the deflections at the time of 100 days and of 0 day, is due to the creep and shrinkage effects of the

concrete and the CLT. This value is not negligible and calls for further investigation through a dedicated experimental campaign.

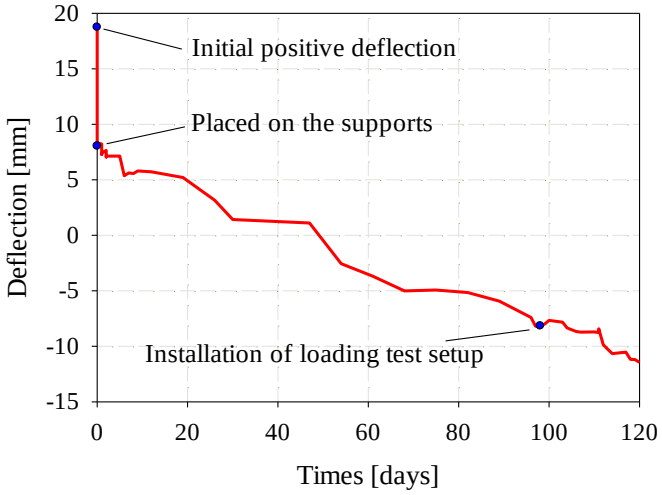

Figure 13: Evolution of the midspan deflection over time of the specimen HBF2.

4.2.6 Experimental results and discussion

4.2.6.1 Observations and failure mode

Figure 14 presents the evolution of force and elongation of the force jack obtained from both flexural tests. The global response of the specimens was almost linear until the failure of the specimens at load levels of 590 KN and 725 KN for tests HBF1 and HBF2, respectively. It should be noted that the self-weight of the specimen and of the loading system is not included in force-elongation curves.

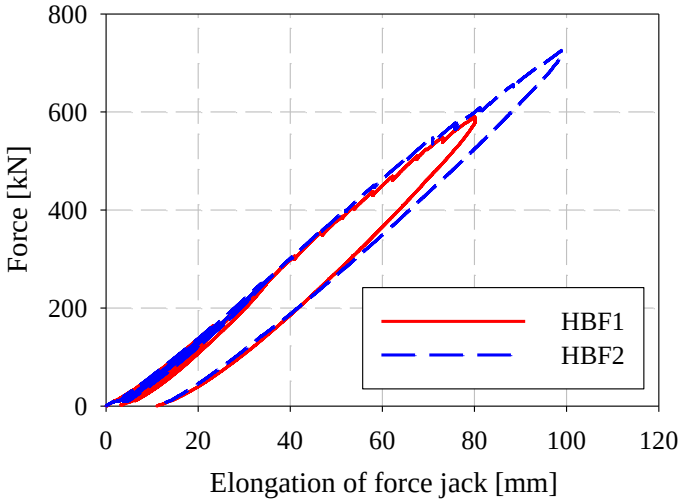

Figure 14: Evolution of the force and elongation of force jack in flexural tests.

For the test HBF1, apart from the cracks due to the shrinkage and creep, the first crack of the concrete in the notched connectors was observed during the first initial cycle of bending test at a load level of 160 kN (see Figure 15a). At the load level of 290 kN, cracks appeared in the concrete (Figure 15b) and in the timber layer (Figure 15c), at the notched connector near the point supports on both faces of the specimen, precisely 69 cm from the extremity of the specimen. These cracks propagated and led

to a local shear rupture of the concrete panel and the CLT panel (see Figure 15d) at a load level of 590 kN, corresponding to a maximum elongation of the force jack of 80 mm.

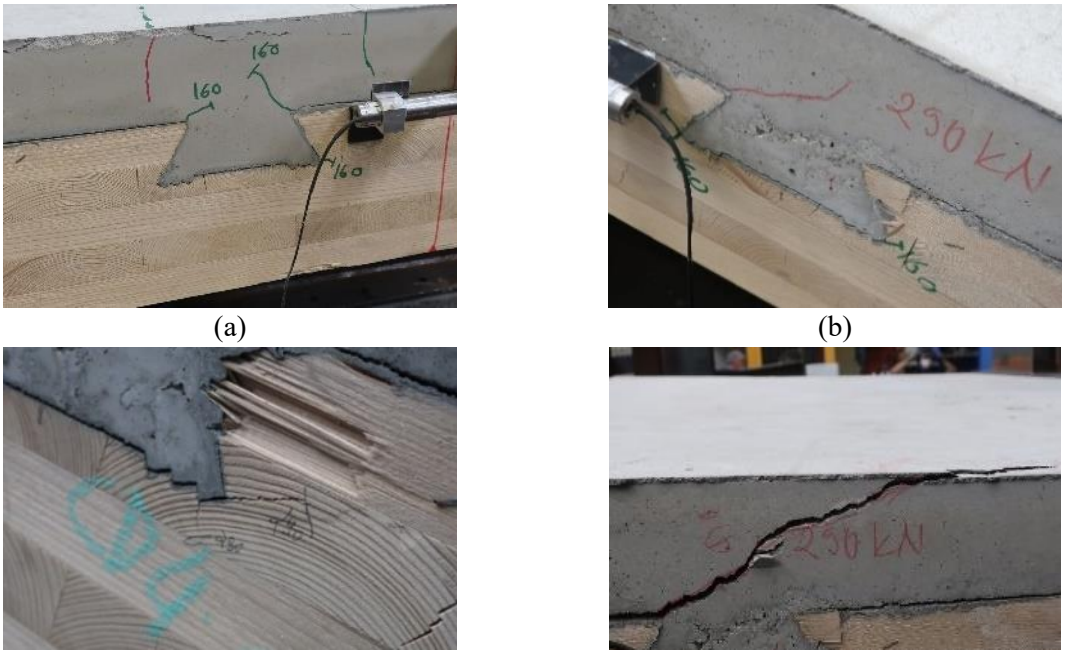

(a) (b)

(c) (d)

Figure 15: Observations during the test HBF1.

For the test HBF2, cracks were observed in notched connectors during the first cycle at a load level of 158 kN (see Figure 16a). At the connectors of the two extremities of the specimen, cracks appeared at the load level of 250 kN (see Figure 16b,c). At a load level of 725 kN, many wood planks were ruptured (see Figure 16d,e) and loud noises of wood rupture were heard. It was decided to stop the loading in order to avoid a brittle collapse of the system, as the failure seemed to be governed by the rupture of the CLT layers in tension. In addition, a large elongation of the force jack, reported at 99 mm, was already obtained.

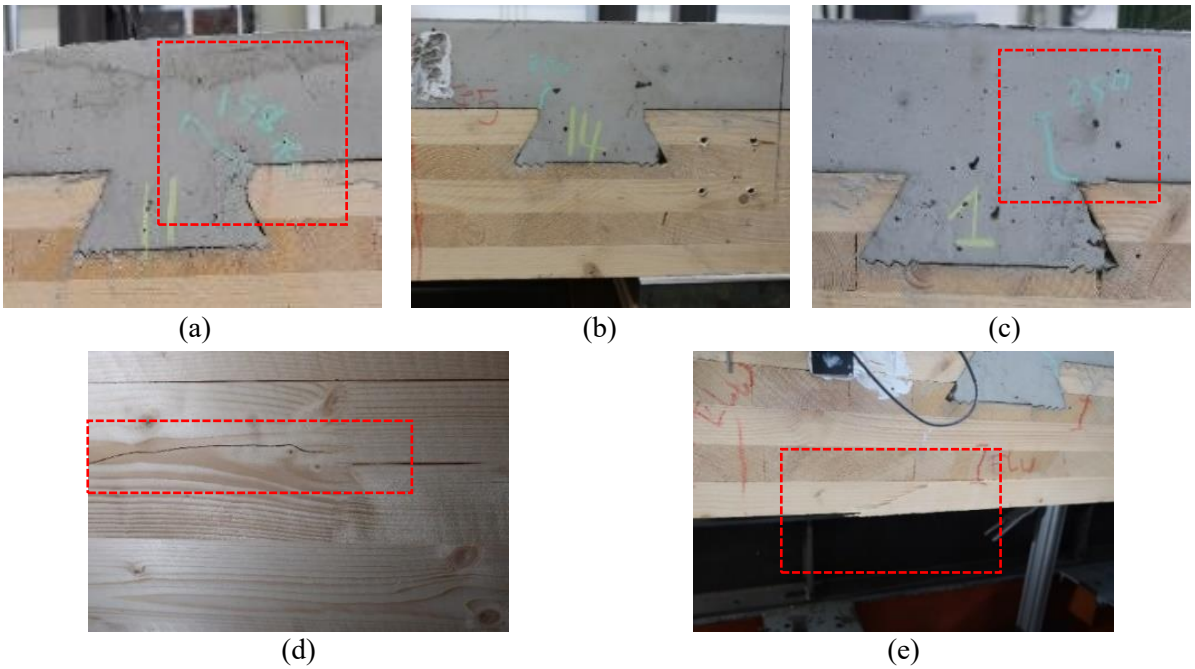

(a) (b) (c)

(d) (e)

Figure 16: Observations during the test HBF2.

4.2.6.2 Force-midspan deflection curves

Figure 17a illustrates the envelop curves of the midspan deflection measured by point C3 from DIC measurement method in function of the force. It should be reminded that the self-weight of the specimen and of the loading system, corresponding to 68.1 kN, was not included in the force measurement during the flexural tests. The self-weight of the specimen was estimated by using the configuration shown in Figure 3 with the material properties given in section 4.2.3, while the loading system that consists of the two transversal and the longitudinal HEA-300 beams has a total weight of 7.6 kN.

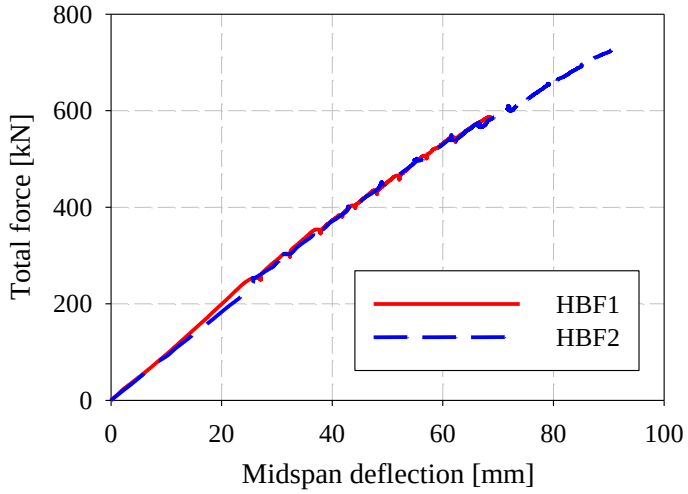

a. Measured at point C3 by DIC method

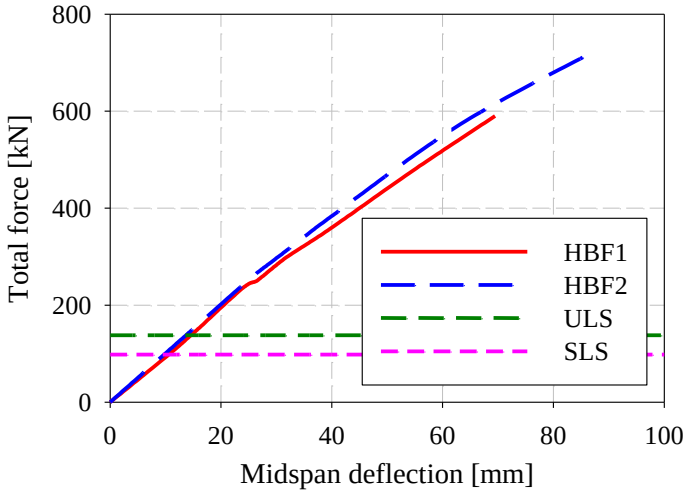

b. Modified by Eq. (7)

Figure 17: Evolution of the force and midspan deflection derived from DIC method.

The deflection measured by point C3 presented in Figure 17a included the settlement of the support system (see Figure 18). The red line denotes the rigid movement of the slab due to the settlement from the support system, and blue curve represents the actual deflection obtained from flexural tests. The symbols m_1 and m_2 refer to deflections obtained from CD1 and CD2 sensors, respectively, while m_3 denotes the midspan deflection recorded from DIC method. From the deflection diagram as shown in Figure 18, the deflection measured from CD1 and CD2 sensors near the supports, and from sensor C3 of DIC method at midspan of the specimen were contributed by the deflections due to the settlement of

the support system and the deflection induced by the applied load, f. The actual midspan deflection, f_3, can be determined as follows:

$$f_3 = \frac{m_3 - 0.5(m_1+m_2)}{1 - 0.5(\alpha+\beta)} \quad (7)$$

where parameters α and β were determined equal to 0.15. The details of formula in eq. (7) and value of parameters α and β can be found in Annex B. Accordingly, the actual midspan deflections of test HBF1 and test HBF2 were modified using eq. (7) and are presented in Figure 17b. At the failure load level, the midspan deflection of tests HBF1 and HBF2 were 69 mm and 88 mm, respectively.

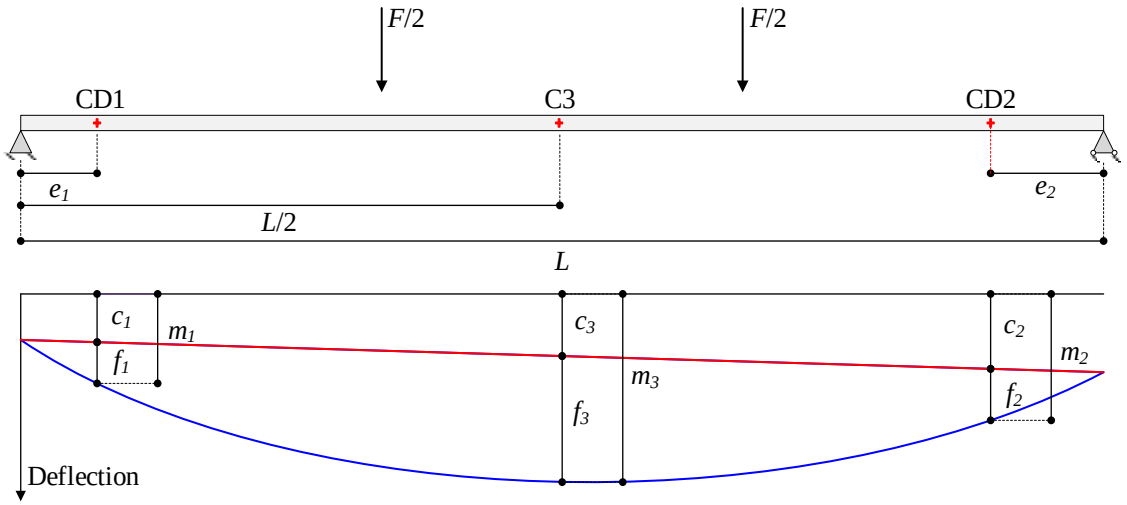

Figure 18: Displacement correction of flexural tests.

It can be obviously seen from the results of the flexural tests (Figure 17b) that the design of the CLT-concrete slab is not limited by the strength, as a very high value of the force was obtained if compared to the design level of load combinations.

4.2.6.3 Slips and uplifts

Figure 19 presents the evolution of the slips in function of the force for both tests. The maximum slips obtained for tests HBF1 and HBF2 were 2.38 mm and 0.66 mm, respectively. For test HBF1, the large values of the slips measured by sensors CG4 and CG5 were relative displacements caused by shear cracks near the point supports (see Figure 15d), whereas the slips measured by sensors CG1, CG2, CG3, CG6, CG7, and CG8 were limited at values between 0.19 mm and 0.33 mm. With both linear supports in test HBF2, the distribution of the slips became regular (see Figure 19b). In addition, the evolution of the uplifts at points U1 and U2 for test HBF2 is described in Figure 20. The uplifts remained limited at 0.43 mm. Due to errors in the interpretation of the DIC method of points U1 and U2 for test HBF1, the results are not presented here.

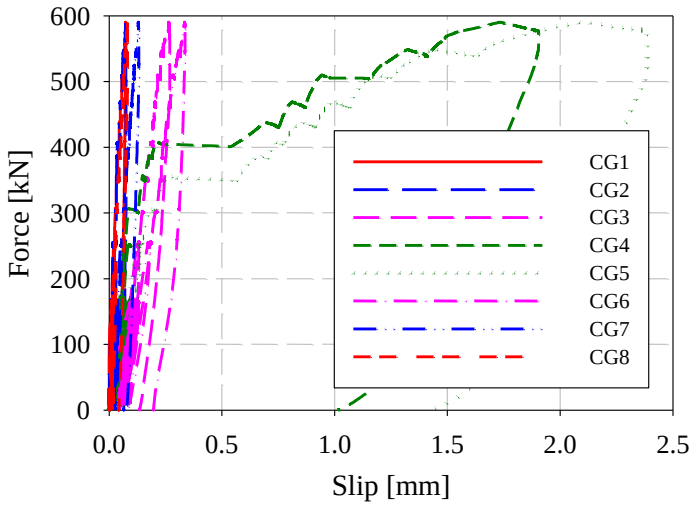

a. Test HBF1

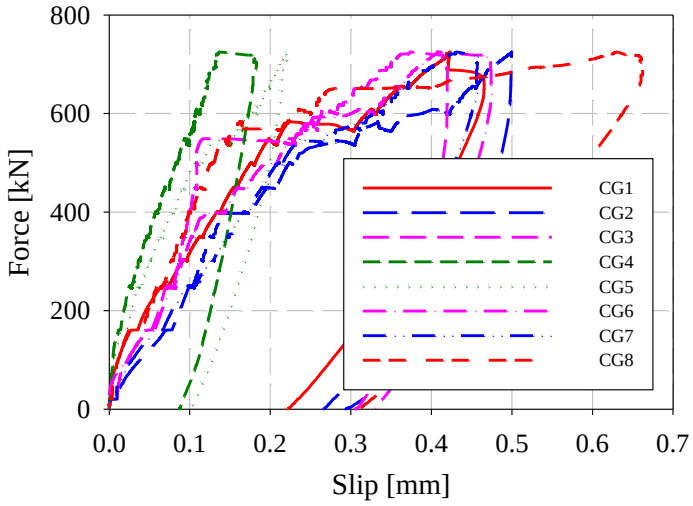

b. Test HBF2

Figure 19: Evolution of slips in function of force in flexural tests.

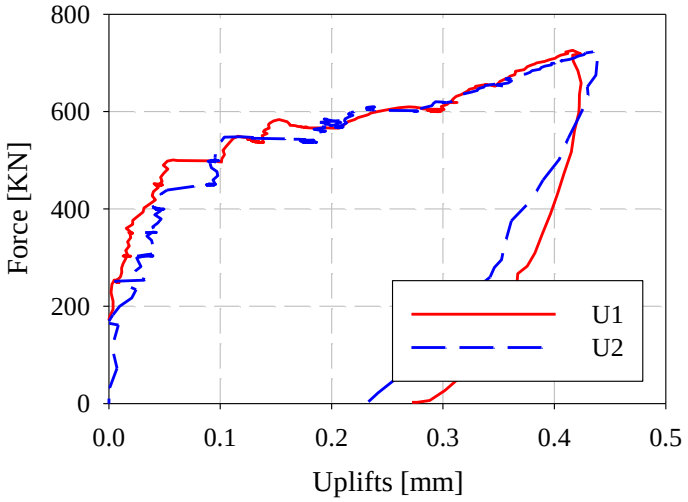

Figure 20: Evolution of uplifts in function of force for flexural test HBF2.

4.2.6.4 Bending stiffness and flexural capacity

Table 4 presents the results of the tested TCC floors considered in one meter. The maximum force was recorded from the force jack and the corresponding midspan deflection was obtained from the corrected curve as shown in Figure 17b. The bending stiffness of the CLT-concrete composite floor, *EI*, is found using eq. (8):

$$EI=\frac{\Delta F\times c}{48\Delta\delta}(3L^2-4c^2) \tag{8}$$

where ΔF is the change in force between 10 percent and 40 percent of the maximum force F_{max}; $\Delta\delta$ is the corresponding increment of the midspan deflection to ΔF; c is the distance between the support and the loading point; and L is the clear span of the specimen. In addition, the maximum experimental bending moment $M_{exp.}$ is calculated using a four-point bending test configuration and the applied maximum force F_{max} in the expression of $M_{exp}=F_{max}\times c$ where c is the distance from the support to the loading point.

Table 4: Results of TCC floors derived from flexural tests considered per meter width.

TCC test	F_{max} [kN/m]	$\delta_{F_{max}}$ [mm]	EI [Nmm^2/m]	M_{exp} [kNm/m]
HBF1	184	69	1.40×10^{13}	200
HBF2	227	88	1.52×10^{13}	251
Ratio (HBF1/HBF2)	0.81	0.78	0.92	0.80

From the comparison in Table 4, the TCC floor supported by the point support system (HBF1) logically delivers a lower structural performance compared to the floor supported by the linear support system (HBF2). Between tests HBF1 and HBF2, the maximum load-carrying capacity and maximum flexural bending moment display a similar ratio of approximately 80 percent. For bending stiffness, a difference of only 8 percent is observed. It should be noted that the bending stiffness is derived from the computation method in eq. (8) which adopts the relationship of force and corresponding midspan deflection within intervals of 10 percent and 40 percent of maximum force F_{max}.

4.2.6.5 Comparison

The results of the effective bending stiffness obtained from this study are compared with those of the CLT-concrete composite floor using different types of connection systems obtained in the study of Jiang et al. [3], Müller [26], Mai et al. [27], and Shahnewaz et al. [28]. The test setup, configuration of connection system, and failure mode of flexural tests of each study are presented from Figure 21 to Figure 24. The comparison is summarized in Table 5. The value in brackets denotes the bending stiffness ratio in each case to test HBF2.

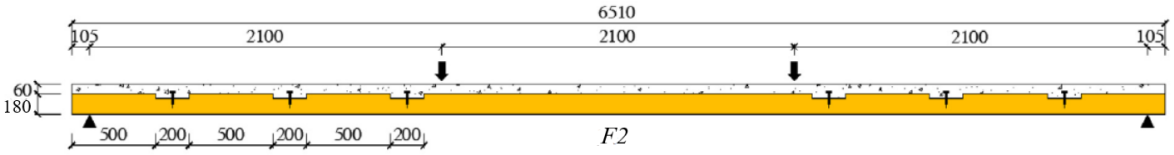

a. Test setup

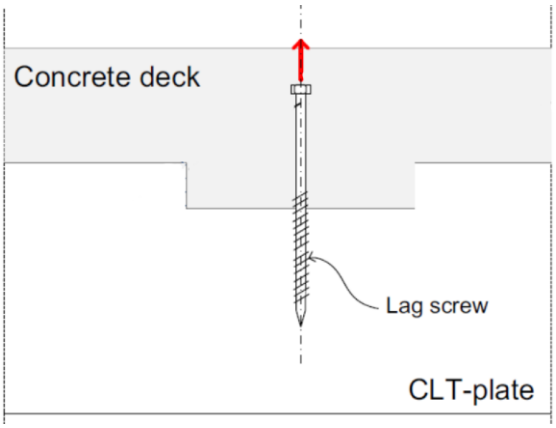

b. Connection system c. Failure of specimen F2

Figure 21: Flexural test of Jiang et al. [3].

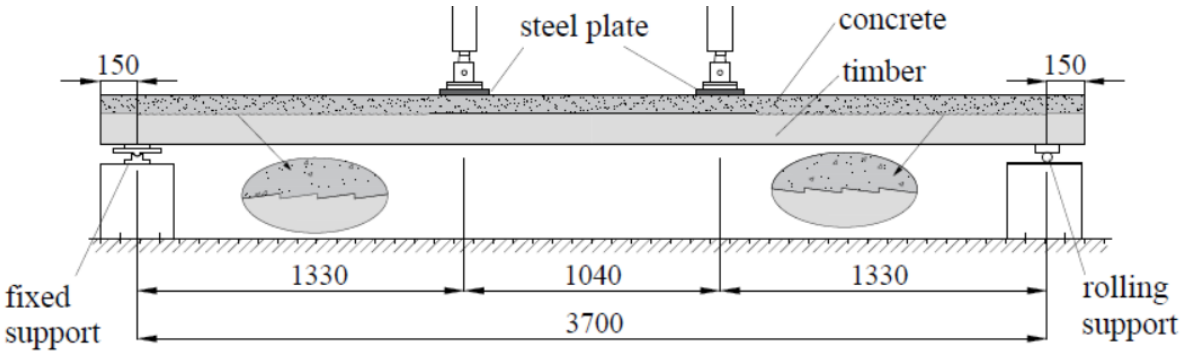

a. Test setup

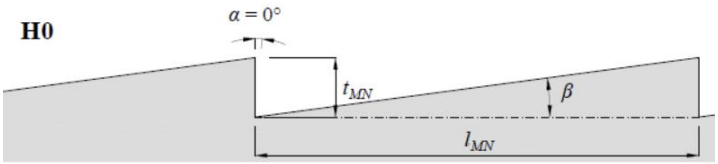

b. Micro-notch c. Bending tension failure

Figure 22: Flexural test of Müller [26].

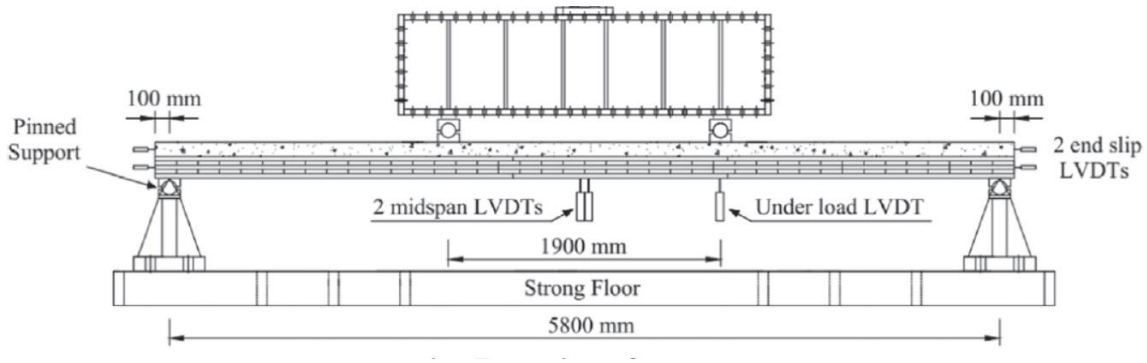

a. Test setup

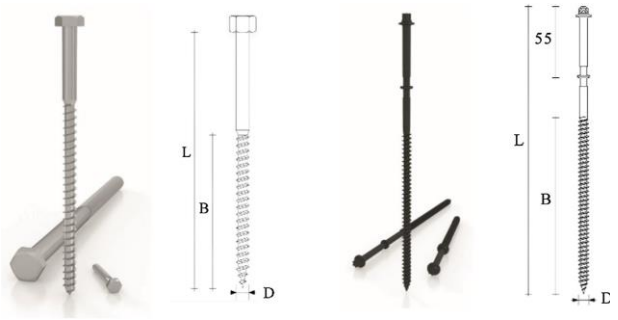

Coach screw (Bolt) VB connector

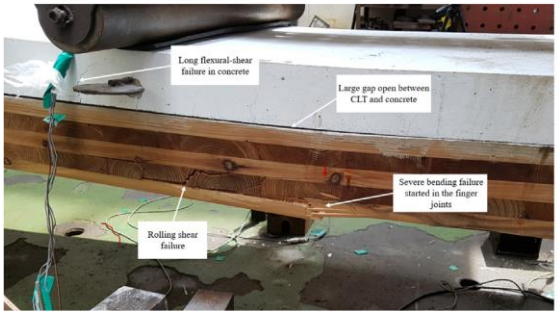

b. Connection system c. Typical failure mode in flexural tests

Figure 23: Flexural tests of Mai et al. [27].

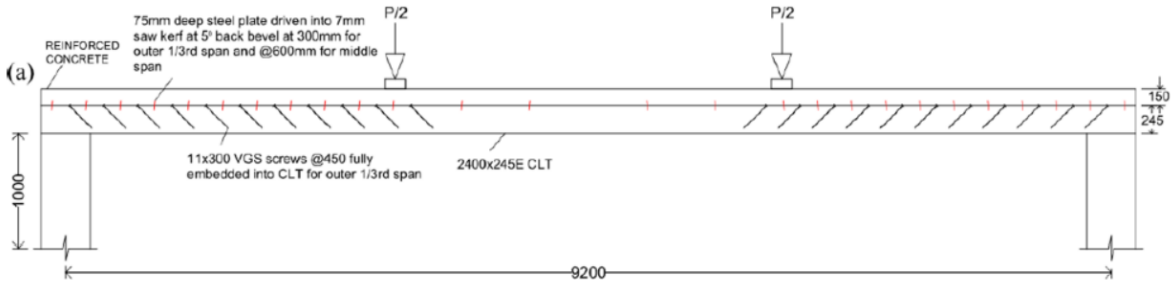

a. Test setup

b. Steel plates c. Failure mode

Figure 24: Flexural tests of Shahnewaz et al. [28].

Jiang et al. [3] studied a 5-layer-CLT concrete composite floor using the notched connector and additional screws as the connection system (see Figure 21). The notched connection had dimensions of 200 mm of length and 25 mm of thickness. Two lag screws with a diameter of 10 mm were installed in each notch. The concrete panel had a strength class of C30/37 while the CLT panel was manufactured out of structural lumber with a strength grade C24. The composite specimen was tested to failure. At the ultimate load level, timber near midspan of the composite floor experienced bending failure. Notched connections along the span were nearly undamaged, and only one fine concrete crack appeared at one corner of the notch closest to one of the supports. The bending stiffness is reported to be 12 percent higher compared to the one in this study.

Müller [26] conducted a 4-point bending test on a 3.7 m long, 3-layer-CLT concrete floor using micro-notches with a length of 30 mm and a depth of 4 mm and additional stirrup as the connection system (see Figure 22). The concrete panel had a thickness of 80 mm, while the CLT panel had a thickness of 100 mm, both of which were smaller than in the present study of test HBF2. In terms of material properties, a concrete mixture with a strength class of C30/37 and the CLT panel made of spruce/fir timber lamellas with a strength class of C24 were adopted. The results indicated that the failure was governed by the bending tension in the CLT panel. The concrete top layer remained mostly undamaged during the testing. The effective bending stiffness of the composite floor of HO-CLT is found to be 39 percent lower compared to that of the composite floor in this study.

Mai et al. [27] evaluated the capacity of CLT concrete composite floors by performing a full-scale testing on three floor specimens with a length of 6 m and thickness of 250 mm which included 100 mm of concrete and 150 mm of 5-layer CLT panel (see Figure 23). The ‘‘B” and ‘‘SFS” in the designation of specimens, as reported in Table 5, indicate the type of connector, and the following notations represent the angle and the spacing of the connector. It should be mentioned that the total thickness of the composite floor studied in [27] and in this research were identical, despite differences in the thickness of the concrete and CLT panel. Two types of connectors, including bolts and VB connectors, were adopted in composite floors. The material properties of the specimen were derived from the characterization test with a compressive strength of concrete of 27.29 MPa and CLT properties equal to E12 class according to Korean standards. The tension and shear failure mechanisms at the midspan of the CLT panel were seen as the typical failure in TCC floors. After the bending failure started, the rolling shear failure subsequently propagated in the cross-layer of the CLT panel, causing localized layer delamination. The concrete parts were likely to remain undamaged until the maximum load. The finding demonstrates that the effective bending stiffness exhibits slightly higher values compared to the effective bending stiffness of composite floor in this study, ranging from 1 percent to 17 percent.

Shahnewaz et al. [28] presented experimental investigations on two identical timber concrete composite floors with steel plates and screws as shear connectors. Each specimen was comprised of 245 mm thick, 7-ply CLT panels with a 150 mm concrete topping (see Figure 24). The CLT was grade E1M5 according to Canadian standard while the concrete tested at the day of flexural test had a compressive strength of 50 MPa. The failure of the TCC floors occurred in the timber part due to the bending failure in the CLT panel. The effective bending stiffness of both cases is approximately four times higher than the ones in this study.

Table 5: Comparisons of the bending stiffness obtained in this study and in literature.

Research	Specimen	Thickness [mm]		Connection	Bending stiffness [Nmm^2/m]
		concrete	CLT		
This study	HBF2	85	165	Notches [90×50mm]+stirrup	1.52×10^{13} (1.00)
Jiang et al. [3]	F2	80	180	Notches [200×25mm]+screws	1.66×10^{13} (1.10)
Müller [26]	H0-CLT	80	100	Micro-notches [30×4mm]	0.93×10^{13} (0.61)
Mai et al. [27]	B-45-s150	100	150	Bolt	1.78×10^{13} (1.17)
	SFS-45-s150	100	150	VB connector	1.82×10^{13} (1.20)
	SFS-90-s150	100	150	VB connector	1.53×10^{13} (1.01)
Shahnewaz et al. [28]	S6-HR-1	150	245	Steel plate+screws	5.70×10^{13} (3.75)
	S6-HR-2	150	245	Steel plate+screws	5.86×10^{13} (3.86)

Based on comparisons in Table 5, in overall, the effective bending stiffness of the CLT-concrete composite floor in this study was found to be comparable and consistent only for slabs with similar dimensions in the studies of Jiang et al. [3] and Mai et al. [27]. The increase in total thickness of the composite floor resulted in an increase of effective bending stiffness as demonstrated in the research of Shahnewaz et al. [28] and vice versa, as shown in the research of Müller [26]. However, such a conclusion should be limited, as there might be other conditions that may influence on the behavior of the connection such as mechanical properties of the concrete and CLT panels, number and spacing of connector, and support condition of specimen.

4.2.7 Conclusion

The global behavior of the HOBOA composite floor was conducted by a series of two flexural tests. The specimens with the same configurations were tested. Two different support conditions were adopted in the test setup. The specimen of the first test (HBF1) was supported on a linear support at one end, and on two point supports at the other end, resulting in bi-dimensional bending behavior (deflections in both directions). The specimen of the second test (HBF2) was lying on two linear supports, resulting in one-dimensional bending behavior (deflection in longitudinal direction). The material properties of concrete and timber were also tested in order to determine the actual values. Before conducting bending test, the shrinkage effect of the composite floor of test HBF2 was also quantified over a period of approximately three months using only its self-weight. After the end of the shrinkage test, the difference of the midspan deflection was obtained around 16 mm during the 100 days of testing period. This value is not negligible and calls for further investigation through a dedicated experimental campaign.

In bending tests, high bending resistances were obtained. The global response of the specimens was almost linear until the failure of the specimens at load levels of 590 KN and 725 KN for tests HBF1 and HBF2, respectively. In test HBF1, the specimen was failed by a local shear rupture in the concrete panel near the point supports, while in test HBF2, it was concluded that the failure was governed by the bending rupture of the CLT panel of the composite floor. Besides, deduced from the test results, the bending stiffness of the test HBF1 was about 8 percent lower than that of the test HBF2. Indeed, having

point supports at one end, the deflection between point supports (transversal deflection) of specimen HBF1 has an impact on the longitudinal deflection, thus making specimen HBF1 less stiff than specimen HBF2. In addition, a comparison was made between the effective bending stiffness obtained in this study and in the literature. The results indicated that the bending stiffness determined from the experimental tests was comparable to that reported in other studies, confirming the effectiveness of the HOBOA system.

4.3 Analytical method for CLT-concrete floor in uniaxial bending

4.3.1 Introduction

It is essential for practical engineers to dispose of a simple but accurate design method for computing the capacity and the performance of structural elements. In the first attempt, this section presents the estimation of the structural performance of composite floors using the uniaxial bending method. The gamma method is adopted to estimate the capacities of both specimens in flexural tests. Furthermore, the influence of connection stiffness and the comparison of relative slip between shear tests and flexural tests are also investigated. The structure of this section is described as follows. The gamma method for the 5-layer CLT-concrete composite floor is explained in subsection 4.3.2. Then, resistance and bending stiffness of tests HBF1 and HBF2 are computed in subsection 4.3.3. In subsection 4.3.4, the comparison between the test results and estimations of the gamma method are made. Lastly, shear force and relative slip curves of the notched connector obtained from pushout tests and flexural test are compared in subsection 4.3.5.

4.3.2 Analytical gamma method

A simplified computation method, mostly known as “gamma method”, provided in Annex C of Eurocode 5 [29], is usually adopted for the design of timber-concrete composite floors. This method was developed by Stussi [30] and Mohler [31]. It is able to take into account the partial degree of connection (the stiffness of the connection) for the determination of the effective bending stiffness, and the strength of the composite floors. The method is developed based on the assumptions of a linear elastic behavior of materials, of a uniformly distributed shear connection, and of sinusoidal or parabolic load. The degree of shear connection is considered in the form of a γ-factor, being equal to 0 for no composite action and 1 for full connection. For the application of the gamma method to the CLT panel, the longitudinal layers of the CLT panel are assumed to carry flexural stresses, whereas the transversal layers are considered as a semi-rigid connection between the longitudinal layers. This method is usually valid for a CLT-concrete composite slab with a three-layer CLT panel. Jiang et al. [3] proposed a modification in the gamma method to apply particularly to CLT-concrete composite floor with 5-layer CLT panels. In their approach, the effective bending stiffness is the sum of two parts (see Figure 25). The first part consists of the concrete panel with the middle and bottom longitudinal layers of the CLT panel while the second part is only the top longitudinal layer of the CLT panel.

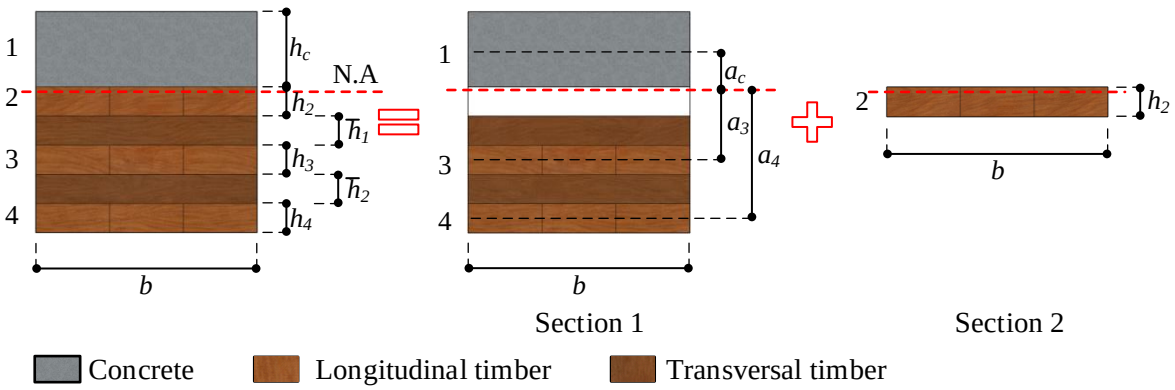

Figure 25: Computation of 5-layer CLT-concrete slabs [3].

For section 1, the stiffness of the connection between the concrete layer and the middle longitudinal layer of the CLT panel is computed as the combination of the stiffness of the notch connector and the rolling shear stiffness of the cross-layer between the top and middle longitudinal layers of the CLT panel. This combined stiffness is given by:

$$\left(\frac{K}{s}\right)_c = \frac{(K_c/s_{eff}) \times (G_R b/\bar{h}_1)}{(K_c/s_{eff}) + (G_R b/\bar{h}_1)} \tag{9}$$

where K_c is the slip modulus of notched connectors; s_{eff} is the effective spacing of notched connectors; G_R is the rolling shear modulus of timber; b is the width of the slab and $\bar{h}_1$ is the height of the first cross-layer of CLT panel, respectively. In addition, when the connector spacings are varied in regard to shear force along the span, the effective spacing of notched connector s_{eff} can be determined using eq. (11):

$$s_{eff} = 0.75 s_{min} + 0.25 s_{max} \tag{10}$$

where s_{min} and s_{max} are signified as the minimum and maximum connector spacings, respectively. The effective bending stiffness of the 5-layer CLT concrete composite section can be computed by:

$$(EI)_{eff} = (EI)_{eff,1} + (EI)_{eff,2} = \sum_{i=c;3;4} (E_i I_i + \gamma_i E_i A_i a_i^2) + E_2 b_2 h_2^3/12 \tag{11}$$

where

$$A_i = b_i h_i \tag{12}$$

$$I_i = b_i h_i^3/12 \tag{13}$$

$$\gamma_3 = 1 \tag{14}$$

$$\gamma_c = \left[1 + \frac{\pi^2 E_c A_c}{L^2} \times \left(\frac{s}{K}\right)_c\right]^{-1} \tag{15}$$

$$\gamma_4 = \left[1 + \frac{\pi^2 E_4 A_4 \bar{h}_2}{G_R b_4 L^2}\right]^{-1} \tag{16}$$

$$a_3 = \frac{\gamma_c E_c A_c (h_c/2 + h_2 + \bar{h}_1 + h_3/2) - \gamma_4 E_4 A_4 (h_3/2 + \bar{h}_2 + h_4/2)}{\sum_{i=c;3;4} \gamma_i E_i A_i} \tag{17}$$

$$a_c = \frac{h_c}{2} + h_2 + \bar{h}_1 + \frac{h_3}{2} - a_3 \tag{18}$$

$$a_4 = \frac{h_3}{2} + \bar{h}_2 + \frac{h_4}{2} + a_3 \tag{19}$$

in which, the subscript i (c, 2, 3, or 4) refers to an i-layer of the structural layers of the composite section (see Figure 25); E_i, I_i, A_i, b_i and h_i refer to the young modulus, the moment of inertia, the area, the width, and the height of the i-layer, respectively; a_i is the distance from the centroid of the i-layer to the neutral axis of composite section; L is the span of the composite floor; and $\bar{h}_i$ is the height of the i-cross layer.

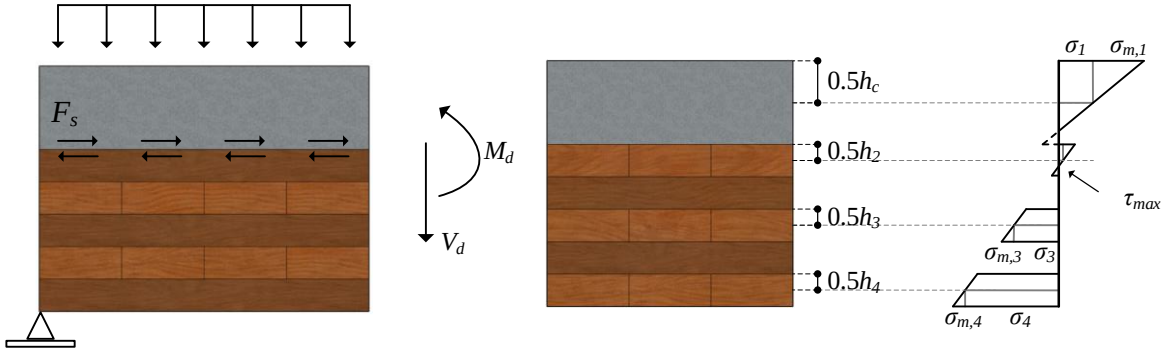

Figure 26: Stress distribution in cross-section.

The load-carrying capacity of the CLT concrete composite floor at the ultimate limit state can be limited by the compressive or tensile stresses of the concrete panel, combined bending and axial tensile stresses in the bottom layer of the CLT panel, longitudinal shear, rolling shear stress of the CLT cross-section, or shear force acting on shear connectors. The cross-sectional normal stress, maximum shear stress, and force acting on connector of the composite floor (see Figure 26) are defined in accordance with the Eurocodes 5 [29] and are expressed as follows:

$$\sigma_i = \frac{\gamma_i E_i a_i}{(EI)_{eff}} M_d \tag{20}$$

$$\sigma_{m,i} = \frac{0.5 E_i h_i}{(EI)_{eff}} M_d \tag{21}$$

$$\tau_{max} = \frac{\gamma_4 E_4 h_4 a_4 + 0.5 E_3 (a_3 + 0.5 h_3)^2}{(EI)_{eff}} V_d \tag{22}$$

$$\tau_r = \frac{\gamma_i E_i h_i a_i}{(EI)_{eff}} V_d \ (i=3 \text{ or } 4) \tag{23}$$

$$F_s = \frac{\gamma_c E_c A_c a_c s}{(EI)_{eff}} V_d \tag{24}$$

where σ_i, $\sigma_{m,i}$, τ_{max}, τ_r, F_s, M_d, and V_d, signify the axial stress, bending stress, longitudinal shear stress, rolling shear stress, the load-carrying capacity on the connectors, bending moment, and maximum shear force, respectively. It is necessary to verify that the ultimate limit conditions are satisfied for each material strength of the CLT-concrete composite floor, as follows:

- Compressive stress on concrete panel (top):

$$\sigma_{c,t} = \sigma_c + \sigma_{m,c} \leq f_{cd} \tag{25}$$

- Tensile stress on concrete panel (bottom):

$$\sigma_{c,b} = -\sigma_c + \sigma_{m,c} \leq f_{ctd} \tag{26}$$

- Combined bending and axial tension:

$$\frac{\sigma_4}{f_{t,0,d}} + \frac{\sigma_{m,4}}{f_{m,0,d}} \leq 1 \tag{27}$$

- Longitudinal shear stress in composite cross-section:

$$\tau_{max} \leq f_{vd} \tag{28}$$

- Rolling shear stress in CLT section:

$$\tau_r \leq f_{rd} \tag{29}$$

- Verification of the fasteners:

$$F_s \leq F_N \tag{30}$$

where f_{cd}, f_{ctd}, $f_{t,0,d}$, $f_{m,0,d}$, f_{vd}, f_{rd}, and F_N are the design concrete compressive strength, design concrete tensile strength, design tensile strength of timber parallel to grain, design bending strength of timber parallel to grain, design shear strength of timber, design rolling shear strength of the cross-layer of the CLT panel, and strength of the connection system, respectively.

4.3.3 Numerical application of the gamma method

The parameters for the numerical application of the gamma method to the configuration of tests HBF1 and HBF2 are given in Table 6 and Table 7. Table 6 presents the geometrical configuration and slip modulus for the computation of the gamma method.

Table 6: Parameters for the gamma method of tests HBF1 and HBF2.

Test	K_s [N/mm/m]	K_u [N/mm/m]	h_c [mm]	h_2,h_3,h_4 [mm]	$\bar{h}_1,\bar{h}_2$ [mm]	L [mm]
HBF1	1.49×10^6	1.03×10^6	85	33	33	6440
HBF2						6540

Concerning mechanical properties of materials, mean values were adopted. For the concrete, the mean value of concrete compressive strength, f_{cm}, obtained from compression tests (see Table 1) was used for the computation of the gamma method. Using the relation between E_{cm} and f_{cm} given in Eurocode 2 [32], modulus of elasticity of concrete, E_{cm}, was derived.

For the timber, the mean value of compressive strength parallel to grain direction, $f_{c,0}$, obtained in characterization tests (see section 4.2.3.2) was used in relations provided by EN 384 [33] in order to obtain other mechanical properties of timber, including mean value of bending strength f_m, mean value of tensile strength parallel to grain $f_{t,0}$, and mean modulus of elasticity parallel to grain $E_{0,mean}$. The relations between mechanical properties given in EN 384 [33] are described as follows:

$$f_{c,0,k} = 4.3 f_{m,k}^{0.5} \tag{31}$$

$$f_{t,0,k} = -3.07+0.73 f_{m,k} \tag{32}$$

where $f_{c,0,k}$, $f_{m,k}$, and $f_{t,0,k}$ are the characteristic compressive strength parallel to grain, characteristic bending strength, and characteristic tensile strength parallel to grain, respectively. It should be noted that the relations given in eq. (31) and eq. (32) use characteristic values. In order to adopt these formulae, the mean value can be converted to the characteristic value supposing a normal distribution as suggested in ASTM D2915 [34]:

$$\bar{x}=\frac{x}{1\text{-}1.645Cov.} \tag{33}$$

where $\bar{x}$ is the mean value, x is the characteristic value, and $Cov.$ is the coefficient of variation. In terms of the coefficient of variation, a value of 15 percent was implemented in the study conducted by Chen et al. [35]. However, from a conservative perspective, the coefficient of variation of 17 percent obtained from compression tests of timber (see section 4.2.3.2) was adopted to determine f_m and $f_{t,0}$. Accordingly, the mean values of bending strength and tensile strength parallel to grain are found : f_m=38 MPa and $f_{t,0}$=23 MPa. For the mean modulus of elasticity, it was derived from Table 1 in the standard EN 338 [11] with $E_{0,mean}$ of 11500 MPa. Table 7 reports the mechanical properties of concrete and timber for the application of the gamma method.

Table 7: Mechanical properties of concrete and timber for the application of the gamma method.

Parameter	E_c [MPa]	E_2,E_3,E_4 [MPa]	G_R [MPa]	f_{cm} [MPa]	$f_{t,0}$ [MPa]	f_m [MPa]	f_v [MPa]	f_r [MPa]	F_N [kN]
Value	36689	11500	60	55	23	38	5.56	1.49	437

The results of the resistance F_{max}, effective bending stiffness $(EI)_{eff}$, and γ-factors of the specimens in tests HBF1 and HBF2 are given in Table 8. It is found that γ_c is reduced from 0.60 to 0.56 for test HBF1 and from 0.61 to 0.57 for test HBF2 when slip modulus of the connector at ULS (K_u) is used instead of slip modulus of the connector at SLS (K_s). This results in a difference of approximately 1.6 percent for test HBF1 and test HBF2 for the estimation of the flexural stiffness between the cases using slip modului K_s and K_u. The resistance of the composite floor is limited by the CLT panel under combined bending and axial tension in both tests with the value ranging from 195 kN to 200 kN per meter width. There is a minimal difference in the maximum force, regardless of whether K_s or K_u is employed. In this study, the failure mode governed by tensile stress of the concrete is not discussed for the design of CLT-concrete composite floor (see [36], [37]). The details of the numerical application of the gamma method as reported in Table 8 can be found in Annex C.

Table 8:The effective bending stiffness and failure load obtained from the gamma method expressed in Eurocode 5 [29], later modified by Jiang et al. [3].

Tests		$(K/s)_c$ [N/mm^2/m]	γ_c	γ_4	F_{max} [kN/m]	$(EI)_{eff}$ [N.mm^2/m]
HBF1	K_s	1.10×10^6	0.60	0.95	200	1.59×10^{13}
	K_u	0.94×10^6	0.56	0.95	196	1.56×10^{13}
HBF2	K_s	1.10×10^6	0.61	0.95	196	1.59×10^{13}
	K_u	0.94×10^6	0.57	0.95	195	1.57×10^{13}

4.3.4 Comparison of experimental and analytical results

In this section, the midspan deflections and resistances of the composite floor obtained from the computation using the gamma method are compared against the results deduced from the experimental tests. The analytical computation is carried out using either K_s or K_u as the stiffness of the connector. Figure 27 illustrates the comparison of the force-deflection curves obtained from tests HBF1 and HBF2 and from the computations using the gamma method with slip modulus of the connection system K_s or K_u. As a reminder, the self-weight of specimens is not included in force-deflection curves.

From this figure, it can be observed that the gamma method provides a good estimation of the deflections for low to moderate load values but is logically not able to capture the nonlinear behavior near collapse. It was shown that the gamma method exhibits a better correlation in the test HBF2, as linear supports were used for both supports, corresponding to the one-dimensional behavior. Test HBF1 generates higher deflection which is contributed by additional deflection between point supports in transversal direction. Even if it is not consistent to apply this one-dimensional bending model in this case, the rest of the discussion will still include the test HBF1, in order to see if this 1D computation can anyway be considered as a good approximation in the case of point supports. In order to set in evidence, the effect of the efficiency of the connection, computations by the gamma method with γ_c=0 (fully no

composite floor) and γ_c=1 (full composite floor) are also provided in the figure. This result shows that the connection system tends to achieve almost full degree of connection.

This efficiency of the connection system can be quantified by the degree of composite action (*DCA*), which can be computed using eq (34):

$$DCA = \frac{(EI)_{exp.} - (EI)_{no}}{(EI)_{ful} - (EI)_{no}} \tag{34}$$

where, $(EI)_{full}$ and $(EI)_{no}$ refer to effective bending stiffnesses with full and no degree of connection, respectively. The bending stiffnesses $(EI)_{full}$ and $(EI)_{no}$ are determined using eq. (11) by assuming the degree of shear connection γ_c=1 for full composite floor and γ_c=0 for non-composite floor. As a result, a high degree of composite action is found at 84 percent for test HBF2. When point supports are adopted in test HBF1, the degree of composite action is "virtually" slightly decreased to a value of 76 percent.

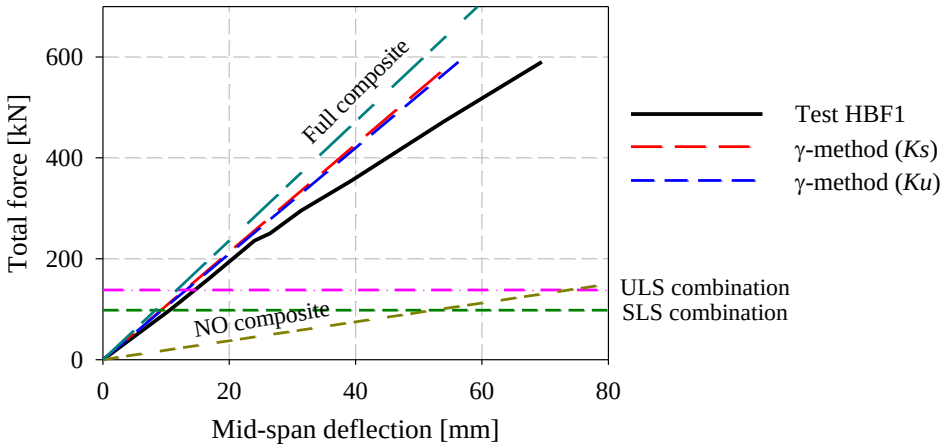

a. Test HBF1

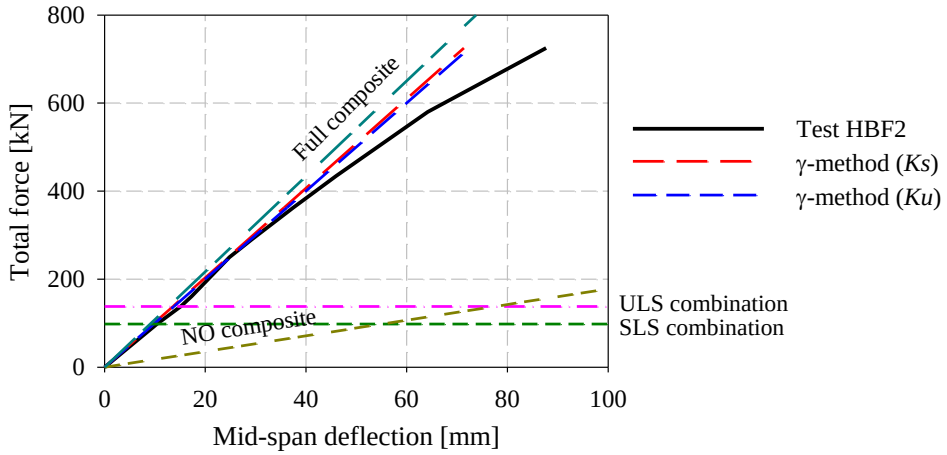

b. Test HBF2

Figure 27: Force-deflection curves of the gamma methods and flexural tests.

For a more detailed comparison of the bending stiffness, Table 9 and Table 10 report the deflections obtained experimentally and analytically by the gamma method for tests HBF1 and HBF2, respectively. SLS and ULS refer to load levels obtained from load combinations at the serviceability limit state and at the ultimate limit state, respectively. The ratios between the deflections obtained from the gamma

method and the one from the flexural test are given in brackets. Since the gamma method is developed based on the assumptions of a linear elastic behavior of materials, the comparisons between the gamma method and experimental tests are considered only in the linear elastic behaviour, which appears to be valid until a half of maximum force obtained (F_{max}/2).

Table 9: The deflections [mm] computed by the gamma method and experimental test at various load levels (SLS, ULS, collapse/2, and collapse) of the test HBF1.

Load level	Flexural test HBF1	Gamma method	
		K_s	K_u
SLS (98 kN)	10.57	9.20 (0.87)	9.35 (0.88)
ULS (138 kN)	14.57	12.95 (0.89)	13.17 (0.90)
F_{max}/2 (295 kN)	31.37	27.69 (0.88)	28.15 (0.90)
F_{max} (590 kN)	69.49	55.38 (0.80)	56.29 (0.81)

Table 10: The deflections [mm] computed by the gamma method and experimental test at various load levels (SLS, ULS, collapse/2, and collapse) of the test HBF2.

Load level	Flexural test HBF2	Gamma method	
		K_s	K_u
SLS (98kN)	10.42	9.64 (0.93)	9.80 (0.94)
ULS (138 kN)	15.11	13.58 (0.90)	13.80 (0.91)
F_{max}/2 (362.5 kN)	37.47	35.68 (0.95)	36.25 (0.97)
F_{max} (725 kN)	87.69	71.35 (0.81)	72.50 (0.83)

It can be seen that a change of about 1 percent in the midspan deflection is obtained by adopting K_u in comparison to the case with K_s. This small difference indicates that the connection system in this study is very stiff. For test HBF1, under the influence of bi-dimensional bending behavior, the difference with the experimental deflection is approximately 12 to 13 percent at SLS, and 10 to 11 percent at ULS. For test HBF2, midspan deflections at SLS and ULS give better estimation compared to test HBF1, with an error from 3 to 10 percent, but not on the safe side. From this comparison, it was shown that the gamma method is able to estimate the deflection of the composite floor in one-dimensional bending behavior with a difference around 7 percent (test HBF2), while a higher difference of around 13 percent in the global deflection (test HBF1) is obtained for the composite floor in bi-dimensional bending behavior due to additional deflection in transversal direction. For a better understanding of the bi-dimensional bending behavior, more sophisticated model should be considered.

To further analysis the composite floor in one-dimensional bending behavior, the estimation of the flexural capacity of the test HBF2 is also made using the gamma method with the slip modulus K_u and compared with the experimental results, as illustrated in Figure 28. It should be noted that the maximum experimental bending moment $M_{d,exp.}$ is calculated using a four-point bending test configuration and the applied maximum force F_{max}. The finding indicated that the flexural capacity estimated using the gamma method is found to be 14 percent lower compared to the experimental one. Besides, the values of applied

bending moments corresponding to SLS and ULS load combinations are approximately 34 kNm/m and 48 kNm/m, respectively. These values are significantly lower than the bending resistance.

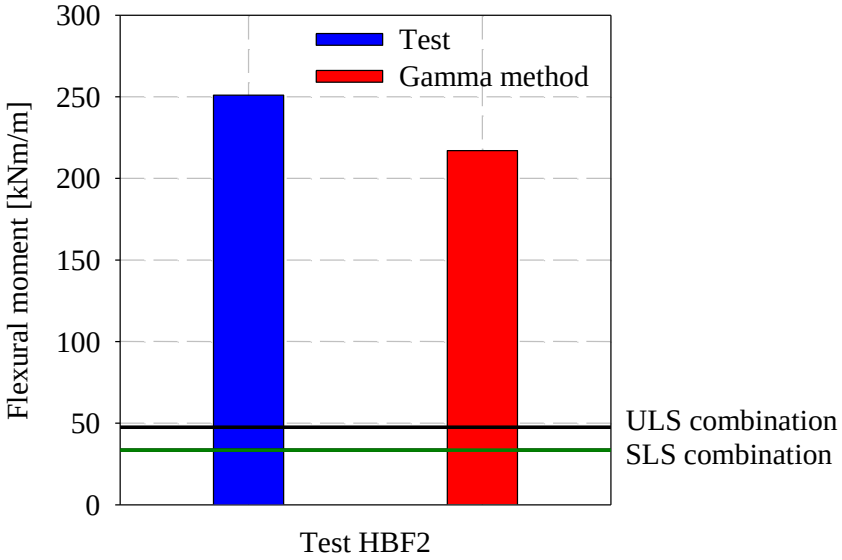

Figure 28: Flexural capacity obtained from the gamma method and experimental test HBF2.

4.3.5 Effect of the partial connection of the composite floor in uniaxial bending

The relative influence of the stiffness of the notch connector and of the rolling shear stiffness of the wood layers on the bending stiffness of the CLT-concrete floor in uniaxial bending is studied. The configuration of the bending test HBF2 is used for this investigation. The following four cases are investigated :

- In case I, the stiffness is obtained by the gamma method with actual stiffnesses of both the connector $K=K_s=1.49\times10^6$ N/mm/m and of the cross-layers of the CLT, $G_R=60$ MPa.
- In case II, a high shear stiffness of the connector $K=10^9$ N/mm/m and a rolling shear stiffness of the cross-layers of the CLT $G_R=60$ MPa are used, in order to consider only the suppleness of the wood cross-layers.
- Case III is the “Bernoulli” case or full composite case, in which a high shear stiffness of the connector $K=10^9$ N/mm/m and a high rolling shear stiffness of the cross-layers of the CLT $G_R=10^6$ MPa are used. With such stiffnesses the section of CLT panel remains plane under bending.
- In case IV, the number of the connectors is reduced approximately to 50 percent value of the one in the experimetal test. Values of the stiffness of the connectors and of the rolling shear of the wood layers are the one adopted in case I.

The effective bending stiffness computed for the four cases are given in Table 11. The table reports also the values of the γ parameters, as well as the ratio between the values obtained in each case with the value of case I.

First of all, the degree of shear connections of case I is respectively $\gamma_c = 0.61$ and $\gamma_4 = 0.95$ for the notch connection and for the CLT layers.

If the suppleness of the wood-concrete connection is not considered (case II), the flexural stiffness increases by 4 percent. The limited gain of the flexural stiffness is due to the fact that the composite action of case I is already high; thus, further increasing the composite action does not improve the stiffness of the composite floor. If the Bernoulli assumption is assumed (case III), the flexural stiffness is 13 percent larger than in case I. Finally, if the number of the connectors is reduced by 50 percent, the flexural stiffness is only decreased by 3 percent.

Table 11: Parametric study on the influence of the degree of shear connection on effective bending stiffness.

Case	G_R [GPa]	K_s [N/mm/m]	$(K/s)_c$ [N/mm^2/m]	γ_c [-]	γ_4 [-]	Test HBF2	
						$(EI)_{eff}$ [N.mm^2]	Ratio [-]
I	60	1.49×10^6	1.10×10^6	0.61	0.95	1.59×10^{13}	1.00
II	60	10^9	1.81×10^6	0.72	0.95	1.66×10^{13}	1.04
III	10^6	10^9	29.8×10^9	1.00	1.00	1.80×10^{13}	1.13
IV	60	1.49×10^6	0.79×10^6	0.52	0.95	1.54×10^{13}	0.97

As a general conclusion, the global loss of bending stiffness due to partial interaction is little, yet noticeable. It is mainly due to the rolling shear effects in the wood, and trying to increase further the wood-concrete connection stiffness would not have a noticeable effect. Thus, it is possible to further optimize the design with respect to the number, the spacing and the geometry of the connectors.

4.3.6 New estimation of the force-slip curve of connectors deduced from the bending test

In pushout tests as well as in flexural tests, the loading was paused several times in order to observe the cracks and the damages in the specimens. Such pauses have generated creep deformations. In this regard, this section is devoted to comparing the shear force-slip curve derived from the flexural test and the one from the pushout tests with and without the plateaus of the curves created by the pauses. For the consistency in the comparison, only test HBF2 was regarded due to the one-dimensional behavior achieved from its linear support condition.

For the test, the slip of the notched connector was obtained from measurement, while the longitudinal shear force F_N is determined using eq. (24), which relies on the shear force V corresponding to four-point flexural load levels. The longitudinal shear forces applied to the notched connectors are computed at different load levels and presented in Table 12. The corresponding slips are determined as a mean value of the slips obtained from sensors CG1, CG4, CG5, and CG8. Figure 29 shows the mean force-slip curves obtained from the pushout tests and from the flexural test.

Table 12: Obtained average slips at different load levels of flexural test HBF2.

	$0.2F_{max}$	$0.4F_{max}$	$0.6F_{max}$	$0.8F_{max}$	F_{max} (725 kN)
F_N [kN]	93	156	219	282	345
Slip [mm]	0.016	0.062	0.103	0.163	0.353

It can be seen from Figure 29 that larger slips were obtained in the pushout tests (green curve) than in the flexural test (red curve) for the same levels of shear forces. This can be due to the horizontal

plateaus related to the pauses that were made during the loading of pushout tests and flexural test HBF2 for observing the evolution of the damages in the specimens. After removing these horizontal plateaus, the modified force-slip curve (black curve) in the pushout tests fits well with the one (blue curve) obtained from the flexural test. The slip modulus derived from the modified force-slip curve of pushout tests (black curve in Figure 29) in both service and ultimate conditions are K_s=3.2×10^6 N/mm/m and K_u=1.85×10^6 N/mm/m, 2.15 and 1.79 times the initial slip moduli of pushout tests.

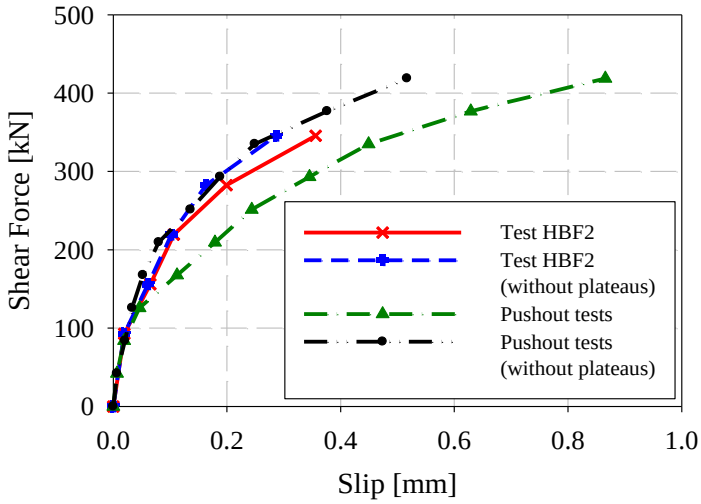

Figure 29: Comparison of shear force-slip curves.

4.3.7 Conclusion

The gamma method provided in Eurocode 5 [32], later modified by Jiang et al. [3], was adopted to determine the effective bending stiffness, midspan deflection, and load-carrying capacity of the composite floors. The gamma method provided a better estimation for test HBF2 compared to test HBF1. This is because linear supports were used for both supports for test HBF2, whereas point supports were used for test HBF1. Furthermore, in order to investigate the relative influence of the stiffness of the notch connector and of the rolling shear stiffness of the wood layers on the bending stiffness of the CLT-concrete floor, a number of sensitivity cases were studied. The results showed that the stiffness of the wood-concrete connection with the spacing as adopted in the test was already high, and trying to increase further the wood-concrete connection stiffness would not have a noticeable effect. Therefore, it was possible to further optimize the design with respect to the number, the spacing and the geometry of the connectors. Force-slip curves derived from the flexural test and from pushout tests were afterwards compared in order to verify the effect of timber creep due to pauses and cyclic loading during the tests. As a result, a close correlation of force-slip curves was obtained, when removing slips caused by pauses and cyclic loading during the tests. It should be noted that the slip modulus derived from the modified force-slip curve of pushout tests at SLS and ULS were 2.15 and 1.79 times the initial slip moduli, respectively.

4.4 Bi-dimensional effects on CLT-concrete composite floor

4.4.1 Introduction

Point supports were used in the experimental flexural test HBF1 (see Figure 3a), resulting in bi-dimensional bending effect (deflections in both directions). It should be acknowledged that the typical CLT panel can withstand two-dimensional loading due to its crosswise arrangement of timber boards between each layer. Combined with the topping concrete panel, the behavior of the composite floor in transversal direction should be considered.

In this section, CLT-concrete composite floor in bi-dimensional bending effect is studied. The first objective of this study aims to develop and validate models of the composite floor using a simple engineering software [7], including a beam grid model in subsection 4.4.2 and a orthotropic plate model in subsection 4.4.3. The validation of both models is described in subsection 4.4.4. The second objective involves the sensitivity investigation of different assumptions such as loading and boundary conditions, the cracking condition of the concrete, and the torsional stiffness of the composite floor on the behavior of the CLT-concrete floor system using the orthotropic plate model, as will be presented in subsection 4.4.5.

4.4.2 Beam grid model of the composite floor in bi-dimensional bending

A beam grid model was generated in a commercial finite element program [7]. In this model, the CLT-concrete composite floor was discretized into *m* bands in transversal direction and *n* bands in longitudinal direction (see Figure 30a). The longitudinal and transversal beams share common nodes at the intersections (see Figure 30b). The loading system consisting of three HEA-300 beams, was modelled following the installation in the test setup (see Figure 30c). A pinned-fixed connector element and fixed-fixed connector elements were used for connecting HEA-300 to HEA-300 beams and for connecting HEA-300 beams to the grid beams, respectively, in this model.

In order to take into account the composite cross-section of the slab, an equivalent height of the beam cross-section was computed by equating the effective stiffness obtained from the gamma method with the equivalent stiffness of concrete cross-section (see Figure 31). The equivalent height in transversal and longitudinal directions can then be determined, respectively, by:

$$h_{c,eq,\,L} = \left(12 \frac{(EI)_{eff,L}}{E_c b_L} \right)^{1/3} \tag{35}$$

$$h_{c,eq,T} = \left(12 \frac{(EI)_{eff,T}}{E_c b_T} \right)^{1/3} \tag{36}$$

where $(EI)_{eff,L}$ and $(EI)_{eff,T}$ are the effective bending stiffness of each band in longitudinal and transversal direction respectively; E_c is the modulus of elasticity of concrete; b_L and b_T are the width of each band in longitudinal and transversal directions, respectively.

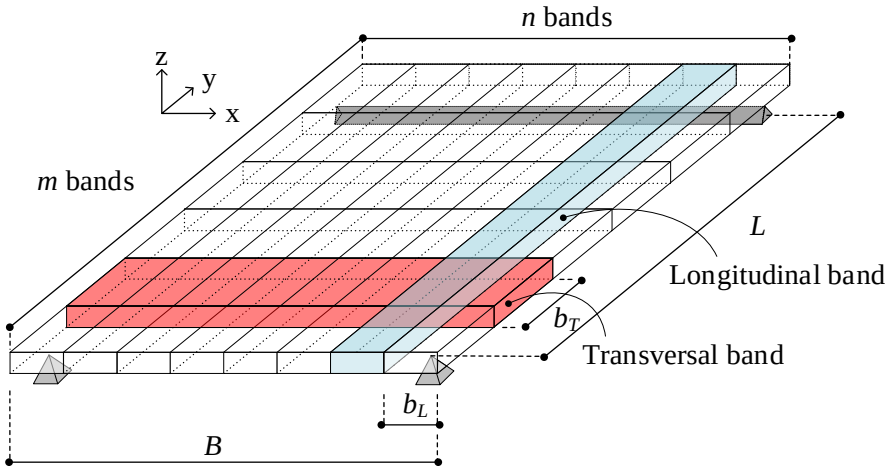

a. Division of slab into several bands

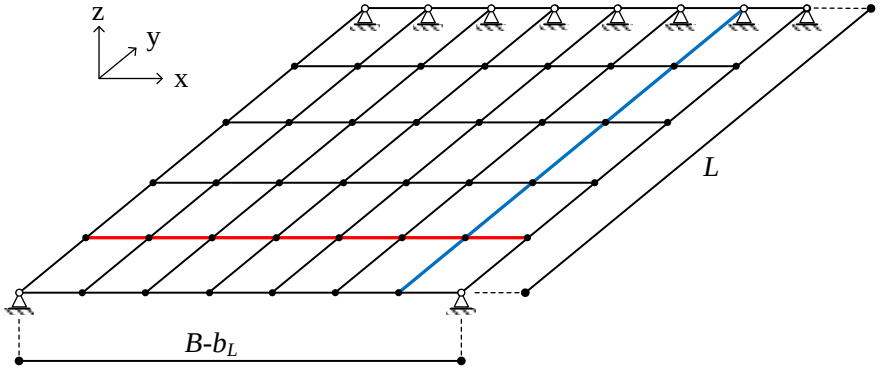

b. Beam grid model

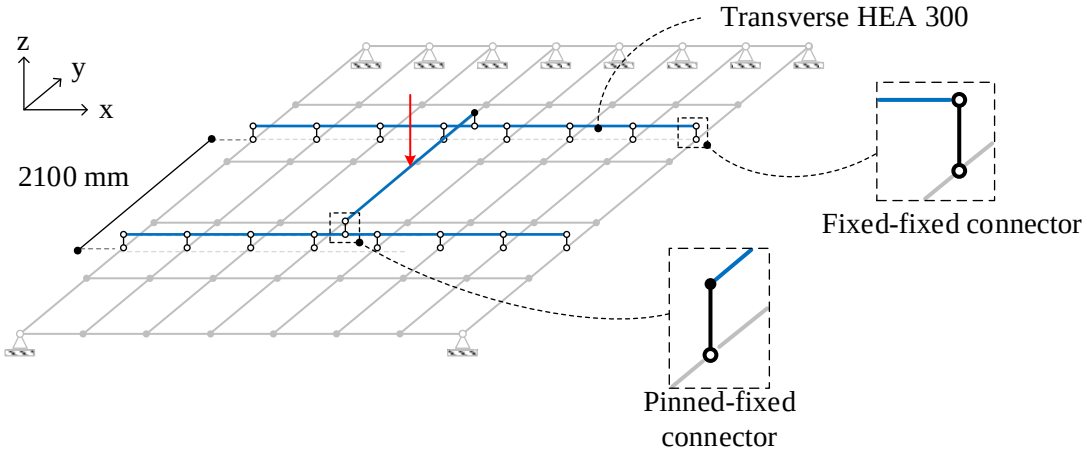

c. Loading system in beam grid model

Figure 30: Beam grid model of the flexural test HBF1.

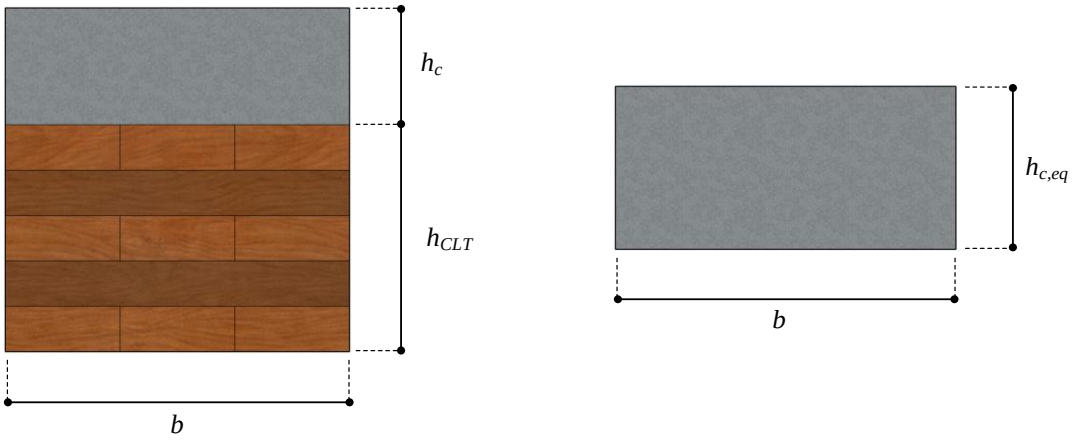

a. Composite cross-section b. Equivalent concrete cross-section

Figure 31: Composite section and equivalent concrete section.

The effective bending stiffness in longitudinal direction can be adopted using the gamma method expressed in Eurocode 5 [29], later modified by Jiang et al. [3], which is described in section 4.3.2.

In transversal direction of the composite floor, three effective layers of composite cross-section were considered, consisting of the top concrete layer and two longitudinal timber layers of the CLT panel, in order to compute the effective bending stiffness (see Figure 32a). It should be noted that no composite action was considered at the interface layer of composite floor in transversal direction since no connection system was adopted, and the friction between concrete and CLT panel was neglected. Therefore, the concrete panel and CLT panel acted independently as shown in Figure 32a. According to the computation detail in Annex C of Eurocode 5 [29], the effective bending stiffness of the composite floor in transversal direction (see Figure 32b) can be described by eq. (37):

$$(EI)_{eff,T} = \sum_{i=c;2;3} (E_i I_i + \gamma_i E_i A_i a_i^2) \tag{37}$$

where

$$\gamma_c = 0 \tag{38}$$

$$\gamma_2 = 1 \tag{39}$$

$$\gamma_3 = \left[1 + \frac{\pi^2 E_3 A_3 \bar{h}_2}{G_R b_4 L^2}\right]^{-1} \tag{40}$$

$$a_3 = \frac{\gamma_c E_c A_c (h_c/2 + \bar{h}_1 + h_2/2) - \gamma_3 E_3 A_3 (h_2/2 + \bar{h}_2 + h_3/2)}{\sum_{i=c;2;3} \gamma_i E_i A_i} \tag{41}$$

in which, the subscript i (c, 2, or 3) refers to an i-layer of the structural layers of the composite section in transversal direction; E_i, I_i, A_i, b_i and h_i refer to the young modulus, the moment of inertia, the area, the width, and the height of the i-layer; a_i is the distance from the centroid of the i-layer to the neutral axis of composite section; L is the span of the composite floor in transversal direction; $\bar{h}_i$ is the height of the i-cross layer; and γ_i is the degree of shear connector of the i-layer.

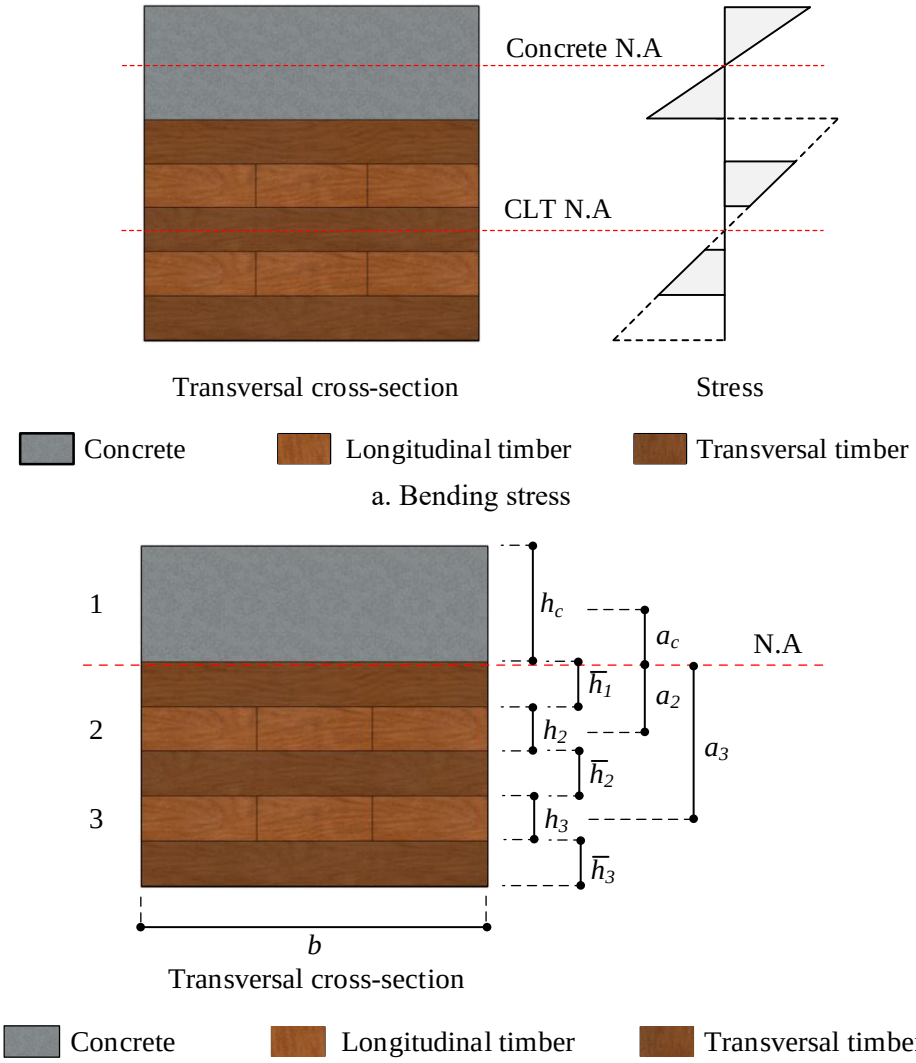

Figure 32: Bending stress and computation of effective bending stiffness of the composite floor in transversal direction.

The parameters for the beam grid model of tests HBF1 and HBF2 are given in Table 13. Again, parameters m and n denote the number of bands in transversal and longitudinal directions, respectively; b and L represent the width and length of the beam grid models; b_L and b_T signify the width of the respective longitudinal and transversal beams; and c is the distance between the support to the nearest loading system.

Table 13: Parameters for beam grid models of tests HBF1 and HBF2.

Test	m	n	b [mm]	L [mm]	b_L [mm]	b_T [mm]	c [mm]
HBF1	12	8	3200	6440	400	537	2170
HBF2	12	8	3200	6540	400	545	2220

4.4.3 Orthotropic plate model of the composite floor in bi-dimensional bending

4.4.3.1 Geometry of model

The bi-dimensional behavior of composite floor systems can also be modelled in a more refined way by an orthotropic plate model available in the same engineering program [7] as for the beam grid model. The geometry of the orthotropic plate model is simulated based on experimental setups. Figure 33 visualizes the orthotropic plate models of test HBF1 and test HBF2 in the engineering program. To model the loading condition on plate models at SLS load level (F_{sls}=98 kN), a point load F_z of 49 kN is applied on the middle of the top surface of two HEA-300 beams, which are integrated into plate models.

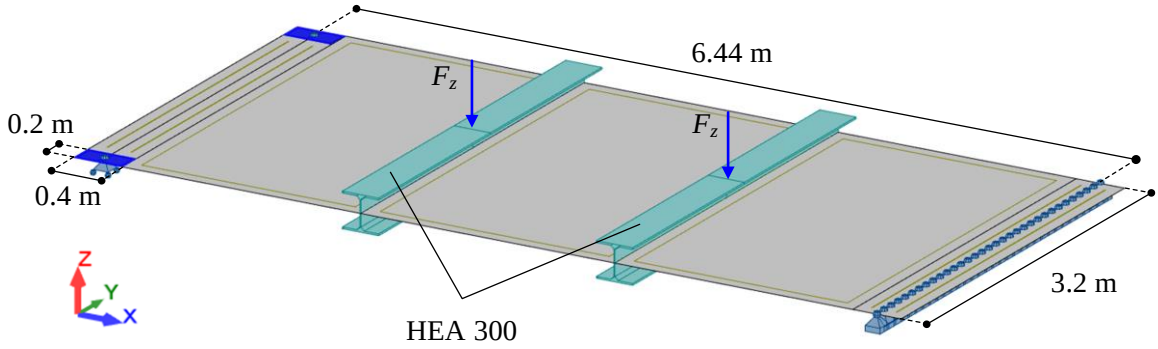

a. Test HBF1

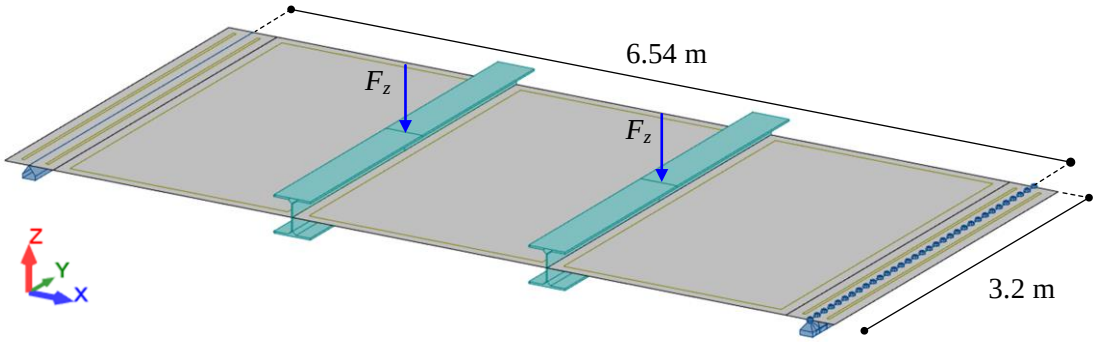

b. Test HBF2

Figure 33: Orthotropic plate models of flexural tests.

For the linear support system, pinned support is applied to a line along the transversal direction of the model. To model the point support system in test HBF1, a plate of high modulus of elasticity with dimensions of 400 mm in length and 200 mm in width, corresponding to the actual configuration in the experimental test setup, is modelled. A pinned support is then applied to a node in the middle of the plate (see Figure 34).

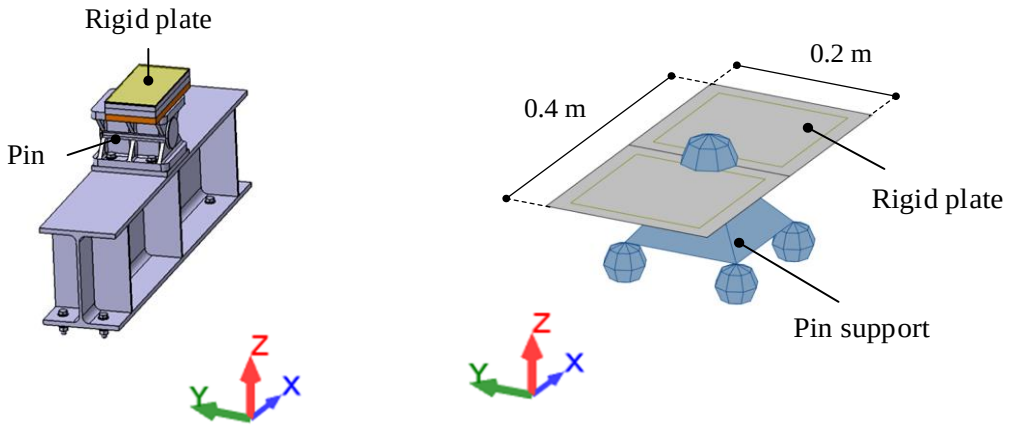

a. Experimental test b. Orthotropic plate model

Figure 34: Model of the point support in test HBF1.

4.4.3.2 Stiffness

Figure 35 presents the definition of main axes (x, y, and z) and forces in the orthotropic plate element. The forces include:

- Moments: 2 bending moments (M_x ; M_y) and 1 torsional moment (M_{xy}=M_{yx})
- Out-of-plane forces: 2 shear forces (N_{xz} ; N_{yz})
- In-planes forces: 2 normal forces (N_x ; N_y) and 1 shear force (N_{xy}=N_{yx})

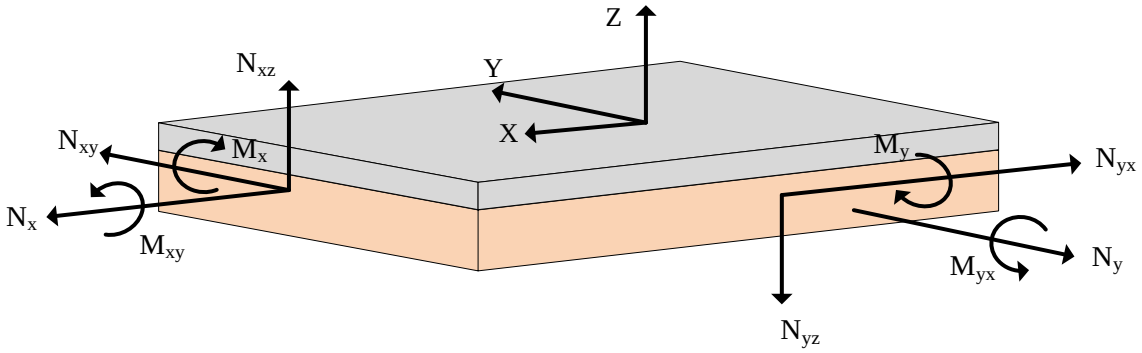

Figure 35: Definition of main axes and main directions for orthotropic plate.

The stiffness matrix of orthotropic plate, C, is established in the following form:

$$C = \begin{bmatrix} D_{11} & D_{12} & 0 & 0 & 0 & 0 & 0 & 0 \\ D_{21} & D_{22} & 0 & 0 & 0 & 0 & 0 & 0 \\ 0 & 0 & D_{33} & 0 & 0 & 0 & 0 & 0 \\ 0 & 0 & 0 & D_{44} & 0 & 0 & 0 & 0 \\ 0 & 0 & 0 & 0 & D_{55} & 0 & 0 & 0 \\ 0 & 0 & 0 & 0 & 0 & D_{66} & D_{67} & 0 \\ 0 & 0 & 0 & 0 & 0 & D_{76} & D_{77} & 0 \\ 0 & 0 & 0 & 0 & 0 & 0 & 0 & D_{88} \end{bmatrix} \quad (42)$$

where

$[D_{11}-D_{33}]$ describes the flexural stiffness matrix;

$[D_{44}-D_{55}]$ describes the shear stiffness matrix;

$[D_{66}-D_{88}]$ describes the membrane stiffness matrix.

In stiffness matrix C, the terms D_{11} and D_{22} are signified as the bending stiffness of the composite floor in longitudinal direction $(EI)_{eff}$ and transversal direction $(EI)_{eff,T}$, respectively. The gamma method, which uses the slip modulus of notched connector at serviceability limit state, K_s, is adopted to define the bending stiffness.

The term D_{33} represents the value of torsional stiffness GI which is included in the model by combining the torsional stiffnesses of the concrete panel $(GI)_{con}$ and of the CLT panel $(GI)_{CLT}$ using eq.(43):

$$GI=(GI)_{con}+(GI)_{CLT} \tag{43}$$

where G_{con} and G_{CLT} are shear moduli of concrete panel and CLT panel, respectively. The off-diagonal terms D_{12} and D_{21} in matrix stiffness C, can be determined using eq (44):

$$D_{12}=D_{21}=\sqrt{v_{xy}v_{yx}D_{11}D_{22}} \tag{44}$$

where v is the Poisson ratio of plate model. In this study, the Poisson ratios of timber are assumed to be zero and the contribution of Poisson ratio of concrete is neglected ($v_{xy}=v_{yx}=0$). Accordingly, terms D_{12} and D_{21} are then equal to zero. It should be noted that the off-diagonal terms in stiffness matrix C were also disregarded in other studies (see [38] and [39]).

In this study, only the flexural stiffness matrix is considered in the plate model while shear stiffness matrix and membrane stiffness matrix are not discussed. It was verified in the model that the changes of values in membrane stiffness and shear stiffness matrix had no influence on the performance of the composite floor model. The computation formulae for terms in shear stiffness matrix and membrane stiffness matrix can be found in [39] and [40]. Table 14 reports the parameters to be used in stiffness matrix C of plate models. The numerical application of effective bending stiffness of the composite floor in transversal direction is described in Annex D.

Table 14: Parameters for stiffness matrix in orthotropic plate models of tests HBF1 and HBF2.

Test	Support condition	$(EI)_{eff}$ [kN.m^2/m]	$(EI)_{eff,T}$ [kN.m^2/m]	GI [kN.m^2/m]
HBF1	2 linear supports	15900	2848	958
HBF2	1 linear and 2 point supports	15900	2848	958

4.4.4 Comparison between beam grid model and orthotropic plate model

Table 15 summarizes the comparison of midspan deflection in longitudinal ($w_{max,L}$) and transversal ($w_{max,T}$) directions, which were deduced from experimental tests, beam grid models, and orthotropic plate models at the SLS load level. The values in brackets are the ratio of the results obtained from beam grid models and orthotropic plate models to those obtained from flexural tests. It should be noted that the experimental midspan deflection between point supports in transversal direction for test HBF1 was not available.

Table 15: The midspan deflections [mm] deduced from experimental tests, beam grid model, and orthotropic plate model at SLS load level.

Test	Flexural test		Beam grid model			Orthotropic plate model		
	$w_{max,L}$ [mm]	$w_{max,T}$ [mm]	$w_{max,L}$ [mm]	$w_{max,T}$ [mm]	$\frac{w_{max,T}}{w_{max,L}}$	$w_{max,L}$ [mm]	$w_{max,T}$ [mm]	$\frac{w_{max,T}}{w_{max,L}}$
HBF1	10.57	--	9.59 (0.91)	1.11	0.12	10.22 (0.97)	3.13	0.21
HBF2	10.42	0	9.72 (0.93)	0		9.70 (0.93)	0	

Compared to experimental results, the beam grid model underestimates the midspan deflection in longitudinal direction approximately 9 percent and 7 percent for tests HBF1 and HBF2, respectively. Besides, the ratio between transversal and longitudinal deflection for test HBF1 $w_{max,T}/w_{max,L}$ is 12 percent. For the orthotropic plate model, the midspan deflection is underestimated around 3 percent and 7 percent for test HBF1 and test HBF2, respectively. The ratio of $w_{max,T}/w_{max,L}$ is 21 percent.

In the model of test HBF2, consistent results are obtained between beam grid model and orthotropic plate model. However, for the model of composite floor in bi-dimensional bending effect (test HBF1), the plate model provides more satisfactory results than the beam grid model. The orthotropic plate model should be preferred as it delivers a more refined representation of the transversal behavior. However, the lack of local experimental measurements does not allow to fully validate its accuracy.

4.4.5 Discussion on modelling options of the orthotropic plate model

The plate model developed in section 4.4.3 used simplified assumptions to define the behavior of the composite floor in bi-dimensional bending effect. In order to gain more insights and to refine the modelling of the composite floor in bi-dimensional bending effect, different assumptions of the support condition, loading condition, torsional stiffness, and bending stiffness of the composite floor in transversal direction were made. In this study, such assumptions and investigated parameters are first addressed in section 4.4.5.1. Then, section 4.4.5.2 investigates the influence of the loading configurations, the support conditions, and torsional stiffness on the performance of the plate model. Next, section 4.4.5.3 reviews the performance of the composite floor when concrete notched section is included in the concrete section of the composite floor in transversal direction. Lastly, the effect of distributed loading, which is usually considered in the practice design, is studied in section 4.4.5.4. It should be noted that the orthotropic plate model developed in section 4.4.3 and the configuration of test HBF1 are adopted in this study.

4.4.5.1 Assumptions and investigated parameters

The details of the parameters investigated, including the bending stiffness of composite floor in transversal direction, support condition, and loading condition, are described in the following sections.

A. Bending stiffness of composite floor in transversal direction

The assumption used in section 4.4.3 ignores the contribution of the concrete notch section to the effective bending stiffness of the plate model in transversal direction. The dimensions of the notch might be significant and should not be neglected. This section proposes other options to take into account the contribution of the notch to compute the effective bending stiffness of composite floor in transversal direction.

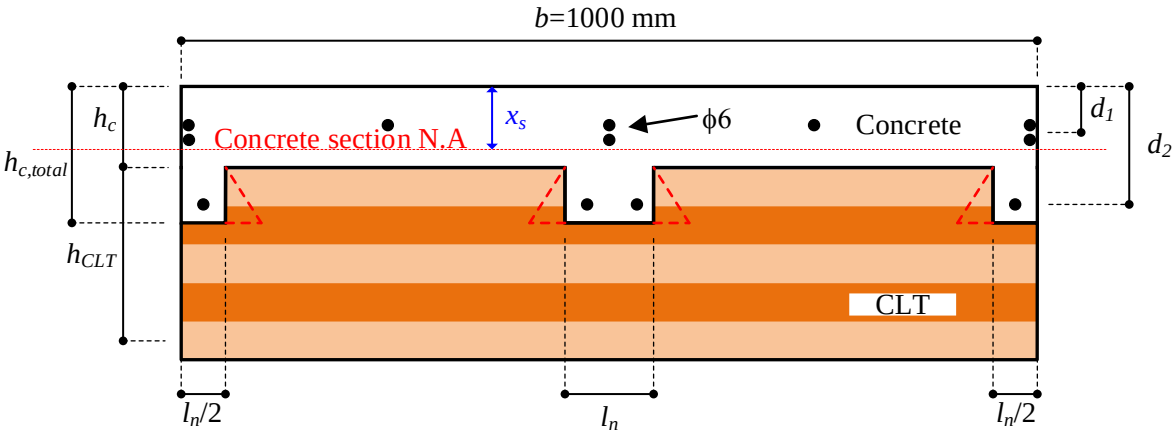

Figure 36: Cross-section of composite floor in transversal direction per one meter width.

Figure 36 shows the cross-section of the composite floor in transversal direction per meter width. To simplify the manual calculation, the dovetail-shape notched connector was considered in rectangular shape. Assuming no composite action in transversal direction, the effective bending stiffness in transversal direction $(EI)_{eff,T}$ can be computed using eq. (37) which was described in section 4.4.2. Three hypotheses regarding the effective bending stiffness of concrete in transversal direction were considered.

For the first hypothesis, referred as hypothesis I, the concrete notched section was neglected, as it was done in the beam grid model presented in section 4.4.2 and the orthotropic plate model discussed in section 4.4.3.

For the second hypothesis, referred as hypothesis II, the cross-section of the concrete panel with presence of concrete notched section was considered and assumed to be in uncracked condition along the transversal direction of the composite floor. Accordingly, the concrete part in transversal direction of the composite floor was transformed into a concrete T-beam which provides the necessary reinforcement to control the cracking. The effective bending stiffness of concrete in transversal direction $(EI)_{eff,T,con}$ can be computed using eq. (45):

$$(EI)_{eff,T,con.}=E_c\left[\frac{2l_n x_s^3}{3}+\frac{2l_n\left(h_{c,total}-x_s\right)^3}{3}+\alpha_e A_{s1}(d_1-x_s)^2+\alpha_e A_{s2}(d_2-x_s)^2+(b-2l_n)\frac{h_c^3}{12}+(b-2l_n)h_c\left(x_s-\frac{h_c}{2}\right)^2\right] \quad (45)$$

where α_e is the ratio between the young modulus of steel and that of concrete, and x_s is the position of neutral axis of the cross-section of the reinforced concrete panel. The parameters α_e and x_s can be determined by using eqs. (46) and (47), respectively:

$$\alpha_e = E_s / E_c \tag{46}$$

$$x_s = \frac{\alpha_e(A_{s1}d_1 + A_{s2}d_2) + 2l_n h_{c,total}^2/2 + (b-2l_n)h_c^2/2}{2l_n h_{c,total} + (b-2l_n)h_c + \alpha_e(A_{s1} + A_{s2})} \tag{47}$$

The parameter E_s is the modulus of elasticity of the reinforcement rebar; d_1 and d_2 are the distance between top surface of the concrete panel to rebars in the middle of the concrete panel and to rebars in the notched connector, respectively; A_{s1} and A_{s2} refer to the reinforcement areas in the concrete panel and in the notched connector, respectively; l_n denotes the length of the notched connector; h_c and $h_{c,total}$ are the thickness of the concrete panel and the total thickness of the concrete panel and notched connector, respectively; and b is the width of the composite floor (see Figure 36).

In the third assumption, referred as hypothesis III, the cross-section of the concrete panel included concrete notched section was considered and assumed to be in cracked condition along the transversal direction of the composite floor. Therefore, the effective bending stiffness of the concrete panel in transversal direction is computed using eq. (48):

$$(EI)_{eff,T,con.} = E_c \left[\frac{b x_s^3}{3} + \alpha_e A_{s1}(d_1 - x_s)^2 + \alpha_e A_{s2}(d_2 - x_s)^2 \right] \tag{48}$$

The neutral axis position of the reinforced concrete panel x_s is assumed to be located in the concrete part above the notched connector ($x_s < h_c$) and can be found using eq. (49):

$$x_s = \frac{\alpha_e(A_{s1} + A_{s2})}{b} \left[\sqrt{1 + \frac{2bA_{s1}d_1 + A_{s2}d_2}{\alpha_e(A_{s1} + A_{s2})^2}} - 1 \right] \tag{49}$$

Table 16 reports the results of effective bending stiffness in transversal direction of the flexural test HBF1. The parameters, including the young modulus and shear modulus of materials as well as the thickness of concrete and CLT panel are described in Table 6 and Table 7.

Table 16: Parameters and effective bending stiffness in transversal direction.

Assumption	x_s [mm]	$(EI)_{eff,T}$ [kN.m^2/m]
Hypothesis I: Concrete without notched section	42.5	2848
Hypothesis II: Concrete with notched section (Uncracked)	50.38	4703
Hypothesis III: Concrete with notched section (Cracked)	21.14	1887

According to Eurocode 2 [32], the cracking bending moment due to tensile stress, can be found using eq. (50):

$$M_{yy,cr} = \frac{(EI)_{eff,T}}{E_c(h\text{-}x_s)} f_{ctm,fl} \tag{50}$$

where $(EI)_{eff,T}$ is the effective bending stiffness of concrete section of composite floor in transversal direction, h is the thickness of the concrete part (using h_c for hypothesis I and $h_{c,total}$ for hypotheses II and III), and $f_{ctm,fl}$ is the flexural tensile strength of the concrete, which can be defined by the following relationship in eq. (51) and is in function of the tensile strength of the concrete, f_{ctm}.

$$f_{ctm,fl} = \{\max(1.6\text{-}h/1000) f_{ctm} ; f_{ctm}\} \tag{51}$$

For the model with the assumption of hypotheses II and III, the tensile stress in the rebars σ_{s2} and tensile stress of the concrete at the lower part of the notched connector $\sigma_{c,inf}$ are computed using the analytical formulae as shown in eqs. (52) and (53), respectively [32]:

$$\sigma_{s2} = \frac{M_{yy,max}}{(EI)_{eff,T}} E_s(d_2\text{-}x_s) \tag{52}$$

$$\sigma_{c,inf} = \frac{M_{yy,max}}{(EI)_{eff,T}} E_{cm}(h\text{-}x_s) \tag{53}$$

where $M_{yy,max}$ is the maximum bending moment along the transversal direction obtained from the plate model, $(EI)_{eff,T}$ is the effective bending stiffness of composite floor in transversal direction with the assumption of hypotheses II or III. It should be noted that the tensile stress $\sigma_{c,inf}$ was only computed when hypothesis II was assumed in studied cases.

B. Support condition

A correct definition of the support condition is necessary for the model of the composite floor. For the point support adopted at one end of the composite floor, two assumptions for the point support condition were considered. The first assumption for the point support was the one described in section 4.4.3, hereby called “plate support” (see Figure 37a). In the second assumption, this point support was made by applying a pinned support to the edge node of the orthotropic plate model, called “node support” (see Figure 37b). For the linear support adopted at the other end of the composite floor, pinned support was applied to a line along the transversal direction of the model, called “line support” (see Figure 37c).

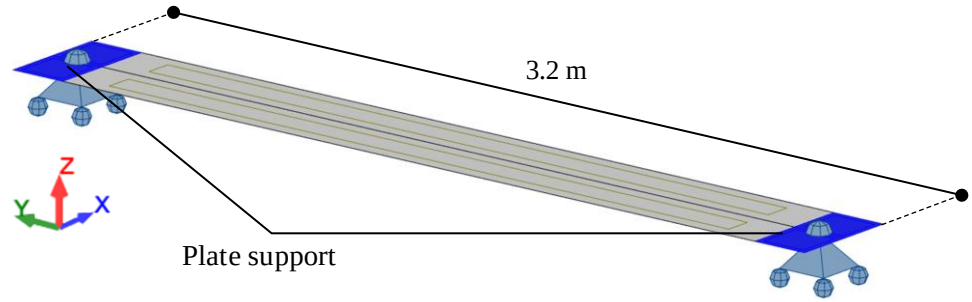

a. Plate support

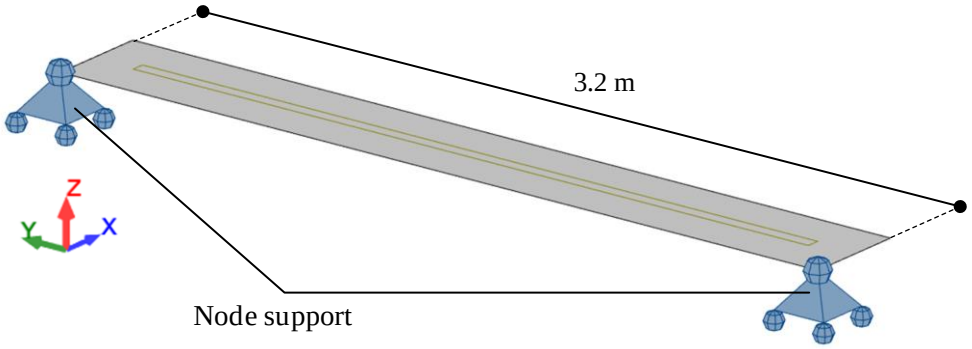

b. Node support

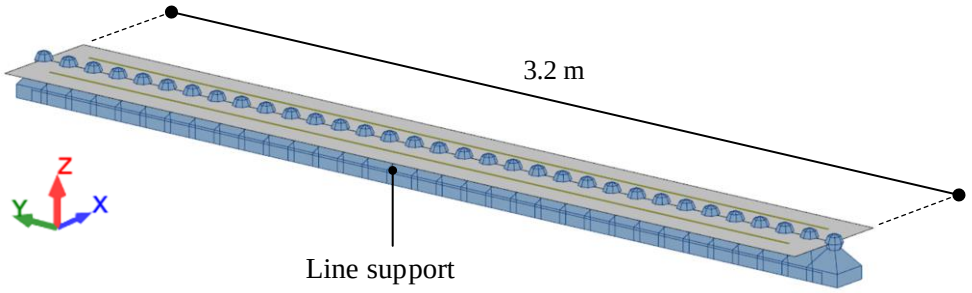

c. Line support

Figure 37: Support conditions in the model of composite floor.

C. Loading condition

In the configuration of the bending test, the loading was applied under 4-point bending condition. In order to understand the effect of different applied loading distributions on the behavior of the composite floor, three different assumptions of loading configurations are considered. The first loading configuration, referred as “linear load”, involved the direct transfer of loads to the composite floor in form of linear loads. A linear load F_z of 15.31 kN/m was applied to a line along the transversal direction of the composite floor (see Figure 38a). In the second loading configuration (see Figure 38b), denoted as “linear-beam load”, the actual loading configuration in flexural test was modeled by integrating steel HEA-300 beams in the composite floor model, which was described in section 4.4.3. For the third loading configuration, the distributed load, signified as “distributed load”, was studied. This loading type was usually considered in practice for the design. At SLS load level, the load was equal to F_z = 6.53 kN/m^2 (see Figure 38c).

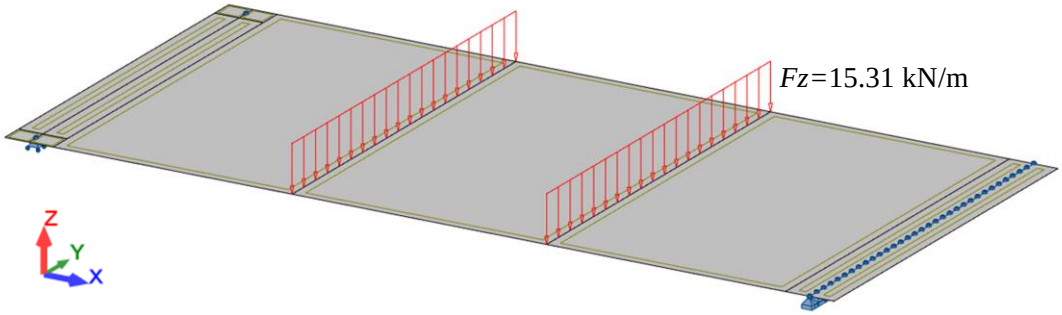

a. Case “Linear load”

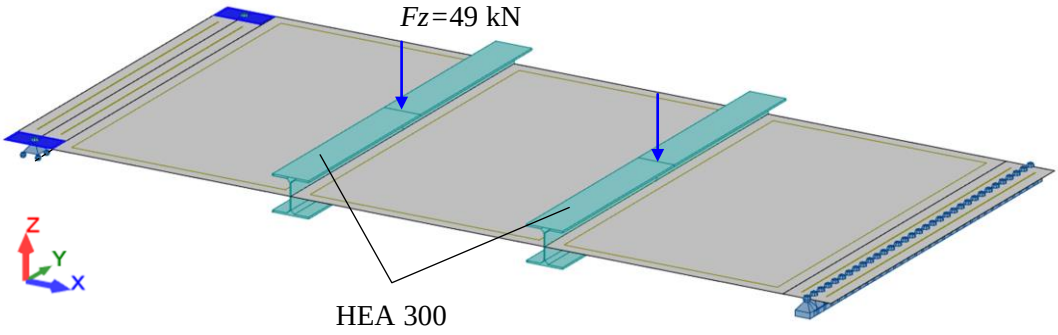

b. Case “Linear-beam load”

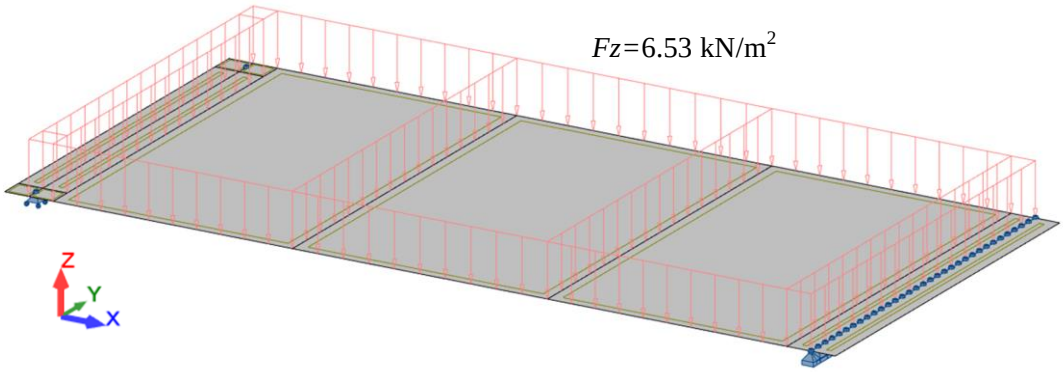

c. Case “Distributed load”

Figure 38: Loading configurations applied on the plate model.

4.4.5.2 Effect of torsional stiffness, loading configuration, and support condition

This section presents study cases for investigating the influence of torsional stiffness, loading configurations, and support conditions on the plate models. Table 17 summarizes the parameters of each case for the investigation from cases P01 to P04. In case P01, the model of the composite floor was made following the assumption studied in section 4.4.3. The plate model was subjected to the linear-beam load configuration and supported by plate supports (point support), while in transversal direction, concrete notched section was disregarded (hypothesis I). In case P02, the loading configuration was investigated by applying the linear load configuration instead of the linear-beam load configuration, while other parameters remained the same as in case P01. Additionally, case P03 was made in order to study the effect of the point support condition by adopting the node support as an alternative to the plate support. Except for the support condition, other parameters in case P03 remained unchanged in

comparison to case P02. In case P04, the influence of torsional stiffness was investigated. The torsional stiffness in case P04 was reduced to zero in order to compare to case P03.

Table 17: Detailed parameters from cases P01 to P04.

Case	Support condition	Loading condition	Torsional stiffness [kN.m^2/m]	Properties in transversal direction	
				Hypothesis	$(EI)_{eff,T}$ [kN.m^2/m]
P01	1 line[1] – 2 plates[2]	Linear-beam[3]	958[4]	Hypothesis I	2848
P02	1 line[1] – 2 plates[2]	Linear[5]	958[4]	Hypothesis I	2848
P03	1 line[1] – 2 Nodes[6]	Linear[5]	958[4]	Hypothesis I	2848
P04	1 line[1] – 2 Nodes[6]	Linear[5]	0	Hypothesis I	2848

Subscribe ([1]) refers to the model of linear support as described in Figure 37c;
Subscribe ([2]) refers to the model of point support as described in Figure 37a;
Subscribe ([3]) refers to the model of linear-beam load configuration as described in Figure 38b;
Subscribe ([4]) refers to the value of torsional stiffness of the composite floor as described in eq.(43);
Subscribe ([5]) refers to the model of linear load configuration as described in Figure 38a;
Subscribe ([6]) refers to the model of point support as described in Figure 37b.

Table 18 reports the results obtained from plate models at SLS load level for cases P01 to P04. The values in brackets are the ratios of the global midspan deflection of each case to that of test HBF1. In overall, compared to test HBF1, the global midspan deflection varied from 3 percent lower to 24 percent higher, while the ratio w_T/w_L varied from 0.31 to 0.77.

For case P01, the obtained global midspan deflection (longitudinal direction) was 10.22 mm, representing 97 percent compared to test HBF1, while the midspan deflection between point supports (transversal direction) was 3.13 and the ratio w_T/w_L was 0.31. In case P02, the midspan deflection increased by 1 percent closer to the experimental results compared to those in case P01. This indicates that the linear-beam loading configuration has a small impact on the behavior of the composite floor.

In addition, using node supports as an alternative of plate supports in case P03 resulted in the global midspan deflection of 11.25 mm and the midspan deflection between point supports of 5.51 mm. Compared to case P02 and test HBF1, the global midspan deflection were increased by about 8 percent and 6 percent, respectively. It can be seen that using node supports resulted in lower structural performance of the composite floor compared to using plate supports in case P02. The findings demonstrate the importance of taking into account actual dimensions of the support when modelling, which can be represented by a rigid plate, in order to obtain accurate results.

In case P04, when torsional stiffness was reduced to zero, midspan deflections in both directions were increased. In comparison to case P03 and test HBF1, the global midspan deflection was increased by 18 percent and 24 percent, respectively. When torsional stiffness was disregarded, the structural performance of composite floor decreased significantly. Thus, torsional stiffness is an important parameter and should be included in the model.

For the comparison between the applied bending moment $M_{yy,max}$ and the cracking bending moment $M_{yy,cr}$, it was observed that the concrete should have experienced cracking before the SLS load level ($M_{yy,max} > M_{yy,cr}$). As the notch was not visible during the test, it is difficult to state if this cracking is realistic. From a practical point of view, it seems prudent to consider the cracking of the notch.

However, as observed during the experimental test, there were no signs of concrete cracking along the transversal direction of test HBF1 until the load level of the failure of the tested specimen, corresponding approximately 4 times higher than SLS load level. This highlights the fact that the transversal behavior of the composite floor cannot be explained without taking into account the effect of the concrete notch.

Table 18: Results obtained from plate models under SLS load level from cases P01 to P04.

Case	w_L [mm]	w_T [mm]	w_T/w_L	$M_{yy,max}$ [kNm/m]	$M_{yy,cr}$ [kNm/m]
HBF1	10.57	--	--	--	--
P01	10.22 (0.97)	3.13	0.31	10.70	11.02
P02	10.34 (0.98)	3.34	0.32	11.31	11.02
P03	11.25 (1.06)	5.51	0.49	13.69	11.02
P04	13.13 (1.24)	10.13	0.77	23.18	11.02

In conclusion, the influence of investigated parameters on the composite floor model can be described as follows:

- Loading configuration: implementing either linear load or linear-beam load configuration has a little influence, less than 1 percent value, on the composite floor model.
- Assumption of the point support: implementing the model of plate support with the actual dimension provides more satisfying results compared to the model of node support.
- Torsional stiffness: the torsional stiffness property needs to be included in the matrix stiffness of the model in order to obtain accurate results.
- The cracking of the notches should be considered.

4.4.5.3 Effect of transversal bending stiffness

This section presents an investigation of the influence of transversal bending stiffness on the composite floor by including the concrete notched section in concrete cross-section along transversal direction, in either uncracked (hypothesis II) or cracked condition (hypothesis III) (see section 4.4.5.1). In this investigation, the model of case P01 was used as the reference (in this case, hypothesis I was considered, neglecting the contribution of the concrete notch section). In case P05, the model was made by assuming hypothesis II, whereas in case P06, hypothesis III was assumed. Table 19 summarizes the detailed parameters for cases P05 and P06.

Table 19: Detailed parameters for cases P05 and P06.

Case	Support condition	Loading condition	Torsional stiffness [kN.m^2/m]	Properties in transversal direction	
				Hypothesis	$(EI)_{eff,T}$ [kN.m^2/m]
P01	1 line[1] – 2 plates[2]	Linear-beam[3]	958[4]	Hypothesis I	2848
P05	1 line[1] – 2 plates[2]	Linear-beam[3]	958[4]	Hypothesis II	4703
P06	1 line[1] – 2 plates[2]	Linear-beam[3]	958[4]	Hypothesis III	1887

Subscribe ([1]) refers to the model of linear support as described in Figure 37c;
Subscribe ([2]) refers to the model of point support as described in Figure 37a;
Subscribe ([3]) refers to the model of linear-beam load configuration as described in Figure 38b;
Subscribe ([4]) refers to the value of torsional stiffness of the composite floor as described in eq.(43).

Table 20 reports the results obtained from the plate models at SLS load level for cases P05 and P06. The values in brackets are the ratios of the global midspan deflection of each case to that of test HBF1. In case P05, when hypothesis II was assumed for the concrete section of the composite floor in transversal direction, a high transversal bending stiffness was obtained. As a result, a high structural performance of the composite floor was achieved. Compared to case P01 and test HBF1, the global midspan deflection was decreased by 3 percent and 6 percent, respectively. However, the concrete at lower part should experience cracking ($M_{yy,max} > M_{yy,cr}$ and $\sigma_{c,inf} > f_{ctm}$).

Table 20: Results obtained from plate models under SLS load level for cases P05 and P06.

Case	w_L [mm]	w_T [mm]	w_T/w_L	$M_{yy,max}$ [kNm/m]	$M_{yy,cr}$ [kNm/m]	$\sigma_{s,2}$ [MPa]	$\sigma_{c,inf}$ [MPa]
HBF1	10.57	--	--	--	--	--	--
P01	10.22 (0.97)	3.13	0.31	10.70	11.02	--	5.75
P05	9.98 (0.94)	2.36	0.24	13.39	8.78	47	8.73
P06	10.42 (0.99)	3.78	0.36	8.57	2.67	101	18.41

In case P06, when hypothesis III was assumed for the concrete section of the composite floor in transversal direction, the global midspan deflection and the ratio w_T/w_L were 10.42 mm and 0.36, respectively. Among all cases in Table 20, case P06 presented the closest value, less than 1 percent value of the global midspan deflection in comparison to the test HBF1. In addition, a tensile stress in the rebar reinforcement of about 101 MPa was computed.

It can be seen that the composite floor model using hypothesis III for concrete cross-section of the composite floor in transversal direction provided the best correlation in terms of midspan deflection in comparison to test HBF1. As a reminder, in this case, the composite floor was made by using the model of plate support and including the value of torsional stiffness computed using eq.(43).

4.4.5.4 Effect of the distributed loading configuration

In the bending test configuration, the applied load was distributed by two steel beams along the vertical direction near midspan zone. Thus, the bi-dimensional behavior of the composite floor was limited. This section presents the effect of a uniformly distributed loading configuration, which is

usually considered in practice for the design. Table 21 summarizes detailed parameters of the plate models from cases P07 to P10. In case P07, a floor model with two line supports (one-dimensional bending behavior) was made as the reference case. From cases P08 to P10, floor models with plate supports at one end (bi-dimensional bending behavior) were investigated. Hypotheses I, II, and III were assumed for the concrete section of the composite floor in transversal direction in cases P08, P09, and P10, respectively.

Table 21: Detailed parameters from cases P07 to P10.

Case	Support condition	Loading condition	Torsional stiffness [kN.m^2/m]	Properties in transversal direction	
				Hypothesis	$(EI)_{eff,T}$ [kN.m^2/m]
P07	2 lines^{1}	Distribute^{7}	958^{4}	Hypothesis I	2848
P08	1 line^{1} – 2 plates^{2}	Distribute^{7}	958^{4}	Hypothesis I	2848
P09	1 line^{1} – 2 plates^{2}	Distribute^{7}	958^{4}	Hypothesis II	4703
P10	1 line^{1} – 2 plates^{2}	Distribute^{7}	958^{4}	Hypothesis III	1887

Subscribe (^{1}) refers to the model of linear support as described in Figure 37c;
Subscribe (^{2}) refers to the model of point support as described in Figure 37a;
Subscribe (^{4}) refers to the value of torsional stiffness of the composite floor as described in in eq.(43);
Subscribe (^{7}) refers to the model of distributed load configuration as described in Figure 38c.

Table 22 reports results obtained from plate models for cases P07 to P09. The value in brackets refers to ratios between the midspan deflection of each case compared to the one of case P07. In overall, global midspan deflections of models in bi-dimensional bending effect ranged from 18 percent value higher to 25 percent value higher in comparison to that in one-dimensional bending effect. In addition, the ratios w_T/w_L varied from 0.32 to 0.55. As expected, it was observed that the structural performance of the composite floor was dependent on the assumption of concrete properties along the transversal direction. In case P09, a higher structural performance was achieved with less deflection when the notched section was included in concrete section, in uncracked condition along the transversal direction (hypothesis II). This was followed by case P08, when the concrete notched section was disregarded, in uncracked condition along the transversal direction (hypothesis I), and case P10, when the notched section was included in concrete section, in cracked condition along the transversal direction (hypothesis III).

Table 22: Results obtained from plate models under SLS load level from cases P07 to P09.

Case	w_L [mm]	w_T [mm]	w_T/w_L	$M_{yy,max}$ [kNm/m]	$M_{yy,cr}$ [kNm/m]	$\sigma_{s,2}$ [MPa]	$\sigma_{c,inf}$ [MPa]
P07	9.17 (1.00)	--	--	--	--	--	--
P08	10.80 (1.18)	4.59	0.43	15.53	11.02	--	6.07
P09	10.25 (1.12)	3.29	0.32	18.63	8.78	65	7.35
P10	11.46 (1.25)	6.25	0.55	13.29	2.67	156	12.45

Based on the results of the bending moment and tensile stress of the concrete panel, it could be observed that the concrete section of the composite floor along the transversal direction experienced

cracking. However, the tensile stress in the rebar reinforcement remained in elastic behavior with the maximum tensile stress of 156 MPa in case P10.

Following the conclusion on the model of composite floor in bi-dimensional bending effect presented in section 4.4.5.3, case P10 can be considered as the most relevant case when the composite floor is subjected to distributed loads. From Table 22, compared to floor in one-dimensional bending effect (case P 07), the floor in bi-dimensional bending effect obtained an increase in midspan deflection by 25 percent and obtained a ratio w_T/w_L of 55 percent. This significant midspan deflection between point supports should be taken into consideration in the design, as it can have implications as follows:

- Fixation of façades: A high deflection between point supports (transversal deflection) of the composite floor can impose limitations on the architectural use of the structure, particularly for materials that are sensitive to excessive displacement.
- Transversal cracks on the supports: The increased deflection between point supports of the composite floor may lead to the development of cracks on the supports.

4.4.5.5 Summary of the discussion on modelling options of the orthotropic plate model

Based on the results obtained in the investigations of the model of composite floor in bi-dimensional bending effect, the following conclusions can be drawn:

- When point supports are used, an orthotropic plate model should be used in the design. It should take into account the actual dimensions of the support, and the torsional stiffness of the composite floor.
- The computation of the transversal bending stiffness of the composite floor should take into account the presence of the notch, and their eventual cracking.
- Load distributed by steel HEA-300 beams (linear-beam load) or by linear loading configuration delivered comparable outcome with a difference of less than 1 percent value.

The bi-dimensional effects of the composite floor with point supports subjected to a distributed loading were found as follows:

- Increase of the global midspan deflection by up to 25 percent compared to model in one-dimensional bending effect;
- The deflection between point supports can represent around 55 percent of the global deflection. This should be taken into consideration for the fixation of façades, and for the verification of transversal cracks over the supports.

4.4.6 Conclusion to the Bi-dimensional effects

The behavior of composite floors was assessed using a beam grid model and an orthotropic plate model. Compared to test results at SLS load level, for test HBF2, both beam grid model and orthotropic plate model underestimated the midspan deflection by approximately 7 percent. However, for the model of composite floor in bi-dimensional bending effect (HBF1), it was found that the orthotropic plate model provided more satisfying results with a difference of only 3 percent.

In order to determine a refined model capable of predicting the composite floor in bi-dimensional bending effect, a thorough investigation was then conducted using the orthotropic plate model with different assumptions on the support condition, loading condition, torsional stiffness, and bending stiffness of composite floor in transversal direction. Following the comparison of results between the plate models and experimental test HBF1, the composite floor model should take into account the torsional stiffness and consider the concrete section with presence of the notch, in cracked condition, for computing the transversal bending stiffness. Actual dimensions and stiffness of the support should be considered. If the composite floor model is subjected to uniformly distributed loading configuration, the global midspan deflection can increase up to 25 percent compared to the model of the composite floor in one-dimensional bending effect while the transversal deflection between point supports can represent around 55 percent value of the global deflection. This high transversal deflection should be considered in the practice design.

4.5 Conclusion

This chapter has presented the global behavior of the HOBOA system. The behavior of the composite floor using notched connectors was first characterized by conducting flexural tests. The test results were then used for the verification of the gamma method and simplified numerical models.

Firstly, two full-scale four-point bending tests were carried out on CLT-concrete composite floors, with two different support conditions in the test setup. Test HBF1 was supported by point supports at one end and linear support at the other end of the specimen, resulting in bi-dimensional bending effect. Test HBF2 was supported by two linear supports, resulting in one-dimensional bending effect. In bending tests, high bending resistances were obtained. In addition, a comparison was made between the effective bending stiffness obtained in this study and in the literature. The results indicated that the bending stiffness determined from the experimental tests was comparable to that reported in other studies, confirming the effectiveness of the HOBOA system.

The gamma method given in Eurocode 5 [29], later modified by Jiang et al. [3], was then adopted to determine the effective bending stiffness, midspan deflection, and load-carrying capacity of the composite floor. The results obtained from experimental tests showed a good agreement with estimations obtained from the gamma method. However, the gamma method provided a better estimation for the test in one-dimensional bending effect (test HBF2). Furthermore, the influence of the stiffness of the notch connector and of the rolling shear stiffness of the wood layers on the bending stiffness of the CLT-concrete floor was investigated. Since the stiffness of the wood-concrete connection with the spacing as adopted in the test was already high, trying to increase further the wood-concrete connection stiffness would not have a noticeable effect. Additionally, force-slip curves derived from the flexural test and from pushout tests were afterwards compared in order to verify the effect of timber creep due to pauses and cyclic loading during the tests. As a result, a close correlation of force-slip curves of pushout tests and flexural test was obtained, when removing slips caused by pauses and cyclic loading during the tests.

In addition, to quantify the effect of bi-dimensional bending, a beam grid model and an orthotropic plate model were developed. The results indicated that the orthotropic plate model provided a better result than the beam grid model in terms of global midspan deflection. However, the assumptions used in the orthotropic plate model should be revised in order to establish a refined model capable of

accurately predicting the behavior of composite floor in bi-dimensional bending effect. Thus, a thorough investigation was then conducted using the orthotropic plate model with different assumptions on the support condition, loading condition, torsional stiffness, and bending stiffness of composite floor in transversal direction. It was shown that the composite floor model should take into account the torsional stiffness and consider the concrete section with presence of notch, in cracked condition, for computing the transversal bending stiffness. For the point support, actual dimensions and stiffnesses of the support should be modelled. If the floor model is subjected to uniformly distributed loading, the transversal deflection between point supports can represent around 55 percent of the global deflection. This high transversal deflection should be considered in the practice design.

In conclusion, the CLT-concrete composite floor with new dovetail notched connectors, referred as HOBOA floor system, can be considered as an efficient system in terms of the structural performance based on the results obtained in experimental flexural tests. Besides, the gamma method can be adopted to predict the structural behavior of the composite floor in one-dimensional bending while the developed orthotropic plate model should be able to assess the behavior of the CLT-concrete composite floor in bi-dimensional bending.

4.6 References

[1] Deam, B. L., Fragiacomo, M., & Buchanan, A. H. (2008). Connections for composite concrete slab and LVL flooring systems. Materials and Structures, 41, 495-507.

[2] Lukaszewska, E., Johnsson, H., & Fragiacomo, M. (2008). Performance of connections for prefabricated timber–concrete composite floors. Materials and structures, 41, 1533-1550.

[3] Jiang, Y., & Crocetti, R. (2019). CLT-concrete composite floors with notched shear connectors. Construction and Building Materials, 195, 127-139.

[4] Martins, C., Santos, P., Almeida, P., Godinho, L., Dias, A. 2015. Acoustic performance of timber and timber-concrete floors. Construction and Building Materials 101: 684-691.

[5] Wymelenberg, K., Northcutt, D., Fretz, M., Stenson, J., Marks, E. 2019. Acoustic Lab Testing (ASTM E492-2016, ASTM E90-2016) of CLT and MPP Wall and Floor Assemblies for Multi-Family Residential Application. University of Oregon, Portland, Oregon, USA.

[6] Shephard, A.B., Fischer, E.C., Barbosa, A.R., Sinha, A. 2021. Fundamental Behavior of Timber Concrete-Composite Floors in Fire. Journal of Structural Engineering 147(2): 04020340.

[7] Autodesk, I. (2017). Robot Structural Analysis Professional.

[8] BS EN 206: 2013, Concrete – Specification, performance, production and conformity, British Standards Institution, London, 2013.

[9] Avis-Technique. 3.3/17-925 v1, Panneaux bois `a usages structurel – mur et plancher, Wood structural panels, 2017.

[10] EN 408:2003-08. Timber structures – Structural timber and glued laminated timber – Determination of some physical and mechanical properties. CEN European Committee for Standardization (2003)

[11] European standard EN 338, Structural Timber—Strength Classes, CEN, Brussels (2003).

[12] Kim, K. M., Shim, K. B., & Lum, C. (2011). Predicting tensile and compressive moduli of structural lumber. Wood and Fiber Science, 83-89.

[13] Schneider, M. H., & Phillips, J. G. (1991). Elasticity of wood and wood polymer composites in tension compression and bending. Wood science and technology, 25(5), 361-364.

[14] Conners, T. E., & Medvecz, P. J. (1992). Wood as a bimodular material. Wood and fiber science, 413-423.

[15] Janowiak, J. J., Hindman, D. P., & Manbeck, H. B. (2001). Orthotropic behavior of lumber composite materials. Wood and fiber science, 580-594.

[16] Yadama, V., Wolcott, M. P., & Smith, L. V. (2006). Elastic properties of wood-strand composites with undulating strands. Composites Part A: Applied Science and Manufacturing, 37(3), 385-392.

[17] Shim, K. B., Kim, K. M., & Park, J. S. (2009). Improvement of prediction accuracy of glulam modulus of elasticity by considering neutral axis shift in bending. Wood and Fiber Science, 90-96.

[18] CEN, EN 16351 Timber Structures – Cross Laminted Timber – Requirements,European Committee for Standardization, Belgium, 2015.

[19] EN 789. Timber structures test methods determination of mechanical properties of wood based panels. Brussels, Belgium: European Committee for Standardization, 2004.

[20] Brandner, R., Tomasi, R., Moosbrugger, T., Serrano, E., & Dietsch, P. (2018). Properties, testing and design of cross laminated timber. A State-Of-The-Art Report by COST Action FP1402/WG2.

[21] Ehrhart, T., Brandner, R., Schickhofer, G., & Frangi, A. (2015). Rolling shear properties of some European timber species with focus on cross laminated timber (CLT): test configuration and parameter study. In International Network on Timber Engineering Research: Proceedings of Meeting 48 (Vol. 2015, pp. 61-76). Timber Scientific Publishing, KIT Holzbau und Baukonstruktionen.

[22] Mestek, P. (2011). Punktgestützte Flächentragwerke aus Brettsperrholz (BSP)–Schubbemessung unter Berücksichtigung von Schubverstärkungen (Doctoral dissertation, Technische Universität München).

[23] Gong, M., Tu, D., Li, L., & Chui, Y. H. (2015). Planar shear properties of hardwood cross layer in hybrid cross laminated timber. ISCHP 2015, 85-90.

[24] European standard EN 1994-1-1, Eurocode 4: Design of composite steel and concrete structures - Part 1-1: General rules and rules for buildings, CEN, Brussels (2004).

[25] European standard EN 1990-1-1, Eurocode — Basis of structural design, CEN, Brussels (2004).

[26] Müller, K. (2020). Timber-concrete composite slabs with micro-notches (Doctoral dissertation, ETH Zurich).

[27] Mai, K. Q., Park, A., Nguyen, K. T., & Lee, K. (2018). Full-scale static and dynamic experiments of hybrid CLT–concrete composite floor. Construction and Building Materials, 170, 55-65.

[28] Shahnewaz, M., Jackson, R., & Tannert, T. (2022). CLT concrete composite floors with steel kerf plate connectors. Construction and Building Materials, 319, 126092.

[29] European standard EN 1995-1-1, Eurocode 5: Design of timber structures- Part 1-1: General — Common rules and rules for buildings, CEN, Brussels (2004).

[30] Stüssi, F. Composite Solid Wall Beams; Abhandlung der Int. Ver. für Brückenbau und Hochbau: Zürich, Switzerland, 1947; pp. 249–268.

[31] Möhler K. Über das Tragverhalten von Biegeträgern und Druckstäben mit zusammengesetzten Querschnitten und nachgiebigen Verbindungsmitteln. (In German) Habilitation, Technische Universität Karlsruhe, Germany; 1956.

[32] European standard EN 1992-1-1, Eurocode 2: Design of concrete structures - Part 1-1: General rules and rules for buildings, CEN, Brussels (2004).

[33] Comité Européen de Normalisation CEN, 2004 : EN 384: Structural timber - Determination of characteristic values of mechanical properties and density.

[34] ASTM International. (2010). Standard practice for evaluating allowable properties for grades of structural lumber. ASTM D2915-10.

[35] Chen, Z., Popovski, M., & Symons, P. (2018). Advanced wood-based solutions for mid-rise and high-rise construction: Structural performance of post-tensioned CLT shear walls with energy dissipators. FPInnovations Project, (301012204).

[36] Auclair, S. C. (2020). Design guide for timber-concrete composite floors in Canada. FPInnovation, Point-Claire, QC, Canada, Special Publication SP-540E.

[37] Frangi, A., & Fontana, M. (2003). Elasto-plastic model for timber-concrete composite beams with ductile connection. Structural Engineering International, 13(1), 47-57.

[38] Akter, S. T., Bader, T. K., & Serrano, E. Stiffness of cross-laminated timber (CLT) wall-to-floor-to-wall connections in platform-type structures. In World Conference on Timber Engineering, 2021.

[39] Gustafsson, A. (2019). The CLT Handbook: CLT structures-facts and planning. Swedish Wood.

[40] Blaauwendraad, J. (2012). Plates and FEM. Springer.

This page is intentionally left blank.

CHAPTER 5

Design recommendations for CLT-concrete composite floor

This page is intentionally left blank.

Contents

This page is intentionally left blank.

5.1 Introduction

This chapter presents a proposition for the design procedure for CLT-concrete composite floors (HOBOA system) including the design for the dovetail notched connection system. It is based on the general recommendations given in the technical specification CEN/TS 19103 [1] for timber-concrete composite structures, enhanced by the findings in experimental tests, analytical developments, and numerical studies. The details of the configuration of studied CLT-concrete composite floors and notched connectors are described in section 5.2. For the connection system, the computation methods for strength and stiffness are addressed in section 5.3. Then, sections 5.4 and 5.5 detail the design for the CLT-concrete composite floor in one-dimensional and bi-dimensional bending effects, respectively. It should be noted that comments and explanations found in this chapter are given in the *italic* font.

5.2 Description of studied CLT-concrete composite floors for the design recommendations

This design guidance is proposed to design the HOBOA system with dimensions, support conditions, and section composition as depicted in Figure 1. The configuration of the notched connection is presented in Figure 2. It should be noted that the composite floor is supposed to be subjected strictly to positive bending. With linear supports (conceptualized for supporting walls) at both ends, as shown in Figure 1a, the composite floor is subjected to one-dimensional bending effect, generating deflection along the principal direction alone (X direction). With a linear support at one end and point supports (conceptualized to represent the supporting columns) at the other end, as shown in Figure 1b, the composite floor is subjected to bi-dimensional bending effect, generating deflection along both directions (X and Y directions).

The configuration of the CLT-concrete composite floor (HOBOA system) shall comply with the following characteristics (*defined following what has been tested experimentally*):

For CLT panel:

- Minimum number of plies is 5,
- Thickness of each timber plies is higher than 33 mm,
- Minimum thickness of the CLT panel is 165 mm,
- Principal direction of the CLT panel is consistent with that of the composite floor,
- Strength class C24 or higher is used according to the technical document of CLT product TOT'm X [2].

For concrete panel:

- Minimum thickness of concrete panel is 85 mm,
- Strength class C35/45 or higher is used with the maximum concrete aggregate of 16 mm ($d_g \leq 16$ mm) according to Eurocode 2 [3]. *Lower strength classes of concrete can be adopted following the technical specification CEN/TS 19103* [1], *but they have not been validated experimentally with the specific notched connection under consideration.*

- Anti-cracking steel mesh (placed in the middle of the concrete panel) is at least rebar mesh ST 15, with a dimension of 200 × 200 mm mesh and a diameter of rebars higher than 5.5 mm.

For notched connection:

- The notched connectors are dug across the entire width of the composite floor,
- The notch depth: $d_n \geq 20$ mm. *The technical specification CEN/TS 19103* [1] *proposes 20 mm, but only the dimension of 50 mm has been validated in experimental tests.*
- The notch length: $l_n \geq 90$ mm. *The technical specification CEN/TS 19103* [1] *proposes 150 mm, but the dimension of 90 mm has been validated in experimental tests.*
- The length of timber in front of the notch: $l_v \geq \min\{375 \text{ mm}; 12.5d_n\}$. *The technical specification CEN/TS 19103* [1] *proposes a length of* $12.5d_n$, *but the dimension of 375 mm has been validated in experimental tests.*
- The distance between the notches: $l_s \geq \min\{375 \text{ mm}; 12.5d_n\}$. *The technical specification CEN/TS 19103* [1] *proposes a distance of* $12.5d_n$, *but the dimension of 375 mm has been validated in experimental tests.*
- The angle of the notch: $69° \leq \alpha \leq 115°$. *The technical specification CEN/TS 19103* [1] proposes $80° \leq \alpha \leq 115°$, *but the angle of 69° has been validated in experimental tests.*
- For the steel rebar inside the concrete notch, properties of reinforcement are in accordance with the criterion in Annex C of Eurocode 2 [3]. *Following the experimental tests, the upper bar of the V-shape rebar layer shall be placed in the middle of the concrete slab and the distance between notch corner and rebars,* $l_{n,c}$ *(see Figure 2a), shall be higher than 20 mm.*

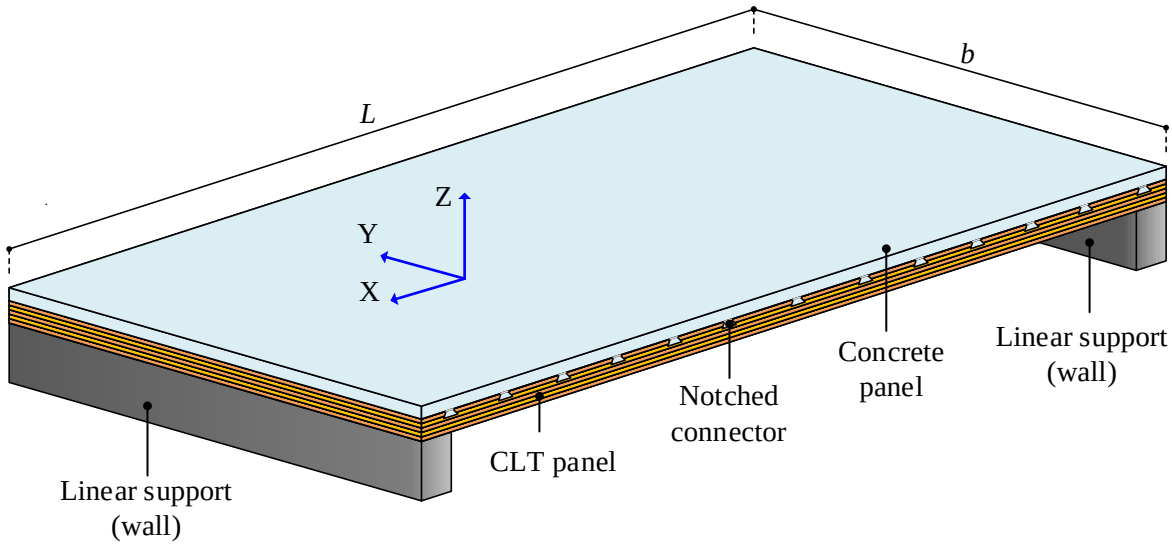

a. One-dimensional bending configuration

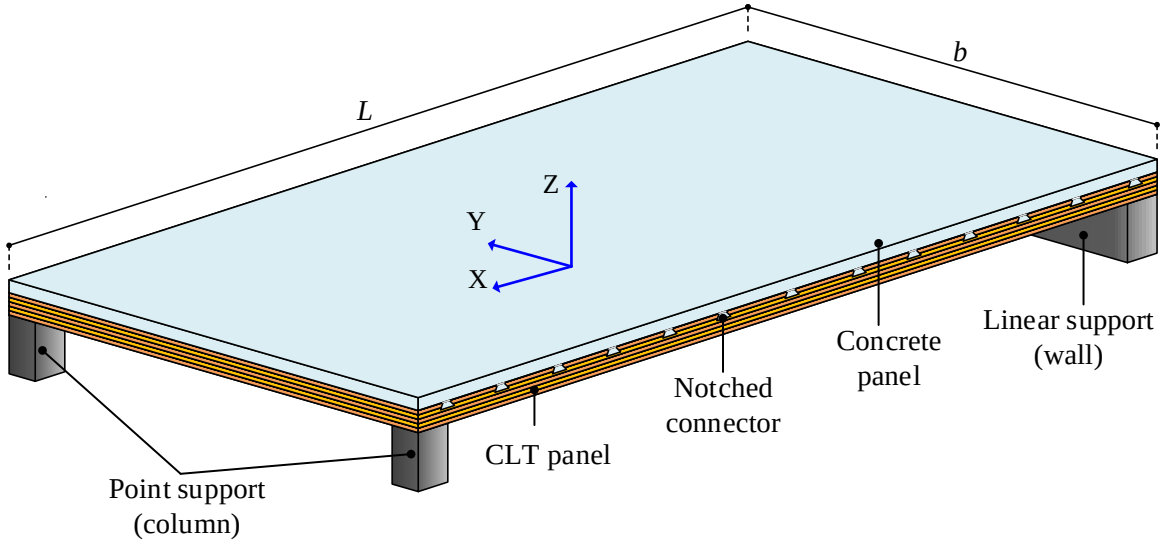

b. Bi-dimensional bending configuration

Figure 1: Configuration of studied CLT-concrete composite floors (HOBOA system).

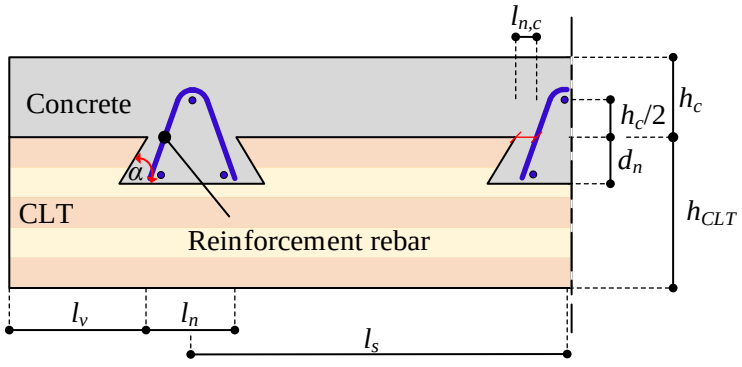

a. Notch connector

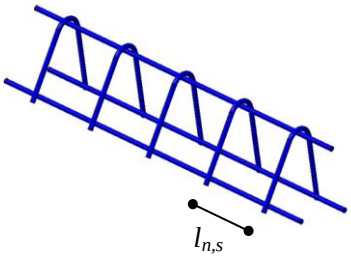

b. V-shape rebar cage

Figure 2: Notched connection system.

5.3 Design of dovetail notched connection system

5.3.1 Slip modulus

The slip modulus of the dovetail notched connector is taken as the value obtained experimentally from pushout tests. Accordingly, the slip moduli at serviceability limit state and ultimate limit state are K_s=1490 kN/m/m and K_u=1030 kN/m/m, respectively. These values of slip moduli were obtained when the notch depth was 50 mm, notch length was 90 mm, concrete strength was a class of C35/45, and timber strength was a class of C24. The use of these values for different notch dimensions should be considered carefully.

5.3.2 Load-carrying resistance

The load-carrying resistance of the notched connector shall fulfill the following criterion:

$$F_{v,Ed} \leq F_{Rd} \tag{1}$$

where

$F_{v,Ed}$ is the design shear force at the interface layer of CLT and concrete panels;

F_{Rd} is the design load-carrying resistance of the notched connection.

The value of load-carrying resistance F_{Rd}, of the notched connection is taken as the minimum value found from the capacities determined for four possible failure modes (see Figure 3) shown in the following equation:

$$F_{Rd} = \min \{F_{Rd,mode\ I}; F_{Rd,mode\ II}; F_{Rd,mode\ III}; F_{Rd,mode\ IV}\} \tag{2}$$

where

$F_{Rd,mode\ I}$ is the shear resistance of concrete notch at shear plane;

$F_{Rd,mode\ II}$ is the compressive resistance of concrete notch at load-bearing surface;

$F_{Rd,mode\ III}$ is the rolling shear resistance of the cross-layer of the CLT panel;

$F_{Rd,mode\ IV}$ is the compressive resistance of the timber parallel to grain at the load-bearing surface.

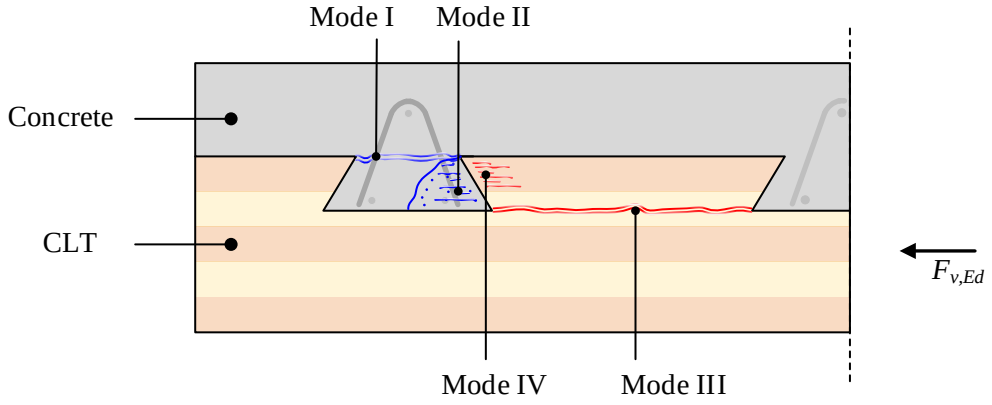

Figure 3: Four possible failure modes for notched connector.

For the failure mode I, the shear resistance of the concrete notch at shear plane is determined using the strut-and-tie model. *It is thus not, strictly speaking, a shear resistance, but this language approximation is also adopted in the technical specification CEN/TS 19103* [1]. *The strut-and-tie model proposed here is a simplification of the one developed in chapter 3.* Figure 4 presents the strut-and-tie model of the concrete notch. *The position of the applied force $F_{v,Ed}$ for the failure mode I ($F_{Rd,mode\ I}$), is approximately one-fourth of the first longitudinal layer's thickness, based on the result observed in chapter 3.* It is worth noting that the concrete shear resistance is determined when V-shape rebars placed inside the concrete notch experience yielding stress. From the strut-and-tie model in Figure 4, the resistance of all compressive nodes, compressive struts, and tensile ties in the notched connector need to be verified with applied loading. If the collapse is guided by the yielding of rebars; therefore, the concrete shear resistance, $F_{Rd,mode\ I}$, can be determined as follows:

$$F_{Rd,mode\ I} = (\cos\theta_{T_{12}} \times \cot\theta_{C_{14}} - \sin\theta_{T_{12}})T_{12} + (\sin\theta_{T_{23}} + \cos\theta_{T_{23}} \times \cot\theta_{C_{34}})T_{23} \quad (3)$$

where

$\theta_{T_{12}}$ is the angle between tie $T_{1\to2}$ and vertical axis;

$\theta_{C_{14}}$ is the angle between strut $C_{1\to4}$ and horizontal axis;

T_{12} is the tensile force of tie $T_{1\to2}$;

$\theta_{T_{23}}$ is the angle between tie $T_{2\to3}$ and vertical axis;

$\theta_{C_{34}}$ is the angle between strut $C_{3\to4}$ and horizontal axis;

T_{23} is the tensile force of tie $T_{2\to3}$.

The tensile forces T_{12} and T_{23} are the tensile forces obtained when V-shape rebar reinforcements of the concrete notch experience yielding stress. The angle $\theta_{C_{14}}$ shall be taken equal to the angle $\theta_{T_{12}}$,while the angle $\theta_{C_{34}}$ shall be taken equal to two times the angle $\theta_{T_{12}}$. Additionally, to prevent separation of the composite floor, it is supposed that rebar reinforcements, which are provided by V-shape rebars, are able to resist a tensile force between timber and concrete panels in order to conform with the design recommendation given in the technical specification CEN/TS 19103 [1].

From failure modes II to IV, the load-carrying resistance shall be determined using the following equations as expressed from eqs. (4) to (7). *The consistency of these equations has been confirmed by comparing the obtained results with ones in experimental tests and numerical simulations as addressed in chapter 3.*

$$F_{Rd,mode\ II} = f_{c,d} b d_n \quad (4)$$

$$F_{Rd,mode\ III} = f_{r,d} b l_{eff} \quad (5)$$

$$F_{Rd,mode\ IV} = f_{c,0} b h_{l,CLT} \quad (6)$$

with

$$l_{eff} = \min\{l_s - l_n;\ 8d_n\} \quad (7)$$

where

$f_{c,d}$ is the design compressive strength of the concrete panel;

b is the width of the CLT-concrete composite floor;

d_n is the notch depth, see Figure 2a;

$f_{r,d}$ is the design rolling shear strength of the cross-layer of the CLT panel;

l_{eff} is the effective length of the cross-layer of the CLT panel;

$f_{c,0}$ is the compressive strength of the timber parallel to grain;

$h_{l,CLT}$ is the thickness of a timber board parallel to grain of the CLT panel;

l_s is the spacing between notched connectors, see Figure 2a;

l_n is the notch length, see Figure 2a.

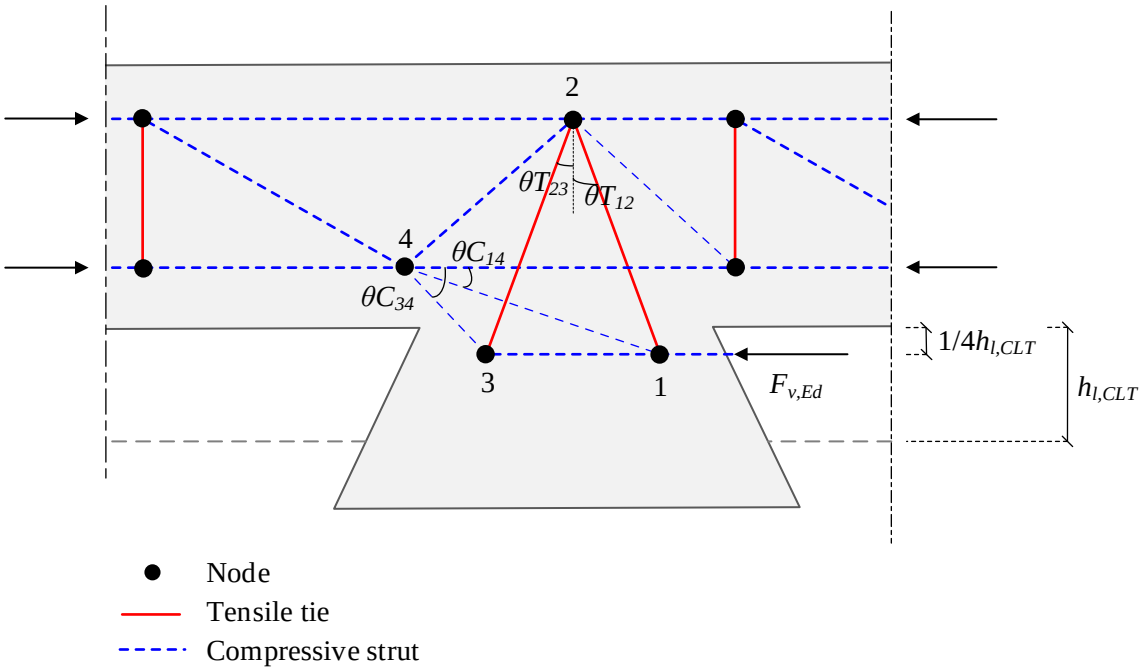

Figure 4: Strut-and-tie model of the concrete notch.

5.4 Design of CLT-concrete composite floor in one-dimensional bending

5.4.1 Effective bending stiffness

The design method is based on the linear elastic formulae found in Annex B of Eurocode 5 [4], later modified by Jiang et al. [5], to be applicable to CLT-concrete composite floors. This method shall satisfy the following assumptions:

- The floor is simply supported with a span L,
- The CLT part is either full length or made with glued end joints,
- The concrete and CLT panels are connected together by means of notched connector with a slip modulus, K,

- The spacing, s, between the notches is constant or varies uniformly according to shear force between s_{min} and s_{max}, with $s_{max} \leq 4s_{min}$,
- The load is acting in the z-direction varying linearly, sinusoidally, or parabolically.

In a calculation of bending stiffness for the CLT panel, the longitudinal layers of the CLT panel are assumed to carry flexural stresses, whereas the transversal layers are considered as a semi-rigid connection between the longitudinal layers. In this context, the distributed shear stiffness at the CLT-concrete interface layer $(K/s)_c$ is determined by combining the shear stiffness of concrete notch K_1 and the rolling shear stiffness of the cross-layer of the CLT panel K_2:

$$\left(\frac{K}{s}\right)_c = \frac{K_1 \times K_2}{K_1 + K_2} \tag{8}$$

with

$$K_1 = \frac{K}{s_{eff}} \tag{9}$$

$$K_2 = \frac{G_R b}{\bar{h}_1} \tag{10}$$

$$s_{eff} = 0.75 s_{min} + 0.25 s_{max} \tag{11}$$

where

K is the shear stiffness of the notched connection;

G_R is the rolling shear modulus of the CLT panel;

b is the width of the composite floor;

s_{eff} is the effective spacing between notched connectors;

s_{min} is the minimum spacing between notched connectors;

s_{max} is the maximum spacing between notched connectors.

The effective bending stiffness of the composite cross-section is the sum of two parts (see Figure 5). The first part consists of the concrete panel with the middle and bottom longitudinal layers of the CLT panel while the second part is the top longitudinal layer of the CLT panel alone. Accordingly, the effective bending stiffness of the 5-layer CLT concrete composite section can be computed as follows:

$$(EI)_{eff} = (EI)_{eff,1} + (EI)_{eff,2} = \sum_{i=c;3;4} (E_i I_i + \gamma_i E_i A_i a_i^2) + E_2 b_2 h_2^3/12 \tag{12}$$

with

$$A_i = b_i h_i \tag{13}$$

$$I_i = b_i h_i^3 / 12 \tag{14}$$

$$\gamma_3 = 1 \tag{15}$$

$$\gamma_c = \left[1 + \frac{\pi^2 E_c A_c}{L^2} \times \left(\frac{s}{K}\right)_c\right]^{-1} \tag{16}$$

$$\gamma_4 = \left[1 + \frac{\pi^2 E_4 A_4 \bar{h}_2}{G_R b_4 L^2}\right]^{-1} \tag{17}$$

$$a_3 = \frac{\gamma_c E_c A_c (h_c/2 + h_2 + \bar{h}_1 + h_3/2) - \gamma_4 E_4 A_4 (h_3/2 + \bar{h}_2 + h_4/2)}{\sum_{i=c;3;4} \gamma_i E_i A_i} \tag{18}$$

$$a_c = \frac{h_c}{2} + h_2 + \bar{h}_1 + \frac{h_3}{2} - a_3 \tag{19}$$

$$a_4 = \frac{h_3}{2} + \bar{h}_2 + \frac{h_4}{2} + a_3 \tag{20}$$

where

E_i are the modulus of elasticity of i-layers of the cross-section;

I_i are the second moment inertia of i-layers of the cross-section;

A_i are the area of i-layers of the cross-section;

b_i are the width of i-layers of the cross-section;

h_i are the thickness of i-layers of the cross-section;

$\bar{h}_i$ are thickness of the i-cross-layers of the CLT panel;

a_i are the distance from the centroid of i-layers to centroid of the composite cross-section;

L is the span of the composite floor.

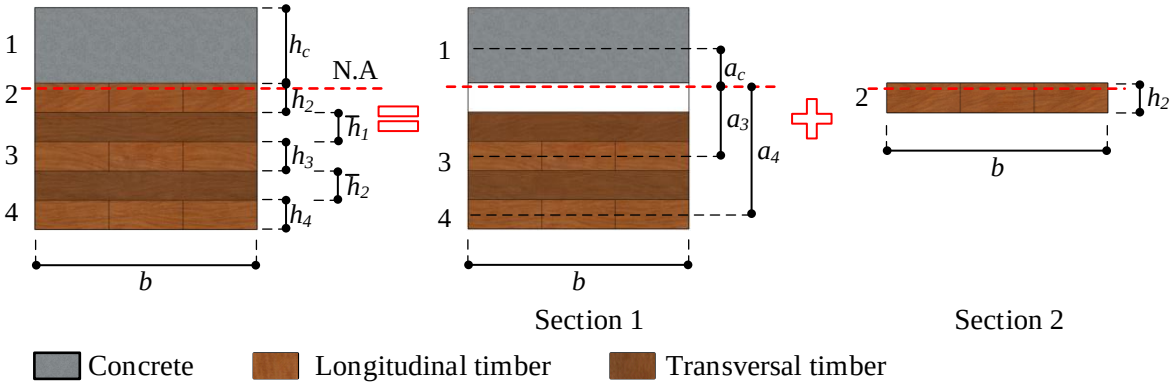

Figure 5: Computation of 5-layer CLT-concrete floors.

5.4.2 Cross-sectional resistance

The cross-sectional normal stress, longitudinal shear stress, rolling shear stress, and force acting on connector of the composite floor (see Figure 6) are defined in accordance with the Eurocodes 5 [4] and are expressed as follows:

$$\sigma_i = \frac{\gamma_i E_i a_i}{(EI)_{eff}} M_d \tag{21}$$

$$\sigma_{m,i} = \frac{0.5 E_i h_i}{(EI)_{eff}} M_d \tag{22}$$

$$\tau_{max} = \frac{\gamma_4 E_4 h_4 a_4 + 0.5 E_3 (a_3 + 0.5 h_3)^2}{(EI)_{eff}} V_d \tag{23}$$

$$\tau_r = \frac{\gamma_i E_i h_i a_i}{(EI)_{eff}} V_d \ (i=3 \text{ or } 4) \tag{24}$$

$$F_s = \frac{\gamma_c E_c A_c a_c s}{(EI)_{eff}} V_d \tag{25}$$

where

σ_i are the axial stresses in *i*-layers of the cross-section;

γ_i are the factors for the efficiency of the mechanical connections of the respective *i*-layers of the cross-section;

M_d is the design bending moment;

$\sigma_{m,i}$ are the bending stresses in *i*-layers of the cross-section;

τ_{max} is the maximum longitudinal shear stress in the cross-section;

V_d is the maximum design shear force in the composite floor;

τ_r is the rolling shear stress in the CLT section;

F_s is the force of the notched connector.

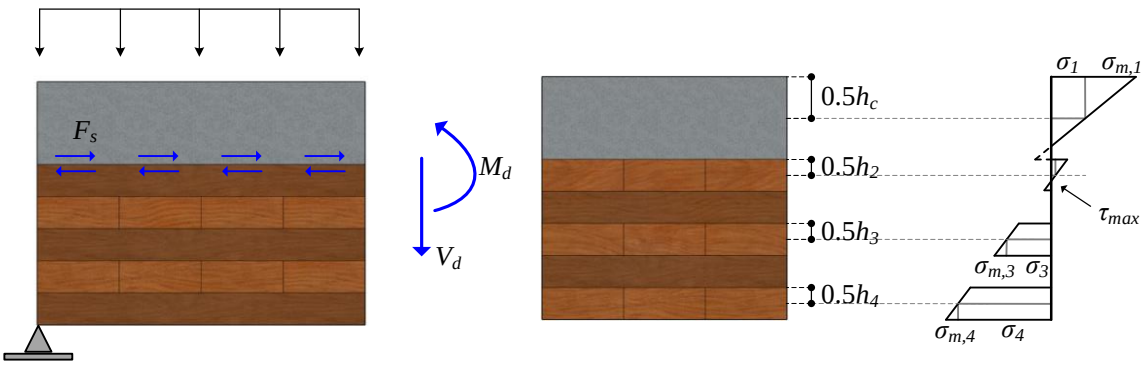

Longitudinal section Cross-section Stress

Figure 6: Stress distribution in cross-section of composite floors.

5.4.3 Long-term behavior

Influenced by load-duration and moisture content, the strength of material at long-term behavior shall be determined using an equation given in Eurocode 5 [4]:

$$f_d = k_{mod} \frac{f_k}{\gamma_m} \tag{26}$$

where

f_d is the design resistance;

f_k is the characteristic resistance;

k_{mod} is a modification factor taking into account the effect of the duration of load and moisture content, which is given in Eurocode 5 [4];

γ_m is the partial factor for a material property, which is given in Eurocode 5 [4].

In addition, stress distribution of composite cross-section at long term behavior is relative to the final mean value of moduli of elasticity of materials and connection system, which is influenced by creep deformations of concrete and timber. The final mean value of moduli of elasticity of materials and connection system are determined as follows [6]:

$$E_{con,fin} = \frac{E_{con,t_0}}{1+\psi_{con}\varphi(\infty,t_0)} \tag{27}$$

$$E_{tim,fin} = \frac{E_{tim}}{1+\psi_{tim}k_{def}} \tag{28}$$

$$K_{ser,fin} = \frac{K_{ser}}{1+\psi_{conn}k'_{def}} \tag{29}$$

$$K_{u,fin} = \frac{K_u}{1+\psi_{conn}k'_{def}} \tag{30}$$

where

$E_{con,fin}$ is the effective long-term modulus of elasticity of concrete;

E_{con,t_0} is the modulus of elasticity of concrete at time t_0 according to Eurocode 2 [3];

ψ_{con} is the coefficient accounting for composite action influence on the effective creep coefficient of concrete;

$\varphi(\infty,t_0)$ is the creep coefficient of concrete from time t_0 to the end of the service life;

$E_{tim,fin}$ is the effective long-term modulus of elasticity of timber;

E_{tim} is the mean modulus of elasticity of timber;

ψ_{tim} is the coefficient accounting for composite action influence on the effective creep coefficient of timber;

k_{def} is the factor for the evaluation of creep deformation accounting for the relevant service class according to Eurocode 5 [4];

$K_{ser,fin}$ is the final slip modulus of the connection for the serviceability limit state design;

K_{ser} is the mean slip modulus of the connection for the serviceability limit state design;

$K_{u,fin}$ is the final slip modulus of connection system for the ultimate limit state design;

K_u is the mean slip modulus of the connection for the ultimate limit state design;

k'_{def} is the deformation factor for the connection. Unless provided by product specifications, the deformation factor k'_{def} shall be as given by formula: $k'_{def} = 2k_{def}$.

The factors ψ_{con} and ψ_{tim} are determined in function of the creep coefficient of concrete, φ, and deformation factor of timber, k_{def}, as detailed in Table 1. Further design stages of creep coefficient at decisive time between t_0 and t_∞ (between 3 years and 7 years, for example) are also described. It should be noted that γ_c as shown in Table 1 is the composite factor of the concrete cross-section according at time t_0, which is defined from the estimation of the gamma method with slip modulus K_{ser} (see section 5.4.1).

Table 1: Modification of creep coefficients for composite action in slab systems.

	For $t = \infty$	For t = 3 to 7 years
Concrete, $\varphi = 3.5$:		
and $k_{def} = 0.6$	$\psi_{con} = 2.6 - 0.8\gamma_c^2$	$\psi_{con} = 2.5 - \gamma_c^{1.1}$
and $k_{def} = 0.8$	$\psi_{con} = 2.3 - 0.5\gamma_c^{2.6}$	$\psi_{con} = 2.2 - 0.8\gamma_c^{1.2}$
Concrete, $\varphi = 2.5$:		
and $k_{def} = 0.6$	$\psi_{con} = 2.0 - 0.5\gamma_c^{1.9}$	$\psi_{con} = 1.9 – 0.6\gamma_c^{1.1}$
and $k_{def} = 0.8$	$\psi_{con} = 1.8 - 0.3\gamma_c^{2.5}$	$\psi_{con} = 1.7 - 0.5\gamma_c^{1.1}$
Timber:		
all cases	$\psi_{tim} = 1.0$	$\psi_{tim} = 0.5$
Connection:		
all cases	$\psi_{conn} = 1.0$	$\psi_{conn} = 0.65$

Note: For $t = 0$, the values of ψ_{con}, ψ_{tim}, and ψ_{conn} are 0.

5.5 Design of CLT-concrete composite floor in bi-dimensional bending

An orthotropic plate model is developed using a simple engineer software to study the bi-dimensional bending effect of the HOBOA system with point supports at one end and linear support at the other end of the specimen. In order to obtain satisfactory results, attention should be paid to the detailing of the model around the point supports. The stiffness and support conditions of the orthotropic plate model are detailed in sections 5.5.1 and 5.5.2, respectively.

5.5.1 Stiffness

For the orthotropic plate model, cross-section properties are defined by stiffness matrix C, as follows:

$$C = \begin{bmatrix} D_{11} & D_{12} & 0 & 0 & 0 & 0 & 0 & 0 \\ D_{21} & D_{22} & 0 & 0 & 0 & 0 & 0 & 0 \\ 0 & 0 & D_{33} & 0 & 0 & 0 & 0 & 0 \\ 0 & 0 & 0 & D_{44} & 0 & 0 & 0 & 0 \\ 0 & 0 & 0 & 0 & D_{55} & 0 & 0 & 0 \\ 0 & 0 & 0 & 0 & 0 & D_{66} & D_{67} & 0 \\ 0 & 0 & 0 & 0 & 0 & D_{76} & D_{77} & 0 \\ 0 & 0 & 0 & 0 & 0 & 0 & 0 & D_{88} \end{bmatrix} \quad (31)$$

where

$[D_{11}-D_{33}]$ describes the flexural stiffness matrix;

$[D_{44}-D_{55}]$ describes the shear stiffness matrix;

$[D_{66}-D_{88}]$ describes the membrane stiffness matrix.

For the orthotropic plate model, it has been verified that only the properties in flexural stiffness matrix influence the structural performance of the composite floor while the variation of values in shear stiffness matrix and membrane stiffness matrix has a little influence. The computation formulae for terms in shear stiffness matrix and membrane stiffness matrix are found in [7] and [8], respectively. In stiffness matrix C, the terms D_{11} and D_{22} are signified as the bending stiffness of composite floor in longitudinal direction $(EI)_{eff}$ and transversal direction $(EI)_{eff,T}$, respectively. The computation method for the bending stiffness of composite floor in longitudinal direction $(EI)_{eff}$, is described in section 5.4.1. For the bending stiffness of composite floor in transversal direction $(EI)_{eff,T}$, the gamma method described in Annex B of Eurocode 5 [4] is adopted by considering three effective layers of composite floor cross-section, consisting of the top concrete layer and two longitudinal timber layers of the CLT panel. It is assumed that no composite action is considered at the interface layer of composite floor in transversal direction. Accordingly, the gamma factor of concrete cross-section γ_c, is taken equal to zero. In addition, the concrete cross-section of composite floor in transversal direction shall include the presence of notch section, in cracked condition (see Figure 7). The following expressions from eqs. (32) to (33) describe the computation of the effective bending stiffness of concrete part in transversal direction.

$$(EI)_{eff,T,con.} = E_c \left[\frac{b x_s^3}{3} + \alpha_e A_{s1} (d_1 - x_s)^2 + \alpha_e A_{s2} (d_2 - x_s)^2 \right] \quad (32)$$

with

$$\alpha_e = E_s / E_{con} \quad (33)$$

$$x_s = \frac{\alpha_e (A_{s1} + A_{s2})}{b} \left[\sqrt{1 + \frac{2 b A_{s1} d_1 + A_{s2} d_2}{\alpha_e (A_{s1} + A_{s2})^2}} - 1 \right] \quad (34)$$

where

E_c is the modulus of elasticity of concrete panel;

b is the width of the composite floor;

x_s is the neutral axis position of the reinforced concrete panel;

α_e is the ratio between modulus of elasticity of steel and that of concrete;

A_{s1} is the reinforcement area in the concrete panel;

d_1 is the distance between the top surface of concrete panel to rebars in concrete panel;

A_{s2} is the reinforcement area in the notched connector;

d_2 is the distance between the top surface of concrete panel to rebars in notched connector;

E_s is the modulus of elasticity of steel.

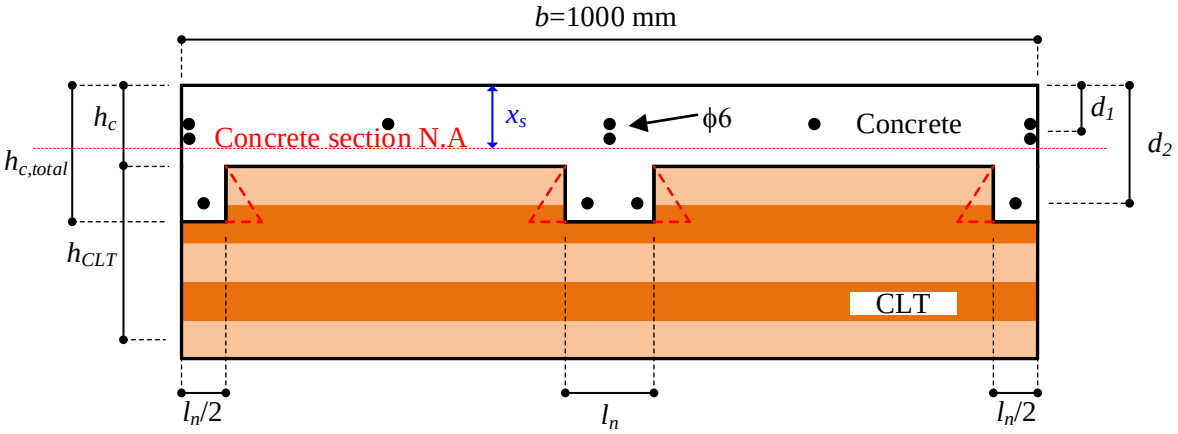

Figure 7: Cross-section of composite floor in transversal direction per one meter width.

Regarding the term D_{33} in the flexural stiffness matrix, it is signified as the torsional stiffness of the composite floor GI, which is included in the plate model by an addition of the torsional stiffness of the concrete panel $(GI)_{con}$ and the CLT panel $(GI)_{CLT}$, whose computation are found in [7]. For the off-diagonal terms of D_{12} and D_{21}, they are disregarded in stiffness matrix [9].

5.5.2 Support condition

Two types of the support configuration are adopted for the TCC floor: linear support which is conceptualized to represent the supporting wall and point support which is conceptualized to represent the supporting column. For the linear support system, pinned supports are applied to a line along the transversal direction of the floor model. To model the point support system, the actual dimensions and stiffnesses of the support shall be modelled in order not to overestimate the transversal deflections.

5.6 Conclusion

This chapter has presented a proposition for the design recommendations for the local and global behavior of the dovetail notched connection system and CLT-concrete composite floors (HOBOA system), respectively. For the notched connector, load-carrying resistance governed by different failure mechanisms are determined using proposed strut-and-tie model and analytical formulae, whereas the stiffness is derived from pushout tests. For the composite floor in one-dimensional bending effect, the detail of the gamma method in Eurocode 5 [4], later modified by Jiang et al. [5], is described and adopted to estimate the bending stiffness and cross-sectional resistances. Additionally, stress distribution in long-term behavior is also provided at the decisive point in time of t=0, t=3, t=7 year, and t=∞ (end of service life). For the composite floor in bi-dimensional bending effect, the developed orthotropic plate model is explained, providing comprehensive model detailing and cross-sectional definition in transversal direction.

5.7 References

[1] CEN/TS 19103 :2021. Eurocode 5 : Design of Timber Structures - Structural design of timber-concrete composite structures – Common rules and rules for buildings. European Committee for Standardization (CEN): Brussels, Belgium, 2021.

[2] Avis-Technique. 3.3/17-925 v1, Panneaux bois à usages structurel – mur et plancher, Wood structural panels, 2017.

[3] European standard EN 1992-1-1, Eurocode 2: Design of concrete structures - Part 1-1: General rules and rules for buildings, CEN, Brussels (2004).

[4] European standard EN 1995-1-1, Eurocode 5: Design of timber structures- Part 1-1: General — Common rules and rules for buildings, CEN, Brussels (2004).

[5] Jiang, Y., & Crocetti, R. (2019). CLT-concrete composite floors with notched shear connectors. Construction and Building Materials, 195, 127-139.

[6] CSTB: Appréciation Technique d'Expérimentation (ATEx). n° 2985_V1, 2022.

[7] Gustafsson, A. (2019). The CLT Handbook: CLT structures-facts and planning. Swedish Wood.

[8] Blaauwendraad, J. (2012). Plates and FEM. Springer.

[9] Akter, S. T., Bader, T. K., & Serrano, E. Stiffness of cross-laminated timber (CLT) wall-to-floor-to-wall connections in platform-type structures. In World Conference on Timber Engineering, 2021.

This page is intentionally left blank.

CHAPTER 6

Conclusions and future research

This page is intentionally left blank.

Contents

This page is intentionally left blank.

6.1 Conclusions

This thesis has addressed the study of a new CLT-concrete floor system, named HOBOA. The connection between materials is made by notches. They do not need to be supplemented by any metallic components linking the wood and the concrete to prevent the separation by uplifts of materials, thanks to their specific shape and to the presence of rebars inside the concrete notch. The research included experimental tests, numerical simulations, and analytical developments in order to understand on one hand the local behavior of the notched connection, and on the other hand the global behavior of the composite floor. It was intended to provide a simple design guideline yet capable of quantifying the behavior of notched connectors and composite floors.

At first, thus, the behavior of the proposed notched connector was studied in order to determine the strength, stiffness, and post-peak performance. The following conclusions obtained from the experimental, numerical, and analytical studies of the notched connector can be drawn:

- The series of three symmetrical pushout tests showed the high shear resistance and stiffness of connectors, but with a low ductility, as the failure mode of all specimens was governed by the rolling shear resistance of the cross-layer of the CLT panel. A comparison was made with other notched connection systems found in literature. It showed that the present notched connector had high resistance and stiffness as other usual notched connections, indicating the efficiency of the dovetail notched connector in the TCC system.
- The numerical model of pushout tests was made by taking into account the actual geometry, interface interactions, material properties, and boundary conditions. It was capable of reproducing the same failure mode and giving a good agreement of the force-slip curve compared to that of pushout tests, validating the model. In addition, various values of timber Poisson ratios and friction coefficients between timber and concrete, taken from the literature, were studied using this validated FE model to investigate their effects on the model. For timber Poisson ratios, a negligible effect was observed. For the interface friction coefficient, the model with the coefficient value of 0.62 suggested by Aira et al. [1] yielded good results in terms of maximum force and stiffness in comparison to pushout test curves. However, with the coefficient value of 0.40 recommended by Eurocode 5 [2], the FE model provided similar results in terms of maximum force, but approximately 15 percent difference concerning the slip moduli compared to the case with the coefficient value of 0.62. On the other hand, in order to investigate the behavior of pure rolling shear of the cross-layer of the CLT panel in the load transfer mechanism from the CLT panel to concrete panel, a new configuration of loading block (middle loading block), was adopted in the FE simulation (C-Ref.M case). The findings demonstrated that the maximum force obtained from the C-Ref.M simulation case was 38 percent value lower and slip moduli at SLS and ULS decreased by 37 percent value in comparison to the simulation of experimental case (C-Ref case). When loading is applied to the CLT-concrete composite floor, the whole CLT section will be subjected to the applied load, resulting in transferring a portion of load via a longitudinal layer of the CLT panel and the rest by rolling shear. Therefore, the resistance and stiffness obtained in C-Ref case should be adopted to define the bending stiffness of the CLT-concrete composite floor.

- The validated experimental pushout test model (C-Ref case) and a new pushout test model with the middle loading configuration (C-Ref.M case) were then adopted to conduct a parametric study with variations in geometries and material properties. The results demonstrated that the connection system maintained high strength and stiffness for all the values of investigated parameters. In addition, it was shown that it should be possible to improve the ductility of the notched connection by prioritizing the shear concrete failure at shear plane of the concrete notch, if a sufficient number of V-shape rebars is placed inside the notch. This prioritization can be obtained by increasing the spacing between the notched connectors. The concrete shear failure should happen for a load 22 percent value larger than the experimental resistance obtained from pushout tests. These numerical results call for an experimental validation.
- Considering four possible different failure mechanisms of the connection system, analytical methods derived from design codes were tested to evaluate the load-carrying capacity of the pushout specimen by a comparison with experimental and numerical results. For the concrete shear resistance at shear plane of the concrete notch, a strut-and-tie model was developed, taking into account the principal stress map and contact forces of the concrete panel obtained from the pushout test model. For the rolling shear resistance of the CLT panel, a simple analytical equation was found applicable to determine the rolling shear resistance of the cross-layer of the CLT panel. However, based on simulation results obtained from C-Ref and C-Ref.M cases, the connection resistance governed by the rolling shear failure in the CLT panel should be equal to 1.38 times the value obtained from such a mentioned equation. The remaining two possible failure mechanisms in the notched connection, including the compressive failure of concrete and the compressive failure of timber at load bearing surface of the concrete notch, were supposed to be estimated by the expression proposed in the technical specification CEN/TS 19103 [3].

Following the comprehensive characterization of dovetail notched connectors, full-scale CLT-concrete composite floors using the abovementioned notches as the connection system were studied. The behavior of the composite floor was characterized by conducting two positive flexural tests. The experimental results were then compared with the ones estimated by the gamma method and simple numerical models. The investigation of composite floors and its results are presented as follows:

- The series of two full-scale four-point bending tests were carried out on CLT-concrete composite floors, with a span of about 6.5 m, and a width of 3.2 m. The first specimen, HBF1, was supported on a linear support at one end, and on two point supports at the other end; the second specimen, HBF2, was lying on two linear supports. Both specimens demonstrated high bending resistances. Due to the support condition, test HBF1 was subjected to bi-dimensional bending effect, whereas test HBF2 was subjected to one-dimensional bending effect. The effective bending stiffness of both CLT-concrete composite floors, derived from the experimental tests, was also found comparable to that reported in other studies in literature.
- The gamma method as expressed in Eurocode 5 [1], later modified by Jiang et al. [4], was adopted to determine the effective bending stiffness, midspan deflection, and load-carrying capacity of the composite floor. The estimations obtained from the gamma method showed

a good agreement with test results. However, the gamma method provided a better estimation for the test in one-dimensional bending effect (test HBF2). A sensitivity analysis of the influence of the connectors' and rolling shear stiffness on the effective bending stiffness of composite floor using the gamma method showed that trying to increase further the wood-concrete connection stiffness would not have a noticeable effect since the stiffness of the wood-concrete connection with the spacing as adopted in the test was already high. Additionally, a comparison of force-slip curves derived from the flexural test and from pushout tests was made. When removing slips caused by pauses and cyclic loadings during the tests, a close correlation of force-slip curves of pushout tests and flexural test was obtained.

- A beam grid model and an orthotropic plate model were developed as a simplified tool to estimate the behavior of the composite floor in bi-dimensional bending. The orthotropic plate model provided a better result than the beam grid model. In order to study different assumptions made in the orthotropic plate model, a further investigation was performed. The results showed that the orthotropic plate model should take into account the torsional stiffness and consider the concrete section with presence of the notch, in cracked condition, for computing the bending stiffness of composite floor in transversal direction. For the point support condition, the actual dimensions and stiffness of the support should be modelled.

The general conclusions drawn from the study of CLT-concrete floors with dovetail notched connectors as the connection system are highlighted as follows:

1. The experimental campaigns have proven the relevance of the HOBOA system. It must be noted that they have been used by Architecture Plurielle in order to obtain an "Atex" certification, allowing the use of HOBOA system. A first building is under construction. It is a raising of an existing building, in Cesson-Sévigné, Rennes, France (see Figure 1).
2. The further analysis and extension of the results by numerical simulations and analytical developments have allowed to better understand both the local behavior of the connection, and the global behavior of the floor system. The findings have been used to write a draft of design guidance, based on the technical specification CEN/TS 19103 [3] that prefigures the new version of Eurocode 5. This first draft must however be looked with caution, as this work is partly based on numerical simulations that call for further experimental validation, and as it has not addressed directly the important aspects of time effects, and of the detailing of the junction between two elements of composite floors.

a. An existing concrete building with the application of HOBOA floor system

b. Installation of CLT panels

c. Installation of V-shape rebar cages and steel meshes.

d. Casting of concrete panel

e. HOBOA floor system after concrete casting

Figure 1: Application of HOBOA floor system on an existing building, in Cesson-Sévigné, Rennes, France (credit: Architecture plurielle).

6.2 Future research

As explained in general conclusions, it should be reminded that this thesis was the first step for the characterization of the local behavior of dovetail notched connectors and the global behavior of CLT-concrete composite floors with the studied notched connection system. A fully comprehensive understanding is hardly achieved in one doctoral thesis, and as usual this work opens a window for future research. Some relevant next steps can be proposed:

- The influence of geometries and material properties of notched connectors on the different failure mechanisms was determined by a numerical study. They should be confirmed by experimental pushout tests;
- The influence of the variation of the mechanical properties, including creep, shrinkage, moisture content of timber and concrete on the structural behavior of composite floors should be addressed through experimental tests;
- The structural behavior of a continuous floor should be taken into account since, in the practical application, the floors of office and residential buildings are sometimes designed as a continuous system.

6.3 References

[1] European standard EN 1995-1-1, Eurocode 5: Design of timber structures- Part 1-1: General — Common rules and rules for buildings, CEN, Brussels (2004).

[2] Aira, J. R., Arriaga, F., Íñiguez-González, G., & Crespo, J. (2014). Static and kinetic friction coefficients of Scots pine (Pinus sylvestris L.), parallel and perpendicular to grain direction. Materiales de Construcción, 64(315), e030-e030.

[3] CEN/TS 19103 :2021. Eurocode 5 : Design of Timber Structures - Structural design of timber-concrete composite structures – Common rules and rules for buildings. European Committee for Standardization (CEN): Brussels, Belgium, 2021.

[4] Jiang, Y., & Crocetti, R. (2019). CLT-concrete composite floors with notched shear connectors. Construction and Building Materials, 195, 127-139.

Annex A: Timber characterization tests

Timber characterization tests were conducted to determine the actual properties of timber, including the modulus of elasticity in longitudinal compression E_L, in transverse compression E_T, rolling shear modulus G_R, compression strength in longitudinal compression $f_{c,0}$, in transverse compression $f_{c,90}$, and the rolling shear strength f_r. The characterization tests are presented as the follows: the longitudinal compression, transverse compression and rolling shear tests.

1. Longitudinal compression test

The test samples had a cross-section of 32×32 mm and a height of 145 mm. The compression tests were carried out in accordance with EN 408 [1] on 12 samples (HBL01 to HBL12). The force was measured by a force sensor, whereas the relative displacement was determined as the mean value of the four LVDT displacement sensors. The modulus of elasticity in longitudinal compression E_L and compression strength in longitudinal compression $f_{c,0}$ are defined as follows:

$$E_L = \frac{L_0(F_{0.4}-F_{0.1})}{A_0(w_{0.4}-w_{0.1})} \tag{1}$$

$$f_{c,0} = \frac{F_{c,0}}{A_0} \tag{2}$$

where L_0, A_0 and $F_{c,0}$ are the initial length of the sample, the initial area of the sample and the maximum force obtained in longitudinal compression test, respectively. $w_{0.4}$ and $w_{0.1}$ are the relative displacements corresponding to 40 percent of maximum force $F_{0.4}$ and 10 percent of maximum force $F_{0.1}$, respectively. Figure 1 presents the force-displacement curves of all 12 tests. It should be noted that the relative displacements are computed as an average value of the four displacement sensors.

[1] EN 408:2003-08. Timber structures – Structural timber and glued laminated timber – Determination of some physical and mechanical properties. CEN European Committee for Standardization (2003)

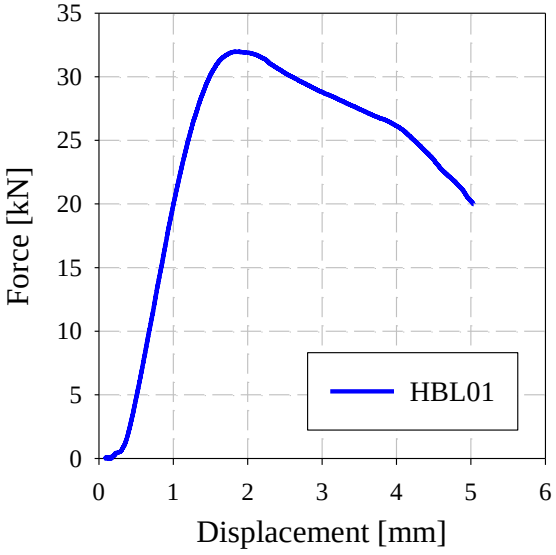

a. Test HBL01.

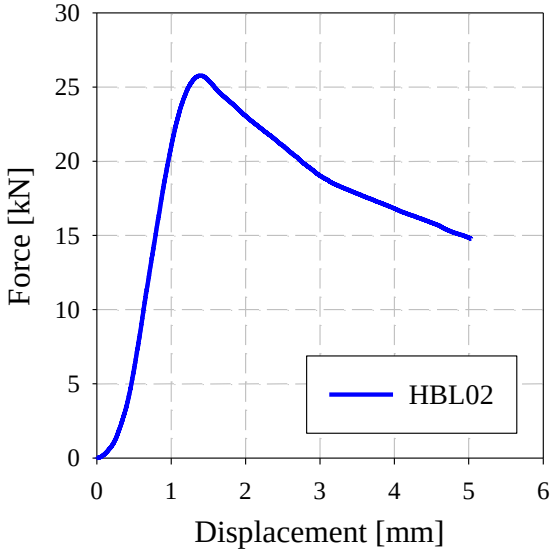

b. Test HBL02.

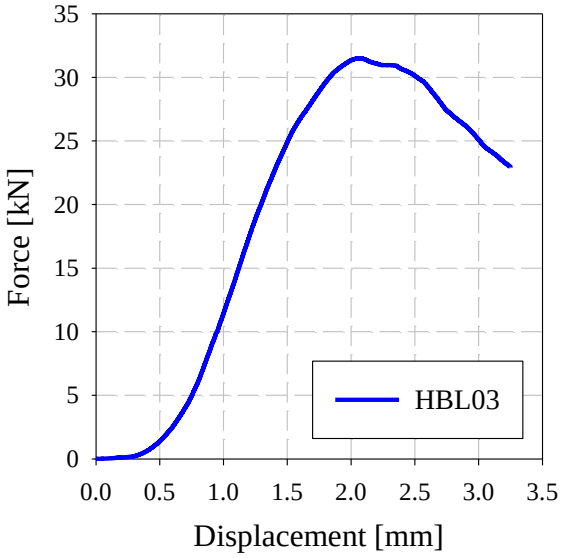

c. Test HBL03.

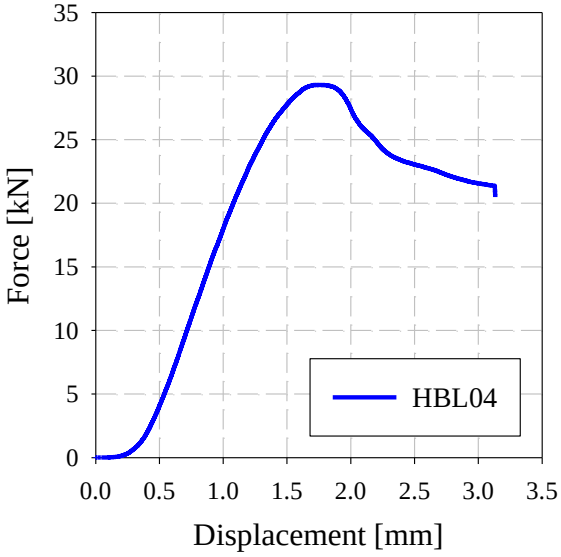

d. Test HBL04.

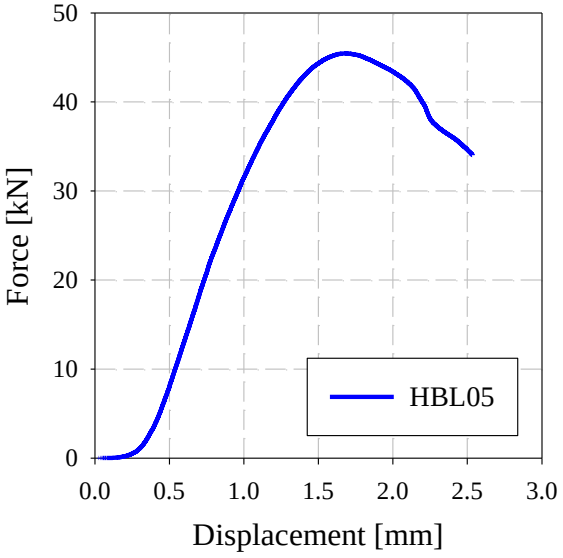

e. Test HBL05.

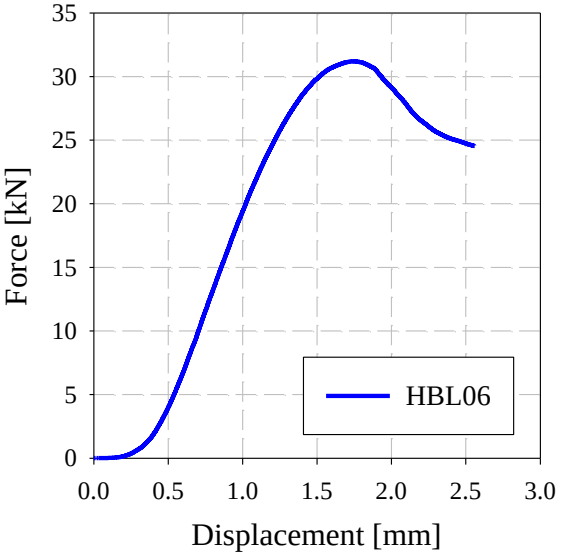

f. Test HBL06.

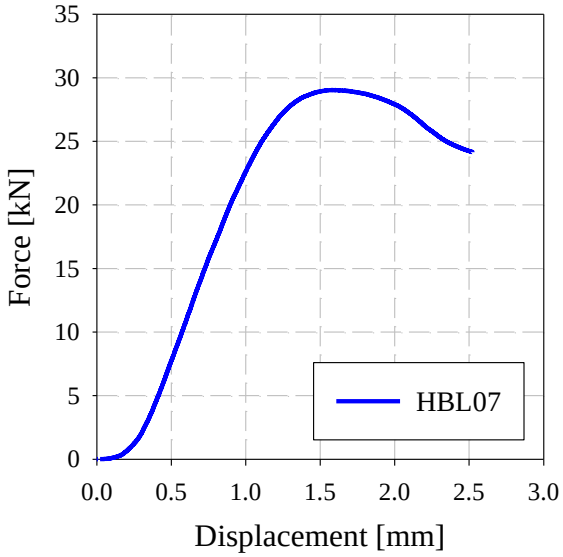

g. Test HBL07

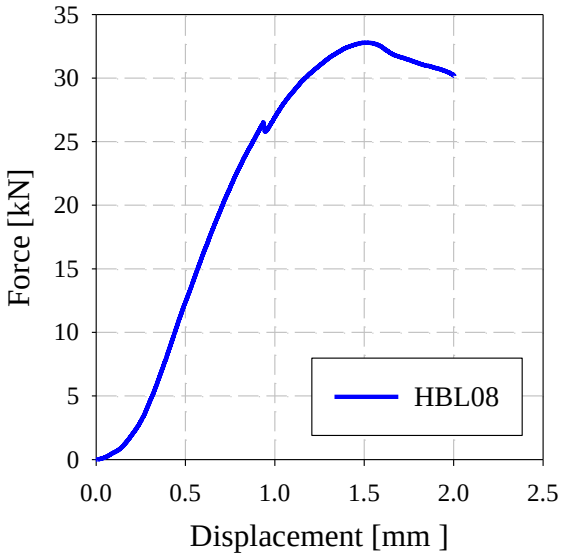

h. Test HBL08

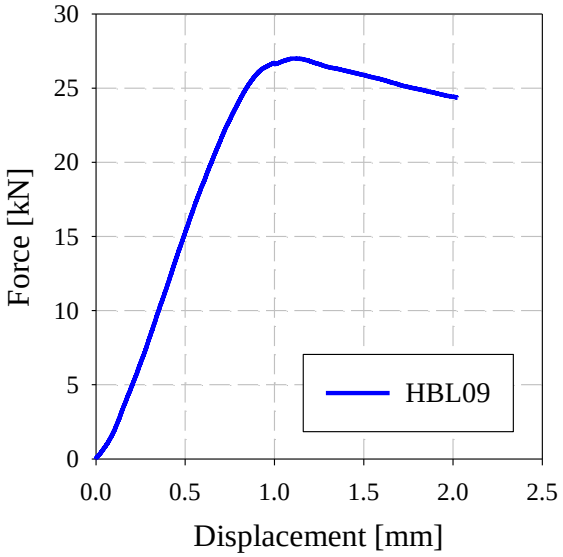

i. Test HBL09

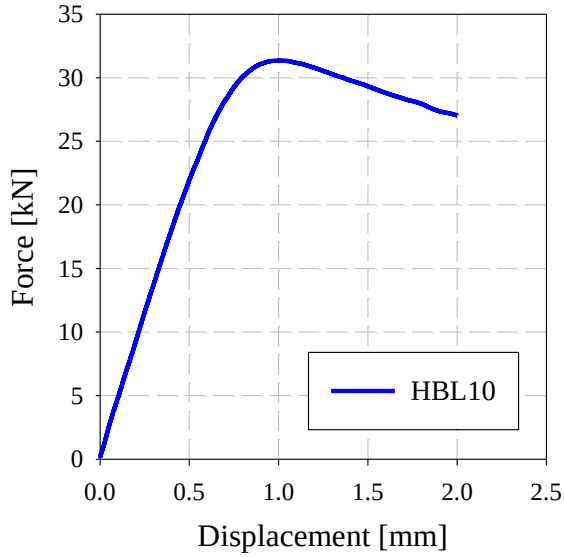

j. Test HBL10

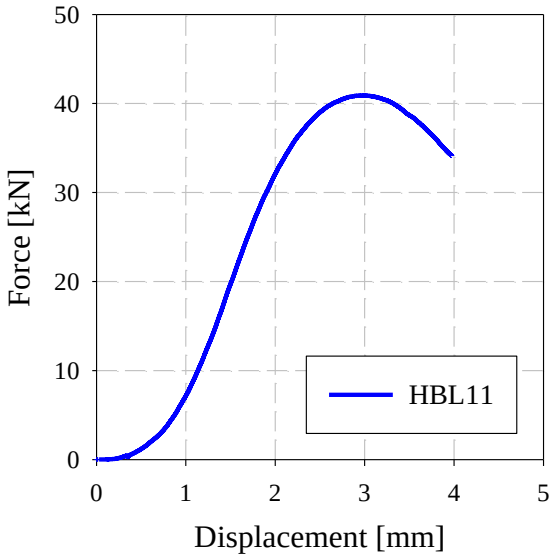

k. Test HBL11

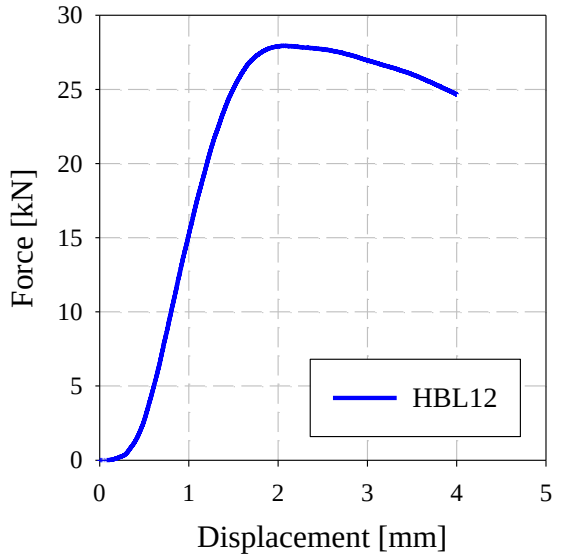

l. Test HBL12

Figure 1: Force-displacement curves of longitudinal compression tests.

The parameters for determining the modulus of elasticity and compression strength in longitudinal compression are derived from the force-displacement curves in Figure 1 and subsequently reported in Table 1.

Table 1: Modulus of elasticity and resistance of longitudinal compression tests.

Specimen	$F_{c,0}$ [kN]	F_{04} [kN]	F_{01} [kN]	$w_{0.4}$ [mm]	$w_{0.1}$ [mm]	E_L [MPa]	$f_{c,0}$ [MPa]
HBL 01	31.97	12.79	6.40	0.77	0.56	4992	31.22
HBL 02	25.77	10.31	5.15	0.32	0.15	4990	25.17
HBL 03	31.50	12.60	6.30	1.11	0.81	3411	30.77
HBL 04	29.31	11.72	5.86	0.77	0.57	4681	28.62
HBL 05	45.46	18.18	9.09	0.70	0.52	8271	44.39
HBL 06	31.21	12.48	6.24	0.78	0.58	5172	30.48
HBL 07	29.03	11.61	5.80	0.62	0.44	5159	28.35
HBL 08	32.79	13.11	6.56	0.52	0.36	6460	32.02
HBL 09	27.00	10.80	5.40	0.37	0.22	5526	26.36
HBL 10	31.36	12.57	6.27	0.27	0.13	7176	30.62
HBL 11	40.90	16.36	8.18	1.38	1.05	3976	39.95
HBL 12	27.94	11.17	5.59	0.85	0.63	4269	27.28

The results described in Table 1 are summarized in Table 2, in which $\bar{x}$ and s denote the mean value and the standard deviation, respectively.

Table 2: Material properties of timber under longitudinal compression tests.

Test	Number of specimens	Moisture content [%]	Modulus of elasticity		Strength	
			$\bar{x}$ [MPa]	s [MPa]	$\bar{x}$ [MPa]	s [MPa]
Long. compression	12	10.2	5317	1325	31.3	5.3

2. Transverse compression test

The test samples had a cross-section of 25×25 mm and a height of 145 mm. The compression tests were carried out in accordance with EN 408 [1] on 8 samples (HBP01 to HBP08). The force was measured by a force sensor, whereas the relative displacement was determined as the mean value of the four LVDT displacement sensors. The modulus of elasticity in transverse compression E_T and compression strength in transverse compression $f_{c,90}$ are defined as follows:

$$E_T = \frac{L_0(F_{0.4}-F_{0.1})}{A_0(w_{0.4}-w_{0.1})} \tag{3}$$

$$f_{c,90} = \frac{F_{c,90}}{A_0} \tag{4}$$

[1] EN 408:2003-08. Timber structures – Structural timber and glued laminated timber – Determination of some physical and mechanical properties. CEN European Committee for Standardization (2003)

where L_0, A_0 and $F_{c,90}$ are the initial length of the sample, the initial area of the sample and the maximum force obtained in transverse compression test, respectively. $w_{0.4}$ and $w_{0.1}$ are the relative displacements corresponding to 40 percent of maximum force $F_{0.4}$ and 10 percent of maximum force $F_{0.1}$, respectively. Figure 2 presents the force-displacement curves of all 8 tests. It should be noted that the relative displacements are computed as an average value of the four displacement sensors.

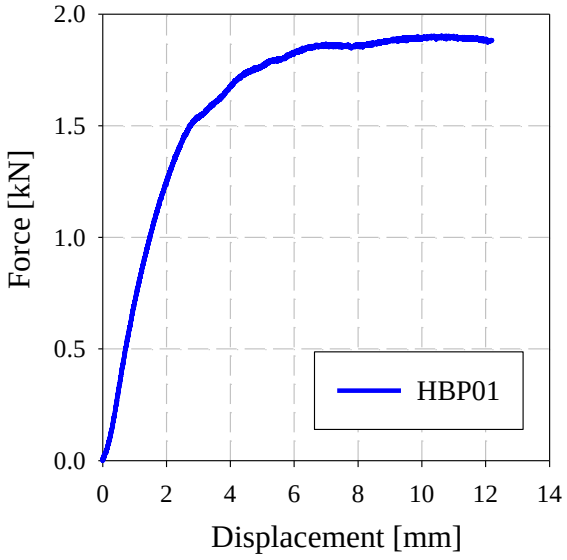

a. Test HBP01.

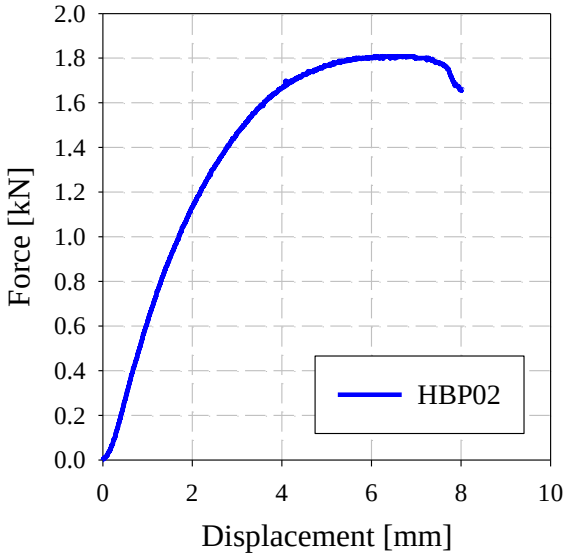

b. Test HBP02.

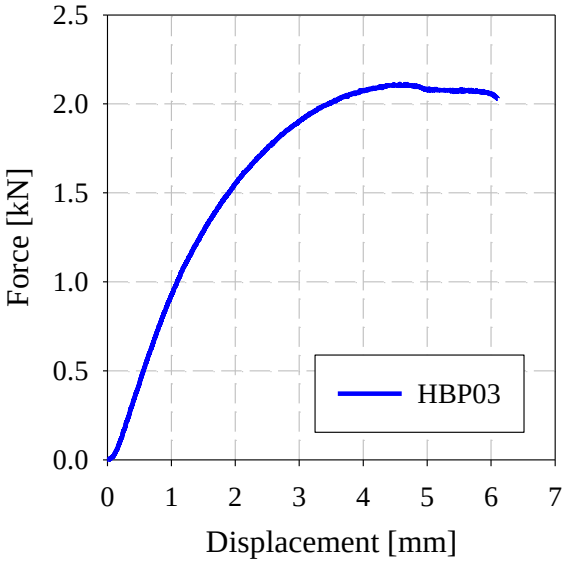

c. Test HBP03.

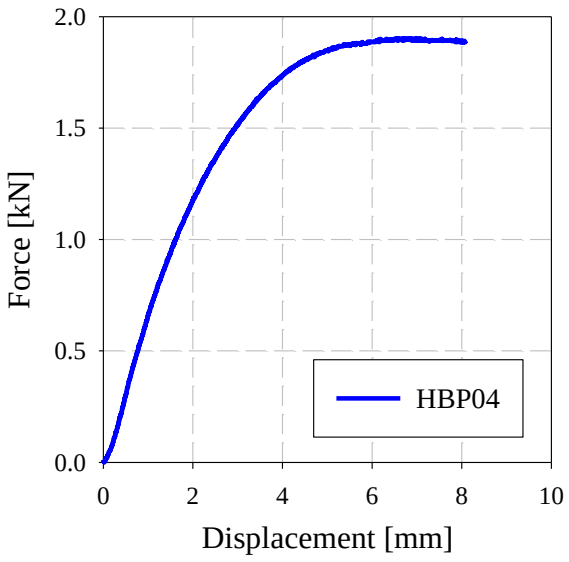

d. Test HBP04.

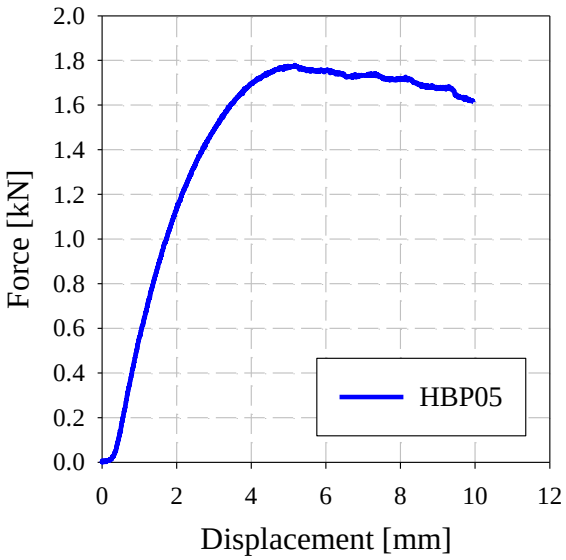

e. Test HBP05.

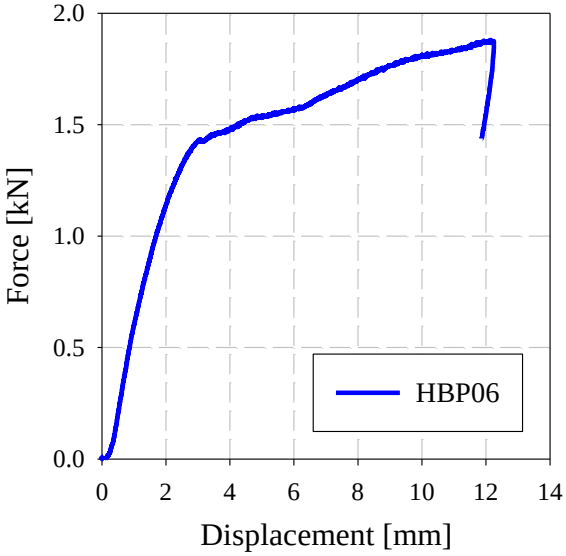

f. Test HBP06.

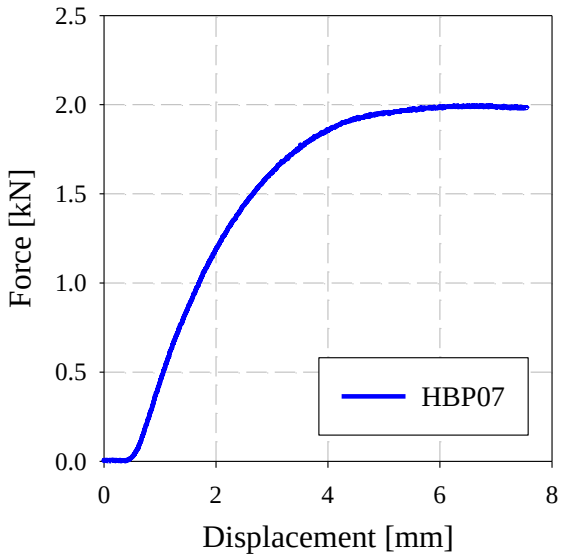

g. Test HBP07.

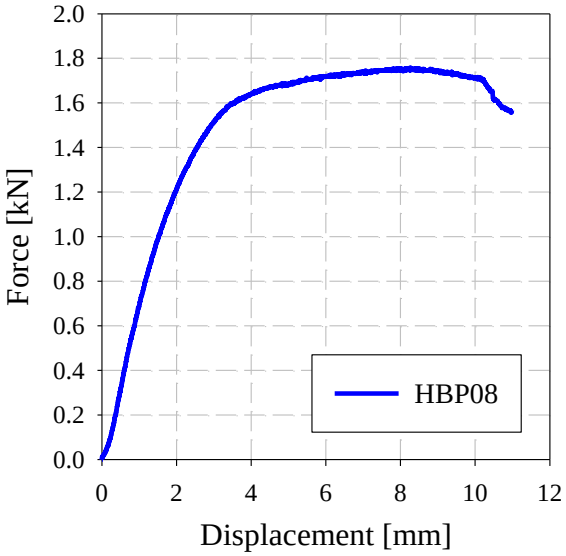

h. Test HBP08.

Figure 2: Force-displacement curves of transverse compression tests.

The parameters for determining the modulus of elasticity and strength in transverse compression are derived from the force-displacement curves in Figure 2 and subsequently reported in Table 3.

The results reported in Table 3 are summarized in Table 4, in which $\bar{x}$ and s denote the mean value and the standard deviation, respectively.

Table 3: Modulus of elasticity and resistance of transverse compression tests.

Specimen	$F_{c,90}$ [kN]	F_{04} [kN]	F_{01} [kN]	$w_{0.4}$ [mm]	$w_{0.1}$ [mm]	E_T [MPa]	$f_{c,90}$ [MPa]
HBP 01	1.9	0.76	0.19	1.07	0.34	156	3.04
HBP 02	1.8	0.72	0.18	1.17	0.38	138	2.89
HBP 03	2.11	0.84	0.21	0.91	0.34	224	3.38
HBP 04	1.90	0.76	0.19	1.16	0.35	140	3.04
HBP 05	1.77	0.71	0.17	1.22	0.53	153	2.84
HBP 06	1.88	0.75	0.18	1.24	0.48	149	3.0
HBP 07	1.99	0.79	0.199	1.41	0.74	178	3.19
HBP 08	1.75	0.70	0.175	1.01	0.33	155	2.81

Table 4: Material properties of timber under transverse compression tests.

Test	Number of specimens	Moisture content [%]	Modulus of elasticity		Strength	
			$\bar{x}$ [MPa]	s [MPa]	$\bar{x}$ [MPa]	s [MPa]
Trans. compression	8	9.6	162	26	3	0.2

3. Rolling shear test

Seven samples (HBS01 to HBS07) with three lamination layers (one cross-layer sandwiched by two longitudinal layers) were extracted from the CLT panel. These samples had dimensions of 99 mm thick by 140 mm large by 269 mm long. The force was measured by a force sensor, whereas the relative displacements were determined as the mean value of two LVDT displacement sensors. The rolling shear strength f_r and the rolling shear modulus G_R were respectively computed by [2]:

$$f_r = \frac{F_{max} \times \cos\alpha}{L_R \times w} \tag{5}$$

$$G_R = \frac{t_c}{L_R \times w} \times \frac{F_{0.5}\text{-}F_{0.2}}{s_{0.5}\text{-}s_{0.2}} \times \cos\alpha \tag{6}$$

where F_{max} is the maximum force. L_R and w are the height and the width of the specimen, respectively. t_c is the thickness of the cross-layer. α is the inclination angle of the specimen (α is taken as 14^0). $s_{0.5}$ and $s_{0.2}$ are the relative displacements corresponding to 50 percent of maximum force $F_{0.5}$ and 20 percent of maximum force $F_{0.2}$, respectively. Figure 3 presents the force-displacement curves of all 7 tests.

[2] Gong, M., Tu, D., Li, L., & Chui, Y. H. (2015). Planar shear properties of hardwood cross layer in hybrid cross laminated timber. ISCHP 2015, 85-90.

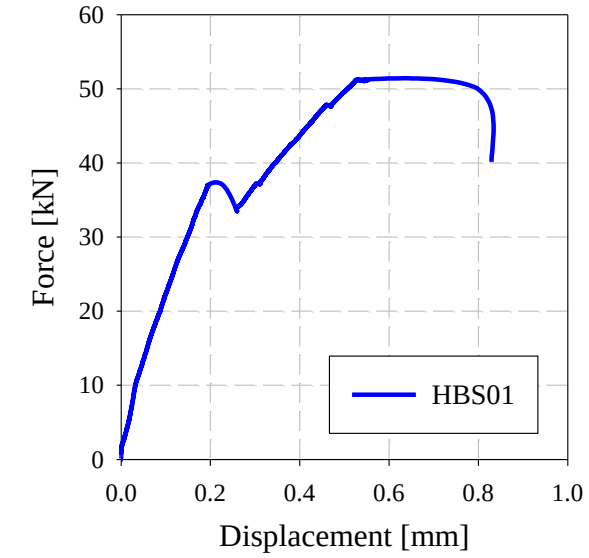

a. Test HBS01.

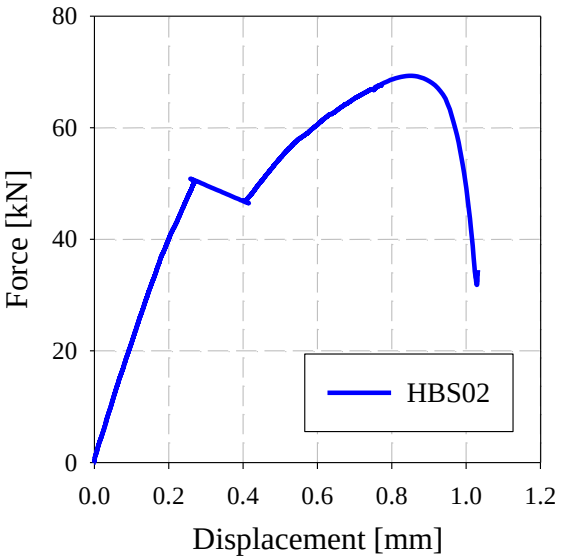

b. Test HBS02.

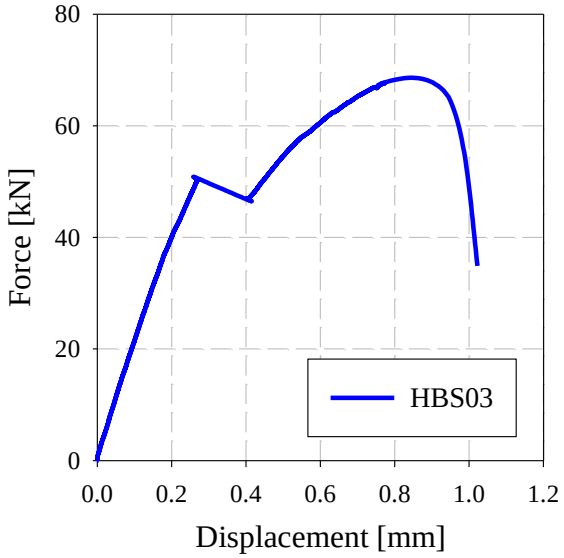

c. Test HBS03.

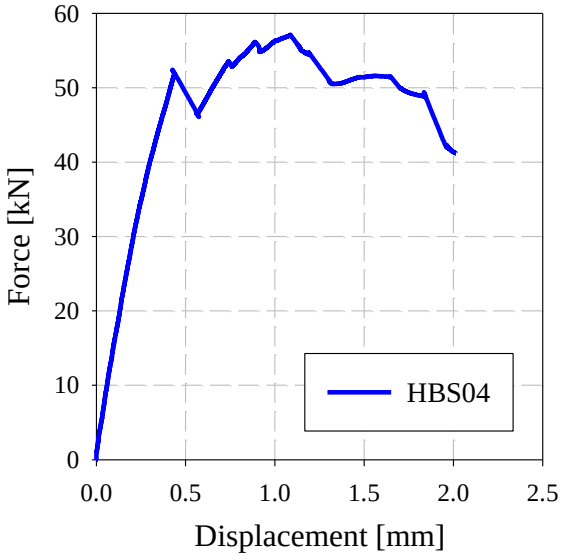

d. Test HBS04.

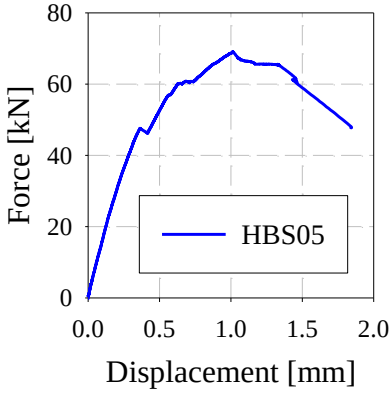

e. Test HBS05.

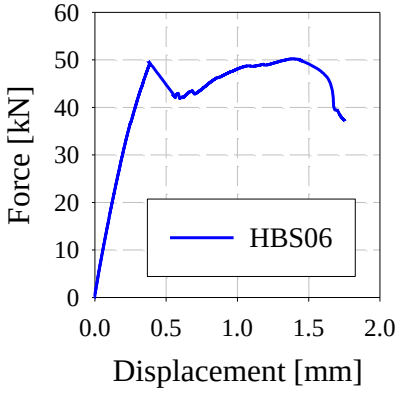

f. Test HBS06.

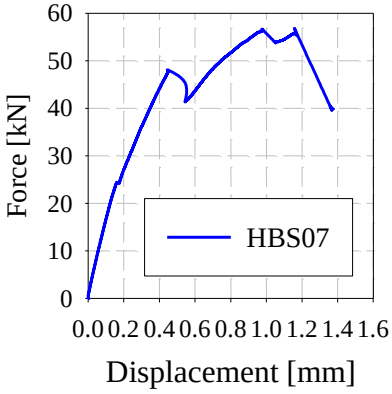

g. Test HBS07.

Figure 3: Force-displacement curves of rolling shear tests.

The parameters for determining rolling shear strength and rolling shear modulus are derived from the force-displacement curves in Figure 3 and reported in Table 5.

Table 5: Rolling shear strength and rolling shear modulus obtained in rolling shear tests.

Specimen	F_{max} [kN]	F_{05} [kN]	F_{02} [kN]	$s_{0.5}$ [mm]	$s_{0.2}$ [mm]	G_R [MPa]	f_r [MPa]
HBS 01	51.27	25.63	10.26	0.12	0.03	149	1.30
HBS 02	67.69	33.85	13.54	0.16	0.06	165	1.74
HBS 03	67.70	33.85	13.54	0.16	0.06	165	1.74
HBS 04	57.00	28.50	11.40	0.20	0.07	113	1.45
HBS 05	68.96	34.48	13.79	0.23	0.08	116	1.76
HBS 06	50.22	25.11	10.04	0.16	0.06	125	1.27
HBS 07	56.44	28.22	11.29	0.21	0.07	96	1.43

The results reported in Table 6 are summarized in Table 4, in which $\bar{x}$ and s denote the mean value and the standard deviation, respectively.

Table 6: Mechanical properties of the timber obtained in rolling shear tests.

Number of specimens	Moisture content [%]	Rolling shear modulus		Rolling shear strength	
		$\bar{x}$ [MPa]	s [MPa]	$\bar{x}$ [MPa]	s [MPa]
7	9.25	133	25	1.49	0.17

This page is intentionally left blank.

Annex B: Corrected midspan deflection curves of bending tests

In experimental tests, vertical displacement of supports was noticed and needed to take into account. Figure 1 presents the displacement correction of flexural tests. The red line denotes the rigid movement of the slab due to the settlement from the support system, and blue curve represents the actual deflection obtained from flexural tests. The symbols m_1 and m_2 refer to deflections obtained from CD1 and CD2 sensors, respectively, while m_3 denotes the midspan deflection recorded from point C3 of DIC method. The deflection obtained from CD1 and CD2 sensors near the supports, and from sensor C3 of DIC method at midspan of the specimen were contributed by the actual deflection generated from the settlement of the support system, c, and actual deflection induced by the applied load, f.

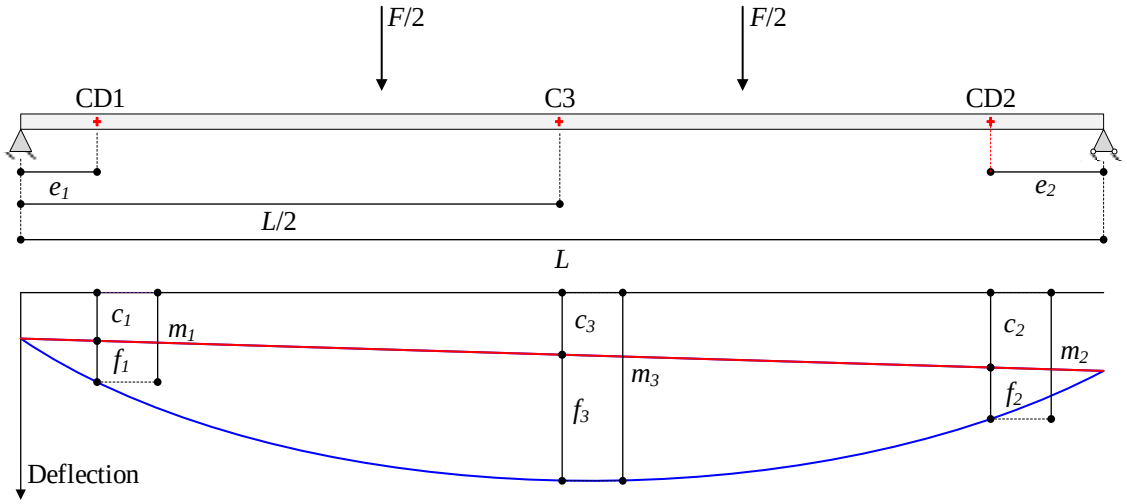

Figure 1: Displacement correction of flexural tests.

The deflections m_1, m_2, and m_3 measured at position of CD1, CD2, and C3 can be written as following equations:

$$m_1=c_1+f_1 \quad (1)$$

$$m_2=c_2+f_2 \quad (2)$$

$$m_3=c_3+f_3 \quad (3)$$

The actual deflections f_1 and f_2 are computed in function of f_3 as follows:

$$f_1=\alpha f_3 \quad (4)$$

$$f_2=\beta f_3 \quad (5)$$

From the graphical detail of the deflection in Figure 1, the ratio of loading position on the composite floor can be written:

$$\frac{1}{2}=\frac{c_2-c_3}{c_2-c_1} \quad (6)$$

Accordingly, from eqs. (1)&(4) and (2)&(5), support deflections c_1 and c_2 can be found:

$$c_1=m_1 - \alpha f_3 \tag{7}$$

$$c_2=m_2 - \beta f_3 \tag{8}$$

Using eqs. (6), (7), and (8), the actual midspan deflection, f_3, can be determined as follows:

$$f_3=\frac{m_3-0.5(m_1+m_2)}{1-0.5(\alpha+\beta)} \tag{9}$$

It should be noted that the deflection at any given point x along the length L, can be determined using given equation.

$$f(x)=\frac{F}{2EI}\left(-\frac{x^4}{12}+\frac{Lx^3}{6}-\frac{L^3x}{12}\right) \tag{10}$$

Adopting eq. (10) in eqs. (4) and (5), value α and β can be determined accordingly.

$$\alpha=\frac{f_1}{f_3}=\frac{f(0.3m)}{f(L/2)}=0.15$$

$$\beta=\frac{f_2}{f_3}=\frac{f(L-0.3m)}{f(L/2)}=0.15.$$

Annex C: Numerical application of the gamma method to composite floor in longitudinal direction

This section presents the application of the gamma method for the estimation of effective bending stiffness, and load-carrying capacity of composite specimen of test HBF1 and test HBF2.

1. Input data

The input data for the numerical application of the gamma method are given in the following sections. Figure 1 illustrates the configuration of cross-section of the composite specimen in longitudinal direction.

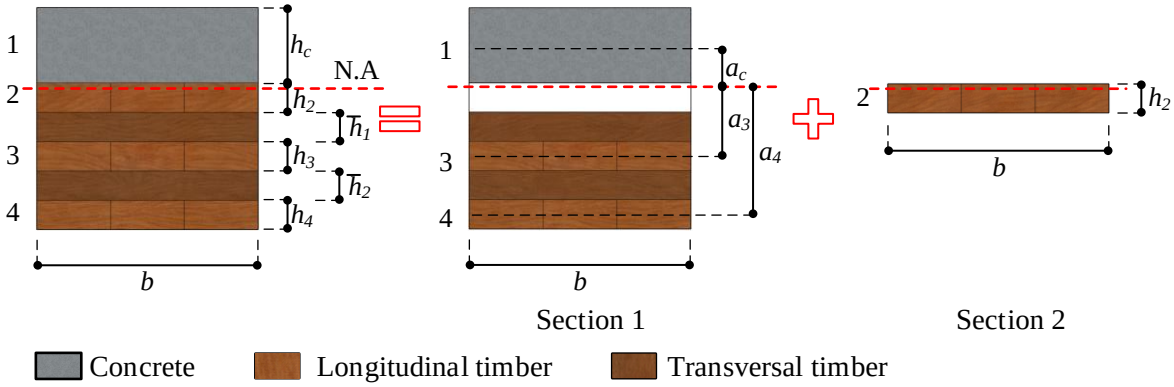

Figure 1: Computation of 5-layer CLT-concrete slabs.

1.1 Specimen configuration

Span of composite specimen	$L=\begin{cases}6440 \text{ mm} & \text{for test HBF1}\\ 6540 \text{ mm} & \text{for test HBF2}\end{cases}$
Distance between support and loading point of bending test setup	$c=\begin{cases}2170 \text{ mm} & \text{for test HBF1}\\ 2220 \text{ mm} & \text{for test HBF2}\end{cases}$
Width of composite specimen	b = 1000 mm
Height of composite specimen	h = 250 mm

1.2 Concrete section

Height of concrete layer	h_c = 85 mm
Area of concrete section	A_c = 8500 mm^2
Mean value of concrete compressive strength	f_{cm} = 55 MPa
Mean modulus of elasticity of concrete	E_c = 36689 MPa

1.3 CLT section

Height of each layer of CLT panel	$\begin{cases} h_2, h_3, h_4 = 33 \text{ mm} \\ \overline{h}_1, \overline{h}_2 = 33 \text{ mm} \end{cases}$
Area of each layer of CLT panel	$A_2, A_3, A_4 = 33000 \text{ mm}^2$
Mean modulus of elasticity of each layer of CLT panel	$E_2, E_3, E_4 = 11500 \text{ MPa}$
Rolling shear modulus	$G_R = 60 \text{ MPa}$
Tensile strength parallel to grain	$f_{t,0} = 23 \text{ MPa}$
Bending strength parallel to grain	$f_m = 38 \text{ MPa}$
Shear strength	$f_v = 5.56 \text{ MPa}$
Rolling shear strength	$f_r = 1.49 \text{ MPa}$

1.4 Notched connectors

Slip modulus at the serviceability limit state	$K_s = 1.49\times10^6 \text{ N/mm}$
Slip modulus at the ultimate limit state	$K_u = 1.03\times10^6 \text{ N/mm}$
Minimum spacing	$s_{min} = 500 \text{ mm}$
Maximum spacing	$s_{max} = 625 \text{ mm}$
Effective spacing	$s_{eff} = 531.25 \text{ mm}$

2. Bending stiffness

2.1 Test HBF1

2.1.1 Using slip modulus K_s ($K_s = 1.49\times10^6$ N/mm)

Combined distributed stiffness,

$$\left(\frac{K}{s}\right)_c = \frac{\left(K_c/s_{eff}\right)\times\left(G_R b/\overline{h}_1\right)}{\left(K_c/s_{eff}\right)+\left(G_R b/\overline{h}_1\right)} = \frac{\left(1.49\times10^6/531.25\right)\times(60\times1000/33)}{\left(1.49\times10^6/531.25\right)+(60\times1000/33)} = 1.10\times10^6 \text{ N/mm}^2$$

Concrete gamma coefficient γ_c,

$$\gamma_c = \left[1+\frac{\pi^2 E_c A_c}{L^2}\times\left(\frac{s}{K}\right)_c\right]^{-1} = \left[1+\frac{\pi^2\times36689\times85000}{6440^2}\times1.10\times10^6\right]^{-1} = 0.60$$

Gamma coefficient of middle longitudinal layer of CLT panel γ_3, γ_3=1,

Gamma coefficient of bottom longitudinal layer of CLT panel γ_4,

$$\gamma_4 = \left[1+\frac{\pi^2 E_4 A_4 \bar{h}_2}{G_R b_4 L^2}\right]^{-1} = \left[1+\frac{\pi^2 \times 11500 \times 33000 \times 33}{60 \times 1000 \times 6440^2}\right]^{-1} = 0.95$$

a_3 distance,

$$a_3 = \frac{\gamma_c E_c A_c (h_c/2 + h_2 + \bar{h}_1 + h_3/2) - \gamma_4 E_4 A_4 (h_3/2 + \bar{h}_2 + h_4/2)}{\sum_{i=c;3;4} \gamma_i E_i A_i}$$

$$= \frac{0.60 \times 36689 \times 85000 \times (85/2+33+33+33/2) - 0.95 \times 11500 \times 33000 \times (33/2+33+33/2)}{0.60 \times 36689 \times 85000 + 1 \times 11500 \times 33000 + 0.95 \times 11500 \times 33000} = 80.29 \text{ mm}$$

a_c distance,

$$a_c = \frac{h_c}{2} + h_2 + \bar{h}_1 + \frac{h_3}{2} - a_3 = 85/2+33+33+33/2-80.29 = 44.71 \text{ mm}$$

a_4 distance,

$$a_4 = \frac{h_3}{2} + \bar{h}_2 + \frac{h_4}{2} + a_3 = 33/2+33+33/2+80.29 = 146.29 \text{ mm}$$

Effective bending stiffness $(EI)_{eff}$

$$(EI)_{eff} = (EI)_{eff,1} + (EI)_{eff,2} = \sum_{i=c;3;4} \left(E_i I_i + \gamma_i E_i A_i a_i^2\right) + E_2 b_2 h_2^3/12$$

$$= 36689 \times 1000 \times 85^3/12 + 0.60 \times 36689 \times 85000 \times 44.71^2 + 11500 \times 1000 \times 33^3/12 + 1 \times 11500 \times 33000 \times 80.29^2$$
$$+ 11500 \times 1000 \times 33^3/12 + 0.95 \times 11500 \times 33000 \times 146.29^2 + 11500 \times 1000 \times 33^3/12$$
$$= 1.59 \times 10^{13} \text{ Nmm}^2$$

2.1.2 Using slip modulus K_u (K_u = 1.03×10^6 N/mm)

Combined distributed stiffness,

$$\left(\frac{K}{s}\right)_c = \frac{(K_c/s_{eff}) \times (G_R b/\bar{h}_1)}{(K_c/s_{eff}) + (G_R b/\bar{h}_1)} = \frac{(1.03 \times 10^6/531.25) \times (60 \times 1000/33)}{(1.03 \times 10^6/531.25) + (60 \times 1000/33)} = 0.94 \times 10^6 \text{ N/mm}^2$$

Concrete gamma coefficient γ_c,

$$\gamma_c = \left[1+\frac{\pi^2 E_c A_c}{L^2}\times\left(\frac{s}{K}\right)_c\right]^{-1} = \left[1+\frac{\pi^2\times 36689\times 85000}{6440^2}\times 0.94\times 10^6\right]^{-1} = 0.56$$

Gamma coefficient of middle longitudinal layer of CLT panel γ_3, γ_3=1,

Gamma coefficient of bottom longitudinal layer of CLT panel γ_4,

$$\gamma_4 = \left[1+\frac{\pi^2 E_4 A_4 \bar{h}_2}{G_R b_4 L^2}\right]^{-1} = \left[1+\frac{\pi^2\times 11500\times 33000\times 33}{60\times 1000\times 6440^2}\right]^{-1} = 0.95$$

a_3 distance,

$$a_3 = \frac{\gamma_c E_c A_c(h_c/2+h_2+\bar{h}_1+h_3/2)-\gamma_4 E_4 A_4 (h_3/2+\bar{h}_2+h_4/2)}{\sum_{i=c;3;4}\gamma_i E_i A_i}$$

$$= \frac{0.56\times 36689\times 85000\times(85/2+33+33+33/2)-0.95\times 11500\times 33000\times(33/2+33+33/2)}{0.56\times 36689\times 85000+1\times 11500\times 33000+0.95\times 11500\times 33000} = 78.07 \text{ mm}$$

a_c distance,

$$a_c = \frac{h_c}{2}+h_2+\bar{h}_1+\frac{h_3}{2}-a_3 = 85/2+33+33+33/2-78.07 = 46.93 \text{ mm}$$

a_4 distance,

$$a_4 = \frac{h_3}{2}+\bar{h}_2+\frac{h_4}{2}+a_3 = 33/2+33+33/2+78.07 = 144.07 \text{ mm}$$

Effective bending stiffness $(EI)_{eff}$

$$(EI)_{eff} = (EI)_{eff,1}+(EI)_{eff,2} = \sum_{i=c;3;4}\left(E_i I_i+\gamma_i E_i A_i a_i^2\right)+E_2 b_2 h_2^3/12$$

$$= 36689\times 1000\times 85^3/12+0.56\times 36689\times 85000\times 46.93^2+11500\times 1000\times 33^3/12+1\times 11500\times 33000\times 78.07^2$$
$$+11500\times 1000\times 33^3/12+0.95\times 11500\times 33000\times 144.07^2+11500\times 1000\times 33^3/12$$
$$= 1.56\times 10^{13} \text{ Nmm}^2$$

2.2 Test HBF2

2.2.1 Using slip modulus K_s (K_s = 1.49×10^6 N/mm)

Combined distributed stiffness,

$$\left(\frac{K}{s}\right)_c = \frac{\left(K_c/s_{eff}\right)\times\left(G_R b/\bar{h}_1\right)}{\left(K_c/s_{eff}\right)+\left(G_R b/\bar{h}_1\right)} = 1.10\times10^6 \text{ N/mm}^2$$

Concrete gamma coefficient γ_c,

$$\gamma_c = \left[1+\frac{\pi^2 E_c A_c}{L^2}\times\left(\frac{s}{K}\right)_c\right]^{-1} = 0.61$$

Gamma coefficient of middle longitudinal layer of CLT panel γ_3, γ_3=1,

Gamma coefficient of bottom longitudinal layer of CLT panel γ_4,

$$\gamma_4 = \left[1+\frac{\pi^2 E_4 A_4 \bar{h}_2}{G_R b_4 L^2}\right]^{-1} = 0.95$$

a_3 distance,

$$a_3 = \frac{\gamma_c E_c A_c(h_c/2+h_2+\bar{h}_1+h_3/2)-\gamma_4 E_4 A_4 (h_3/2+\bar{h}_2+h_4/2)}{\sum_{i=c;3;4}\gamma_i E_i A_i} = 80.65$$

a_c distance,

$$a_c = \frac{h_c}{2}+h_2+\bar{h}_1+\frac{h_3}{2}-a_3 = 44.35 \text{ mm}$$

a_4 distance,

$$a_4 = \frac{h_3}{2}+\bar{h}_2+\frac{h_4}{2}+a_3 = 146.65 \text{ mm}$$

Effective bending stiffness $(EI)_{eff}$

$$(EI)_{eff} = (EI)_{eff,1}+(EI)_{eff,2} = \sum_{i=c;3;4}\left(E_i I_i+\gamma_i E_i A_i a_i^2\right)+E_2 b_2 h_2^3/12 = 1.59\times10^{13} \text{ Nmm}^2$$

2.2.2 Using slip modulus K_u (K_u = 1.03×10^6 N/mm)

Combined distributed stiffness,

$$\left(\frac{K}{s}\right)_c = \frac{\left(K_c/s_{eff}\right)\times\left(G_R b/\bar{h}_1\right)}{\left(K_c/s_{eff}\right)+\left(G_R b/\bar{h}_1\right)} = 0.94\times10^6 \text{ N/mm}^2$$

Concrete gamma coefficient γ_c,

$$\gamma_c = \left[1+\frac{\pi^2 E_c A_c}{L^2}\times\left(\frac{s}{K}\right)_c\right]^{-1} = 0.57$$

Gamma coefficient of middle longitudinal layer of CLT panel γ_3, γ_3=1,

Gamma coefficient of bottom longitudinal layer of CLT panel γ_4,

$$\gamma_4 = \left[1+\frac{\pi^2 E_4 A_4 \bar{h}_2}{G_R b_4 L^2}\right]^{-1} = 0.95$$

a_3 distance,

$$a_3 a_3 = \frac{\gamma_c E_c A_c(h_c/2+h_2+\bar{h}_1+h_3/2)-\gamma_4 E_4 A_4 (h_3/2+\bar{h}_2+h_4/2)}{\sum_{i=c;3;4}\gamma_i E_i A_i} = 78.48$$

a_c distance,

$$a_c = \frac{h_c}{2}+h_2+\bar{h}_1+\frac{h_3}{2}-a_3 = 46.52 \text{ mm}$$

a_4 distance,

$$a_4 = \frac{h_3}{2}+\bar{h}_2+\frac{h_4}{2}+a_3 = 144.48 \text{ mm}$$

Effective bending stiffness $(EI)_{eff}$

$$(EI)_{eff} = (EI)_{eff,1}+(EI)_{eff,2} = \sum_{i=c;3;4}\left(E_i I_i+\gamma_i E_i A_i a_i^2\right)+E_2 b_2 h_2^3/12 = 1.57\times10^{13} \text{ Nmm}^2$$

3. Load-carrying capacity

3.1 Test HBF1

3.1.1 Using slip modulus K_s (K_s = 1.49×10^6 N/mm)

- Compressive stress on concrete panel:

$$\sigma_{c,t}=\sigma_c+\sigma_{m,c} \le f_{cm} \leftrightarrow \left(\frac{\gamma_c E_c a_c}{(EI)_{eff}}+\frac{0.5E_c h_c}{(EI)_{eff}}\right)\frac{F_{max}c}{2} = f_{cm}$$

$$\rightarrow F_{max} = \frac{2f_{cm}}{\left(\frac{\gamma_c E_c a_c}{(EI)_{eff}}+\frac{0.5E_c h_c}{(EI)_{eff}}\right)c} = \frac{2\times 55}{\left(\frac{0.60\times 36689\times 45}{1.59\times 10^{13}}+\frac{0.5\times 36689\times 45\times 85}{1.59\times 10^{13}}\right)\times 2170} = 317 \text{ kN}$$

- Combined bending and axial tension:

$$\frac{\sigma_4}{f_{t,0}}+\frac{\sigma_{m,4}}{f_m} \le 1 \leftrightarrow \left(\frac{\gamma_4 E_4 a_4}{(EI)_{eff}\times f_{t,0}}+\frac{0.5E_4 h_4}{(EI)_{eff}\times f_m}\right)\frac{F_{max}c}{2} = 1$$

$$\rightarrow F_{max} = \frac{2}{\left(\frac{\gamma_4 E_4 a_4}{(EI)_{eff}\times f_{t,0}}+\frac{0.5E_4 h_4}{(EI)_{eff}\times f_m}\right)c} = \frac{2}{\left(\frac{0.95\times 11500\times 146}{1.59\times 10^{13}\times 23}+\frac{0.5\times 11500\times 33}{1.59\times 10^{13}\times 38}\right)\times 2170} = 200 \text{ kN}$$

- Longitudinal shear stress in composite cross-section:

$$\tau_{max} \le f_{vd} \leftrightarrow \frac{\gamma_4 E_4 h_4 a_4+0.5E_3(a_3+0.5h_3)^2}{(EI)_{eff}}\times\frac{F_{max}}{2} = f_v \rightarrow F_{max} = \frac{2f_v(EI)_{eff}}{\gamma_4 E_4 h_4 a_4+0.5E_3(a_3+0.5h_3)^2}$$

$$= \frac{2\times 5.56\times 1.59\times 10^{13}}{0.95\times 11500\times 33\times 146+0.5\times 11500\times(33+0.5\times 80)^2} = 2112 \text{ kN}$$

- Rolling shear stress in CLT section:

$$\tau_r \le f_{rd} \leftrightarrow \frac{\gamma_3 E_3 h_3 a_3}{(EI)_{eff}}\times\frac{F_{max}}{2} = f_r \rightarrow F_{max} = \frac{2f_r(EI)_{eff}}{\gamma_3 E_3 h_3 a_3} = \frac{2\times 1.49\times 1.59\times 10^{13}}{1\times 11500\times 33\times 80} = 1554 \text{ kN}$$

- Verification of the fasteners:

$$F_s \le F_N \leftrightarrow \frac{\gamma_c E_c A_c a_c s}{(EI)_{eff}} \times \frac{F_{max}}{2} = F_N \rightarrow F_{max} = \frac{2F_N(EI)_{eff}}{\gamma_c E_c A_c a_c s} = \frac{2\times437\times1.59\times10^{13}}{0.60\times36689\times85000\times45\times531} = 314 \text{ kN}$$

Based on results obtained from the above computations when using slip modulus K_s, it shows that the failure of the composite floor is governed by combined bending and axial tension in CLT part with load-carrying capacity of F_{max} = 200 kN.

3.1.2 Using slip modulus K_u (K_u = 1.03×10^6 N/mm)

- Compressive stress on concrete panel:

$$\sigma_{c,t} = \sigma_c + \sigma_{m,c} \le f_{cm} \rightarrow F_{max} = \frac{2f_{cm}}{\left(\frac{\gamma_c E_c a_c}{(EI)_{eff}} + \frac{0.5E_c h_c}{(EI)_{eff}}\right)c} = 314 \text{ kN}$$

- Combined bending and axial tension:

$$\frac{\sigma_4}{f_{t,0}} + \frac{\sigma_{m,4}}{f_m} \le 1 \rightarrow F_{max} = \frac{2}{\left(\frac{\gamma_4 E_4 a_4}{(EI)_{eff}\times f_{t,0}} + \frac{0.5E_4 h_4}{(EI)_{eff}\times f_m}\right)c} = 196 \text{ kN}$$

- Longitudinal shear stress in composite cross-section:

$$\tau_{max} \le f_{vd} \rightarrow F_{max} = \frac{2f_v(EI)_{eff}}{\gamma_4 E_4 h_4 a_4 + 0.5E_3(a_3 + 0.5h_3)^2} = 2101 \text{ kN}$$

- Rolling shear stress in CLT section:

$$\tau_r \le f_{rd} \rightarrow F_{max} = \frac{2f_r(EI)_{eff}}{\gamma_3 E_3 h_3 a_3} = 1572 \text{ kN}$$

- Verification of the fasteners:

$$F_s \le F_N \rightarrow F_{max} = \frac{2F_N(EI)_{eff}}{\gamma_c E_c A_c a_c s} = 315 \text{ kN}$$

Based on results obtained from the above computations when using slip modulus K_u, it shows that the failure of the composite floor is governed by combined bending and axial tension in CLT part with load-carrying capacity of F_{max} = 196 kN.

3.2 Test HBF2

3.2.1 Using slip modulus K_s (K_s = 1.49×10^6 N/mm)

- Compressive stress on concrete panel:

$$\sigma_{c,t}=\sigma_c+\sigma_{m,c} \le f_{cm} \rightarrow F_{max} = \frac{2f_{cm}}{\left(\frac{\gamma_c E_c a_c}{(EI)_{eff}} + \frac{0.5E_c h_c}{(EI)_{eff}}\right)c} = 311 \text{ kN}$$

- Combined bending and axial tension:

$$\frac{\sigma_4}{f_{t,0}} + \frac{\sigma_{m,4}}{f_m} \le 1 \rightarrow F_{max} = \frac{2}{\left(\frac{\gamma_4 E_4 a_4}{(EI)_{eff} \times f_{t,0}} + \frac{0.5E_4 h_4}{(EI)_{eff} \times f_m}\right)c} = 196 \text{ kN}$$

- Longitudinal shear stress in composite cross-section:

$$\tau_{max} \le f_{vd} \rightarrow F_{max} = \frac{2f_v(EI)_{eff}}{\gamma_4 E_4 h_4 a_4 + 0.5E_3(a_3+0.5h_3)^2} = 2113 \text{ kN}$$

- Rolling shear stress in CLT section:

$$\tau_r \le f_{rd} \rightarrow F_{max} = \frac{2f_r(EI)_{eff}}{\gamma_3 E_3 h_3 a_3} = 1553 \text{ kN}$$

- Verification of the fasteners:

$$F_s \le F_N \rightarrow F_{max} = \frac{2F_N(EI)_{eff}}{\gamma_c E_c A_c a_c s} = 313 \text{ kN}$$

Based on results obtained from the above computations when using slip modulus K_u, it shows that the failure of the composite floor is governed by combined bending and axial tension in CLT part with load-carrying capacity of F_{max} = 196 kN.

3.2.2 Using slip modulus K_u (K_u = 1.03×10^6 N/mm)

- Compressive stress on concrete panel:

$$\sigma_{c,t}=\sigma_c+\sigma_{m,c} \le f_{cm} \rightarrow F_{max} = \frac{2f_{cm}}{\left(\frac{\gamma_c E_c a_c}{(EI)_{eff}} + \frac{0.5E_c h_c}{(EI)_{eff}}\right)c} = 307 \text{ kN}$$

- Combined bending and axial tension:

$$\frac{\sigma_4}{f_{t,0}} + \frac{\sigma_{m,4}}{f_m} \le 1 \rightarrow F_{max} = \frac{2}{\left(\frac{\gamma_4 E_4 a_4}{(EI)_{eff} \times f_{t,0}} + \frac{0.5E_4 h_4}{(EI)_{eff} \times f_m}\right)c} = 195 \text{ kN}$$

- Longitudinal shear stress in composite cross-section:

$$\tau_{max} \le f_{vd} \rightarrow F_{max} = \frac{2f_v(EI)_{eff}}{\gamma_4 E_4 h_4 a_4 + 0.5E_3(a_3+0.5h_3)^2} = 2122 \text{ kN}$$

- Rolling shear stress in CLT section:

$$\tau_r \le f_{rd} \rightarrow F_{max} = \frac{2f_r(EI)_{eff}}{\gamma_3 E_3 h_3 a_3} = 1570 \text{ kN}$$

- Verification of the fasteners:

$$F_s \le F_N \rightarrow F_{max} = \frac{2F_N(EI)_{eff}}{\gamma_c E_c A_c a_c s} = 315 \text{ kN}$$

Based on results obtained from the above computations when using slip modulus K_u, it shows that the failure of the composite floor is governed by combined bending and axial tension in CLT part with load-carrying capacity of F_{max} = 195 kN.

Annex D: Numerical application of gamma method to composite floor in transversal direction

This section presents the application of the gamma method for the estimation of effective bending stiffness of test HBF1 and test HBF2 with slip modulus of notched connectors at the serviceability limit state K_s.

1. Input data

The input data for the numerical application of the gamma method are given in the following sections. Figure 1 illustrates the configuration of cross-section of the composite specimen in transversal direction.

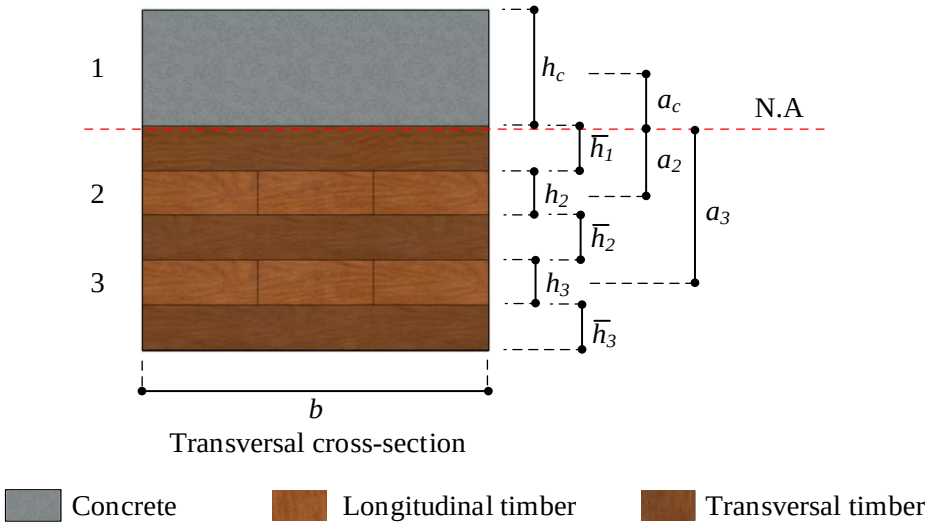

Figure 1: Cross-section of composite floor in transversal direction.

1.1 Specimen configuration

Width of composite specimen	b = 1000 mm
Height of composite specimen	h = 250 mm
Span of composite specimen	l= 3200 mm

1.2 Concrete section

Height of concrete layer	h_c = 85 mm
Area of concrete section	A_c = 8500 mm^2
Mean modulus of elasticity of concrete	E_c = 36689 MPa

1.3 CLT section

Height of each layer of CLT panel	$\begin{cases} h_2, h_3 = 33 \text{ mm} \\ \bar{h}_1, \bar{h}_2 = 33 \text{ mm} \end{cases}$
Area of each layer of CLT panel	A_2, A_3 = 33000 mm^2
Mean modulus of elasticity of each layer of CLT panel	E_2, E_3, = 11500 MPa
Rolling shear modulus	G_R = 60 MPa

1.4 Notched connectors

Slip modulus at the serviceability limit state	$K_s = 1.49 \times 10^6$ N/mm
Slip modulus at the ultimate limit state	$K_u = 1.03 \times 10^6$ N/mm

2. Bending stiffness

Gamma coefficient of concrete γ_c, γ_c=0 (no connection at interface layer),

Gamma coefficient of middle longitudinal layer of CLT panel γ_2, γ_2=1,

Gamma coefficient of bottom longitudinal layer of CLT panel γ_3,

$$\gamma_3 = \left[1 + \frac{\pi^2 E_3 A_3 \bar{h}_2}{G_R b L^2}\right]^{-1} = \left[1 + \frac{\pi^2 \times 11500 \times 33000 \times 33}{60 \times 1000 \times 3200^2}\right]^{-1} = 0.83$$

a_2 distance,

$$a_2 = \frac{\gamma_c E_c A_c (h_c/2 + \bar{h}_1 + h_2/2) - \gamma_3 E_3 A_3 (h_2/2 + \bar{h}_2 + h_3/2)}{\sum_{i=c;2;3} \gamma_i E_i A_i}$$

$$= \frac{0 \times 36689 \times 85000 \times (85/2+33+33/2) - 0.83 \times 11500 \times 33000 \times (33/2+33+33/2)}{0 \times 36689 \times 85000 + 1 \times 11500 \times 33000 + 0.83 \times 11500 \times 33000} = -30 \text{ mm}$$

a_c distance,

$$a_c = \frac{h_c}{2} + h_2 + \bar{h}_1 + \frac{h_2}{2} - a_2 = 85/2+33+33/2+30 = 122 \text{ mm}$$

a_3 distance,

$$a_3 = \frac{h_2}{2} + \bar{h}_2 + \frac{h_3}{2} + a_2 = 33/2+33+33/2-30 = 36 \text{ mm}$$

Effective bending stiffness $(EI)_{eff}$

$$(EI)_{eff} = \sum_{i=c;2;3} (E_i I_i + \gamma_i E_i A_i a_i^2)$$

$= 36689 \times 1000 \times 85^3/12 + 0 \times 36689 \times 85000 \times 122^2 + 11500 \times 1000 \times 33^3/12 + 1 \times 11500 \times 33000 \times 30^2$

$+ 11500 \times 1000 \times 33^3/12 + 0.83 \times 11500 \times 33000 \times 36^2$

$= 2.85 \times 10^{13}$ Nmm^2

Titre : **Comportement du plancher composite en CLT-béton avec connecteurs encoche en forme de queue d'aronde**

Mots clés : Connecteurs encoches, planchers composites en béton-CLT, essais pushout, essais de flexion, méthode gamma, modèle bielle-tirant, modèle de plaque orthotrope, modèle poutre-triangle, simulation EF.

Résumé : Cette thèse présente une étude des planchers composites en CLT-béton dont la connexion est réalisée par une encoche en utilisant des études expérimentales, numériques et analytiques.

Tout d'abord, le comportement du connecteur est caractérisé. Trois essais pushout sont réalisés pour déterminer la résistance, la rigidité et la ductilité du connecteur. Ensuite, un modèle aux éléments finis (EF) des essais pushout est également développé et validé par rapport aux résultats expérimentaux. De plus, une étude paramétrique utilisant le modèle EF validé est réalisé pour étudier l'influence des propriétés des matériaux et des géométries du connecteur. En parallèle des essais expérimentaux et des études numériques, des méthodes analytiques sont aussi adoptées pour évaluer la résistance du connecteur et sont comparées aux résultats expérimentaux et numériques.

Le comportement global des planchers mixtes est ensuite étudié. Une série de deux essais de flexion à quatre points avec différentes conditions d'appui (effets de flexion uni-dimensionnelle et bi-dimensionnelle) est d'abord réalisée pour caractériser les propriétés mécaniques des planchers mixtes. La méthode gamma est ensuite adoptée et comparée aux résultats d'essais. Une bonne corrélation est obtenue, en particulier dans le cas des essais en flexion uni-dimensionnelle. Pour estimer le comportement du plancher composite en flexion bidimensionnelle, un modèle de plaque orthotrope est développé.

Enfin, les résultats obtenus sur le comportement local du système de connexion et sur le comportement global du plancher composite en béton-CLT ont été utilisés pour rédiger des recommandations de calcul.

Title : **Behavior of CLT-concrete composite floor with dovetail notched connectors**

Keywords : Dovetail-shaped notched connectors, CLT-concrete composite floors, pushout tests, flexural tests, gamma method, beam grid model, orthotropic plate model, strut-and-tie model, FE simulation.

Abstract : This doctoral thesis presents a study of CLT-concrete composite floors with dovetail notched connectors using experimental, numerical, and analytical studies.

First, the behavior of notched connector is characterized. Three pushout tests are conducted to determine the strength, stiffness, and ductility of the notched connector. Then, the finite element (FE) model is developed based on test results. Furthermore, a parametric study using the validated FE model is conducted to investigate the influence of geometries and material properties of the notched connector. In parallel to experimental tests and numerical studies, analytical methods are developed to evaluate the load-carrying capacity of the pushout specimen and verified with experimental and numerical results.

Following the findings obtained from the study of notched connectors, the global behavior of CLT-concrete composite floors with notched connectors is studied. Two four-point bending tests with different support conditions (one-dimensional and bi-dimensional bending behaviors) are first conducted to characterize the mechanical properties of composite floors. Next, the gamma method is adopted and compared with test results. A good correlation is obtained, particularly in the case of test in one-dimensional bending. To estimate the behavior of the composite floor in bi-dimensional bending, an orthotropic plate model is developed.

Lastly, the findings in both the local behavior of the notched connector and the global behavior of the CLT-concrete composite floor have been used to draft a design guidance.